Beam Dynamics Challenges in the Muon $g-2$ Experiment

Brynn MacCoy

A dissertation
submitted in partial fulfillment of the
requirements for the degree of

Doctor of Philosophy

University of Washington
2023

Reading Committee:
Peter Kammel, Chair
David Hertzog
Gray Rybka

Program Authorized to Offer Degree:
Physics

University of Washington

Abstract

Beam Dynamics Challenges in the Muon $g-2$ Experiment

Brynn MacCoy

Chair of the Supervisory Committee:

Professor Peter Kammel
Physics

The muon's anomalous magnetic moment a_μ has hinted at physics beyond the standard model for nearly 20 years. The Muon $g-2$ experiment at Fermilab aims to measure a_μ to 140 parts per billion (ppb) precision. The 460 ppb result from its first data run (Run-1), released in 2021, agreed with the previous 2006 Brookhaven Muon $g-2$ result. The experimental average stands in tension with the standard model theory a_μ prediction by 4.2σ. The result of Run-2/3 data analysis is set be released in summer 2023, and will improve on the Run-1 precision by a factor of two. With the data collected in all six runs, the experiment is on track to produce a 140 ppb measurement of a_μ. If the experiment and theory central values are both unchanged, the tension would exceed 5σ. The measurement is accomplished by injecting muons into a magnetic storage ring and precisely measuring two observable frequencies: ω_a, the muons' anomalous precession frequency, and $\tilde{\omega}'_p$, the precession frequency of protons which determines the magnetic field strength experienced by the muons. This thesis presents a selection of muon beam dynamics effects which are critical for reaching the experiment precision goal. A system of detectors assists with the challenging beam injection into the storage ring, and a measurement of the injected beam provides input for simulating the stored beam dynamics. A new method is introduced to reduce a critical systemic caused by time dependence in the stored beam momentum, enabled by a detector which directly profiles the stored beam. Finally the analysis of $\tilde{\omega}'_p$, the muon-weighted magnetic field, for the Run-2/3 result is presented. Systematics of $\tilde{\omega}'_p$ due to beam effects are evaluated in detail, and shown to be sub-dominant.

Acknowledgements

The list of people who have supported me on this quest is too long to do them justice. However, the biggest thanks of all goes to my advisor Peter Kammel, whose endless zeal for particle physics and capacity for solving complex problems are a true inspiration. Thank you for believing I could accomplish this work, working on detectors with me late at night in the lab, and supporting me through all the ups and downs of graduate school. A huge thank you also to my mentor Dave Hertzog for pushing me to prioritize the important problems and guiding me to grow as a physicist.

All the members of the UW muon group, past and present, have helped me learn and have fun at the same time. In particular, my office mates Hannah Binney and Josh LaBounty shared this journey and battled the FermiGrid with me. Christine Claessens encouraged me and developed the MiniSciFi detector beyond what I dreamed, and Lara Dippel's assistance on the MiniSciFi was crucial. Erik Swanson connected me with the muon-weighted magnetic field analysis, which turned into a major part of my thesis work. Thanks also to the CENPA engineers and staff who made this work possible, especially David Peterson, Tim Van Wechel, Ryan Roehnelt, and Tom Burritt.

Endless gratitude goes to all my fellow Muon $g-2$ collaborators. David Tarazona, Tyler Barrett, Elia Bottalico, James Mott, Anna Driutti, and Renee Fatemi were wonderful colleagues, resources, and beam dynamics enthusiasts. Saskia Charity and Brendan Kiburg created a welcoming space in the Bloch field analysis team, and Simon Corrodi simplified all sorts of complex tasks on the experiment. Jim Morgan spent countless hours finessing the beam for the studies Peter and I dreamed up.

I am grateful to my PhD committee members Gray Rybka, Miguel Morales, Gordon Watts, David Kaplan, and Ellen Garvens, especially my thesis readers for the immensely helpful feedback. Thank you especially to Miguel for being the first physics professor to truly believe in me as a physicist. Even further back, thank you to my high school math teacher Hong Nguyen for showing me that the mathematical description of the universe can be so cool.

Finally, I could not have reached the finish line without all the love and support of my friends and family, human and feline. Thanks especially to my husband Reid for keeping me going with laughter and coffee, and to Mom and Dad for your unfailing love and sacrifice and for making my education a priority.

DEDICATION

To every physics enthusiast who feels like they don’t quite fit.

“Isn’t it splendid to think of all the things there are to find out about?”

— L. M. Montgomery, *Anne of Green Gables*

Contents

List of Figures

List of Tables

Glossary

- **SM**: The standard model theoretical framework of particle physics
- **BSM**: Beyond the standard model physics
- **FNAL**: Fermi National Accelerator Laboratory, or Fermilab, which hosts the current Muon $g-2$ experiment
- **BNL**: Brookhaven National Laboratory, where the previous Muon $g-2$ experiment was located
- **ppm**: Parts per million
- **ppb**: Parts per billion
- **Run**: Few-month data collection period, e.g. Run-1; six runs were completed in total.
- **dataset**: Subdivision of a Run, typically around 2 weeks
- **ctags**: Decay positron counts in the calorimeters, used for statistics weighting
- **IBMS**: Inflector Beam Monitoring System detectors, which profile the beam at injection to the storage ring
- **SiPM**: Silicon photomultiplier, a type of light sensor based on Geiger-mode avalanche photodiodes
- **SciFi**: Scintillating fiber, an optical fiber embedded with scintillating material
- **NMR**: Nuclear magnetic resonance; NMR probes are used to map the magnetic field.
- **Muon-weighted magnetic field**: The magnetic field experienced by the muons, called $\tilde{B}$, or $\tilde{\omega}'_p$ in terms of the proton NMR frequency
- **FR**: Fast rotation, the beam rotation around the ring at the cyclotron frequency. FR analysis is used to reconstruct the beam momentum distribution.
- τ-p **correlation**: Correlation between the beam injection time and stored momentum caused by the kicker magnet, which distorts the FR reconstruction
- **MiniSciFi**: Minimally Intrusive Scintillating Fiber detector, which directly profiles the stored beam
- **Betatron oscillation**: Oscillation of the beam transverse to its nominal orbit, caused by the restoring force of the quadrupole electric field
- β **function**: The function which describes the beam envelope
- **emittance**: The quantity which describes the invariant beam phase space area, also called ϵ

- **dispersion**: The function which describes the momentum dependence of the beam trajectory
- **momentum offset**: A particle's relative momentum difference from the nominal momentum, also called δ
- **COD**: Closed orbit distortion, a distortion of the beam orbit in the ring caused by field nonuniformities

Chapter 1

Introduction

The anomalous magnetic moment of the muon a_μ is the deviation of the muon's gyromagnetic ratio from 2,

$$a_\mu \equiv \frac{g_\mu - 2}{2} \, . \tag{1.1}$$

a_μ can be predicted by standard model (SM) theory and is an excellent experimental test of the standard model. The muon magnetic moment has been measured with increasing precision since the 5%-precision measurement at the Nevis cyclotron in 1957 [1]. Most recently in 2021 the E989 Fermilab (FNAL) Muon $g-2$ experiment released a measurement of a_μ to 460 parts per billion (ppb) precision [2] from its first data collection run. Previously, the E821 Brookhaven National Lab (BNL) Muon $g-2$ experiment measured a_μ to 540 ppb with the final result released in 2006 [3]. The combined experiment average stands in tension with the current SM-predicted value by 4.2σ, or 4.2 times the uncertainty in the SM calculation and experimental value combined (Figure 1.1 and Table 1.1). This discrepancy suggests new physics beyond the standard model (BSM), but is not yet at the discovery level of 5σ. Recent developments in the hadronic contribution to the SM value may reduce this tension (Section 1.2.3); work is underway in the theory community to understand the discrepancies and evaluate the impact on the SM value.

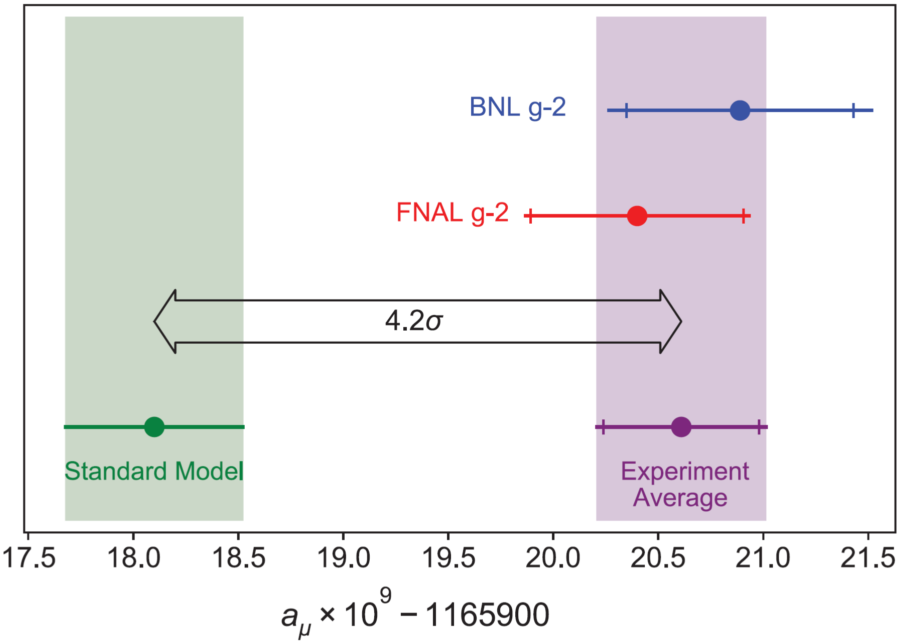

Figure 1.1: The experimental and standard model theory values of a_μ are in tension by 4.2σ as of 2021. The 2006 BNL experiment result (blue) and 2021 Fermilab experiment result (red) are combined to give the experiment average (purple), with inner bars indicating the statistical contributions to the total uncertainties. The SM value is that recommended by the Muon $g-2$ Theory Initiative in 2020 [4]. Reproduced from [2].

	value (uncertainty) $\times 10^{11}$	**uncertainty [ppb]**
BNL experiment a_μ^{BNL} [3]	116 592 080(63)	540
FNAL experiment a_μ^{FNAL} [2]	116 592 040(54)	460
Experiment average a_μ^{Exp} [2]	116 592 061(41)	350
Standard Model a_μ^{SM} [4]	116 591 810(43)	369
	difference (uncertainty) $\times 10^{11}$	**significance**
$\Delta a_\mu = a_\mu^{Exp} - a_\mu^{SM}$ [2]	251(59)	4.2σ

Table 1.1: Experimental and standard model (SM) theory values of a_μ. The experiment average is the combined result including the 2021 FNAL and 2006 BNL results. The difference between the experiment and SM values corresponds to a 4.2σ tension.

The Fermilab Muon $g-2$ experiment aims to measure a_μ to an unprecedented 140 ppb precision, $\sim 4\times$ more precise than the previous BNL measurement. The target precision is split into 100 ppb each for systematic and statistical uncertainties, and the statistics goal requires $21\times$ the data collected at BNL. The basic method is to inject polarized muons into a magnetic storage ring and measure their spin precession frequency via the spectrum of the decay positrons using calorimeter detectors. The experimental result a_μ is extracted using a ratio of the measured spin precession frequency to the magnetic field in the storage ring, both of which must be measured to high precision. The Fermilab experiment re-uses the same well-understood storage ring magnet from BNL, which required a large-scale effort to transport it from Brookhaven, NY to Batavia, IL. It is nevertheless a completely independent experiment, featuring entirely new and upgraded major systems including the calorimeter detectors, magnetic field tracking probes, and polarized muon production beamline (all discussed in detail in Chapter 2). The Fermilab experiment completed its first production data taking run, called Run-1, in 2018. The final data taking run, Run-6, is in progress and will finish by summer 2023. The combined datasets collected from Run-1 to Run-6 will allow the experiment to reach its final a_μ precision goal. The next result to be released will comprise Run-2 and Run-3 ("Run-2/3") datasets, producing a $\sim 2\times$ improved precision over the Run-1 result.

The remainder of this chapter presents the magnetic dipole moment interaction with an electromagnetic field, the SM prediction for the muon anomalous magnetic moment and aspects which are actively developing, and a selection of BSM scenarios which could explain the observed tension Δa_μ. Chapter 2 describes the Fermilab Muon $g-2$ experiment method and observables, design of the experiment, and procedure for extracting a_μ with corrections for experimental effects. In particular, dynamic motion of the muon beam leads to effects which must be understood and corrected. This thesis then focuses on the author's contributions to the Muon $g-2$ experiment. Chapter 3 describes the Inflector Beam Monitoring System (IBMS), a detector system developed to assist with the challenging injection of the muon beam into the $g-2$ storage ring magnet. Chapter 4 introduces fundamental beam dynamics concepts which are applied throughout the subsequent chapters, and describes the characteristic beam properties in the $g-2$ experiment. Chapter 5 discusses an IBMS measurement of the injected beam parameters which provided a check for complex beamline simulations and delivered realistic conditions for beam injection modeling in the $g-2$ simulation software. Chapter 6 describes the momentum distribution of the muon beam in the storage ring and a corresponding effect which critically impacts systematics, motivating the development of a detector to directly measure the stored beam. The measurement strategy to characterize the momentum distribution is presented along with the analysis outlook. Chapter 7 presents the analysis of the magnetic field experienced by the muons in the storage ring for the Run-2/3 datasets, which is one of the two necessary observables to extract the a_μ result. This muon-weighted magnetic field was the main contribution from this author for both the Run-1 and Run-2/3 result. Finally, Chapter 8 concludes with a summary of the impacts of each of these contributions and an outlook for Muon $g-2$.

1.1 Magnetic dipoles

Quantum mechanical magnetic moments can be broadly understood by analogy to the classical case. Classical current distributions generate magnetic dipole moments $\vec{\boldsymbol{\mu}}$, to lowest order in a multipole expansion of the magnetic vector potential. The magnetic moment from a current $\vec{\boldsymbol{J}}$ is defined as [5]

$$\vec{\boldsymbol{\mu}} = \frac{1}{2}\int \vec{\boldsymbol{x}}' \times \vec{\boldsymbol{J}}(\vec{\boldsymbol{x}}')d^3x' \,. \tag{1.2}$$

For a current made up of particles with charge q and mass m with total orbital angular momentum $\vec{\boldsymbol{L}} = \sum_i m\vec{\boldsymbol{x}}_i \times \vec{\boldsymbol{v}}_i$, the magnetic moment can be written as

$$\vec{\boldsymbol{\mu}} = \frac{q}{2m}\vec{\boldsymbol{L}} \,. \tag{1.3}$$

In an external magnetic field $\vec{\boldsymbol{B}}$, the field exerts a torque on the magnetic moment [5]

$$\vec{\boldsymbol{\tau}} = \vec{\boldsymbol{\mu}} \times \vec{\boldsymbol{B}} = \frac{q}{2m}\vec{\boldsymbol{L}} \times \vec{\boldsymbol{B}} = -\frac{q}{2m}\vec{\boldsymbol{B}} \times \vec{\boldsymbol{L}} \tag{1.4}$$

and the Hamiltonian is given by $H = -\vec{\boldsymbol{\mu}} \cdot \vec{\boldsymbol{B}}$. With $\vec{\boldsymbol{\tau}} = d\vec{\boldsymbol{L}}/dt = \vec{\boldsymbol{\omega}} \times \vec{\boldsymbol{L}}$, the magnetic moment therefore precesses at the frequency

$$\vec{\boldsymbol{\omega}} = -\frac{q}{2m}\vec{\boldsymbol{B}} \,. \tag{1.5}$$

In quantum mechanics, a charged particle with spin angular momentum $\vec{\boldsymbol{S}}$ has a magnetic moment given by [6]

$$\vec{\boldsymbol{\mu}} = g\frac{q}{2m}\vec{\boldsymbol{S}} \,, \tag{1.6}$$

which now includes the dimensionless factor g called the gyromagnetic ratio, with g classically equal to 1 (Eq. 1.3). The Hamiltonian is then

$$H = -g\frac{q}{2m}\vec{\boldsymbol{S}} \cdot \vec{\boldsymbol{B}} \tag{1.7}$$

and the precession frequency is $\vec{\boldsymbol{\omega}} = -g\frac{q}{2m}\vec{\boldsymbol{B}}$.

The Dirac equation for a massive spin 1/2 particle with charge e in an electromagnetic field is [7]

$$\left(i\gamma^\mu D_\mu - m\right)\psi = 0 \,, \tag{1.8}$$

using the covariant notation $D_\mu = \partial_\mu + ieA_\mu$ with electromagnetic potential A_μ. Multiplying the Dirac equation by $(i\gamma^\mu D_\mu + m)$ gives

$$\left(D_\mu^2 + \frac{e}{2}F_{\mu\nu}\sigma^{\mu\nu} + m^2\right)\psi = 0\,, \tag{1.9}$$

where the $\frac{e}{2}F_{\mu\nu}\sigma^{\mu\nu}$ term corresponds to a magnetic moment interacting with the electromagnetic field. This leads to the Hamiltonian

$$H = \frac{\vec{\boldsymbol{p}}^2}{2m} + V(r) + \frac{e}{2m}\vec{\boldsymbol{B}}\cdot\left(\vec{\boldsymbol{L}} + 2\vec{\boldsymbol{S}}\right) \tag{1.10}$$

in the non-relativistic limit, with $\vec{\boldsymbol{S}} = \vec{\boldsymbol{\sigma}}/2$. Comparing the $\vec{\boldsymbol{B}}\cdot\vec{\boldsymbol{S}}$ term with Eq. 1.7, the Dirac equation therefore predicts $g = 2$ instead of the classical value of 1. Corrections to this prediction arise from interactions which behave as an $F_{\mu\nu}\sigma^{\mu\nu}$ term. Experimental hints of a discrepancy with the Dirac-predicted g value came from larger-than-predicted measurements of the hyperfine splitting of hydrogen in 1947 [8,9].

In quantum electrodynamics (QED), the tree-level diagram for a charged particle interacting with a photon (Figure 1.2) corresponds to the matrix element [7]

$$\mathcal{M}_0^\mu = -e\bar{u}(q_2)\gamma^\mu u(q_1) = -e\bar{u}(q_2)\left[\left(\frac{q_1^\mu + q_2^\mu}{2m}\right) + \frac{i}{2m}\sigma^{\mu\nu}p_\nu\right]u(q_1)\,, \tag{1.11}$$

using the Gordon identity for γ^μ, where q_1 and q_2 are the initial and final momentum and p is the photon momentum transfer as in Figure 1.2. The $\sigma^{\mu\nu}p_\nu$ term corresponds to the magnetic moment with the coefficient $e/2m = ge/4m$, so $g = 2$ at tree level. In general, corrections to g correspond to loops which modify the $\sigma^{\mu\nu}p_\nu$ term through interactions with virtual particles. The most general parity-conserving Lorentz covariant QED vertex (Figure 1.2) at any-loop order corresponds to the matrix element [7]

$$\mathcal{M}^\mu = -e\bar{u}(q_2)\left[F_1\left(\frac{p^2}{m^2}\right)\gamma^\mu + F_2\left(\frac{p^2}{m^2}\right)\frac{i}{2m}\sigma^{\mu\nu}p_\nu\right]u(q_1)\,. \tag{1.12}$$

At tree level, the form factors are $F_1 = 1$ and $F_2 = 0$. With loop contributions, F_1 modifies the electric charge and F_2, with its $\sigma^{\mu\nu}p_\nu$ structure, modifies the magnetic moment. In the non-relativistic limit with $p^2/m^2 \to 0$,

$$g = 2\left(F_1(0) + F_2(0)\right) \equiv 2\left(1 + a\right)\,, \tag{1.13}$$

where $F_1(0) = 1$ and the dimensionless factor $a \equiv F_2(0)$ is known as the anomalous magnetic moment.

To first order in the QED coupling constant α, only one 1-loop diagram contributes to F_2 (Figure 1.3). In 1948

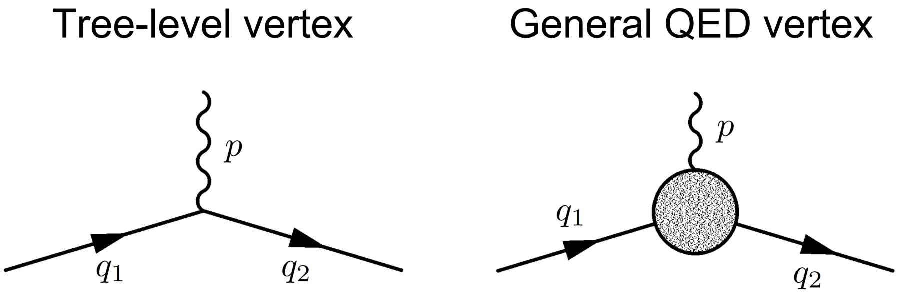

Figure 1.2: QED tree-level diagram (left) corresponding to $g = 2$, and general QED vertex including loops (right) corresponding to $g = 2(1 + a)$. Reproduced from [7].

Julian Schwinger first calculated this leading-order diagram, known as the Schwinger term [10]:

$$F_2(0) = \frac{\alpha}{2\pi} \approx 0.00116\,. \tag{1.14}$$

This is the dominant contribution to the anomalous magnetic moment a, and it is the same for all leptons because it only depends on α. This prediction was confirmed with an experimental measurement of the electron g factor using gallium spectroscopy later that year [11]. Further QED terms contribute at $O(\alpha^2)$ and higher.

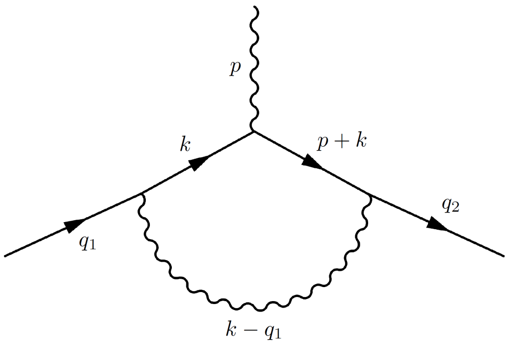

Figure 1.3: Diagram of the Schwinger term, the only 1-loop diagram which contributed to a with a value $\alpha/2\pi$. Reproduced from [7].

1.2 Anomalous magnetic moment in the standard model

The muon anomalous magnetic moment a_μ can be calculated in the standard model (SM) to a precision on par with the experimental value by including all interactions, categorized as electromagnetic (QED), electroweak, and hadronic contributions (Figure 1.4),

$$a_\mu^{SM} = a_\mu^{QED} + a_\mu^{EW} + a_\mu^{had}\,. \tag{1.15}$$

The QED contribution includes all interactions with leptons and photons, and has been calculated to $O(\alpha^5)$. The dominant contribution is the Schwinger term, $\frac{\alpha}{2\pi}$. The electroweak contribution includes weak interactions with W, Z, and Higgs bosons. The hadronic contribution includes strong interactions with quarks and is further divided into hadronic vacuum polarization (HVP) and hadronic light-by-light (HLbL) scattering terms.

$$a_\mu^{had} = a_\mu^{HVP} + a_\mu^{HLbL} \tag{1.16}$$

Each contribution is discussed further in this section below.

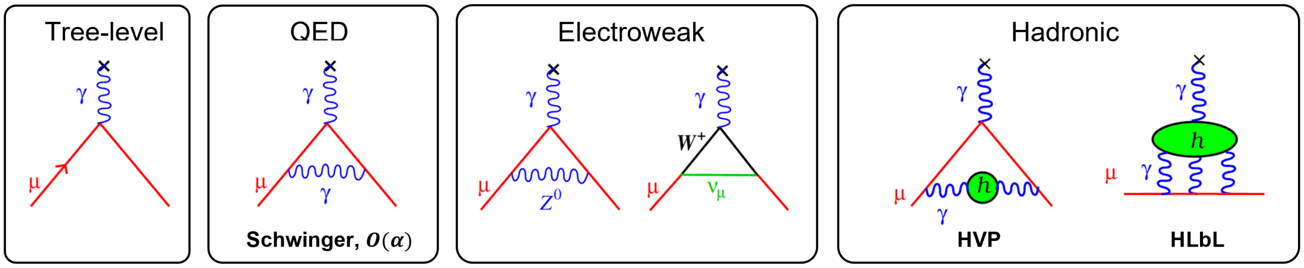

Figure 1.4: Leading-order diagrams for each contribution to a_μ in the standard model.

The Muon $g-2$ Theory Initiative [4] was formed to evaluate the standard model calculations from various groups and recommend a single value for a_μ^{SM}, in many cases combining different approaches for each contribution. The recommended values published in 2020 are shown in Table 1.2. The uncertainty on a_μ^{SM} is dominated by the hadronic terms, although their relative contributions are small compared to the dominant QED contribution. Recent developments in lattice QCD calculations and experimental cross sections present possible discrepancies with the a_μ^{HVP} calculation (discussed in Section 1.2.3). The Theory Initiative is reviewing these and plans to recommend an updated value by late 2023 (likely after the Run-2/3 experiment result is released).

contribution	value (uncertainty) $\times 10^{11}$	uncertainty [ppb]
a_μ^{QED}	116 584 718.931(104)	0.9
a_μ^{EW}	153.6(1.0)	9
a_μ^{HVP}	6845(40)	343
a_μ^{HLbL}	92(18)	154
Total a_μ^{SM}	116 591 810(43)	369

Table 1.2: Contributions to a_μ^{SM} recommended by the Muon $g-2$ Theory Initiative in 2020 [4].

1.2.1 Quantum electrodynamic contributions

The QED contribution a_μ^{QED} comprises powers of the QED coupling constant, which is the fine structure constant $\alpha \equiv e^2/4\pi$.

$$a_\mu^{QED} = \sum_n C_n(\frac{\alpha}{\pi})^n \tag{1.17}$$

a_μ^{QED} has been calculated to $O(\alpha^5)$ (10 loops) using perturbation theory, which is possible because α is relatively small [4]. The first-order Schwinger term with $C_1 = 1/2$ is the same for all leptons, but higher-order terms depend on the lepton mass. a_μ^{QED} terms of $O(\alpha^2)$ and above include a mass-independent component as well as components which depend on the mass ratios m_μ/m_e and m_μ/m_τ from diagrams with closed fermion loops, where m_e and m_τ are the electron and τ lepton masses.

The 2020 Theory Initiative recommended value (Table 1.2) uses the value of α measured by the Cs atom-interferometry experiment, α^{-1}(Cs) = 137.035 999 046(27) [12]. Using a value of α determined from Rb recoil velocity [13] or the electron anomalous magnetic moment [14] does not significantly affect a_μ^{QED} at the calculated precision. The dominant sources of uncertainty on a_μ^{QED} are the estimate of the next order $O(\alpha^6)$ QED term and the experimental uncertainty on α, but this is negligible compared to the overall uncertainty on a_μ^{SM}.

1.2.2 Electroweak contributions

The electroweak (EW) contribution a_μ^{EW} includes loops with $W^\pm$, Z, and Higgs bosons. a_μ^{EW} is suppressed by the heavy EW boson masses, and is on the same order as the difference between the experimental and SM a_μ values. The 1-loop contribution is given by [4]

$$a_\mu^{EW(1)} = \frac{G_F}{\sqrt{2}}\frac{m_\mu^2}{8\pi^2}\left[\frac{5}{3} + \frac{1}{3}\left(1 - 4\sin^2\theta_W\right)^2\right] = 194.79(1) \times 10^{-11} \tag{1.18}$$

where $\sin^2\theta_W = 1 - M_W^2/M_Z^2 \simeq 0.223$ corresponds to the weak mixing angle, with boson masses M_W and M_Z; $G_F = \frac{g^2}{4\sqrt{2}M_W^2} = 1.16637(1) \times 10^{-5}\,\text{GeV}^{-2}$ is the Fermi constant, with weak coupling constant g. The factor of $1/M_W^2$ in G_F, rather than g itself, causes the weak interaction to be weak relative to QED [15]. It also means that a_μ^{EW} is suppressed by a factor of $m_\mu^2/M_W^2 \approx 10^{-6}$ compared to the QED contribution [4]. Compared to the EW contribution of the electron anomalous magnetic moment a_e, however, a_μ^{EW} is larger by a factor of $m_\mu^2/m_e^2 \approx 43,000$, and muons are therefore more sensitive to this contribution.

a_μ^{EW} has been calculated to 2 loops; 2-loop diagrams with heavy bosons and a photon are enhanced by a relatively large factor of $\log\left(M_Z^2/m_\mu^2\right)$, reducing the total a_μ^{EW} by $\sim$20% [4]. The estimated 3-loop contribution is negligible, of $O(10^{-12})$ [16], but is included to leading order in the recommended a_μ^{EW} value (Table 1.2). The dominant source of uncertainty on a_μ^{EW} is hadronic effects from quarks in the 2-loop diagrams [4, 17].

1.2.3 Hadronic contributions

The hadronic contributions a_μ^{HVP} (hadronic vacuum polarization) and a_μ^{HLbL} (hadronic light-by-light scattering) include all interactions with quarks, and are difficult to calculate directly because perturbation theory cannot be applied for quantum chromodynamics (QCD) interactions in the dominant low-energy regime. The uncertainty on the total a_μ^{SM} is dominated by the hadronic uncertainties, particularly from a_μ^{HVP}.

Hadronic vacuum polarization

The HVP contribution a_μ^{HVP} is the leading-order (LO) hadronic contribution to a_μ^{SM}, contributing at $O(\alpha^2)$. The Theory Initiative recommended a ∼0.6%-precision value for a_μ^{HVP} which combines results from multiple groups using a data-driven dispersive approach (Table 1.2). However, recent developments in the HVP calculation stand to significantly impact the standard model value. Lattice QCD calculations approaching a similar precision are in tension with the data-driven value. Additionally, a new experimental result for the dominant hadronic cross section used in the data-driven calculation is in tension with all previous experimental measurements. Work and discussion to understand these results is ongoing, and the discrepancies must be understood and resolved before an updated a_μ^{SM} value can be determined.

Data-driven dispersive: In the more traditional data-driven approach, the LO HVP loop is expressed as a dispersion integral over the cross section of a virtual photon decaying into hadrons, which is determined from e^+e^- annihilation [4].

$$a_\mu^{HVP,LO} = \frac{\alpha^2}{3\pi^2}\int_{M_\pi^2}^{\infty}\frac{K(s)}{s}R(s)ds \tag{1.19}$$

Here s is the center-of-mass energy squared, M_π is the π^0 mass, $K(s) \sim 1/s$ is a QED kernel function which weights low energies more strongly [16], and $R(s)$ is a ratio of cross sections [4]:

$$R(s) = \frac{\sigma^0(e^+e^- \to \text{hadrons})}{\sigma_{pt}} \tag{1.20}$$

where σ^0 is the bare cross section (excluding vacuum polarization effects) for $e^+e^- \to$hadrons, and $\sigma_{pt} = 4\pi\alpha^2/3s$ is the lowest-order pointlike muon pair cross section. The contributions to $R(s)$ for the different final states are shown in Figure 1.5. The low-energy weighting from $K(s)$ means that $e^+e^- \to \pi^+\pi^-$ is the dominant cross section. Measurements of $e^+e^- \to$ hadrons cross sections from many different experiments, for example the

$e^+e^- \to \pi^+\pi^-$ measurements shown in Figure 1.6, are combined to obtain the data-driven $R(s)$ input. The calculated LO contribution is $a_\mu^{HVP,\,LO} = 6931(40) \times 10^{-11}$. Next-to-leading order and next-to-next-to-leading order (NLO and NNLO) HVP contributions are obtained using similar data-driven dispersion calculations with double and triple integrations [4].

The dominant source of uncertainty on a_μ^{HVP} is the hadronic cross sections, both the experimental uncertainties and discrepancies between experiments, particularly the $\pi^+\pi^-$ channel from BaBar and KLOE [18]. Improvements are expected with in-progress analyses of $\pi^+\pi^-$ and other channels from BaBar, KLOE, SND, and other experiments. If experiment discrepancies are resolved, a ∼2× reduction in the data-driven uncertainty may be possible by 2025 [19].

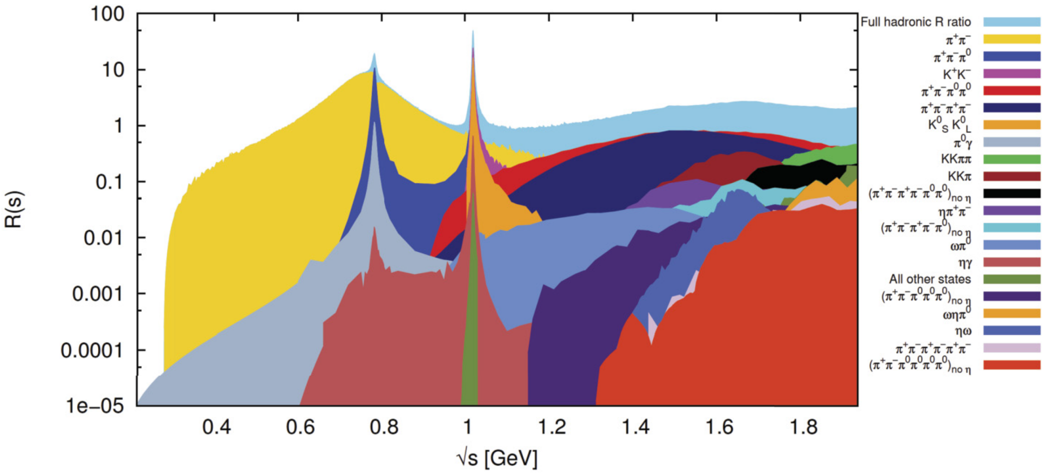

Figure 1.5: Contributions to the hadronic cross section ratio $R(s)$ for different final states, with the total shown in light blue. Reproduced from [18].

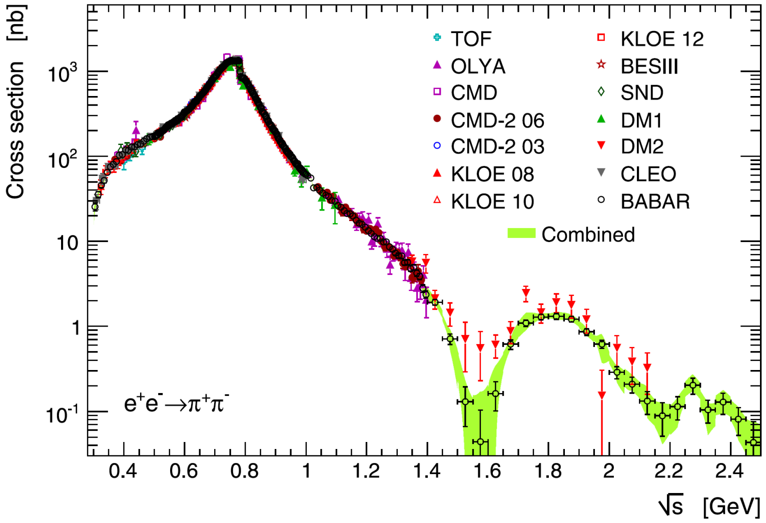

Figure 1.6: $e^+e^- \to \pi^+\pi^-$ cross sections measured by different experiments, with the average used by one group shown in the green band. Reproduced from [20].

Hadronic cross section: In February 2023 the CMD-3 collaboration released a new result for the measured $e^+e^- \to \pi^+\pi^-$ cross section which disagrees with previous measurements by other experiments [21]. This was the combined result from analysis of data collection runs in 2013 and 2018, with a total of 3.4×10^7 $\pi^+\pi^-$ events in the important low-energy range $< 1\,\text{GeV}$, representing 10 to 100 times more statistics than the previous-generation CMD-2 experiment, depending on energy range. The CMD-3 (Cryogenic Magnetic Detector) operates at the Novosibirsk VEPP-2000 e^+e^- collider. The experiment scanned over center-of-mass collider energies $\sqrt{s}$ in the range $0.32\,\text{GeV}$ to $1.2\,\text{GeV}$ and measured the pion form factor F_π via the ratio of events $N_{\pi^+\pi^-}/N_{e^+e^-}$. The $e^+e^- \to \pi^+\pi^-$ cross section was determined from a fit to F_π.

As shown in Figure 1.7, the resulting cross section is generally larger over the measured energy range than all previous measurements. Individual analyses of the 2013 and 2018 datasets, which were separated by detector and collider upgrades, are in good agreement with each other and with the combined result. The contribution to $a_\mu^{HVP,\,LO}$ from $e^+e^- \to \pi^+\pi^-$ was calculated in the energy range $0.6\,\text{GeV}$ to $0.88\,\text{GeV}$, making up $> 50\%$ of the total $a_\mu^{HVP,\,LO}$ integral. This $a_\mu^{HVP,\,LO}$ contribution is also in tension with previous measurements (Figure 1.7); if confirmed it would bring a_μ^{SM} in closer agreement with experiment, possibly within $\lessapprox 1.5\sigma$.

This surprising result has been the focus of much recent discussion among the experts, for example in the *Scientific seminar and discussion on new CMD-3 result* organized by the Theory Initiative [22]. So far no clear experimental issue or other explanation for the difference has emerged. The SND experiment, which also operates at the VEPP-2000 collider, is in the process of analyzing new $\pi^+\pi^-$ channel results, which will provide an important comparison with the CMD-3 result. Understanding the discrepancy is critical before the impact on a_μ^{SM} can be determined.

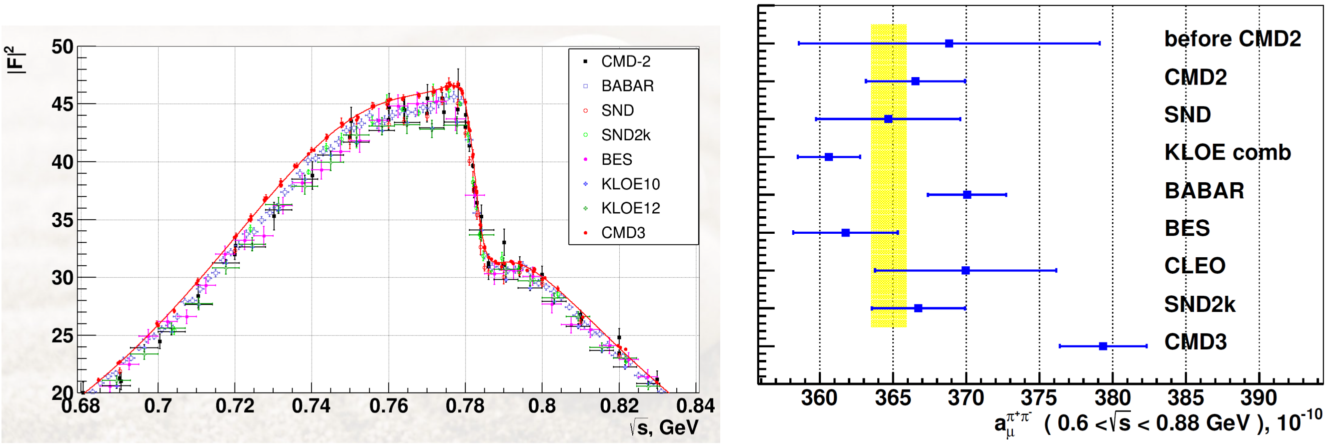

(a) Pion form factor measured by CMD-3 compared with measurements by previous experiments over part of the low-energy range which is most important for a_μ^{HVP}. The extracted $e^+e^- \to \pi^+\pi^-$ cross section is larger than previous measurements over the majority of the range. Reproduced from [22].

(b) Calculated $a_\mu^{HVP,LO}$ contribution from $e^+e^- \to \pi^+\pi^-$ in the energy range 0.6 GeV to 0.88 GeV. The CMD-3 result (bottom) is in tension with all previous measurements. Reproduced from [21].

Figure 1.7

Lattice QCD: Lattice QCD is an independent method to calculate a_μ^{HVP} directly from first principles. The calculation is performed on a discrete grid in Euclidean time. As of 2020, the lattice QCD results were not at the required precision to be included in the recommended a_μ^{HVP} value. However, the BMW20 calculation released in 2021 had sub-percent precision near that of the data-driven calculations [23], and was in tension with the data-driven value by 2.1σ. It also represents a value of a_μ^{SM} which is in closer agreement with the experimental value, at a tension of only 1.5σ. Figure 1.8 shows the difference between SM and experimental values of a_μ for different values of a_μ^{HVP} from lattice QCD and data-driven dispersion calculations.

Recent lattice QCD calculations consider different Euclidean time regions separately using three windows, called short distance (SD), intermediate (W), and long distance (LD), to disentangle effects due to different lattice distances [24] (Figure 1.9). Lattice QCD is most precise in the intermediate window, and this region is used for initial comparisons. In this window the tension between the BMW20 and data-driven values increases to 3.7σ. As of May 2023, a comparison of $a_\mu^{HVP,W}$ calculations in the W window between several groups showed good agreement, and a consensus value in this window was established [25]. The data-driven dispersion integral can also be calculated in this window [26]. Figure 1.9 shows the tension with the corresponding data-driven calculation of $a_\mu^{HVP,W}$. One possibility for further investigation is to use finer windows in the intermediate region to locate the discrepancy. SD windows are currently being evaluated. In order to reach a consensus on the full a_μ^{HVP} contribution, it will be critical to carefully compare different calculations using different lattice spacings. An average lattice-QCD-calculated value of a_μ^{HVP} with $\sim$0.5% precision may be achieved by 2025 if results are consistent between groups [19].

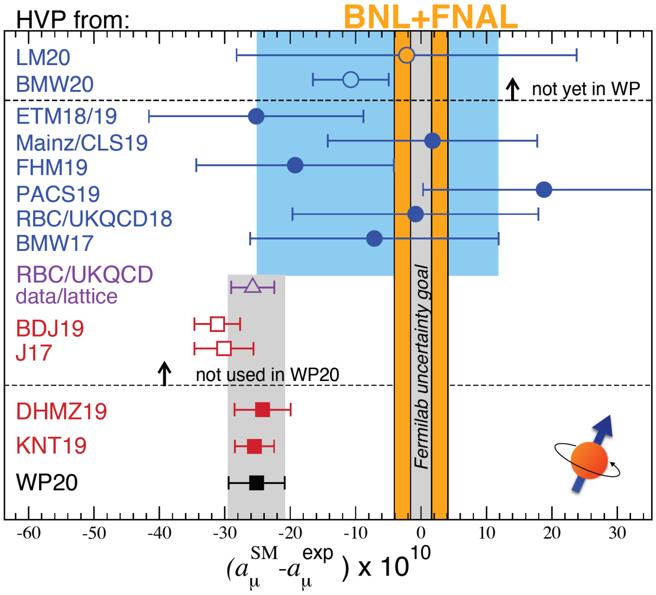

Figure 1.8: Difference between SM and experimental (orange band) values of a_μ if different values of a_μ^{HVP} are used. The Theory Initiative recommended value (WP20, black) used only the data-driven calculations (red), as lattice QCD results (blue) were not at a comparable precision. The purple RBC/UKQCD "data/lattice" point is a hybrid of the two methods, combining a lattice calculation in the intermediate Euclidean time window with a data-driven calculation in the short-distance and long-distance windows [27]. Results above the lower dashed line were not used in the 2020 Theory Initiative recommendation. Lattice results above the upper dashed line, including the BMW20 result, were not yet available in 2020 when the Theory Initiative recommendation was made. If the average a_μ^{HVP} lattice results (blue band) were used instead of the data-driven results, it would reduce the tension between a_μ^{SM} and a_μ^{Exp}. Reproduced from [26].

Hadronic light-by-light scattering

The HLbL contribution a_μ^{HLbL} is on the same order as the next-to-leading-order HVP, $\mathcal{O}(\alpha^3)$. HLbL scattering corresponds to a photon interacting with a hadronic blob, which interacts with the muon via three virtual photons [28]. Similar to the HVP calculation, the HLbL contribution can be calculated using a phenomenological dispersive approach or from first principles with lattice QCD. Results from the two approaches are in good agreement [4]. The 2020 Theory Initiative recommended value for a_μ^{HLbL} corresponds to a weighted average of results from both approaches (Figure 1.10), with a precision of $\sim$20% (Table 1.2). For an overall a_μ^{SM} precision matching the experiment target precision, the required precision for a_μ^{HLbL} would be 10%.

The dispersive calculation is more difficult than the analogous HVP calculation because the HLbL scattering amplitude is a four-point function, whereas the HVP is a two-point function [4]. The dominant contribution is calculated with a data-driven and model-independent method. The main sources of uncertainty in the dispersive

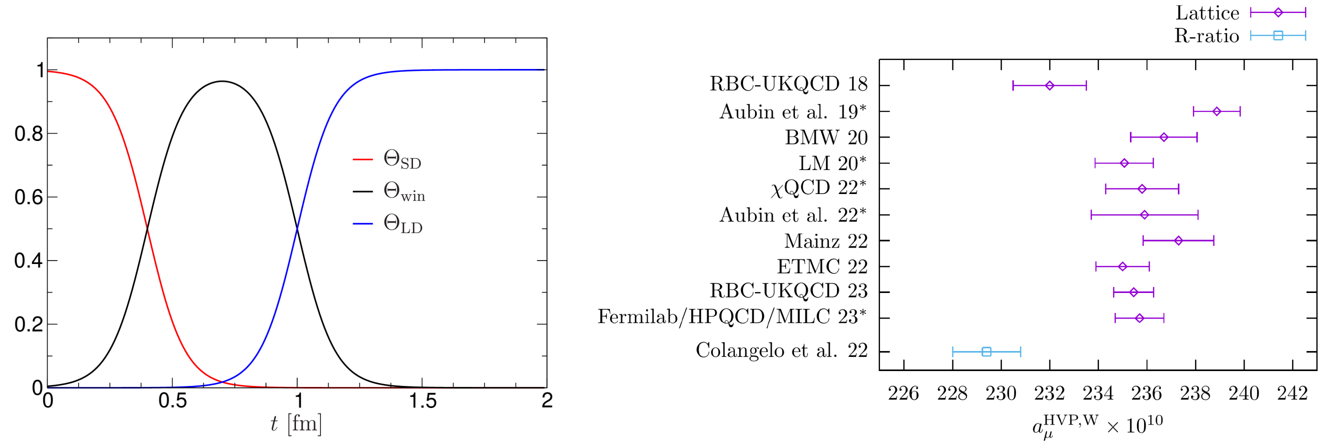

(a) Euclidean time window weight functions used to separate lattice QCD regimes. Calculations in the intermediate window (black) are most precise. Reproduced from [24].

(b) Comparison of $a_\mu^{HVP,W}$ in the intermediate window shows tension between lattice QCD (purple) and data-driven (blue) results. Reproduced from [25].

Figure 1.9

HLbL calculation [4] are model-dependent estimates and short distance constraints for large momenta, which enter in the sub-dominant contributions. Work is underway to improve these estimates, and the dispersive calculation is expected to reach the 10% precision target by 2025 [26].

The lattice QCD value has been calculated by two groups using distinct methods, finite volume QED in the case of the RBC-UKQCD group and infinite volume QED in the case of the Mainz group, which handle the zero-momentum photon limit differently. Cross-checks and internal consistency checks have demonstrated reliability [4]. Both groups are improving their calculations and working to reduce uncertainty, and RBC-UKQCD recently calculated a new result using infinite volume QED. The lattice QCD calculation is expected to achieve 10% precision by 2025 [26].

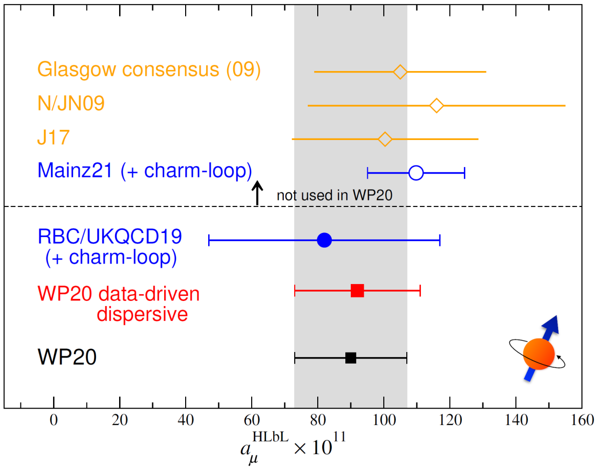

Figure 1.10: HLbL contribution a_μ^{HLbL} from dispersive calculation (red), lattice QCD (blue), and earlier estimates (orange) not used in the 2020 Theory Initiative recommendation (black). Reproduced from [26].

1.3 New physics beyond the standard model

The tension Δa_μ between the experimental and SM values currently stands at 4.2σ, suggesting new physics beyond the standard model (BSM) if the tension persists. Similar to the electroweak contribution (Section 1.2.2), sensitivity to new physics with energy scale Λ is proportional to m^2/Λ^2, and muons are therefore more sensitive than electrons by a factor of $m_\mu^2/m_e^2 \approx 43,000$. With their sensitivity to new physics and their relatively long lifetime of 2.2 µs compared to the heavier τ lepton, muons are an excellent probe of BSM physics. Figure 1.11 shows general forms of possible 1-loop BSM physics contributions to a_μ.

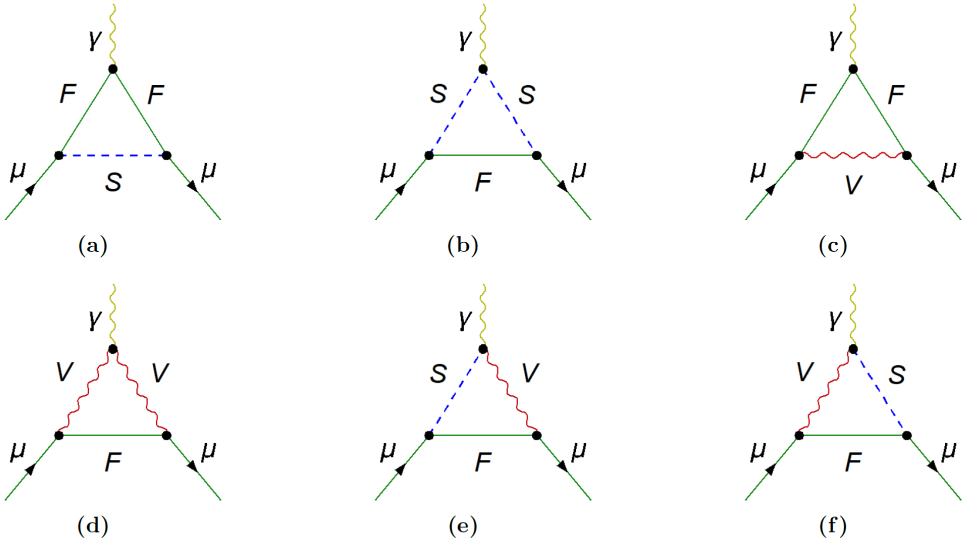

Figure 1.11: General possible 1-loop diagrams for BSM physics contributions to a_μ, with a generic new fermion F, new scalar S, and new vector field V. Reproduced from [29].

Any contribution to a_μ must be CP-conserving, flavor-conserving, and loop induced. Further, the operator corresponding to a_μ in the QFT vertex (e.g. Eq. 1.12) connects left-handed and right-handed muons, so a_μ flips the muon's chirality [29]. This chirality-flipping requirement leads to several characteristics of possible BSM physics. The contribution should correspond to $\Delta a_\mu^{BSM} = C_{BSM} \cdot m_\mu^2/\Lambda^2$ with a coupling coefficient C_{BSM}. Many BSM models contribute both to a_μ and to the muon mass m_μ, so the coefficient is related to a shift in the muon mass with $C_{BSM} \sim \Delta m_\mu^{BSM}/m_\mu$. For BSM models with no mass shift where the muon mass is induced by BSM loops, called "radiative muon mass" scenarios, $C_{BSM} \sim O(1)$ [30]. With the existing Δa_μ tension, this would impose an upper limit on the BSM mass scale of $\Lambda \lessapprox O(2\,\mathrm{TeV})$.

Many new possibilities for BSM physics have been proposed, and some remain viable with constraints imposed by other experiments. Most models require mass scales $\Lambda \lessapprox O(1\,\mathrm{TeV})$. One popular class of models is supersymmetry (SUSY). Because the minimal supersymmetric standard model (MSSM) has two Higgs vacuum expectation values (VEVs), v_u and v_d, whereas the SM has just one Higgs VEV, SUSY candidates contribute to a_μ with an enhancement factor $\tan\beta = v_u/v_d$ [29]. Enhancement factors $\tan\beta \approx 3$–40 with SUSY particle mass $100\,\mathrm{GeV}$ to $500\,\mathrm{GeV}$ [30] could explain the observed Δa_μ, but this mass scale would be observable at the large hadron collider (LHC). The lack of BSM physics observed at the LHC and in dark matter searches significantly constrains the possible parameter space for SUSY and other proposed models.

Many other proposed theories involve extensions to the SM with one or more new fields. The magnitude and sign of the observed Δa_μ eliminates many single-field extensions. Remaining single-field extensions include the dark photon, two-Higgs doublet model (2HDM), and leptoquarks. The dark photon model introduces a new massive gauge boson which would mix with SM photons and therefore interact with SM fermions with a coupling strength $\epsilon \cdot e$ [16]. The simplest dark photon scenarios are excluded by the observed Δa_μ, the measured electron anomalous magnetic moment a_e, and experimental results from several dark photon production channels, but scenarios with further extensions such as a new dark Z boson are possible in very limited parameter spaces [29]. The 2HDM introduces a second Higgs doublet with a corresponding $\tan^2\beta$ enhancement [31], but only specific 2HDM variants with constrained parameter spaces are viable to explain Δa_μ [29]. Scalar leptoquarks, bosons which interact with SM leptons and quarks, are motivated both by Δa_μ and by quark flavour anomalies. However, the parameter space for leptoquarks is also tightly constrained by the observed Δa_μ and by the physical muon mass [29]. Simple three-field models with either two scalars and one fermion or one scalar and two fermions can explain Δa_μ and accommodate dark matter together in a relatively large parameter space [29].

The experimental measurement of a_μ motivates and provides important constraints on possible BSM physics, together with LHC results and dark matter searches. Future Muon $g-2$ results with an ultimate precision of 140 ppb will therefore be critical to determine realistic BSM physics scenarios.

Chapter 2

Fermilab Muon $g-2$ Experiment

2.1 Measurement method

The E989 Fermilab Muon $g-2$ experiment measures a_μ by injecting polarized muons into a magnetic storage ring. In a uniform vertical magnetic field $\vec{\boldsymbol{B}}$, the muons undergo cyclotron motion and orbit around the ring; their momenta $\vec{\boldsymbol{p}}$ precess with angular frequency

$$\vec{\boldsymbol{\omega}}_{\boldsymbol{c}} = \frac{e}{\gamma m}\vec{\boldsymbol{B}} \tag{2.1}$$

in the horizontal plane, where e is the muon charge, m is the muon mass, and γ is the relativistic Lorentz factor.

The injected muons' spins are initially polarized in the horizontal ring plane, perpendicular to $\vec{\boldsymbol{B}}$. The relativistic muons experience Larmor precession (as in Section 1.1) and Thomas precession (the relativistic correction), and the spins precess with angular frequency [32]

$$\vec{\boldsymbol{\omega}}_{\boldsymbol{s}} = \left[\frac{g_\mu e}{2m} - (1-\gamma)\frac{e}{\gamma m}\right]\vec{\boldsymbol{B}}\,. \tag{2.2}$$

If $g_\mu = 2$ the spins would precess at the same frequency as the momenta, but because $g_\mu > 2$ the spins precess faster than the momenta (by $\sim 3\%$ in the Muon $g-2$ experiment configuration) and $\omega_s > \omega_c$. The difference, called the anomalous precession frequency ω_a, is proportional to the anomalous magnetic moment a_μ.

$$\vec{\boldsymbol{\omega}}_{\boldsymbol{a}} \equiv \vec{\boldsymbol{\omega}}_{\boldsymbol{s}} - \vec{\boldsymbol{\omega}}_{\boldsymbol{c}} = -\left(\frac{g_\mu - 2}{2}\right)\frac{e}{m}\vec{\boldsymbol{B}} = -a_\mu\frac{e}{m}\vec{\boldsymbol{B}} \tag{2.3}$$

A precise measurement of a_μ requires precise measurements of both B and ω_a. Eq. 2.3 can be expressed in terms of precisely known experimental quantities. Using the electron magnetic moment $\mu_e = g_e\,(e\hbar/4m_e)$,

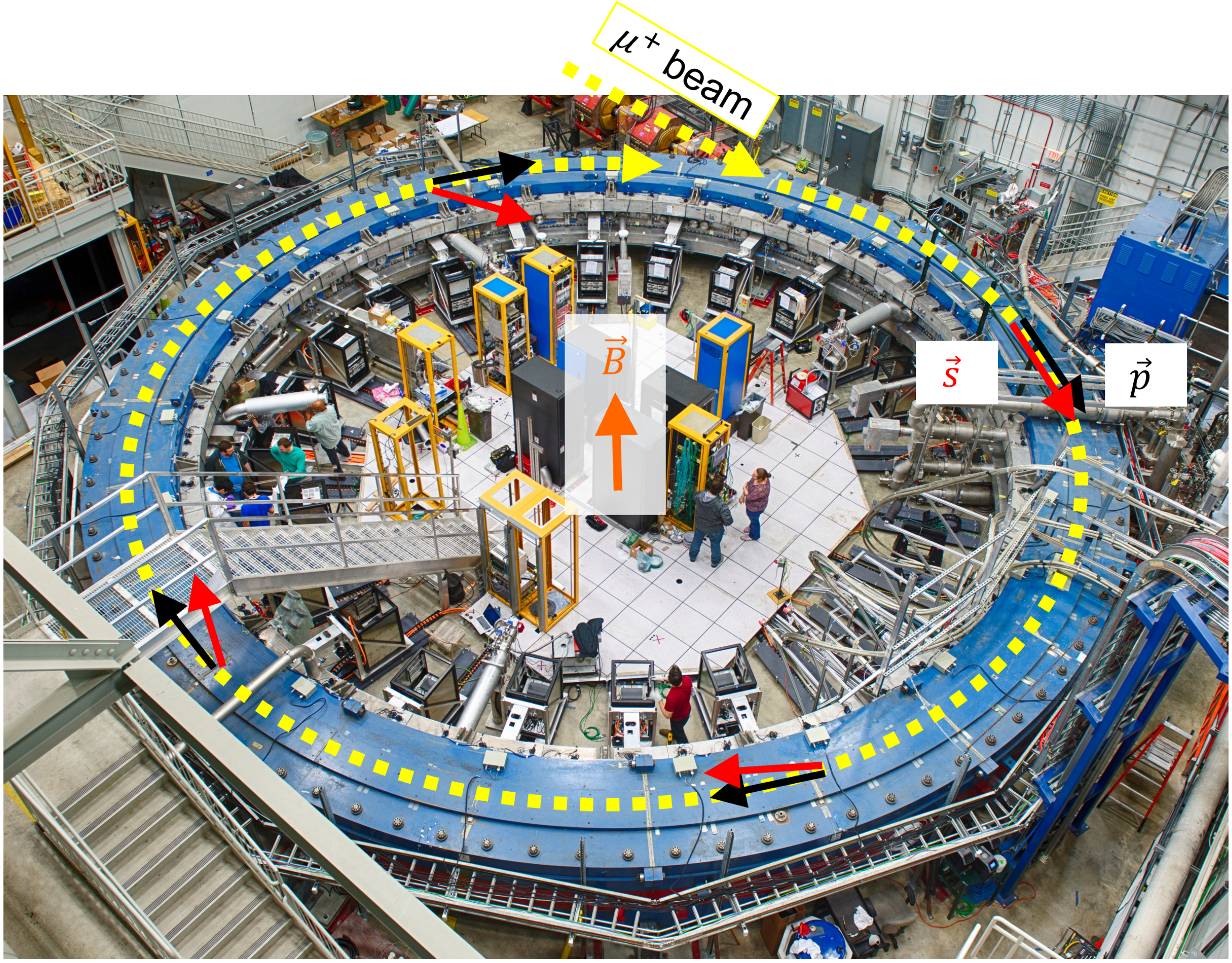

Figure 2.1: Polarized muons are injected into the $g-2$ storage ring, which provides a vertical magnetic dipole field. Because $g_\mu > 2$, their spins precess slightly faster than their momenta. The difference is exaggerated in this figure; in reality, the spins rotate one extra time for each 29.3 turns around the ring.

the proton magnetic moment $\mu_p = g_p\,(e\hbar/4m_p)$, and the proton precession frequency $\omega_p = 2\mu_p B/\hbar$, a_μ can be expressed as

$$a_\mu = \frac{\omega_a}{\tilde{\omega}'_p(T_r)} \frac{\mu'_p(T_r)}{\mu_e(H)} \frac{\mu_e(H)}{\mu_e} \frac{m_\mu}{m_e} \frac{g_e}{2} \tag{2.4}$$

where

- μ'_p is the magnetic moment of protons in a shielded water sample, measured at reference temperature $T_r = 34.7\,^\circ\mathrm{C}$,
- $\tilde{\omega}'_p = 2\mu'_p(T_r)\tilde{B}/\hbar$ is the shielded proton precession frequency at reference temperature T_r, in the magnetic field averaged over the muon distribution $\tilde{B}$, and

- $\mu_e(H)$ is the magnetic moment of an electron bound in hydrogen.

The Muon $g-2$ experimental observables are ω_a and $\tilde{\omega}'_p(T_r)$. Calorimeters measure ω_a via the spectrum of positrons from muon decay, and nuclear magnetic resonance probes measure $\tilde{\omega}'_p(T_r)$ via the precession of shielded protons in the magnetic field. The other terms in Eq. 2.4 are constants which have been measured to high precision by other experiments, shown in Table 2.1.

quantity	source	uncertainty [ppb]
g_e	quantum cyclotron spectroscopy [14]	0.00013
m_μ/m_e	muonium spectroscopy [33]	22
$\mu'_p(T_r)/\mu_e(H)$	hydrogen spectroscopy [34]	10.5
$\mu_e(H)/\mu_e$	bound-state QED calculation [35]	0 (considered exact)
a_μ	E989 Muon $g-2$ goal	140

Table 2.1: Experimental constants and associated uncertainties used to determine a_μ

In the $g-2$ storage ring, the vertical magnetic field focuses the beam radially, but vertical confinement is also required. Electrostatic quadrupoles provide the necessary vertical focusing, and the muons undergo vertical and horizontal betatron motion (Section 4.3). With the presence of an electric field $\vec{\boldsymbol{E}}$ and motion which is not only perpendicular to $\vec{\boldsymbol{B}}$, the full expression for ω_a is given by the Thomas-Bargmann-Michel-Telegdi (Thomas-BMT) equation [5],

$$\vec{\boldsymbol{\omega}}_{\boldsymbol{a}} = -\frac{e}{m}\left[a_\mu \vec{\boldsymbol{B}} - \left(a_\mu - \frac{1}{\gamma^2-1}\right)\frac{\vec{\boldsymbol{\beta}}\times\vec{\boldsymbol{E}}}{c} - a_\mu \frac{\gamma}{1+\gamma}\left(\vec{\boldsymbol{\beta}}\cdot\vec{\boldsymbol{B}}\right)\vec{\boldsymbol{\beta}}\right] \tag{2.5}$$

The $\vec{\boldsymbol{\beta}}\times\vec{\boldsymbol{E}}$ term corresponds to the motional magnetic field from the electric quadrupole field. This term is canceled with the right choice of muon momentum such that $a_\mu - \frac{1}{\gamma^2-1} = 0$; this "magic momentum" $p_0 = 3.094\,\mathrm{GeV}/c$ corresponds to $\gamma = 29.3$. However, the muon beam has a finite momentum spread around p_0 and this term does not perfectly cancel for off-momentum muons, requiring an "electric field correction" to $\vec{\omega}_a$. The $\vec{\boldsymbol{\beta}}\cdot\vec{\boldsymbol{B}}$ term corresponds to motion parallel to $\vec{\boldsymbol{B}}$, and is zero for motion purely perpendicular to $\vec{\boldsymbol{B}}$. Due to the muons' vertical betatron motion which introduces a component of $\vec{\boldsymbol{\beta}}$ parallel to $\vec{\boldsymbol{B}}$, $\vec{\omega}_a$ requires a correction called the "pitch correction".

2.2 Muon beam

The Fermilab Muon Campus beamline creates a polarized beam of muons with central momentum $p_0 = 3.094\,\mathrm{GeV}/c$ for Muon $g-2$ [36,37]. The booster accelerator delivers batches of protons with $8\,\mathrm{GeV}$ kinetic energy to the recycler ring, where the protons are separated into four bunches of $\sim 1 \times 10^{12}\ p^+$ each by a radio frequency (RF) system. The bunches are individually extracted into the M1 line, which delivers them to the AP0 target hall where they strike a pion production target made of Inconel. Secondary particles are collected with a magnetic lithium lens, and positively-charged particles with central momentum $3.11\,\mathrm{GeV}/c$ are selected with a pulsed dipole bending magnet. Nominal-momentum pions with $\gamma = 22.3$ have a characteristic lab frame decay length of $L_\pi = \gamma\tau_\pi\beta c = 173.6\,\mathrm{m}$. The pions decay to muons along the $280\,\mathrm{m} \approx 1.6 L_\pi$ M2 and M3 lines, which capture $3.1\,\mathrm{GeV}/c\ \mu^+$.

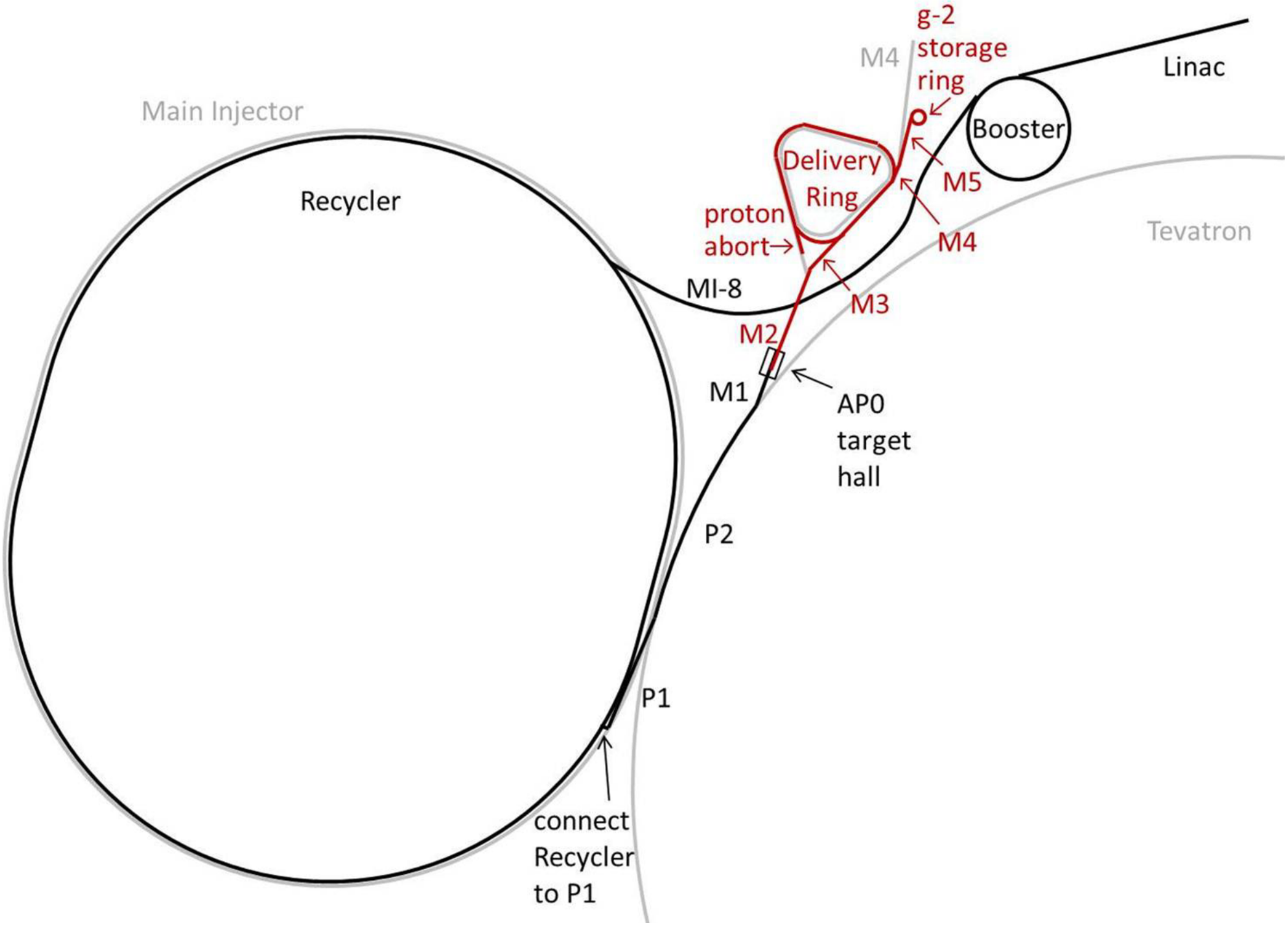

Figure 2.2: The muon campus beamline [36], showing the proton beam in black and the secondary beam (after the pion production target) in red.

Momentum selection produces polarized μ^+. The pion decay $\pi^+ \to \mu^+\nu_\mu$ is a weak interaction, in which the μ^+ have a definite left-handed (LH) helicity state in the center of mass (CM) frame. Forward-decaying μ^+ whose momenta are parallel to the π^+ lab-frame momentum are boosted up in the lab frame. Backward-decaying μ^+ whose momenta are anti-parallel to the π^+ lab-frame momentum are boosted down in the lab frame, flipping their momenta which flips their helicity to right-handed (RH). High-momentum μ^+ therefore have LH helicity and low-momentum μ^+ have RH helicity, so selecting the high-momentum μ^+ in the lab frame produces a LH-polarized

μ^+ beam, with an average polarization of $\sim 95\%$.

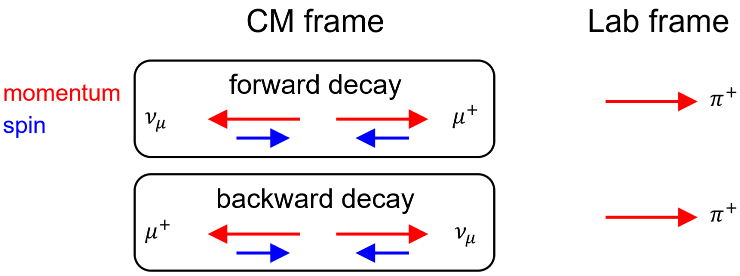

Figure 2.3: Forward-decaying muons are left-hand (LH) polarized and have higher momentum in the lab frame, and backward-decaying muons are right-hand (RH) polarized and have lower momentum in the lab frame. Selecting the high-momentum muons produces a LH-polarized muon beam.

The M3 line consists of a "FODO", or focusing-defocusing, arrangement of quadrupole magnets used to transport beam over long distances. The beam is injected from the M3 line into the $505\,\mathrm{m}$ circumference delivery ring (DR), which separates the p^+ remaining in the beam from the π^+ and μ^+. Because the protons are heavier than the muons but have the same momentum $p = \gamma m \beta$, they have a smaller $\beta = \sqrt{\frac{p^2}{p^2+m^2}}$ and are therefore slower than the muons. Each turn in the DR, the p^+ increasingly lag the μ^+. After 4 turns the p^+ are kicked out with the "abort kicker" and essentially all π^+ have decayed to μ^+. This leaves a beam consisting primarily of polarized μ^+ which is extracted from the DR and transported along the $130\,\mathrm{m}$ M4 and M5 lines to the Muon $g-2$ experiment, located in Muon Campus building 1 (MC-1). The M4 beamline splits out to the Mu2e experiment, such that the Muon Campus can deliver beam to either $g-2$ or Mu2e.

The delivered μ^+ beam has a momentum spread of $\pm 1.6\%$ around the central momentum p_0, but the $g-2$ ring accepts only a $\pm 0.15\%$ bite. A boron carbide momentum cooling wedge was installed just downstream of the DR in the M5 line during Run-2, with the purpose of reducing the momentum spread and increasing the number of μ^+ with momenta in the range accepted by the ring [38]. The wedge is located in a high-dispersion bend region of the beamline where the momenta are spatially separated. It is inserted in the high-momentum side of the beam, cooling the highest momentum μ^+ into the accepted range. The result was a few-percent increase in the fraction of μ^+ stored in the ring.

The beam is nominally delivered in 2 groups of 8 bunches every $1.4\,\mathrm{s}$ (reduced in Run-6 to 1 group of 8 bunches every $1.2\,\mathrm{s}$). The time distribution of each $\sim 150\,\mathrm{ns}$-wide bunch has a characteristic "W" shape caused by the RF proton bunch creation in the recycler, which rotates the beam in longitudinal time-energy phase space to shorten the bunch in time. The time projection of the distribution has a shape like that shown in Figure 2.4; each of the 8 bunches has a unique variation of the distribution.

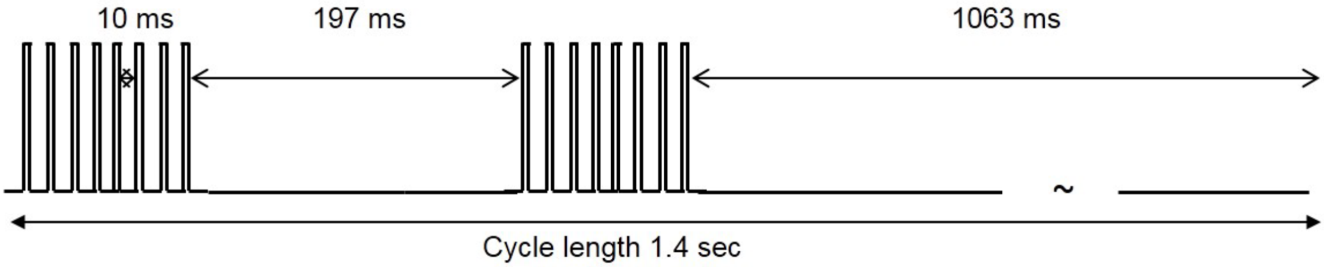

(a) Nominal timing of beam pulses

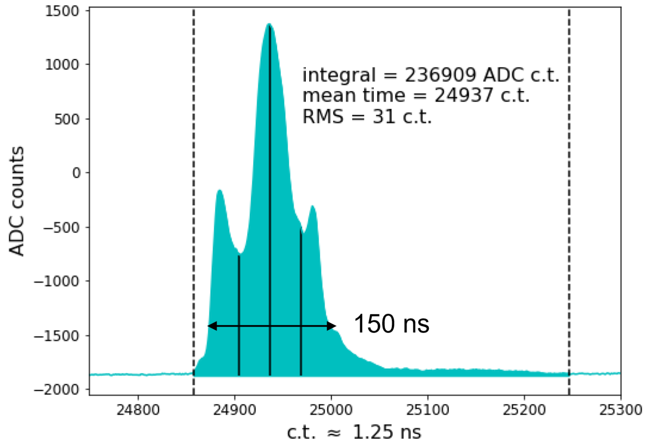

(b) Example time distribution of a single bunch, which is $\sim 150\,\mathrm{ns}$ wide. Figure courtesy of H. Binney [39].

Figure 2.4: Time structure of the muon beam delivered to Muon $g-2$.

2.3 Beam injection

The beam is injected into the storage ring through the "yoke hole" bore in the back leg of the magnet iron. A superconducting inflector magnet, $1.7\,\mathrm{m}$ long with an $18\,\mathrm{mm} \times 56\,\mathrm{mm}$ aperture, cancels the ring's magnetic field to provide a field-free path for the beam (Figure 2.5). The injection path is offset radially by $77\,\mathrm{mm}$ from the nominal ring orbit to avoid interfering with the beam circulating in the ring (Figure 2.6). The narrow inflector together with magnetic fringe fields make the beam injection a challenging process which is discussed further in Chapter 5.

Beam entrance detectors along the injection path provide information about the beam at injection; their locations are indicated in Figure 2.8. The T0 detector consists of a plastic scintillator sheet coupled with optical waveguides to two photomultiplier tubes (PMTs) [39]. The PMT waveforms provide a profile of the incident beam intensity over time, as shown in Figure 2.4. The T0 detector defines the start time for each muon measurement period, called "fills". The Inflector Beam Monitoring System (IBMS) consists of 3 scintillating fiber detectors which provide spatial profiles of the injected beam, discussed in detail in Chapter 3. IBMS1 is located imme-

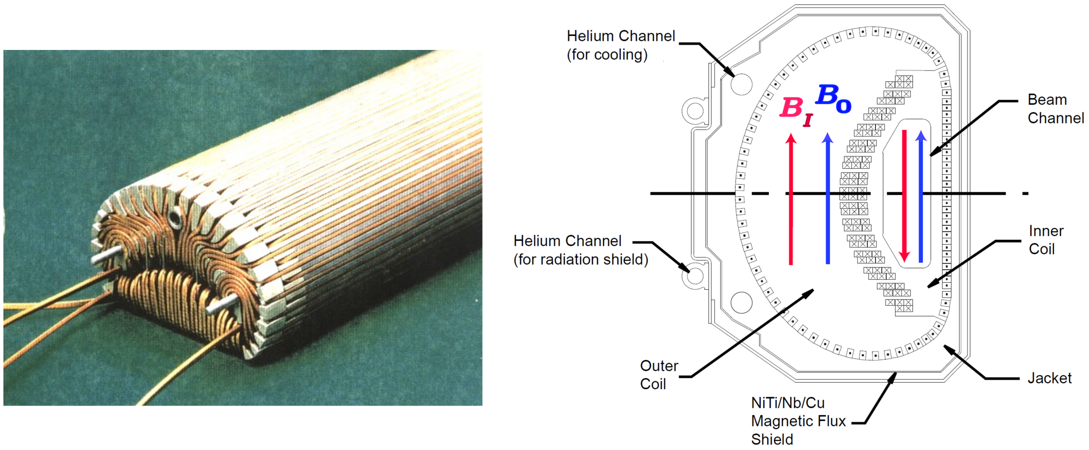

Figure 2.5: The superconducting inflector with $18\,\mathrm{mm} \times 56\,\mathrm{mm}$ aperture provides a field-free path for beam injection into the ring.

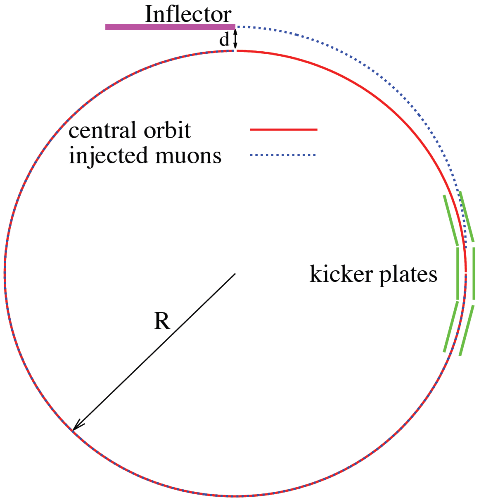

Figure 2.6: The beam is injected at a $77\,\mathrm{mm}$ radial offset from the nominal orbit. Figure courtesy of D. Rubin [40].

diately downstream of the T0 detector; IBMS2 is located immediately upstream of the inflector; and IBMS3 is located downstream of the inflector inside the storage ring. Together these entrance detectors monitor and record the intensity, timing, and spatial distribution of the injected beam for every fill.

2.4 Beam storage in the $g-2$ ring

The storage ring magnet provides a highly uniform vertical magnetic dipole field with nominal strength $B_0 = 1.451\,\mathrm{T}$ in the toroidal muon storage volume. The so-called "magic field" B_0 centers magic momentum ($p_0 = 3.094\,\mathrm{GeV}/c$) muons on the nominal orbit with "magic radius" $R = 7112\,\mathrm{mm}$. The superferric magnet consists of a C-shaped iron yoke and pole pieces excited by superconducting coils, shown in Figure 2.7. The field is stabilized in time with a feedback system, which adjusts the $\sim$5170 A coil current based on the field measured by a selection of fixed NMR probes (Section 2.7). The spatial homogeneity of the field was fine-tuned with iron wedge-shaped shims in the gap between the pole pieces and yoke as well as iron edge shims and iron foil laminations on the pole surfaces, resulting in a 14 ppm RMS uniformity in the storage volume. Concentric surface correction coils on the pole surfaces are configured with a current profile to minimize field gradients, providing an azimuth-averaged uniformity over the transverse storage region of < 1 ppm [41].

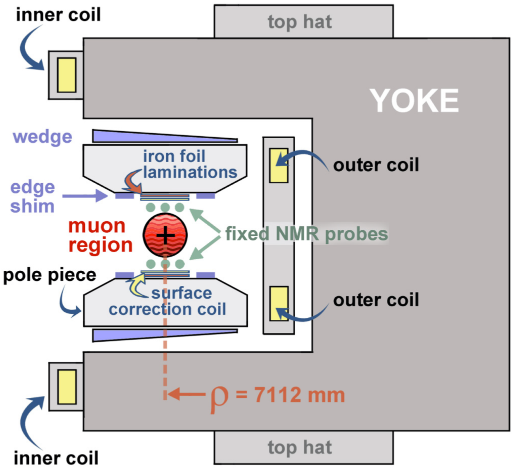

Figure 2.7: Cross section of the C-shaped storage ring magnet, which provides a $1.451\,\mathrm{T}$ vertical dipole field. Reproduced from [41].

Figure 2.8 shows locations of the systems in the storage ring discussed below.

Because the beam is injected at a $77\,\mathrm{mm}$ radial offset to the nominal orbit (Figure 2.6), it intersects the nominal orbit with a $\sim 77\,\mathrm{mm}/7112\,\mathrm{mm} = 10.8\,\mathrm{mrad}$ angle at 90° from the inflector exit. Three pulsed kicker electromagnets located at 90° in the ring switch on a vertical magnetic field which provides a $\sim 10.8\,\mathrm{mrad}$ radially-outward kick, shifting the beam to its nominal orbit [43]. An ideal kick would turn on only during the first turn in the ring with cyclotron period $T_c = 149.2\,\mathrm{ns}$, and the field would be constant over the pulse. The real kicker pulse, shown in Figure 2.9, is time-dependent over T_c and has a ringing tail due to impedance mismatch, such that the muons receive additional kicks over several turns. The three kickers are individually timed to maximize the muon storage fraction for each injected beam bunch. The muons' average orbit radius is called the equilibrium radius. Until late in Run-3, the kickers did not achieve their intended strength and delivered a weaker-than-nominal kick, which centered the beam at a higher-than-nominal equilibrium radius $r_e - R \approx 5\,\mathrm{mm}$ to $7\,\mathrm{mm}$ [42]. During Run-3 the pulser cables were upgraded which allowed an increased kick strength and centered the beam within $1\,\mathrm{mm}$ of the nominal radius [44].

The dipole magnetic field focuses the beam horizontally and contains it in the storage region, and the electric

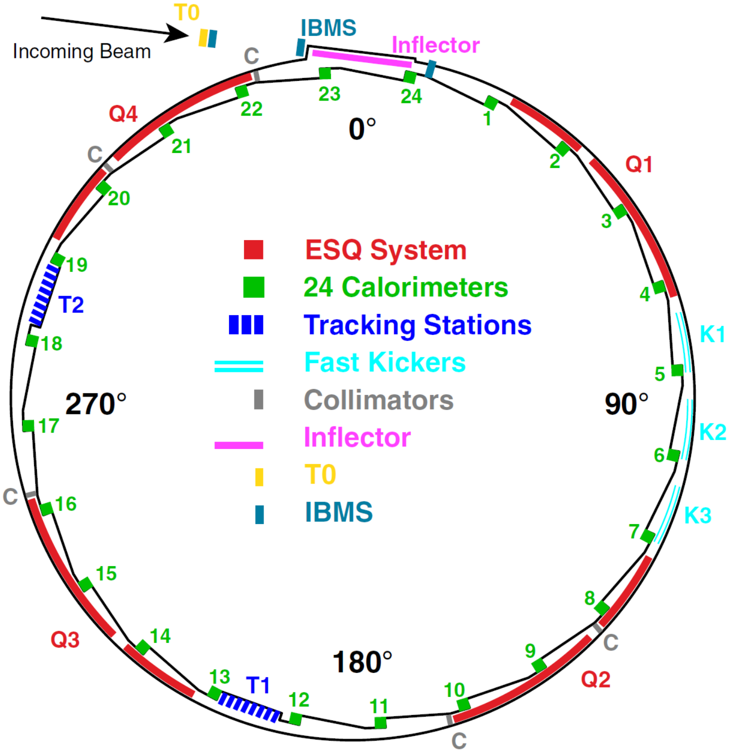

Figure 2.8: Schematic view of the storage ring systems, reproduced from [42].

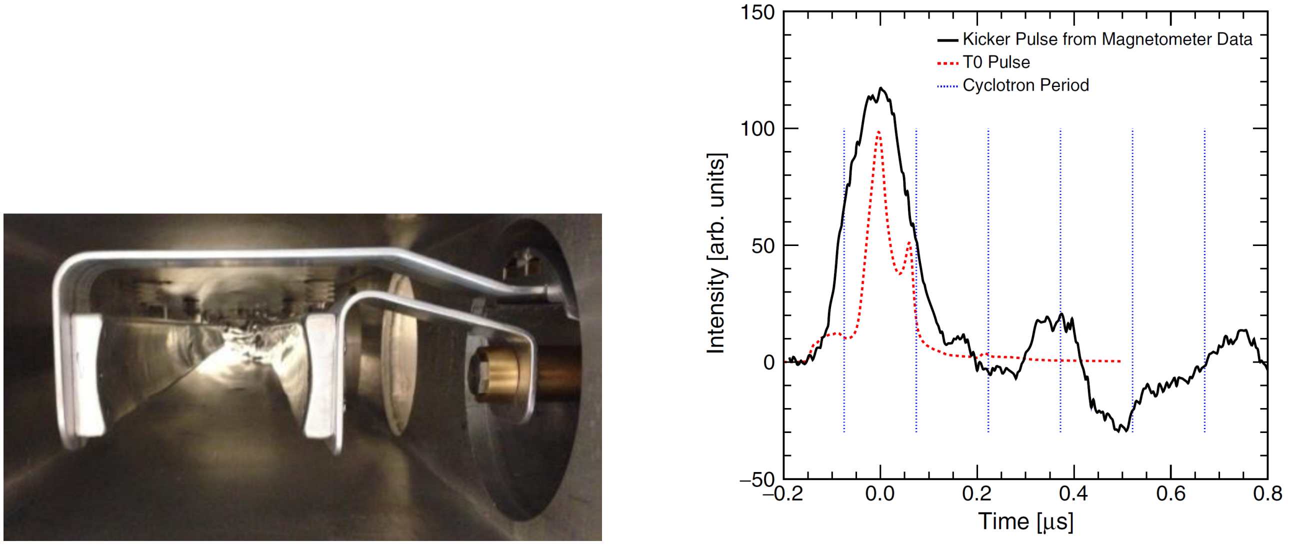

(a) Kicker plates positioned radially inward and outward of the muon storage region provide a pulsed vertical magnetic field to shift the beam onto its nominal orbit.

(b) The kicker pulse (black) compared with a typical injected beam pulse (red) shows that the kick strength varies over the beam injection time, and rings over several cyclotron periods (blue). Reproduced from [42].

Figure 2.9

quadrupole field provides vertical focusing at the expense of horizontal defocusing (Figure 2.10). The electrostatic quadrupoles consist of four electrode plates on all sides of the storage region, positioned in discrete segments (four short and four long segments) around the ring. The top and bottom plates are set at a positive voltage $+V_q$ and the inner and outer plates are set at $-V_q$, with typical voltages $V_q = 18.2\,\mathrm{kV}$ or $18.3\,\mathrm{kV}$ in Run-2/3. The quad plates are charged before each muon fill and discharged at the end of the $700\,\mu\mathrm{s}$ fill. The quads are also used to intentionally scrape the beam by initially charging selected plates to a lower voltage $< V_q$. This shifts the beam radially and vertically off-center so that muons moving near the edge of the $90\,\mathrm{mm}$ diameter storage region are likely to be lost by scattering on the five collimators positioned in the ring. This scraping is nominally completed and the beam returns to equilibrium by $30\,\mu\mathrm{s}$ after injection.

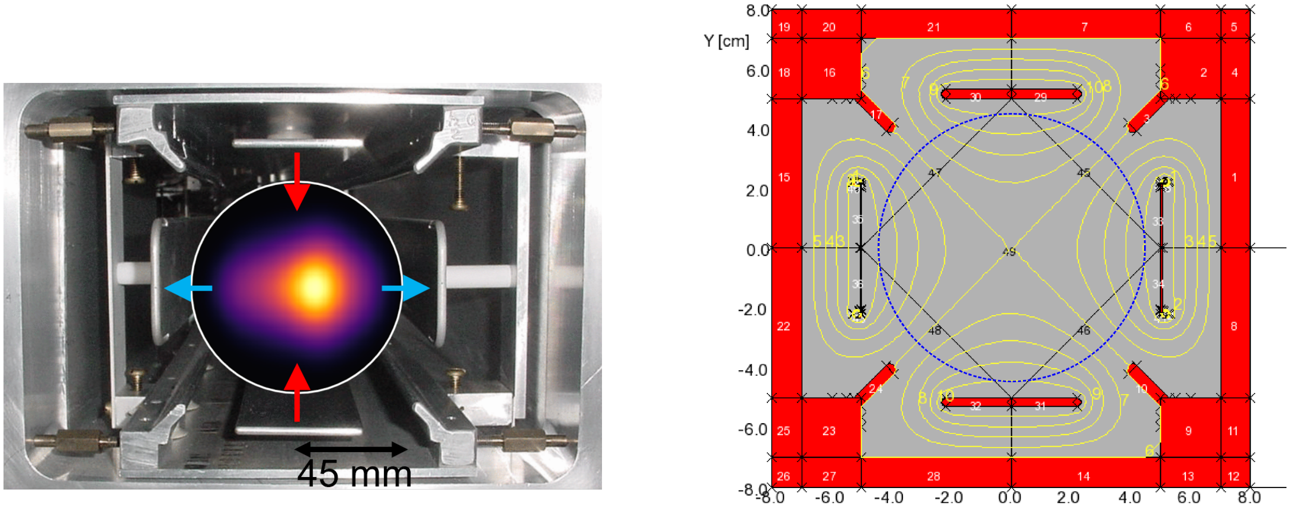

(a) Electrostatic quadrupole plates vertically focus the beam in the storage region, at the expense of horizontal defocusing.

(b) Equipotential lines of the electric quadrupole field in the storage region, reproduced from [36].

Figure 2.10

2.5 Straw trackers

Straw tracking detectors at two locations in the ring reconstruct the stored muon distribution by tracking the paths of the decay positrons, shown schematically in Figure 2.15. Straw tracker stations are located near azimuths 180° and 270° (shown in Figure 2.8), where stations are numbered 12 and 18 according to the neighboring calorimeters. The Mylar straws are filled with argon-ethane gas; each straw is a grounded cathode, and a high voltage wire at the center of each straw is the anode [45]. A decay positron traversing a straw ionizes the gas and induces a voltage signal in the wire. One tracker station consists of eight modules, and a module includes four stereooriented layers of 32 straws each. A tracking algorithm extrapolates the positron trajectory to the point of tangency to reconstruct the muon decay position. The distribution of muon decay positions corresponds to the stored muon beam distribution in a narrow azimuthal range of $\sigma \approx 5^\circ$. The tracker-measured muon distribution over the time of the fill provides beam dynamics information which is necessary for ω_a systematics corrections and uncertainties. The tracker beam profiles also provide input for the muon-weighted magnetic field analysis, discussed in detail in Chapter 7.

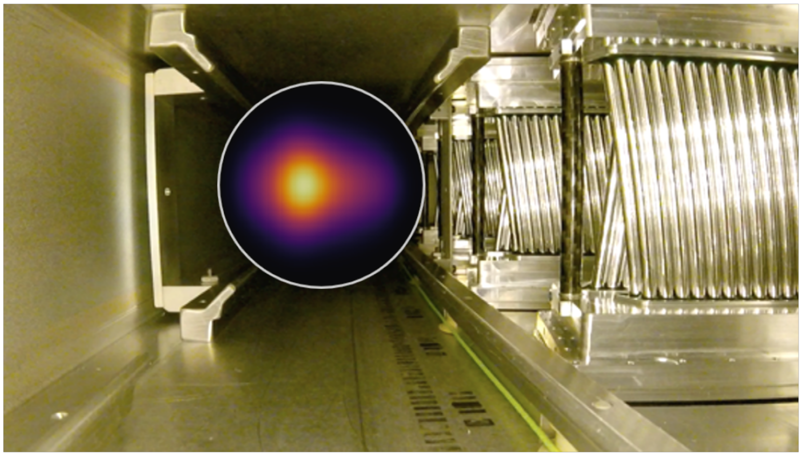

Figure 2.11: The straw tracking detectors reconstruct the muon beam distribution, shown here as an intensity map in the $90\,\mathrm{mm}$ diameter storage region, by tracking the decay positrons.

2.6 Measuring the anomalous precession frequency ω_a

The muon decays to a positron and two neutrinos by the dominant process $\mu^+ \rightarrow e^+\nu_e\bar{\nu}_\mu$ (Figure 2.12), with a rest frame lifetime of $\sim 2.2\,\mu\text{s}$. Because this decay is a weak interaction which violates parity, the decay e^+ energy is correlated with the direction of the μ^+ spin at the time of decay. The e^+ count above an energy threshold is then modulated in time by the anomalous precession frequency ω_a. Calorimeters are used to record the energy and arrival time of the decay e^+, from which ω_a is extracted.

2.6.1 Decay positron spectrum

In the center of mass (CM) frame, the highest e^+ energy configuration occurs when the e^+ is emitted back-to-back with the neutrinos (Figure 2.12). Because the ν has left-handed (LH) helicity and the $\bar{\nu}$ has right-handed (RH) helicity, their summed spin is zero in this configuration. Spin conservation requires that the initial muon spin $\vec{s}_\mu$ is equal to the final positron spin $\vec{s}_e$. Because the decay e^+ has RH helicity in the weak interaction, its momentum $\vec{p}_e$ must also be parallel to $\vec{s}_\mu$. Therefore the highest-energy e^+ are preferentially emitted along the μ^+ spin direction.

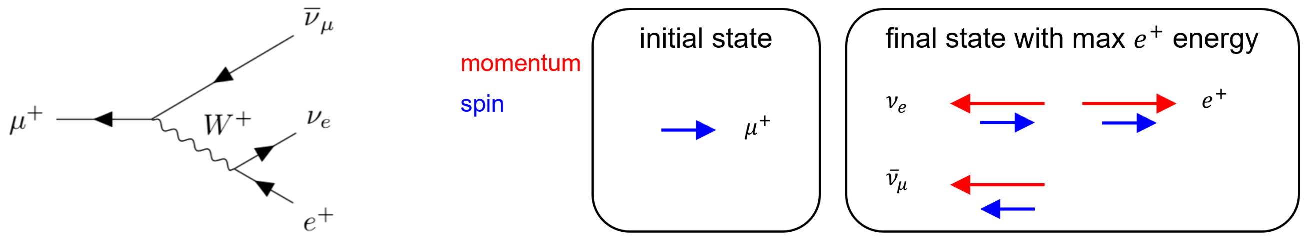

(a) The muon dominantly decays to a positron and two neutrinos

(b) In the highest e^+ energy configuration, the decay e^+ is emitted in the direction of the μ^+ spin before decay.

Figure 2.12: Muon decay by the weak interaction

This energy-spin correlation is present over the full e^+ energy range, with the differential decay distribution in the CM frame given by [36]

$$\frac{d^2P(y,\theta)}{dy\,d\cos(\theta)} \propto N_r(y)\left[1 + A_r(y)cos(\theta)\right] \,, \tag{2.6}$$

where $y = E^*/E^*_{max}$ is the CM frame energy normalized to the maximum possible energy $E^*_{max} = m_\mu c^2/2$ and θ is the angle between $\vec{s}_\mu$ and $\vec{p}_e$. The number distribution $N_r(y)$ increases with E^*, which means higher-energy e^+ are emitted with an overall greater probability. The asymmetry $A_r(y)$ describes the correlation between $\vec{s}_\mu$ and e^+ energy. $A_r(y)$ has its maximum value of 1 for $E^* = E^*_{max}$ and decreases to < 0 for $E^* = 0$, which means higher-energy e^+ are emitted along the $\vec{s}_\mu$ direction with greater probability than lower-energy e^+. Figure 2.13 shows the $N_r(y)$ and $A_r(y)$ distributions.

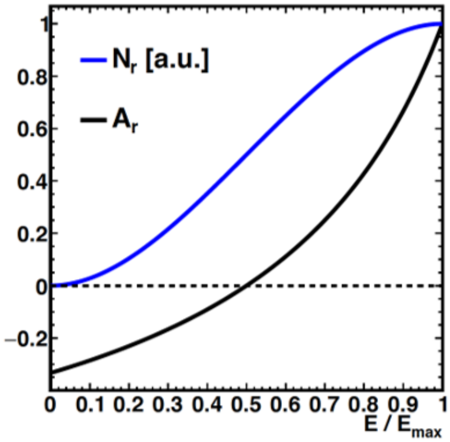

Figure 2.13: The decay e^+ asymmetry and number distributions in the center of mass frame increase for higher e^+ energy, so higher-energy e^+ are more likely to be emitted along the μ^+ spin. Figure courtesy of A. Fienberg [46].

In the lab frame, the energy E of the decay e^+ is boosted along the μ^+ momentum; E increases for $\vec{s}_\mu \parallel \vec{p}_\mu$, and decreases for $\vec{s}_\mu \parallel -\vec{p}_\mu$. The e^+ energy spectrum is modulated by the angle α between $\vec{s}_\mu$ and $\vec{p}_\mu$, which changes at the rate ω_a, as shown in Figure 2.14. The lab frame decay e^+ spectrum is given by the expression [36]

$$N(E,t) = N(E)e^{-t/\gamma\tau_\mu}\left[1 + A(E)\cos(\alpha)\right] \tag{2.7}$$

where $N(E)$ and $A(E)$ are the lab frame number and asymmetry functions; $\gamma\tau_\mu$ is the lab frame μ^+ lifetime; and $\alpha = \omega_a t - \phi(E)$ with $\phi(E)$ the initial $\vec{s}_\mu$ phase.

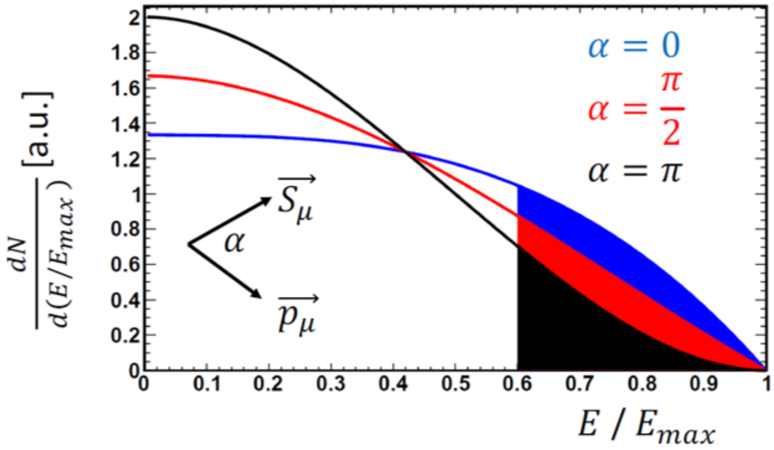

Figure 2.14: The decay e^+ energy spectrum in the lab frame is modulated by ω_a, the rate of change of the angle between the muon's spin and momentum. Figure courtesy of A. Fienberg [46].

The total e^+ count above an energy threshold E_{thr} is then modulated by ω_a as shown in Figure 2.17, and is described by [36]

$$N(E_{thr}, t) = N_0(E_{thr}) e^{-t/\gamma\tau_\mu} \left[1 + A(E_{thr}) \cos(\omega_a t - \phi_0(E_{thr}))\right] \tag{2.8}$$

which is the basic fit function used to extract ω_a from the decay e^+ spectrum. $N_0(E_{thr})$ is the initial beam intensity above E_{thr}, $A(E_{thr})$ is the asymmetry which decreases for lower E_{thr}, and $\phi_0(E_{thr})$ is the ensemble average initial spin phase.

2.6.2 Calorimeter detectors

The decay e^+ have momenta below the ring momentum acceptance, and drift inward toward the ring center (Figure 2.15). Their energy spectrum is measured with 24 electromagnetic calorimeters [47] [48] equally spaced around the inside of the ring, located as shown in Figure 2.8. Each calorimeter consists of a grid of 6×9 lead fluoride (PbF_2) crystals (Figure 2.16) which emit Cherenkov radiation proportional to the deposited energy when struck by a charged particle. Each crystal is coupled to a silicon photomultiplier (SiPM) light sensor read out by programmable gain amplifier electronics. (See Section 3.2 for more information about SiPMs in a different application.) The signals from the 1296 calorimeter channels are digitized over the entire time of the fill by 12-bit waveform digitizers at a rate of 800 MS/s, and recorded by data acquisition (DAQ) frontend software in the main MIDAS-based DAQ system. A laser system feeds laser pulses directly into each crystal for gain monitoring and correction and timing synchronization.

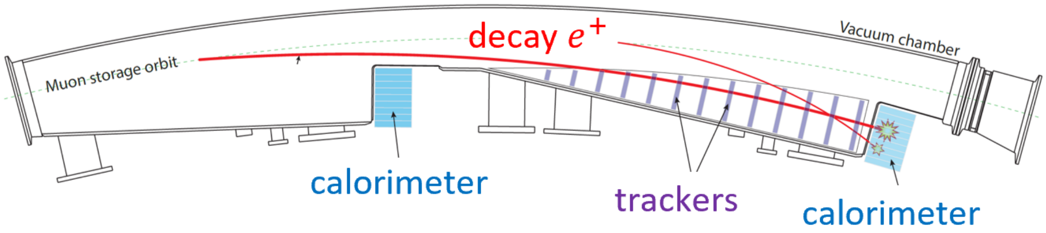

Figure 2.15: Example decay e^+ trajectories in a top view of a segment of the ring. The e^+ drift inward, and a fraction of them deposit energy in a calorimeter. Higher-energy e^+ have larger radii of curvature in the magnetic field, and travel farther before leaving the ring and striking a calorimeter. Straw tracking detectors are positioned in front of two of the calorimeters to reconstruct muon decay vertices (Section 2.5).

2.6.3 Extracting ω_a

The basic five-parameter fit function in Eq. 2.8 only accounts for the muons' anomalous precession, but in reality additional terms are present in the decay e^+ spectrum due to beam dynamics effects. The calorimeter acceptance is spatially nonuniform, so beam motion modulates the e^+ count $N(t)$. The dominant oscillating term is caused

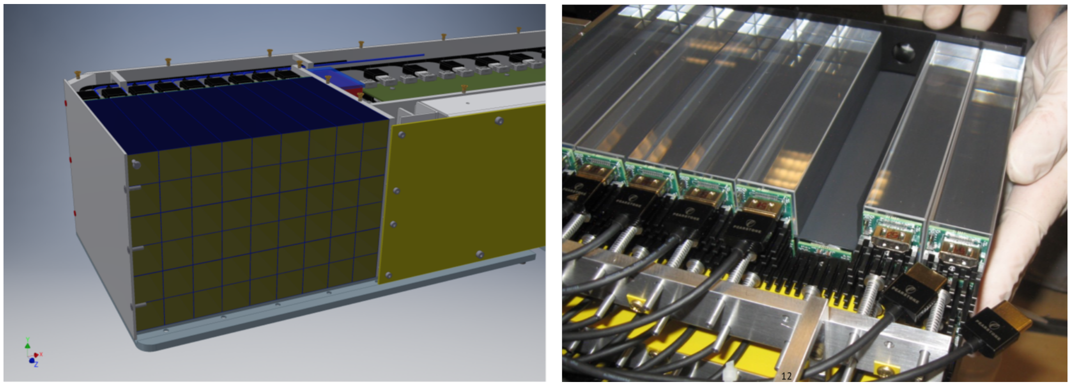

Figure 2.16: Model (left, courtesy of J. Kaspar) and photo (right) of a calorimeter consisting of 54 PbF_2 Cherenkov crystals, each read out by a SiPM.

by the horizontal coherent betatron oscillation (CBO) of the beam; the vertical betatron oscillation of the beam, as well as interference terms between the beam frequencies and ω_a, are also present. These beam oscillations are discussed further in Chapter 4, particularly Section 4.3.4. Effects which have slow time dependence over the fill, such as muon loss by mechanisms other than decay, appear as low-frequency terms. Beam dynamics terms must be included in the fit function to extract an unbiased value of ω_a. Characterizing the beam motion with detector measurements and beam dynamics modeling is necessary to establish a fit function with realistic beam dynamics terms. The full fit function has the general form

$$N(t) = N_0 \cdot \Lambda(t) \cdot N_x(t) \cdot N_y(t) \cdot N_{x,y}(t) \cdot e^{-t/\tau} \left[1 + A(t) \cos(\omega_a t - \phi(t))\right] \ , \tag{2.9}$$

where the function $N_x(t)$ describes horizontal beam motion, $N_y(t)$ describes vertical beam motion, $N_{x,y}(t)$ describes interference between horizontal and vertical terms, $\Lambda(t)$ describes muon loss, $\tau = \gamma\tau_\mu$ is the muon lifetime, and A and ϕ are time-dependent due to CBO modulation [39, 48]. The exact functional form of each term varies among ω_a analysis teams, but fit functions include 22 or more fit parameters which correspond to physical beam dynamics effects. A fast fourier transform (FFT) of the residual difference between the e^+ histogram and the fit shows any beam dynamics frequencies which are not captured in the fit function. A fit function which models all beam dynamics effects corresponds to a flat FFT with no residual frequencies, as shown in Figure 2.17.

For Run-2/3 analysis, the e^+ histogram is fit from time $t_{start} \approx 30.3\,\mu s$ [49] in the fill, after time-dependent beam dynamics effects such as electric quadrupole scraping and the high-intensity beam splash stabilize. The energy threshold is chosen to optimize ω_a statistical precision, balancing increased statistics for lower thresholds vs. increased asymmetry for higher thresholds. The primary analysis method uses an energy threshold of $1100\,\mathrm{MeV}$ and weights the e^+ data by the energy-dependent asymmetry for the best statistical sensitivity. A related method

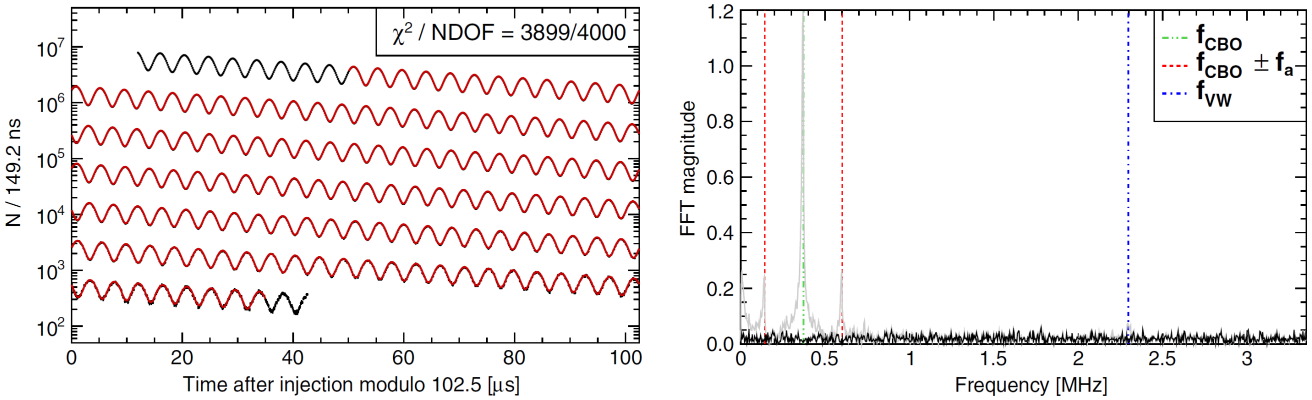

Figure 2.17: Left: Histogram of e^+ counts above an energy threshold over time in the fill (black) and the fit to extract ω_a (red) for an example Run-1 dataset of 4×10^9 e^+. Right: FFT of residuals from the fit, for the full fit function including beam dynamics terms (black) compared with the basic five-parameter fit function (gray) which does not capture the beam dynamics frequencies. Reproduced from [48].

uses a $1700\,\mathrm{MeV}$ threshold with uniform weighting. Other approaches include using a ratio of time-shifted e^+ data subsets to remove the lifetime, and constructing an energy vs. time histogram from a continuous calorimeter energy integral [48].

2.7 Measuring the magnetic field via the proton precession frequency ω_p

The strength of the magnetic field B in the storage ring is measured with pulsed nuclear magnetic resonance (NMR) magnetometer probes, which measure the Larmor precession frequency $\omega'_p(T_r)$ of shielded protons [41], where $\omega'_p \propto B$ as in Eq. 2.10. $T_r = 34.7\,°\mathrm{C}$ is the reference temperature, and the prime indicates calibration to a specific spherical water sample used as the shielded proton sample (Section 2.7.1).

The field strength in terms of ω'_p must be averaged over the muon distribution to represent the field experienced by the muons, denoted as $\tilde{\omega}'_p$. Analysis of the muon-weighted magnetic field in Run-2/3 is discussed in detail in Chapter 7.

2.7.1 Instrumentation

Each pulsed NMR probe consists of a shielded proton sample inside a radio frequency (RF) coil, which is coupled to a resonant circuit to read out and drive the coil [50] (Figure 2.18). A fraction of the protons are magnetized in the field, meaning that their spins are aligned with the vertical magnetic field $\vec{B}$. An RF pulse, called a $\pi/2$ pulse, is applied to the coil to rotate the protons' spins perpendicular to $\vec{B}$. The spins then experience Larmor precession in the magnetic field with frequency ω_p,

$$\omega_p = \frac{g_p e}{2m_p} B\,, \tag{2.10}$$

and simultaneously relax back to alignment with $\vec{\boldsymbol{B}}$. The precession induces a voltage signal, called a free induction decay (FID) signal (Figure 2.19), in the RF coil, with a frequency proportional to the magnetic field strength (Eq. 2.10). This method is sensitive only to the field strength and not the direction so it is treated as purely vertical, i.e. $|B| \approx B_y$, which is a good approximation to O(10 ppb) [41]. The FID signals are digitized with waveform digitizers and recorded by data acquisition (DAQ) frontend software in a MIDAS-based DAQ system which is independent and asynchronous from the detector DAQ.

The frequency ω_p is determined by extracting the time-dependent phase function from a Hilbert transform $\mathcal{H}\left(f(t)\right)$ of the FID signal $f(t)$ [41], which shifts the signal phase in the frequency domain by 90° [50].

$$\phi(t) = \tan^{-1}\left[\frac{f(t)}{\mathcal{H}\left(f(t)\right)}\right] \tag{2.11}$$

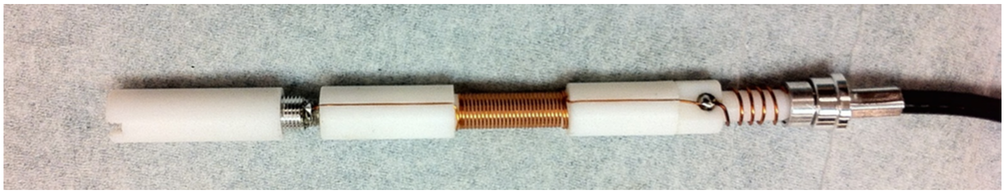

Figure 2.18: NMR probe consisting of the RF coil and holder for the coil and internal proton sample, with a second coil and cable for readout and driving.

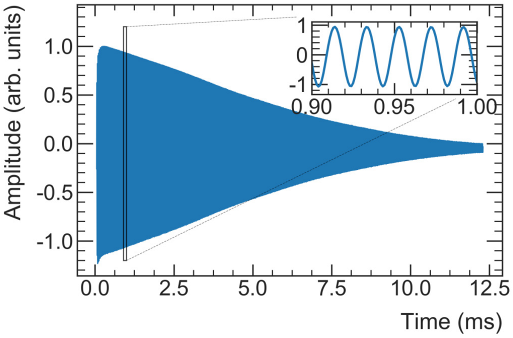

Figure 2.19: Example free induction decay signal, oscillating at the proton precession frequency ω_p, measured by an NMR probe in the storage ring. Reproduced from [41].

The magnetic field in the ring is measured in terms of $\omega'_p(T_r)$ in three stages, as follows [41].

A trolley carrying 17 NMR probes (Figure 2.20) maps the field inside the muon storage region every $\sim$ 3 days. Each probe measures the precession frequency of protons in a cylindrical petroleum jelly sample. The trolley rides around the ring on rails in the vacuum chamber and samples the field at ~ 8000 azimuthal locations (Figure 2.21). A transverse map of the field strength is produced at each azimuth.

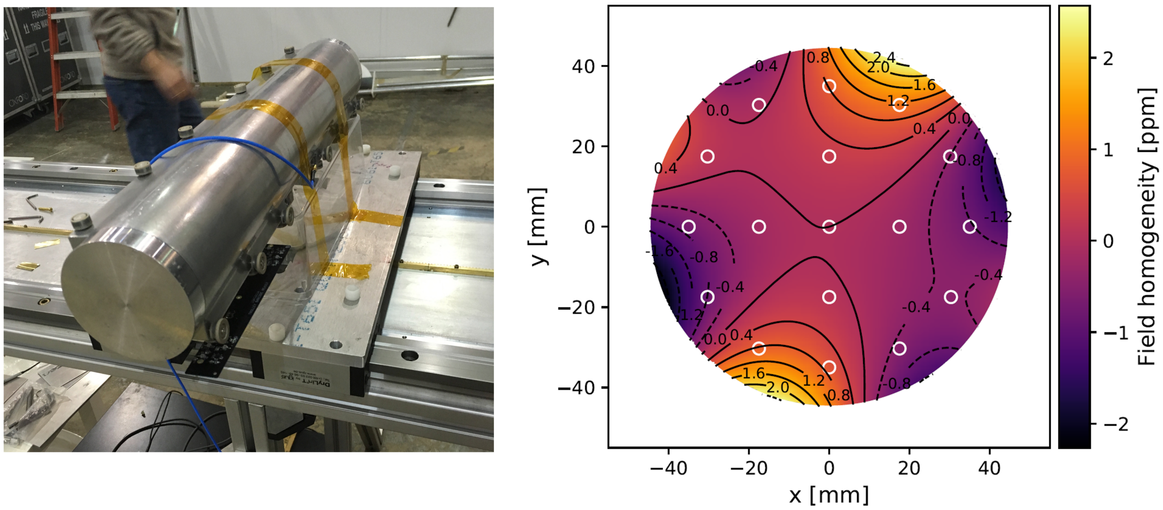

Figure 2.20: The trolley (left) rides around the ring and produces a map of the field in the muon storage region (right, example from Run-1). The white circles indicate the positions of the 17 NMR probes in the trolley, and the field strength is relative to the central probe.

The trolley cannot measure the field during production running when muons are present in the ring because it would interfere with muon storage. A suite of 378 so-called fixed probes, identical to the trolley probes, are mounted to the ring vacuum chamber walls above and below the muon storage region. Seventy-two "stations" of four or six fixed probes each are positioned around the ring (Figure 2.22). The fixed probes track the field over the time between trolley runs, and the trolley maps are then interpolated over the muon measurement time using the drift measured by the fixed probes.

A special calibration probe containing a cylindrical water sample calibrates the trolley probes. The calibration probe is mounted in the ring on a translation stage, which rapidly swaps it to the same position as each trolley probe to measure the same field during special calibration runs. The calibration probe itself is corrected in terms of a well-established NMR standard, namely a spherical water sample at temperature $T_r = 34.7\,°\mathrm{C}$, so that it calibrates the trolley probes in terms of $\omega'_p(T_r)$.

$$\omega'_p(T_r) = \omega^{probe}\left[1 + \delta^{probe}(T_r)\right] \tag{2.12}$$

The general correction $\delta^{probe}(T_r)$ accounts for probe-specific effects including probe materials; geometry, magnetic susceptibility, and diamagnetic shielding of the sample; and measurement temperature. The calibration probes, and subsequently the trolley probes, are corrected in this way.

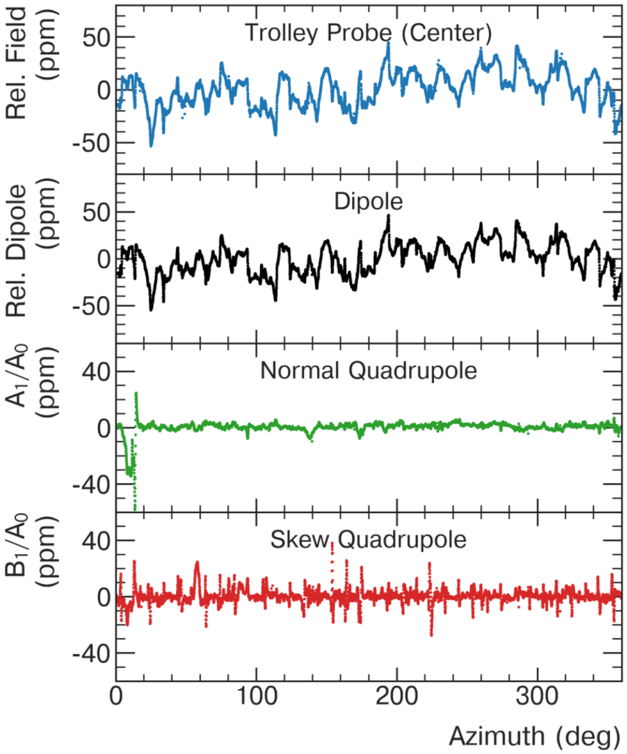

Figure 2.21: Field map vs. azimuth in the ring from a trolley run in Run-1. Relative variation in the frequency ω_p measured by the central trolley probe (top), and relative variation in the dipole (black), normal quadrupole (green), and normal sextupole (red) moments extracted from the trolley field measurements. Reproduced from [41].

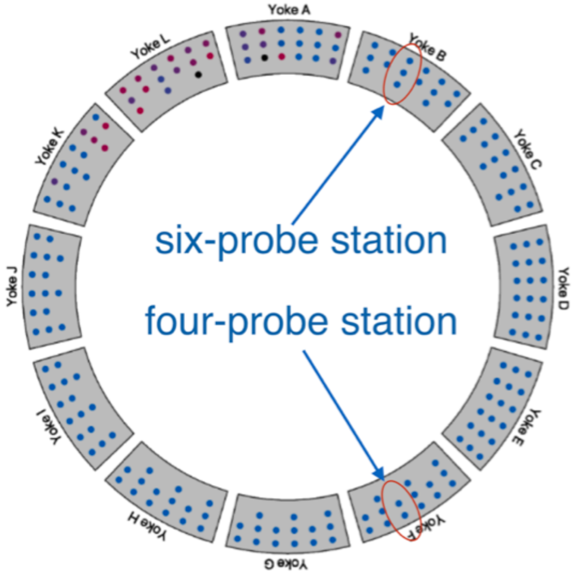

Figure 2.22: The 378 fixed probes are positioned above and below the muon storage region at 72 stations around the ring, each consisting of 4 or 6 probes. Figure courtesy of M. Smith.

2.7.2 Multipoles

The magnetic field strength in the transverse plane $B(x, y)$ can be described by a multipole expansion, which forms a complete basis for a field satisfying Maxwell's equations and the source-free Laplace equation (assuming no longitudinal dependence) [41] [51].

$$B(x, y) = A_0 + \sum_{n=1}^{N} \left(\frac{r}{r_0}\right)^n (A_n \cos(n\Theta) + B_n \sin(n\Theta)) \tag{2.13}$$

Here r and Θ are polar coordinates in the transverse (x-y) plane, N is the multipole order truncation, and $r_0 = 45\,\mathrm{mm}$ is the reference radius for normalization. The constant term A_0 is called the dipole moment, the A_n terms are the normal moments, and the B_n terms are the skew moments. The $n = 1,\ 2,\ 3,\ \&\ 4$ moments are respectively called the quadrupole, sextupole, octupole, and decupole moments; for example, A_1 is the normal quadrupole moment. The expansion can be written more compactly as

$$B(x, y) = \sum_{i=1}^{2N+1} m_i \cdot f_i(r, \Theta)\,. \tag{2.14}$$

Multipoles are indexed by i, with multipole coefficients m_i and expansion basis functions f_i defined as follows.

$$f_i(r, \Theta) = \begin{cases} 1 \text{ for i=1 (dipole)} \\ (r/r_0)^{\frac{i}{2}} \cos\left(\frac{i}{2}\Theta\right) \text{ for } i > 1, i \text{ even (normal)} \\ (r/r_0)^{\frac{i-1}{2}} \sin\left(\frac{i-1}{2}\Theta\right) \text{ for } i > 1, i \text{ odd (skew)} \end{cases} \tag{2.15}$$

Multipole moments m_i have the same units as $B(x, y)$; the functions f_i are unitless. Figure 2.23 shows spatial representations of each multipole. In the Run-2/3 analysis the multipole expansion is nominally truncated at $N = 6$, with the normal 14-pole (m_{12}) the highest-order moment and the skew 14-pole (m_{13}) set to zero.

Table 2.2 shows multipole naming conventions used by the two field analysis teams, called the Bloch and Purcell teams (Section 2.7.3). For historical reasons the m_i naming used by the Purcell team is different from the index i in Eq. 2.15; both the Bloch and Purcell team naming conventions are referenced throughout this thesis.

multipole index i	Bloch name	Purcell name m_i	multipole name
1	Dip	m_1	Dipole
2	NQ	m_2	Normal Quadrupole
3	SQ	m_3	Skew Quadrupole
4	NS	m_5	Normal Sextupole
5	SS	m_4	Skew Sextupole
6	NO	m_7	Normal Octupole
7	SO	m_6	Skew Octupole
8	ND	m_8	Normal Decupole
9	SD	m_9	Skew Decupole
10	N12	m_{10}	Normal 12-pole
11	S12	m_{11}	Skew 12-pole
12	N14	m_{12}	Normal 14-pole
13	S14	m_{13}	Skew 14-pole

Table 2.2: Multipole index and name conventions used by the so-called Bloch and Purcell field analysis teams

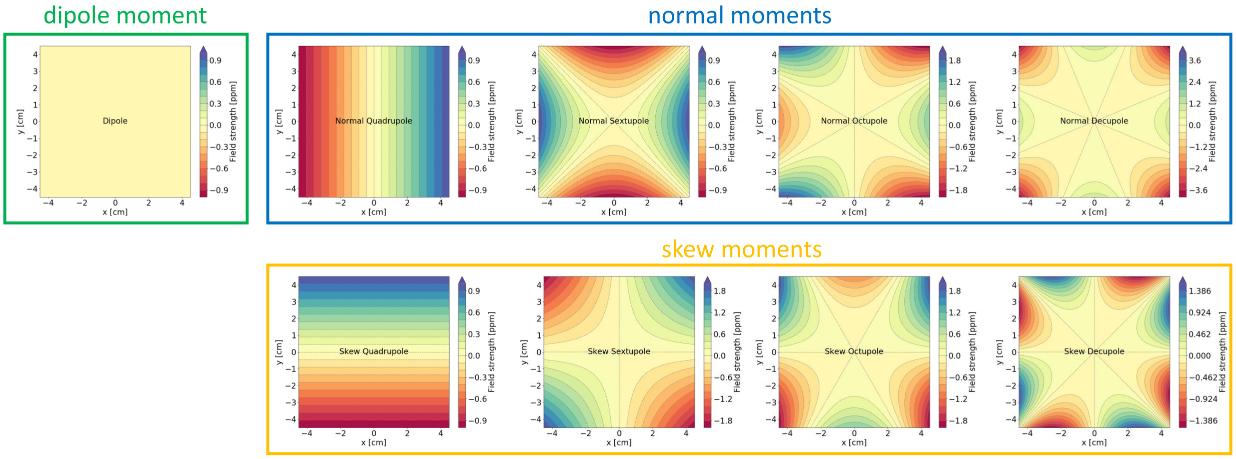

Figure 2.23: 2D spatial distributions corresponding to the normal and skew multipoles. Figure courtesy of S. Charity.

2.7.3 Analysis

The field drift tracked by the fixed probes is used to interpolate the trolley maps over the time between trolley runs; this interval between a pair of trolley runs is known as a trolley pair. The dipole, quadrupole, and sextupole moments (m_1-m_5) at each of the 72 fixed probe stations are predicted using geometrical combinations of the fixed probe measurements. These fixed probe moments are synchronized within a trolley pair to match the bounding trolley runs, then interpolated to 2 s intervals. The synchronization correction includes a linear time-dependent slope between trolley runs due to the field drift over time. This synchronization ties the moments in each fixed probe station to the two trolley runs, and the remaining non-linear drift component is a source of uncertainty in the field tracking. The higher-order multipole moments (m_6 and above) are simply linearly interpolated between the two trolley runs, as they cannot be tracked due to the geometrical arrangement of the fixed probes.

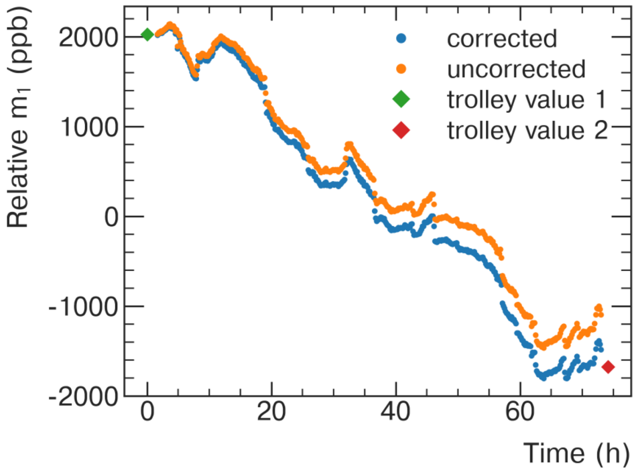

Figure 2.24: Relative drift in the dipole moment tracked by a fixed probe station over a trolley period in Run-1. The trolley run values at the corresponding location are shown in red and green. The fixed probe values (orange) are corrected to synchronize (blue) with the ending trolley run. The corrected fixed-probe-measured field drift is then used to interpolate the trolley field maps over time. Reproduced from [41].

The Bloch and Purcell analysis teams independently perform the field interpolation analysis. Careful cross-checks between the teams build confidence in the analysis results. Both approaches are introduced here, but the muon-weighted field analysis presented in detail in Chapter 7 focuses on field maps produced by the Bloch team.

The field drift between fixed probe stations is tracked by a superposition of measurements from different stations. For a moment m_i measured by the trolley at azimuth θ_k and time t_k, the m_i at time t between trolley runs is given by [51]

$$m_i(\theta_k, t) = m_i(\theta_k, t_k) + \sum_{st} w_{st}(\theta_k) \cdot \Delta m_{i,st}(t, t_k)\,, \tag{2.16}$$

where $\Delta m_{i,st}(t, t_k)$ is the drift of m_i at the station from time t_k to t (after the above synchronization correction), and w_{st} is the weight of the station in the superposition. The Bloch team uses weights w_{st} which decrease linearly with distance, from 1 at the station position to 0 at the next station, so that $m_i(\theta_k)$ is given by a linear superposition of the drift from neighboring stations. The Purcell team uses $w_{st} = 1$ for the nearest station and 0 for all others, so that $m_i(\theta_k)$ is given by the drift of only one nearest station. This is not the only difference between the analysis teams, but it is the main difference for the purpose of this discussion.

The field maps $m_i(\theta, t)$ produced by the Bloch team are called virtual trolley maps. As discussed in Section 7.2, virtual trolley maps are produced in few-hour time intervals $T_{interval}$ using fixed probe moments $m_{i,st}$ averaged over $T_{interval}$ with decay positron count ("ctag") weighting. This was an update in the Run-2/3 Bloch analysis; the Run-1 analysis produced azimuth-averaged field maps.

2.7.4 Units

The nominal field strength $B_0 = 1.451\,\mathrm{T}$ corresponds to an NMR frequency $\omega_p = 61.79\,\mathrm{MHz}$. The NMR FID signals are mixed down to $\sim 50\,\mathrm{kHz}$ before digitization. The field strength measured by the NMR probes, as well as the field multipole moments, are typically reported either in Hz relative to the mixing frequency $61.74\,\mathrm{MHz}$, or in ppm of $61.79\,\mathrm{MHz}$. Therefore, a field of strength $B = B_0$ would be reported as $50\,\mathrm{kHz}$, or in ppm as $50\,\mathrm{kHz}/61.79\,\mathrm{MHz} \approx 809.2$ ppm. A field of strength $B = B_0(1 + \delta_B \text{ ppm})$ would be reported as $(809.2 + \delta_B)$ ppm.

2.8 Extracting a_μ from the measured frequencies

The anomalous magnetic moment a_μ is extracted from the ratio of observable frequencies $\mathcal{R}'_\mu \equiv \omega_a/\tilde{\omega}'_p(T_r)$ according to Eq. 2.4. The measured frequencies must be corrected for experimental effects caused by beam dynamics and time-dependent fields. Including corrections, the ratio $\mathcal{R}'_\mu$ can be written

$$\mathcal{R}'_\mu = \frac{f_{clock}\, \omega_a^m \,(1 + C_e + C_p + C_{ml} + C_{pa} + C_{dd})}{f_{calib}\, \langle \omega_p(x, y, \theta) \times M(x, y, \theta)\rangle \,(1 + B_k + B_q)}\,. \tag{2.17}$$

In the numerator, ω_a^m is the measured anomalous precession frequency, f_{clock} is the master clock unblinding factor, and the C_i factors are beam dynamics corrections to ω_a^m. Characterizing the beam with detector measurements and beam dynamics modeling is critical for calculating these C_i corrections. In the denominator, $\tilde{\omega}'_p(T_r)$ is expressed in terms of the absolute NMR calibration factor f_{calib} and the muon-weighted proton NMR frequency $\tilde{\omega}_p = \langle \omega_p(x, y, \theta) \times M(x, y, \theta)\rangle$, where M is the stored muon distribution (discussed in detail in Chapter 7). The B_i factors are corrections to $\tilde{\omega}'_p$ for transient field effects which change over time in the fill relative to the NMR-measured ω'_p.

Figure 2.25 shows a breakdown of the Run-1 values of these corrections, as well as uncertainties on the corrections and on the frequencies themselves. The corrections are described below, along with highlights of uncertainties which are significantly improved in Run-2/3 compared to Run-1.

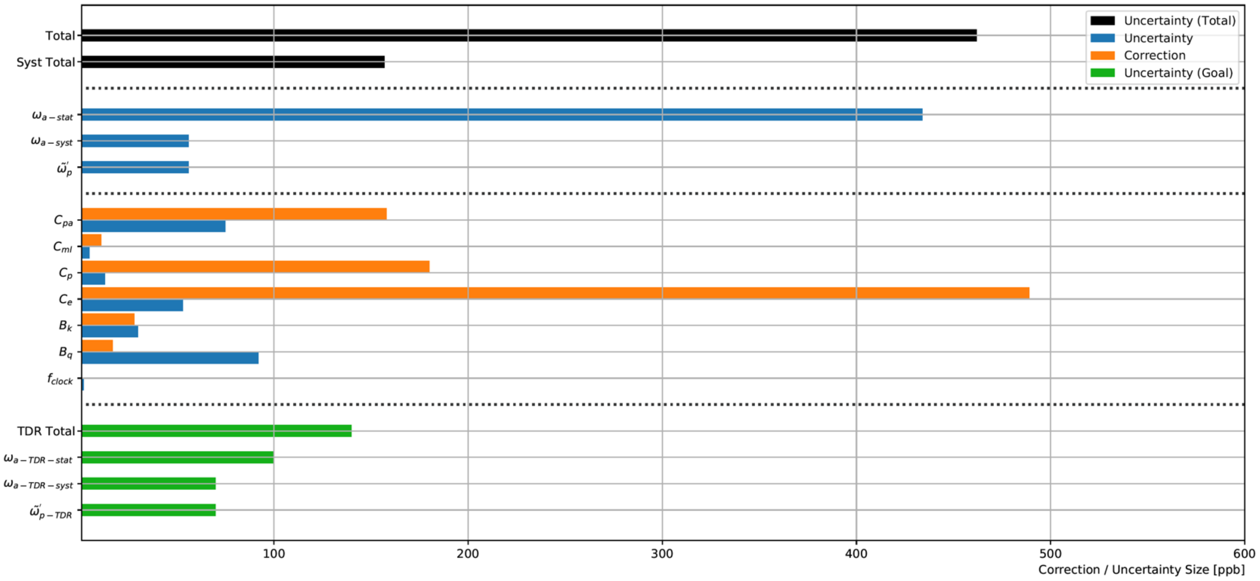

Figure 2.25: Run-1 corrections from Eq. 2.17 (orange) and uncertainties (blue), with total uncertainty in black showing that the Run-1 uncertainty was statistics dominated. For comparison, the target final uncertainty from the Technical Design Report [36] (TDR) is shown in green. Figure courtesy of J. LaBounty.

2.8.1 Corrections to ω_a

$\boldsymbol{f_{clock}}$: The frequency ω_a is measured with a blinding factor to allow an unbiased analysis. The result is only unblinded with collaboration consensus that the analysis is complete, following a rigorous series of cross-checks. The calorimeter digitization clock with nominal frequency $40\,\mathrm{MHz}$ is detuned to a secret value in the range $39.997\,\mathrm{MHz}$ to $39.999\,\mathrm{MHz}$ [52] by Fermilab affiliates external to the collaboration. The unblinding factor f_{clock} converts ω_a^m back to its true frequency.

$\boldsymbol{C_e}$: The electric field correction C_e corrects for the $\vec{E}$ field term in Eq. 2.5, which is not perfectly canceled due to the finite spread of muon momenta. The momentum distribution is reconstructed from the so-called "fast rotation" Fourier analysis of the cyclotron frequencies observed by the calorimeters (Figure 2.26). This analysis reconstructs the muons' equilibrium radii relative to the nominal radius, $x_e = r_e - R$, related to the momenta by $x_e = \Delta p/p_0 \cdot R/(1-n)$ (Section 4.3.1), where Δp is the momentum deviation from p_0 and n is the effective field index for the focusing electric and magnetic fields (Section 4.3.1). The electric quadrupole field centered at radius R increases linearly in strength with distance from R. The electric field correction is given by [42]

$$C_e = 2n(1-n)\beta^2 \frac{\sigma_{x_e}^2 + \langle x_e \rangle^2}{R^2} \tag{2.18}$$

where σ_{x_e} is the width and $\langle x_e \rangle$ is the mean of the distribution of equilibrium radii, and β is the relative velocity of magic momentum muons. The uncertainty on C_e is dominated by the time-varying kick strength, which causes a correlation between injection time and momentum of the stored muons and distorts the momentum reconstruction. This was a significant ω_a systematic uncertainty in Run-1; the Run-2/3 evaluation is in progress, but improved reconstruction methods and simulations are expected to reduce the uncertainty.

$\boldsymbol{C_p}$: The pitch correction C_p corrects for the muons' vertical betatron motion which leads to a nonzero $\vec{\beta}\cdot\vec{B}$ term in Eq. 2.5 [1]. The distribution of vertical betatron amplitudes A_y is reconstructed from the trackers (Figure 2.26). The pitch correction is calculated directly from this distribution by [42]

$$C_p = \frac{n\langle A_y^2\rangle}{4R^2}\,. \tag{2.19}$$

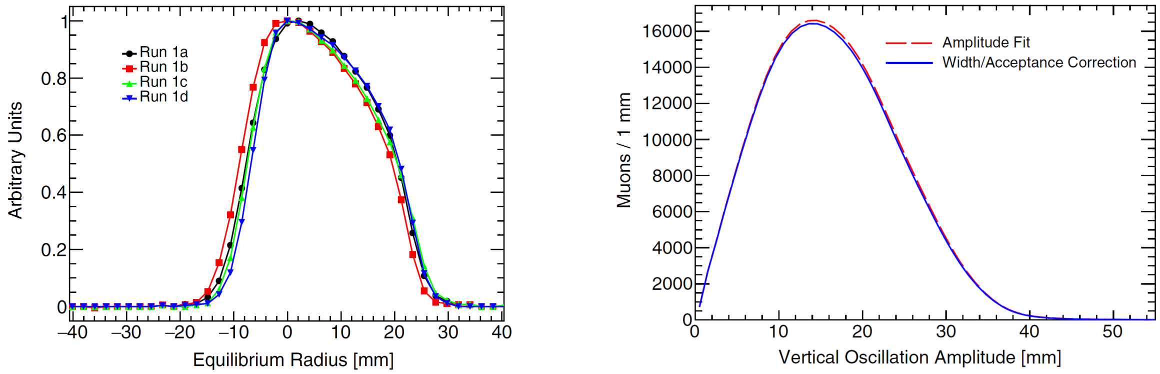

(a) Equilibrium radius reconstruction used to calculate the electric field correction C_e for datasets in Run-1. Reproduced from [42].

(b) Vertical betatron amplitude reconstruction used to calculate the pitch correction C_p for an example dataset in Run-1. Reproduced from [42].

Figure 2.26

$\boldsymbol{C_{ml}}$: The muon loss correction C_{ml} corresponds to a time-dependent average phase which pulls the ω_a fit in Eq. 2.9. Muons which are lost from storage by non-decay mechanisms can cause a net drift in the remaining ensemble-averaged phase ϕ_0 over the time of the fill, biasing ω_a and requiring a correction $C_{ml} = -\Delta\omega_a/\omega_a$. The time dependence comes from a momentum-dependent muon loss rate together with an upstream correlation between momentum and phase [42], and the ω_a shift is

$$\Delta\omega_a \approx \frac{d\phi_0}{dt} = \frac{d\phi_0}{d\langle p\rangle}\frac{d\langle p\rangle}{dt}\,. \tag{2.20}$$

The phase-momentum correlation $d\phi_0/d\langle p\rangle$ was determined from beamline simulation and systematic spin precession data. The rate of change of the ensemble momentum $d\langle p\rangle/dt$ was measured with a systematic bias in the injected muon momentum. Due to reduced muon losses, the correction is irrelevant after Run-1 [39, 54].

---

[1] This conceptual explanation leads to the correct expression for the correction, but the electric field also contributes to the effect. A more complete and accurate discussion is given in [53].

$\boldsymbol{C_{pa}}$: The phase-acceptance correction C_{pa} corresponds to another time-dependent average phase effect. The calorimeter acceptance, and therefore the detected phase ϕ_0, depends on the muon decay position (Figure 2.27). Any time dependence of the transverse beam distribution over the fill couples with the detector acceptance and leads to a time-dependent detected phase $d\phi_0/dt$. The beam distribution time dependence is measured by the trackers, and the detector acceptance and resulting time dependence of the phase was determined from simulation. In Run-1, damaged charging resistors in two electric quadrupole plates caused a time-changing beam distribution which dominated the correction [42]. The uncertainty on C_{pa} was the dominant ω_a systematic uncertainty in Run-1. The resistors were replaced after Run-1, and both the correction and uncertainty are significantly reduced for Run-2/3 but still relevant due to muon losses which cause time dependence of the beam [55, 56].

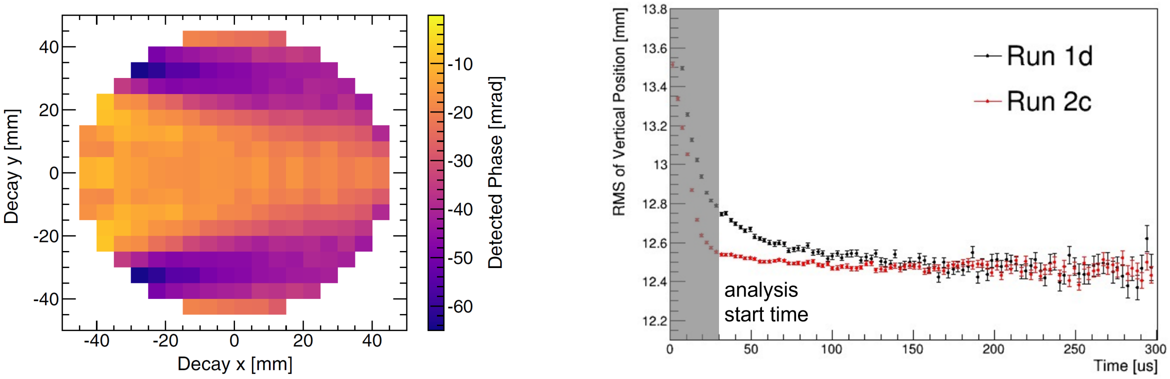

(a) Due to calorimeter acceptance, the detected spin phase depends on the transverse muon decay position (determined here from simulation). Reproduced from [42].

(b) The beam was significantly more stable over time in the fill post-Run-1, after replacing the damaged quadrupole resistors. The vertical beam width (shown here for example datasets in Run-1 and Run-2) dominates the phase-acceptance effect. Figure courtesy of J. Mott [57].

Figure 2.27

$\boldsymbol{C_{dd}}$: The differential decay correction C_{dd} corresponds to another effect from a time-dependent average phase. The muons have a finite momentum spread and a corresponding spread in lab frame lifetimes $\gamma\tau_\mu$. High-momentum muons therefore decay slower than low-momentum muons, causing a momentum-dependent muon loss rate $d\langle p\rangle/dt$. As with the C_{ml} calculation, phase-momentum correlations of the form $\partial\phi_0/\partial a \cdot \partial a/\partial p$ with any momentum-dependent quantity a would then lead to a bias in ω_a. Correlations with the initial horizontal phase space, the injection time due to the time-dependent kick, and the same phase-momentum correlation in the C_{ml} term contribute to C_{dd}. This correction was not included in Run-1, but will be $\mathcal{O}$(15 ppb) for Run-2/3 [58].

2.8.2 Corrections to ω_p

$\boldsymbol{f_{calib}}$: The proton NMR frequency is calibrated to the NMR standard of a spherical water sample at temperature $T_r = 34.7\,^{\circ}\mathrm{C}$ as described in Section 2.7.1. The calibration factor f_{calib} relates the measured frequency ω_p to $\omega_p'(T_r)$.

$\boldsymbol{B_k}$: The kicker transient correction B_k corresponds to a magnetic field perturbation caused by the kickers. The kicker pulse induces eddy currents in the vacuum chamber, generating a magnetic field which decays over the fill. This transient field was measured with two independent magnetometers which use the Faraday-rotated polarization of laser light to sense the field [41]. The correction B_k is given by weighting the magnetic field in time by the muon decay rate, and in azimuth by the extent of the kickers. The uncertainty on B_k is reduced in Run-2/3 compared to Run-1 due to improved magnetometer measurements.

$\boldsymbol{B_q}$: The quad transient correction B_q corresponds to another magnetic field perturbation caused by the electric quadrupoles. Charging the quadrupoles at the start of each fill induces mechanical vibrations in the plates which generates a time-varying magnetic field. Dedicated NMR probes made of non-conductive materials to avoid skin depth effects measured this transient field inside the storage volume [41]. The correction B_q is given by weighting the magnetic field in time by the muon decay rate, and in azimuth by the extent of the quadrupoles. The uncertainty on B_q was the dominant ω_p systematic uncertainty in Run-1, mainly due to incomplete mapping of the effect. The Run-2/3 uncertainty is significantly reduced with a full-ring map of the quad transient field.

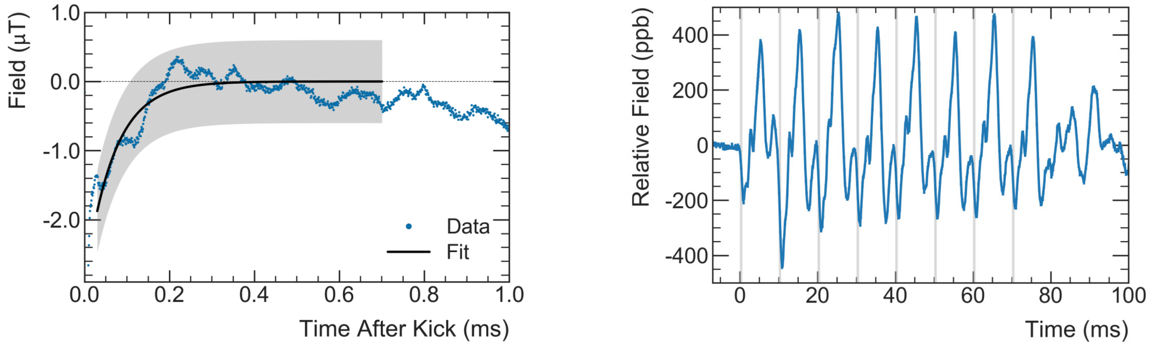

(a) Relative time-dependent magnetic field caused by kicker-induced eddy currents, fitted with an exponential decay over the muon measurement time. Reproduced from [41].

(b) Relative time-dependent magnetic field induced by the charging quadrupoles, shown here for eight quadrupole charging sequences. Gray lines indicate the corresponding muon fill times. Reproduced from [41].

Figure 2.28

2.9 Status of the experiment

Run-6, the final data taking run, is underway and set to finish by summer 2023. The overall statistics goal of 21× more decay positrons than the previous Brookhaven $g - 2$ experiment was exceeded in February 2023. The remainder of Run-6 has been focused on studies to characterize and reduce systematic uncertainties, particularly the injection time vs. stored momentum correlation caused by the kicker which dominates the uncertainty on the electric field correction. Analysis of the data collected in Run-2 and Run-3 ("Run-2/3") is nearly complete and will be the next released result. Run-2/3 represents $\sim 4\times$ more statistics than Run-1 and will reduce the statistics-dominated uncertainty by $\sim 2\times$. Several dominant sources of systematic uncertainty have also been improved since Run-1, highlighted in Section 2.8.

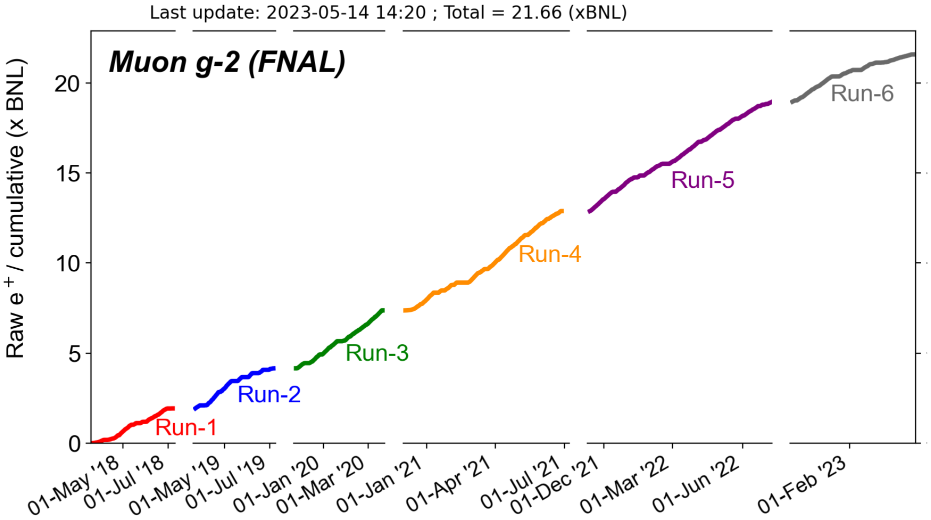

Figure 2.29: Decay positron statistics ("ctags") collected over all data taking runs. The goal of 21× BNL statistics was exceeded during Run-6.

Chapter 3

The Inflector Beam Monitoring System

Because muon storage efficiency is highly sensitive to the characteristics of the incident beam, optimum beam injection is critical to meet the experiment's statistics goals. The Inflector Beam Monitoring System (IBMS) was developed to measure the spatial beam profile along the injection path. Because this development was a major contribution from the author, it is described in detail in this chapter. The IBMS is a tool to assist with beam tuning and injection modeling, and to continuously monitor [1] the beam profile at injection.

The system comprises three detector modules, shown in Figure 3.1. IBMS1 is the upstream-most IBMS module, positioned just outside the magnet yoke hole. IBMS2 is positioned $\sim 2\,\mathrm{m}$ into the $100\,\mathrm{mm}$ diameter yoke hole bore, just upstream of the inflector entrance. IBMS3 is the downstream-most module, positioned $\sim 1\,\mathrm{m}$ downstream of the injection point (inflector exit) inside the storage ring vacuum chamber. IBMS3 is inserted for dedicated beam studies and retracted for normal production running.

Each module consists of a grid of scintillating fibers (SciFis) which emit light in response to incident muons. Each $0.5\,\mathrm{mm}$ diameter fiber is coupled to a $1\,\mathrm{mm}^2$ silicon photomultiplier (SiPM) light sensor. IBMS1 and IBMS2 consist of two planes of 16 SciFis each, oriented in the horizontal and vertical directions. The horizontal (vertical) fiber plane records the vertical "Y" (horizontal "X") beam profile. IBMS3 consists of just one plane of 16 vertical SciFis to record the horizontal beam profile, which is most critical for the injected beam.

Figure 3.2 shows typical beam profiles recorded by each IBMS detector, corresponding to the time-integrated beam intensity recorded by each fiber shown in Figure 3.3.

---

[1] periodically checked by shifters every hour over several years of experiment running time

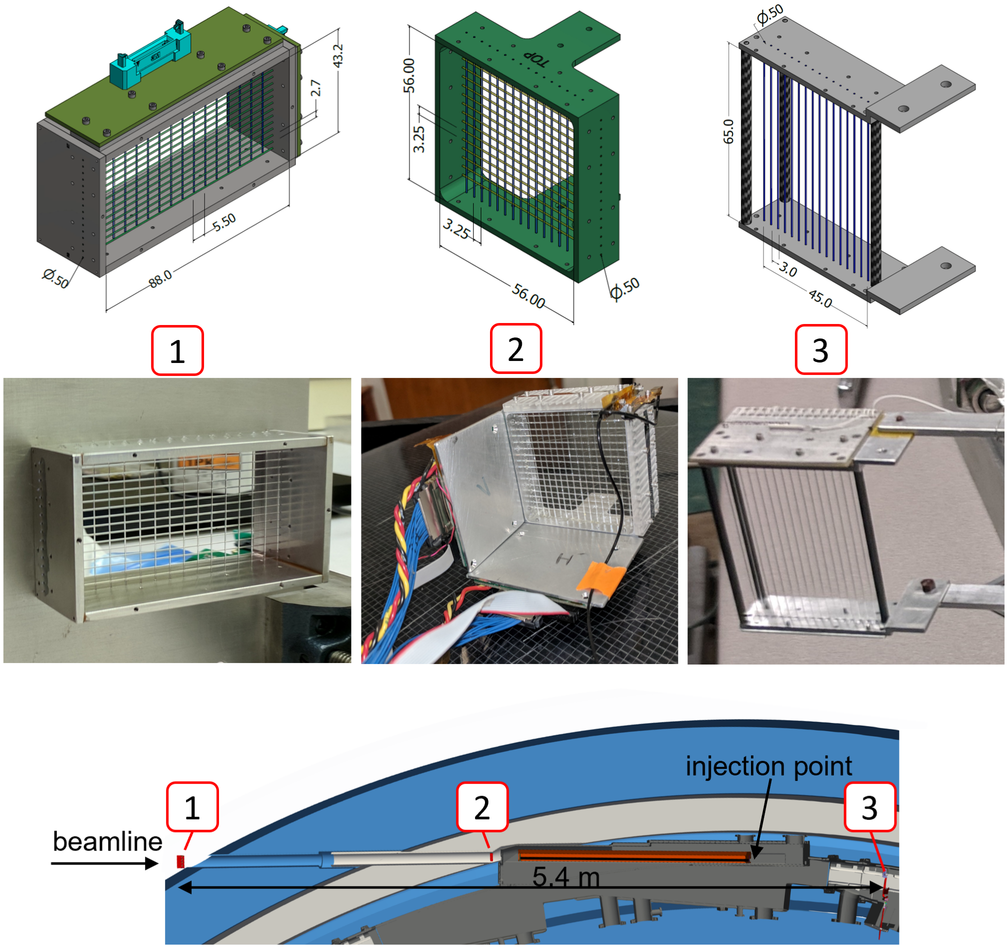

Figure 3.1: IBMS detector modules (top, engineering drawings and assembled detectors) and locations along the injection path (bottom)

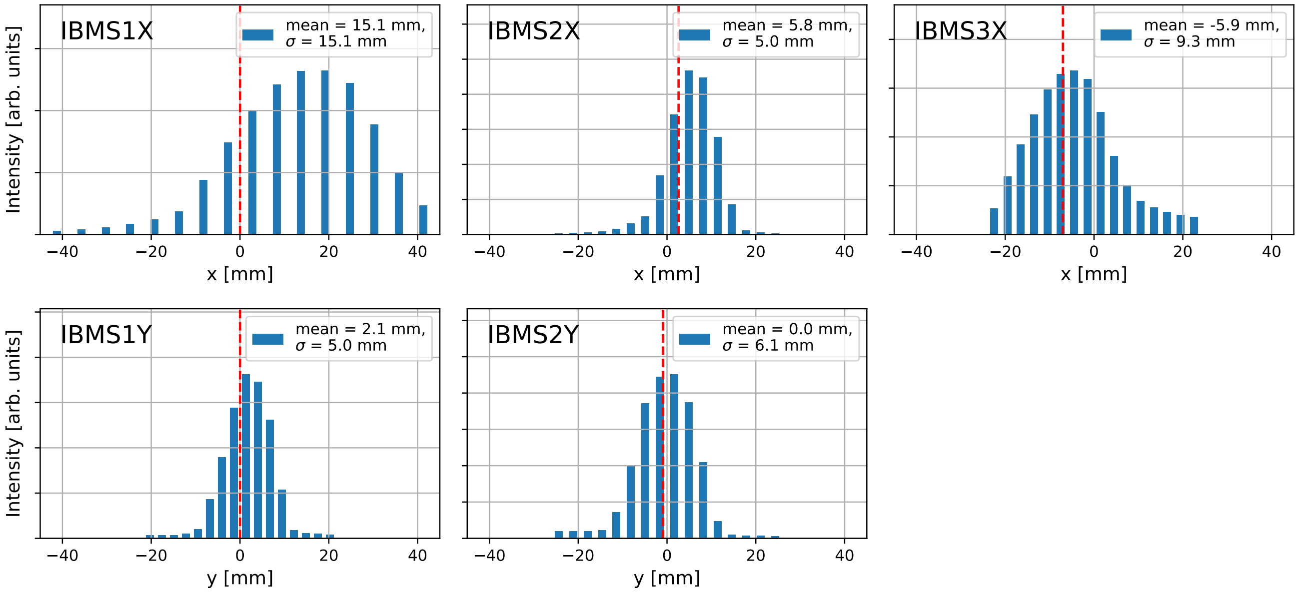

Figure 3.2: Typical IBMS beam profiles in Run-3, corresponding to the time-integrated beam intensity recorded by each fiber. $+x$ is radially in and $+y$ is up.

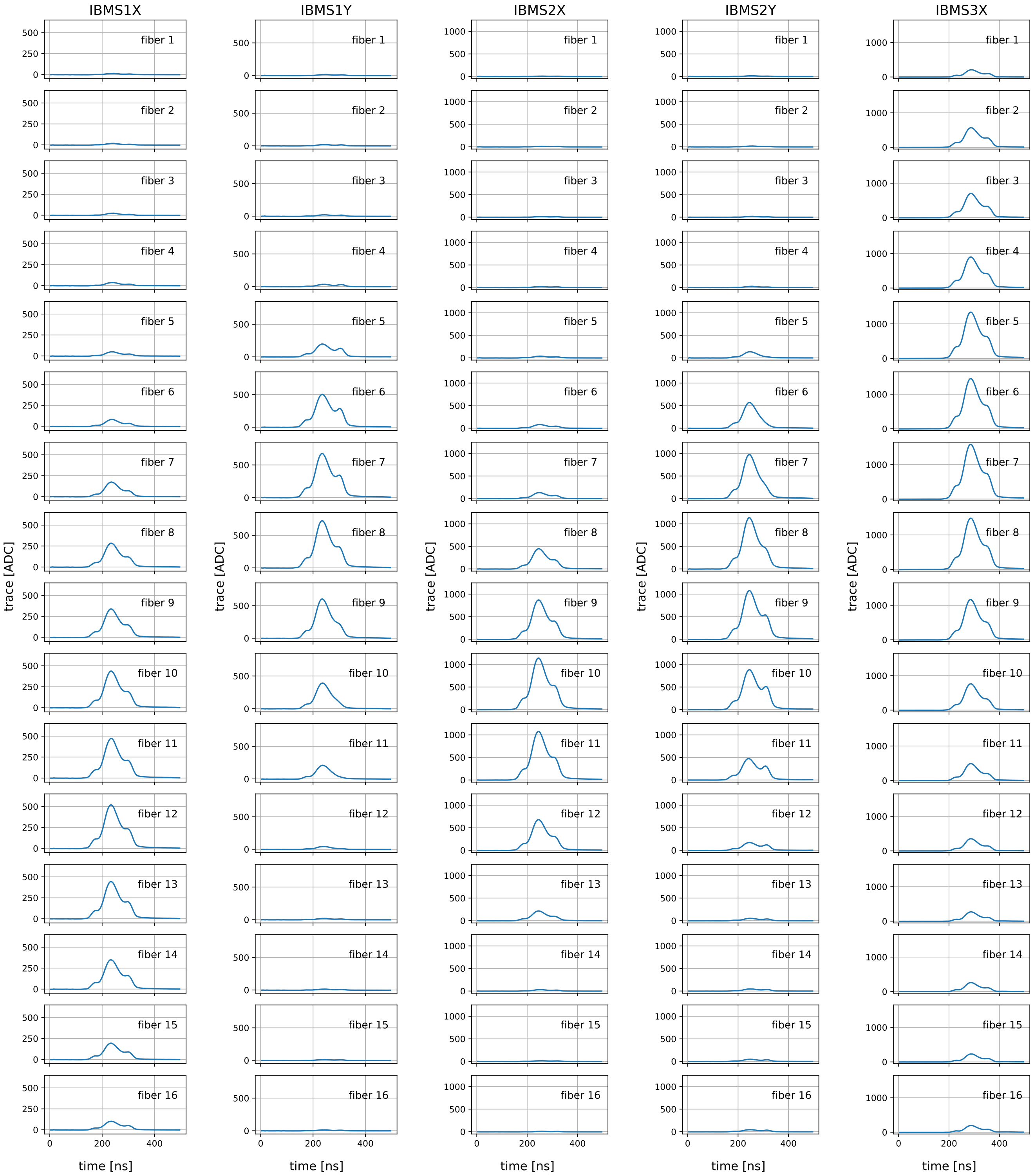

Figure 3.3: Typical IBMS fiber beam traces in Run-3, for injected beam bunch 0. (Fiber numbering starts on the radially outward side for the X planes, and on the top side for the Y planes.) Time-integrated beam traces give the IBMS beam profiles.

3.1 Mechanical design and geometry

The geometry of each detector was optimized for the expected beam profile at each position, as shown in Figure 3.1 and Table 3.1. All three detectors have air gaps set by spacers between the SiPMs and the fiber faces so that the light cone from the fiber fills the SiPM active area.

	X pitch [mm]	Y pitch [mm]	X×Y active area [mm×mm]	SiPM air gap [mm]
IBMS1	5.5	2.7	88.0×43.2	1.0
IBMS2	3.25	3.25	52.0×52.0	0.5
IBMS3	3.0	-	48.0	1.0

Table 3.1: IBMS X and Y fiber geometry

3.1.1 IBMS1

The IBMS1 location outside the magnet yoke hole in open air allowed some flexibility in its positioning and design. The module is housed in an aluminum enclosure for noise shielding, with an opening for the active area. The amplifier electronics are also thermally coupled to the enclosure for heat dissipation. The active SciFi and SiPM area is wrapped in black Tedlar film for light-tightness. The assembly is mounted on a remote-controlled linear X-Y translation stage for repeatable positioning and in-beam fiber calibration. The space also allowed a more modular design for the readout electronics than was possible for IBMS2 (Section 3.2).

3.1.2 IBMS2

The IBMS2 location inside the yoke hole imposed strict space constraints. The module is mounted on an aluminum cart, which also provides noise shielding and thermal coupling for the amplifier electronics. The whole assembly is mounted on a linear rail and carriage system installed inside the $100\,\mathrm{mm}$ diameter bore, which carries the detector $\sim 2\,\mathrm{m}$ downstream to its operating position. Like IBMS1, the active area is wrapped in black Tedlar for light-tightness. The confined space presented an additional challenge in managing heat generated by the amplifier electronics; a fan and split duct connected to the yoke hole allowed operation at $\lesssim 40\,^{\circ}\mathrm{C}$, a safe temperature for the plastic SciFis and optical glue joints.

3.1.3 IBMS3

The IBMS3 location inside the storage ring vacuum chamber and in the ring field presented several unique constraints. The detector is installed in a port originally intended for a third straw tracker module, and the assembly is built with a modified tracker port flange. The SiPM board is mounted directly to the fiber frame in the vacuum, and signals cables connect via vacuum feedthrough to an amplifier board on the air side. The amplifier board is housed in an aluminum enclosure for noise shielding and thermal coupling.

The entire assembly had to be non-magnetic to avoid perturbing the field above the few-ppm level. To verify this, the full assembly was transported to Argonne National Lab (ANL) to measure the field perturbation on a $1.45\,\mathrm{T}$ magnet test stand with an NMR probe, with support from the ANL team. The largest measured perturbation was 3.5 ppm, well within safe limits.

All in-vacuum components had to be low outgassing for the $< 1 \times 10^{-6}\,\mathrm{torr}$ storage ring vacuum. The rate of rise (ROR) of all in-vacuum components was measured in a vacuum test chamber, and all components had ROR well below the reference specification for straw trackers.

The detector is mounted on a vacuum feedthrough linear micrometer which allows manual insertion into the injected beam for dedicated beam measurements, and retraction out of the storage region for production physics running and trolley runs. The simulation team incorporated the detailed IBMS3 model into the *gm2ringsim Geant4*-based Monte Carlo software and verified there was no significant effect on calorimeter e^+ hits.

3.1.4 Surveyed positions

To establish the precise locations where the beam is profiled, each detector position was measured in the coordinate system of the ring. Surveyed positions in Table 3.2 are defined relative to the nominal beamline (at a $1.25\,\mathrm{deg}$ horizontal angle to the tangent line and vertically centered on the ring), the injection point (nominal inflector exit, $12.35\,\mathrm{deg}$ downstream of the 12 o'clock on the ring at a radius $r_{inj} = 7112 + 77\,\mathrm{mm} = 7189\,\mathrm{mm}$), and the nominal orbit ($R = 7112\,\mathrm{mm}$). Positions relative to the ring are shown in Figure 3.4.

	x [mm] relative to NBL (+x radially in)	y [mm] relative to NBL (+y up)	z [mm] along NBL from injection point (+z upstream)
IBMS1	0	0	+4397.0
IBMS2	-2.6	+0.9	+1950.5

	r [mm] from ring center	θ [deg] relative to injection point (+θ clockwise)
IBMS3 (Run-2)	7183.2	8.160
IBMS3 (Run-3+)	7181.2	8.175

Table 3.2: Surveyed IBMS center positions, where NBL is the nominal beamline. Two positions are given for IBMS3 because its mounting hardware was reconfigured between Run-2 and Run-3.

- **IBMS1**: The IBMS1 was vertically aligned with the ring center plane and horizontally aligned with the nominal beamline to better than $1\,\mathrm{mm}$ using fiducial marks. The longitudinal position was estimated using a manual measurement combined with design dimensions.

- **IBMS2**: The position of IBMS2 was surveyed to better than $0.5\,\mathrm{mm}$ using a laser scanner, with reflectors mounted on the IBMS2 assembly. A laser distance meter was used to ensure repeatable positioning.

- **IBMS3**: The IBMS3 internal geometry was measured with a laser scannner at the Fermilab metrology shop, and registered in the ring using external laser fiducials. This survey provided the position of IBMS3 to better than $0.5\,\mathrm{mm}$, with better than $50\,\mu\mathrm{m}$ repeatability provided by limit switches.

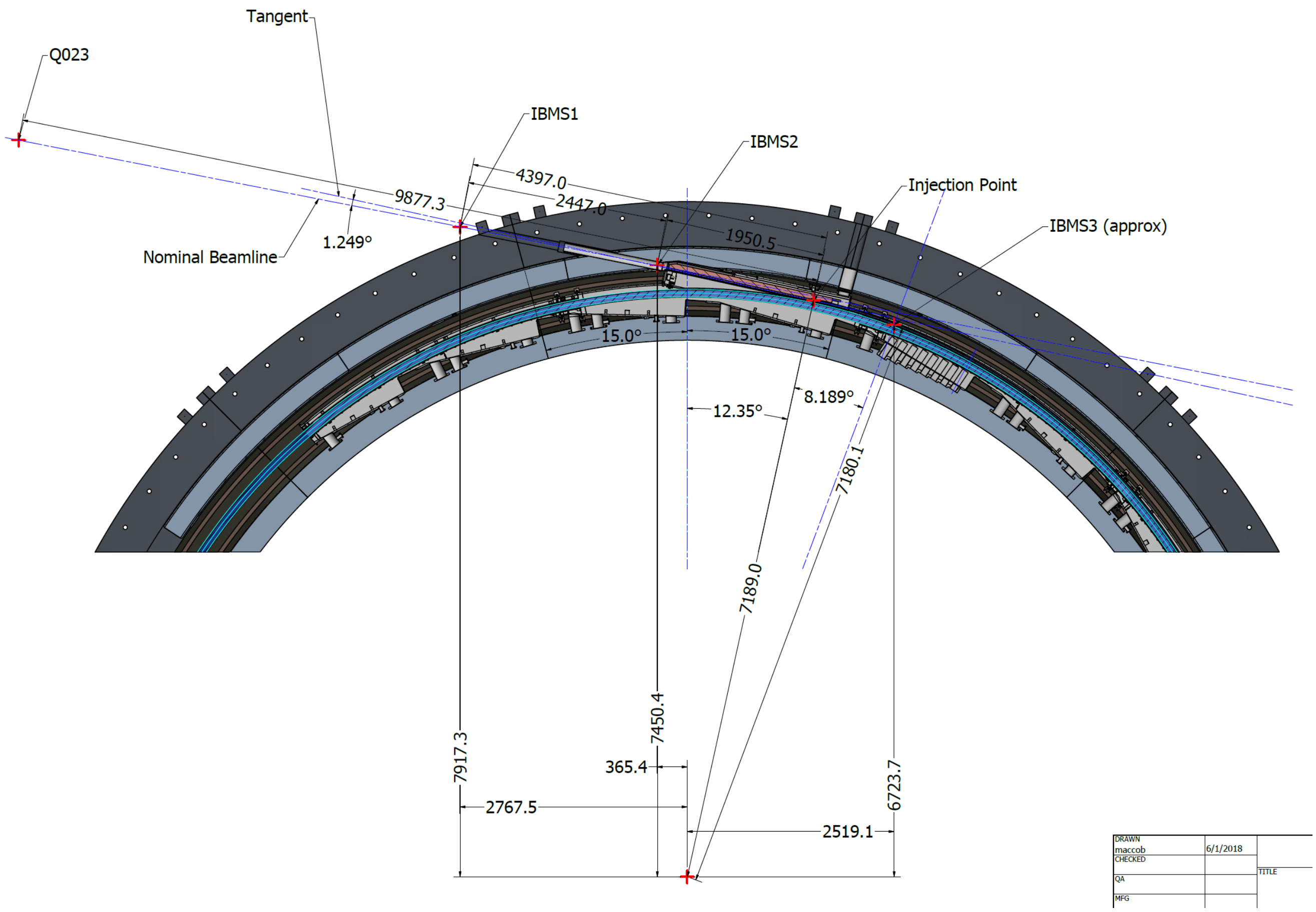

Figure 3.4: IBMS positions in an engineering model of the ring. (IBMS1&2 positions are from the survey; IBMS3 position is from a preliminary measurement, not the final survey.) Note: Q023 is one of the M5 final focus quadrupole magnets, positioned along the nominal beamline.

3.2 Electronics and readout

SiPM light sensors generate a current in response to detected light, and can operate safely in strong magnetic fields. The S12571-010P SiPMs from Hamamatsu were selected for their large dynamic range (10,000 pixels in a $1\,\mathrm{mm}^2$ area) and fast pixel recovery time. Their typical operating voltage is $69.5\,\mathrm{V}$. The SiPMs were soldered onto 16-channel boards which fit onto each 16-fiber detector plane. Low-noise programmable gain amplifiers (PGAs), configurable with 0-18 dB gain in 3 dB increments, convert SiPM currents to voltage signals. The signal voltage gain per SiPM current is determined by the amplifier shunt resistor value, the PGA setting, and the gain of the line drivers which transmit the output signals. The maximum signal gain (with PGA set to 18 dB) is $320\,\mathrm{mV/mA}$ for IBMS1&2 and $1056\,\mathrm{mV/mA}$ for IBMS3. Each amplifier board also includes a temperature sensor. A BeagleBone microcontroller handles control and communication with the amplifier electronics. The amplified analog signals are transported by micro-coax cable to the receiving 12-bit waveform digitizers (CAEN V1742); all 80 channels are digitized for $1\,\mu\mathrm{s}$ per beam pulse at a rate of 1 GS/s, as shown in Figure 3.6, and recorded for every beam pulse.

Each detector has functionally similar electronics with slightly different configurations.

- **IBMS1**: SiPM and amplifier electronics placed on separate boards joined with a right-angle card edge connector.
- **IBMS2**: SiPM and amplifier electronics are combined on one board per fiber plane for efficient use of the confined space in the yoke hole.
- **IBMS3**: SiPM and amplifier boards are separate, similar to the IBMS1 configuration. The SiPM board is mounted directly to the fiber frame in the vacuum; coax signal cables connect the SiPM board via vacuum feedthrough to an amplifier board on the air side.

One challenge during IBMS3 electronics testing was noise pickup on the SiPM signal cables. Possible effects from the pulsed kicker and quadrupoles combined with RF shielding from the vacuum chamber was unknown. The noise performance was better than expected, however, with $\sim 1\,\mathrm{mV}$ noise on a $< 0.8\,\mathrm{V}$ full-scale signal.

3.2.1 Stability monitoring

Electronic test pulses injected directly to the amplifier inputs are used to check the amplifier response and monitor stability. The $\sim 100\,\mathrm{ns}$ square pulses are timed to a few hundred ns after each beam pulse, and the rising edge is used for timing jitter correction in the digitized signals.

The IBMS1&2 detectors include a light injection system which directs pulsed LED light into each SciFi, providing a repeatable measure of the detector response and real-time stability monitoring during operation. Surface-

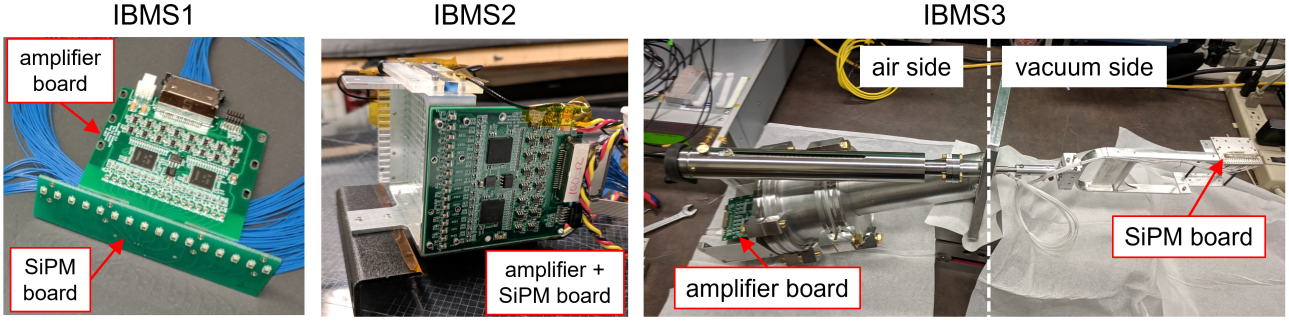

Figure 3.5: The IBMS readout electronics consist of SiPMs read out by a programmable gain amplifier. Each detector's electronics are configured slightly differently depending on mechanical requirements.

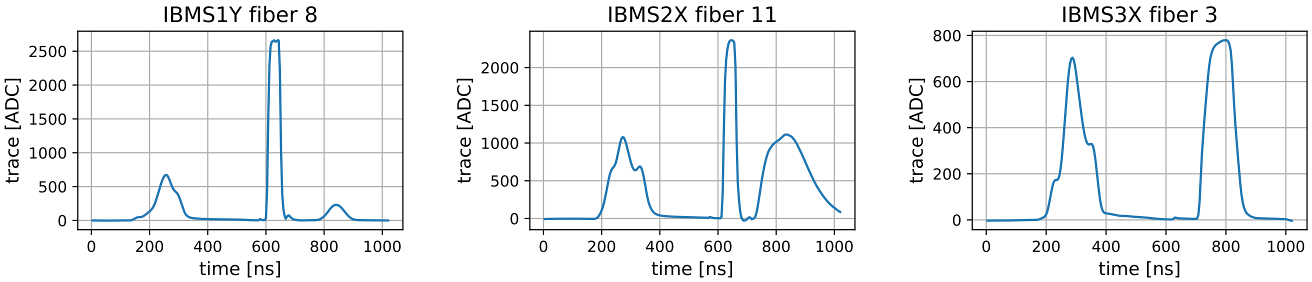

Figure 3.6: Example digitized time-averaged IBMS traces, after subtracting the baseline and correcting timing jitter. The waveform digitizers are triggered just before beam arrival, with the beam pulse appearing between 0 and $500\,\mathrm{ns}$. IBMS1&2 have electronic pulses injected to the amplifier at $\sim 600\,\mathrm{ns}$ and LED light pulses after $700\,\mathrm{ns}$. IBMS3 has an electronic pulse at $\sim 700\,\mathrm{ns}$, and no LED pulse.

mount LEDs are coupled into notched optical fibers which direct a portion of the LED light into each SciFi. The $\sim 200\,\mathrm{ns}$ LED pulses are timed after the beam pulses and electronic pulses. This arrangement allows relative gain monitoring with a single source per detector plane.

3.3 SiPM light sensors

SiPMs are solid-state sensors which can detect single photons [59, 60]. Each SiPM pixel is a Geiger mode reverse-biased avalanche photodiode in series with a quenching resistor, with the bias voltage set above the avalanche breakdown voltage. A photon striking a pixel produces an electron avalanche (with a probability given by the photon detection efficiency, or PDE), increasing the voltage across the resistor and reducing the voltage on the pixel until the current is quenched. The resulting pulse has a $\sim 1\,\mathrm{ns}$ rise and $\sim 40\,\mathrm{ns}$ decay time (in the case of the S12571-010P SiPMs).

In this Geiger mode, one or more photons generate the same current pulse in a single pixel, but photons striking separate pixels produce a combined SiPM current proportional to the number of pixels fired. The probability of a pixel firing in response to an incident photon is given by the PDE times the probability of hitting an unfired pixel.

The number of fired pixels N_f is then given by

$$N_f = N\left(1 - e^{-N_\gamma \cdot PDE/N}\right) \tag{3.1}$$

for N_γ incident photons and N total pixels. For $N_\gamma \cdot PDE \ll N$, $N_f \approx N$ and the SiPM response is appoximately linear. The response becomes increasingly nonlinear with light intensity, as shown in Figure 3.7. The desired operating mode is the linear SiPM response range.

3.4 Characterization

3.4.1 SiPM response

The SiPM current response as a function of light intensity was measured with LED light, which was repeatably aligned with the LED light injection assembly (Section 3.2.1). The light intensity was varied by adjusting the LED supply current, and by placing neutral density foils in front of the LED. The LED light intensity vs. current was separately measured with a photomultiplier tube. Figure 3.7 shows that SiPM currents can exceed $20\,\mathrm{mA}$, and the response is most linear below $\sim\!5\,\mathrm{mA}$. The desired maximum SiPM current was therefore defined as $5\,\mathrm{mA}$.

The SiPM signal current is proportional to the number of firing pixels, and individual pixels can be fired by single photoelectrons (*pe*). SiPM signals are superpositions of single *pe* (Figure 3.7). Single *pe* signals can be resolved when operating with sufficient gain, providing a natural self-calibration of the SiPM signal in terms of *pe*.

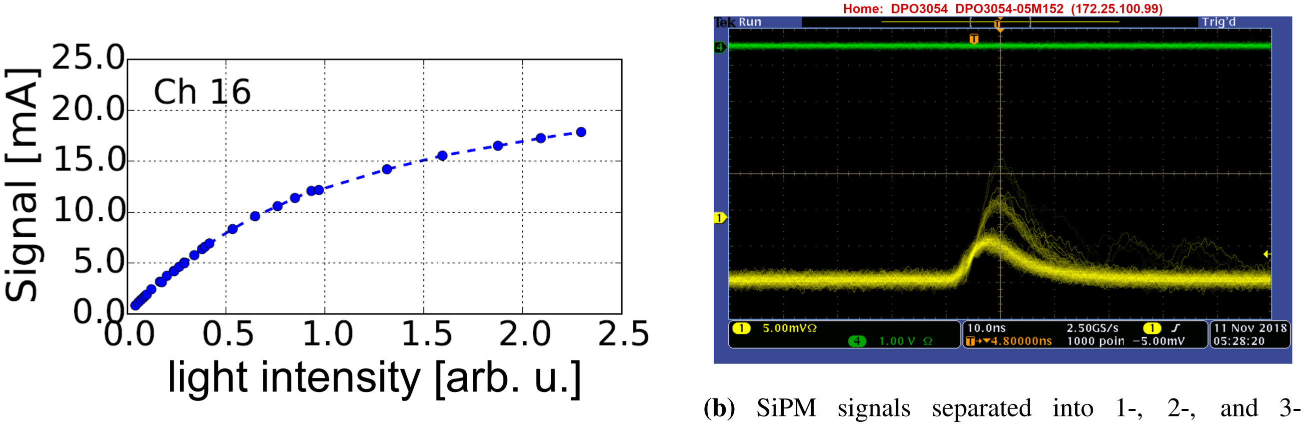

(a) Example SiPM saturation curve shows linear response below $\sim\!5\,\mathrm{mA}$.

(b) SiPM signals separated into 1-, 2-, and 3-photoelectron pulses, seen here with the high-gain calibration amplifier board.

Figure 3.7: SiPM saturation and single photoelectrons

3.4.2 MIPs response

Scintillators are materials which emit light when charged particles pass through the material and excite its atoms and molecules [61]. In the case of organic scintillators such as the polystyrene of the IBMS SciFis, scintillation light is emitted when the molecules' free valence electrons absorb ionizing radiation and produce a flash of light within a few nanoseconds. The scintillator light output is related to the energy the particle deposits by

$$\frac{dL}{dx} = \frac{A\frac{dE}{dx}}{1 + kB\frac{dE}{dx}} \tag{3.2}$$

where dx is the unit path length, and A and kB are parameters of the scintillator (A is the absolute scintillation efficiency; kB relates the density of ionization centers to dE/dx). For small dE/dx, Eq. 3.2 becomes approximately linear with $dL/dx \propto dE/dx$. Relativistic particles such as the injected muons are minimum ionizing particles (MIPs) [62], particles which deposit the minimum energy per unit length in the scintillator and produce a well-defined light output.

A collimated Strontium-90 beta electron source was used to characterize the detector response to MIPs. The source was positioned within a few centimeters of the SciFis of interest, with a scintillation counter on the opposite side of the fiber providing coincidence triggers. The detector was positioned with a linear stage relative to the fixed source and coincidence counter. A special high-gain configuration of the amplifier electronics (with larger-than-nominal shunt resistors) was required to resolve single MIPs signals, which are typically a few *pe*. For maximum efficiency, the SiPMs were coupled flush to the fiber faces with optical grease.

A histogram of the time integrals of individual SiPM pulses shows single *pe* peaks in the envelope of a Landau distribution according to the energy deposited in the scintillator (Figure 3.8). The mean response was $\sim$4 pe/MIP for IBMS1&2 and $\sim$7 pe/MIP for IBMS3. This difference is due to different mounting configurations of the reflective Mylar film on the fiber ends opposite the SiPMs which increases light collection efficiency. Because the calibration procedure required a different detector configuration from the final assembly, the calibration was "transferred" to the final configuration with relative attenuation factors measured with injected LED light in each configuration. These transfer factors had significant channel-to-channel variation and were only consistent to within $\sim 30\%$, which was still sufficient to predict approximate IBMS signals in the beam.

For IBMS1&2, neutral density (ND) filters were placed in front of the SiPMs to set the detector response within the linear SiPM operating range for the expected 7×10^5 muons [36] per $\sim 150\,\mathrm{ns}$ injected beam bunch. The actual beam intensity was lower than expected, estimated very roughly at $\sim 5 \times 10^5$ from IBMS and T0 detectors. The selected ND filters are shown in Table 3.3, along with maximum measured SiPM currents in the beam from a

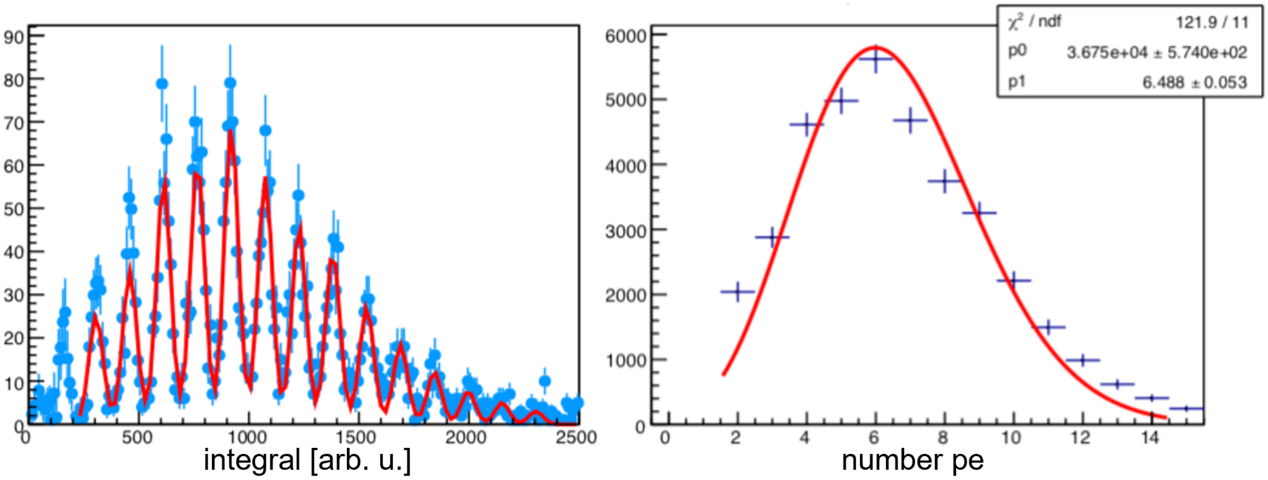

Figure 3.8: Left: The distribution of SiPM pulse integrals from the IBMS3 MIPs response shows single *pe* peaks, each fitted with a Gaussian. Right: A simple Poisson distribution fitted to the *pe* peaks gives the mean pe/MIP for each detector channel (~ 6.5 pe/MIP in this example).

typical run. All channels were well below the $5\,\mathrm{mA}$ desired maximum SiPM current.

	ND optical density ($\log_{10}$(transmission))	ND measured transmission	peak SiPM current [mA]
IBMS1	0.15 (X) 0.6 (Y)	0.75 (X) 0.25 (Y)	0.6
IBMS2	0.6	0.25	0.9
IBMS3	0.15	0.68	2.2

Table 3.3: Selected ND filters and transmissions (measured with LED), and maximum measured SiPM current (from typical beam traces in Run-3).

3.4.3 Relative fiber efficiency calibration

For IBMS1 and IBMS3, the relative fiber efficiencies were calibrated directly in the beam. IBMS1 is mounted on a linear stage and IBMS3 is mounted on a linear micrometer, allowing each detector's transverse position in the beam to be repeatably adjusted. Each detector is displaced by one fiber pitch, and the relative efficiency between two fibers is given by the ratio of beam intensities measured by each fiber at the same position in the beam (Figure 3.9). The beam profiles recorded during production running are corrected by dividing out the measured relative fiber efficiencies (Figure 3.10). Relative efficiencies show excellent fiber uniformity of better than 12% within each detector.

The IBMS2 transverse position cannot be adjusted, so this relative efficiency calibration method was not possible. However, a similar approach could be employed with the detector removed from the yoke hole.

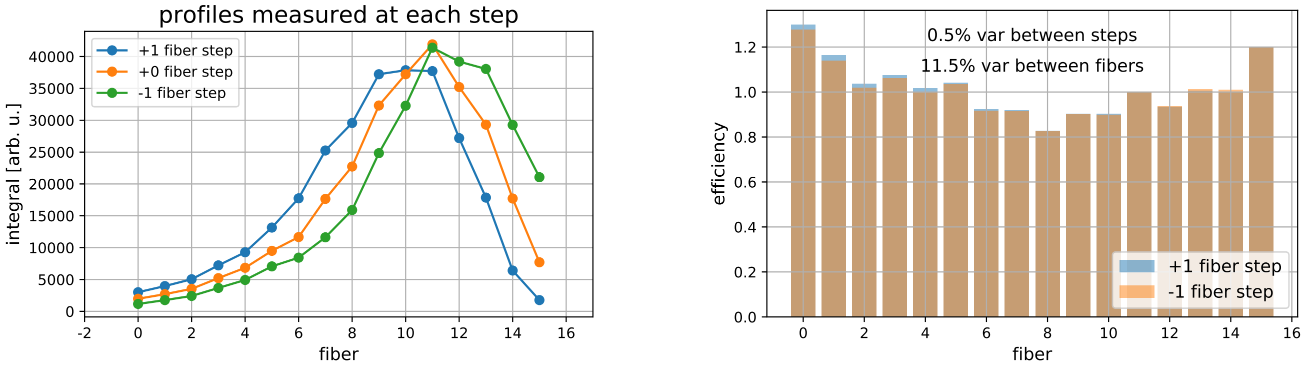

(a) Beam profiles (vs. fiber number) are measured with displacements of +1 fiber pitch, zero (nominal position), and -1 fiber pitch.

(b) Relative fiber efficiencies are extracted from the ratios of different fibers at the same position. Efficiencies calculated from steps in either direction are consistent within $< 1\%$, and fibers are uniform within 12%.

Figure 3.9: Relative fiber efficiency calibration procedure for IBMS1X

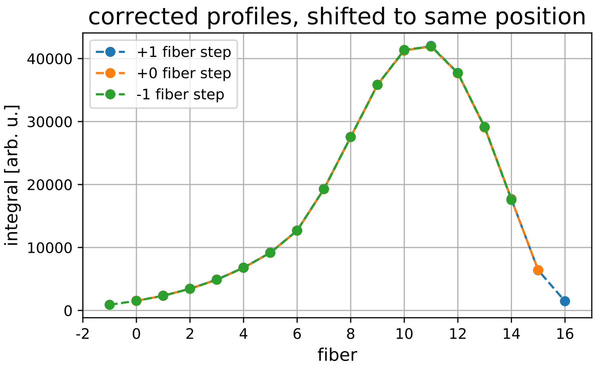

Figure 3.10: Corrected IBMS1X beam profiles (vs. fiber number) with relative fiber efficiencies divided out. Here the displaced profiles are shifted to the same reference position, then overlaid to demonstrate that the method is consistent for steps in either direction.

3.5 Summary

The Inflector Beam Monitoring System (IBMS), consisting of three scintillating fiber detector modules, was developed to profile the injected beam. Optimizing the beam injection is essential for muon storage efficiency, and the IBMS provides a tool to assist with beam tuning, injection modeling, and real-time beam monitoring. Each detector had its own challenges and constraints imposed by the operating environment, leading to a unique design for each module. The detector response was characterized using a radioactive source, and the dynamic range was set with neutral density filters to ensure a linear SiPM response. Relative fiber efficiencies were calibrated directly in the beam. The IBMS detectors have performed reliably and provided feedback about the injected beam over the several years of experiment running time.

Chapter 4

Beam Dynamics Introduction

Understanding the dynamics of the muon beam is necessary to understand why injecting the beam into the $g-2$ ring is a challenging process, how to characterize and measure the injected beam for improved modeling (discussed in Section 5.1), and how to model and reconstruct the stored beam distribution around the ring, for example to calculate the average magnetic field experienced by the muons circulating in the ring (discussed in Chapter 7). This chapter introduces a selection of fundamental beam dynamics concepts which are referenced throughout this thesis. References [63–66] are used throughout the chapter.

4.1 Transverse linear motion

A charged particle moving in electric $\boldsymbol{E}$ and magnetic $\boldsymbol{B}$ fields experiences the Lorentz force.

$$\frac{d}{dt}\left(\gamma m \dot{\boldsymbol{r}}\right) = e\left(\boldsymbol{E} + \dot{\boldsymbol{r}} \times \boldsymbol{B}\right) \tag{4.1}$$

In a beamline with $\boldsymbol{E}$ and $\boldsymbol{B}$ fields perpendicular to the particle's trajectory, the beam motion can be described in a coordinate system moving along the trajectory. Assuming the fields are linear in the transverse coordinates (x, y), consider vertical dipole and transverse quadrupole magnetic fields,

$$B_y(s) = B_{y0}(s) + \frac{dB_y(s)}{dx}x \tag{4.2}$$

$$B_x(s) = \frac{dB_x(s)}{dy}y\,. \tag{4.3}$$

The dipole field B_{y0} steers the beam with bend radius $R(s) = \frac{e}{p_0}B_{y0}(s)$. The quadrupole field with strength $k(s) = -\frac{e}{p_0}\frac{dB_y(s)}{dx} = -\frac{e}{p_0}\frac{dB_x(s)}{dy}$ focuses the beam if $k < 0$ or defocuses the beam if $k > 0$. After some simplification and using the approximation that the transverse beam motion is small relative to the nominal trajectory, i.e. $x,\ y << R$, the equations of motion in (x, y) relative to the nominal trajectory become

$$x''(s) + K_x(s)x(s) = \frac{1}{R(s)}\delta \tag{4.4}$$

$$y''(s) + K_y(s)y(s) = 0 \tag{4.5}$$

with

$$K_x(s) \equiv \left(\frac{1}{R^2(s)} - k(s)\right) \tag{4.6}$$

$$K_y(s) \equiv k(s), \tag{4.7}$$

where s is the path length along the nominal trajectory, derivatives are taken with respect to s, and $\delta = \frac{\Delta p}{p_0}$ is the momentum deviation. Figure 4.1 shows the coordinate system moving along the trajectory.

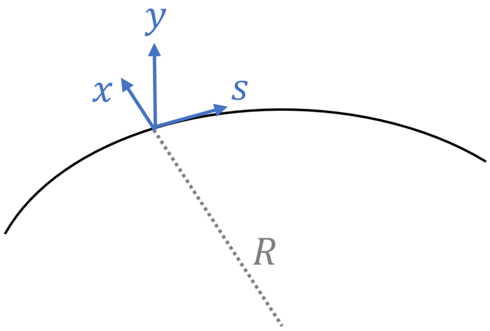

Figure 4.1: Coordinate system moving along the trajectory, with longitudinal coordinate s and transverse coordinates (x, y).

Eqs. 4.4 and 4.5 are known as Hill's equations. The closed form solution to the homogeneous equation with constant $K_x > 0$ has the familiar form of a harmonic oscillator. The general solution has the form

$$x(s) = \sqrt{\epsilon}\sqrt{\beta(s)}\cos[\Psi(s)]\,, \tag{4.8}$$

with the constants ϵ and $\Psi(0) = \Psi_0$ determined by the initial conditions. ϵ is called the emittance and $\beta(s)$, known as the beta function, determines the beam envelope $\sqrt{\epsilon\beta(s)}$.

Substituting $\beta(s) \equiv u^2(s)$ and separating variables u and Ψ,

$$\Psi(s) = \int_0^s \frac{d\sigma}{\beta(\sigma)} \tag{4.9}$$

$$u'' - \frac{1}{u^3} + Ku = 0 \tag{4.10}$$

or equivalently

$$2\beta\beta'' - \beta'^2 + 4K\beta^2 = 4. \tag{4.11}$$

From Eq. 4.9, $\frac{d\Psi}{ds} = \frac{1}{\beta}$. Then the β function is not only a measure of the transverse beam size, but also the wavelength of the betatron oscillation $\lambda = 2\pi\beta$; it relates beam size, phase advance, and betatron wavelength.

The derivative of $x(s)$ gives the divergence angle

$$x'(s) = -\sqrt{\frac{\epsilon}{\beta(s)}}\,[\alpha(s)\cos[\Psi(s)] + \sin[\Psi(s)]] \tag{4.12}$$

where $\alpha(s) \equiv -\beta'(s)/2$. The trajectory $x(s)$ in Eq. 4.8 can then be expressed in terms of initial conditions $x_0 = x(0)$, $\beta_0 = \beta(0)$, $x'_0 = x'(0)$, and $\alpha_0 = \alpha(0)$.

$$x_\beta(s) = \sqrt{\frac{\beta(s)}{\beta_0}}\,\left[x_0\left(\cos[\Psi(s)] + \alpha_0 \sin[\Psi(s)]\right) + x'_0\beta_0 \sin[\Psi(s)]\right] \tag{4.13}$$

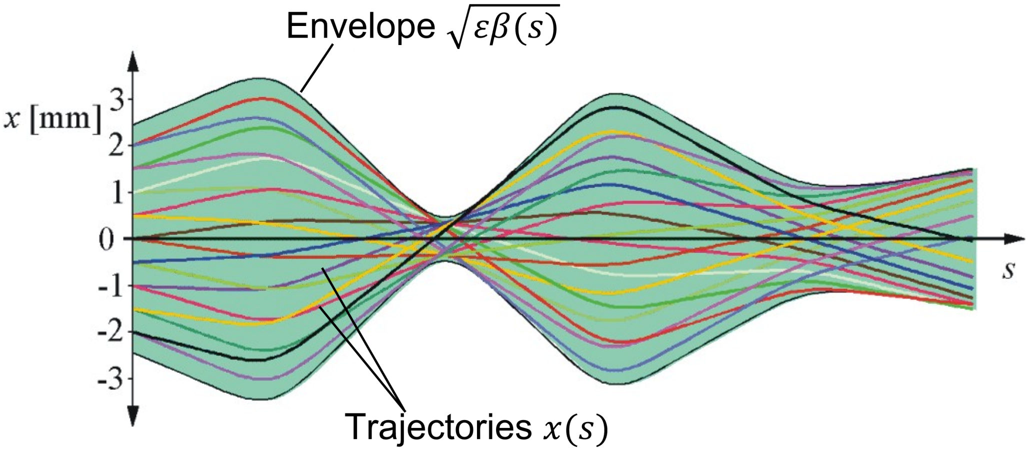

Figure 4.2: Particle trajectories $x(s)$ within an envelope described by the emittance ϵ and the $\beta(s)$ amplitude function. Reproduced from [67].

Piecewise solution and transfer matrices

The trajectory equations Eqs. 4.8 and 4.12 can be written in matrix form. Simple transfer matrices can often describe piecewise solutions for elements with constant k and R, and a full beam lattice structure can be evaluated by multiplying the individual transfer matrices. The evolution of the trajectory is given by

$$\begin{pmatrix} x(s) \\ x'(s) \end{pmatrix} = \boldsymbol{M(s)} \begin{pmatrix} x_0 \\ x'_0 \end{pmatrix} . \tag{4.14}$$

Explicit forms of transfer matrices for a constant dipole field, constant quadrupole field, and field-free drift section are given in Appendix A.

4.1.1 Phase space ellipse

Eqs. 4.8 and 4.12 describe the single particle trajectory in x-x' phase space. The particle's motion in the x-x' plane can be described by an ellipse, shown in Figure 4.3. Eliminating $\Psi(s)$ and introducing $\gamma(s) \equiv \frac{1+\alpha^2(s)}{\beta(s)}$, the equation of the ellipse is

$$\gamma(s)x^2(s) + 2\alpha(s)x(s)x'(s) + \beta(s)x'^2(s) = \epsilon\,. \tag{4.15}$$

The parameters α, β, γ, and ϵ are called Twiss parameters. The emittance ϵ defines the area of the ellipse, $A = \pi\epsilon$.

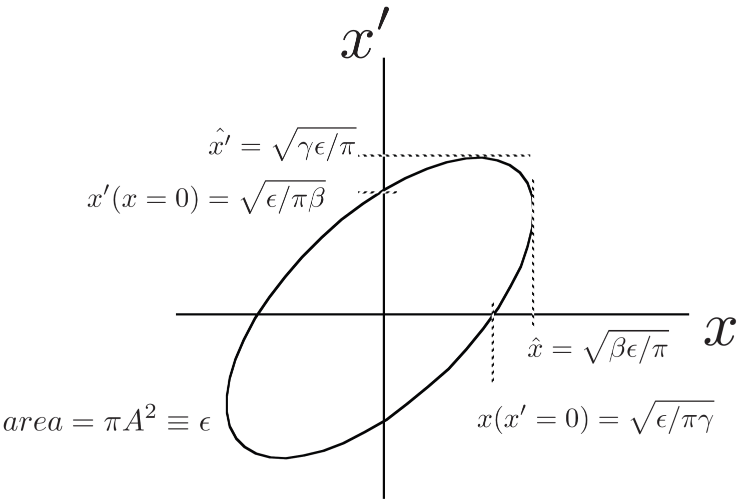

Figure 4.3: Phase space ellipse describing particle motion in x-x'. Figure courtesy of M. Syphers [65].

The ensemble beam distribution in x-x' phase space is equivalently described by the beam matrix $\boldsymbol{\sigma}$,

$$\boldsymbol{\sigma} = \begin{pmatrix} \sigma_x^2 & \sigma_{xx'} \\ \sigma_{xx'} & \sigma_{x'}^2 \end{pmatrix} = \epsilon \begin{pmatrix} \beta & -\alpha \\ -\alpha & \gamma \end{pmatrix} . \tag{4.16}$$

Here σ_x and $\sigma_{x'}$ are the RMS beam widths in x and x' and $\sigma_{xx'}$ is the x-x' covariance. The beam can be transported using the same transfer matrices in Section 4.1, with $\boldsymbol{\sigma_s} = \boldsymbol{\sigma}(s)$ and $\boldsymbol{\sigma_0} = \boldsymbol{\sigma}(0)$.

$$\boldsymbol{\sigma_s} = \boldsymbol{M}\,\boldsymbol{\sigma_0}\,\boldsymbol{M^T} \tag{4.17}$$

4.1.2 Dispersion

To solve the inhomogeneous form of Eq. 4.4 with the nonzero driving term on the right-hand side, a particular solution is added to the homogeneous solution. Define a special trajectory $D(s)$, called the dispersion function, with momentum deviation $\delta = 1$. Eq. 4.4 becomes

$$D''(s) + K_x(s)D(s) = \frac{1}{R(s)} . \tag{4.18}$$

The full solution for the x trajectory is then

$$x(s) = x_\beta(s) + \delta D(s) . \tag{4.19}$$

Off-momentum particles have a momentum-dependent trajectory described by the dispersion, separating the particles in x as shown in Figure 4.4. For the simple case of a constant dipole field with $K_x = \frac{1}{R^2}$, $D = R$ is a solution.

The dispersion $D(s)$ can be described in matrix form using a 3×3 transfer matrix, which generally includes the elements of the corresponding 2×2 matrix in Section 4.1.

$$\begin{pmatrix} D(s) \\ D'(s) \\ 1 \end{pmatrix} = \boldsymbol{M(s)} \begin{pmatrix} D_0 \\ D_0' \\ 1 \end{pmatrix} \tag{4.20}$$

The full trajectory (Eq. 4.19) is described with the same 3×3 matrix which describes the dispersion. Explicit transfer matrices for a constant dipole field and combined constant dipole and quadrupole fields are given in Appendix A.

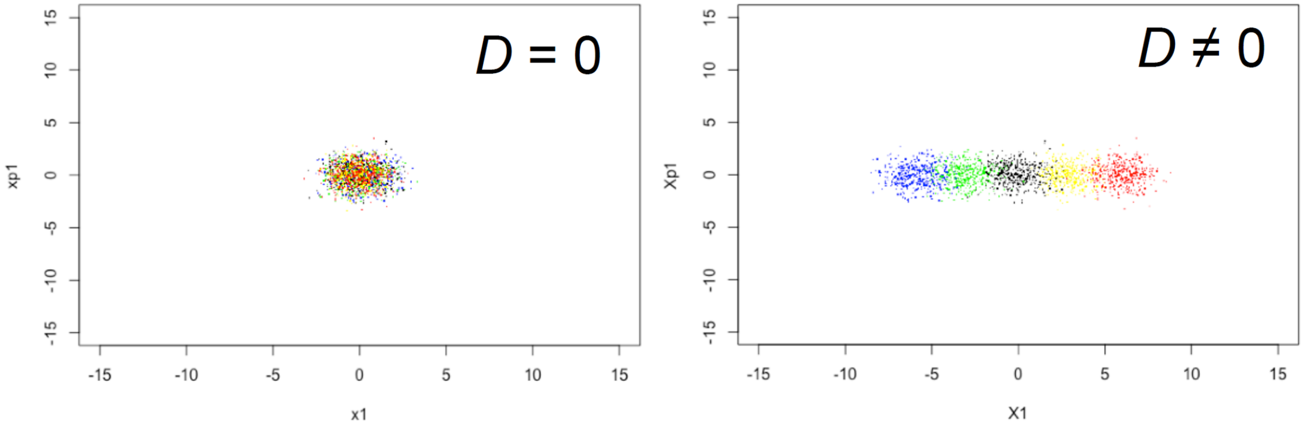

Figure 4.4: Dispersion separates off-momentum particles in x with an offset proportional to their momentum deviation, shown here in x-x' phase space with colors indicating different momenta. Figure courtesy of M. Syphers [65].

$$\begin{pmatrix} x(s) \\ x'(s) \\ \delta \end{pmatrix} = \boldsymbol{M(s)} \begin{pmatrix} x_0 \\ x'_0 \\ \delta \end{pmatrix} \tag{4.21}$$

4.2 Injecting the beam into the Muon $g-2$ ring

Muon beam injection into the $g-2$ storage ring is a challenging and critical step for muon storage [36] [68]. The last stage in transporting the muon beam to the ring is the M5 final focus beamline segment, consisting of 4 magnetic dipole and 6 magnetic quadrupole elements to steer and focus the beam (Section 2.2). Downstream of the M5 line, the beam travels more than $3\,\mathrm{m}$ with no beam elements before injection to the ring, and experiences strong deflecting and focusing forces from the magnetic fringe fields of the ring. As discussed in Section 2.3, the beam enters the ring through the narrow $18\,\mathrm{mm} \times 56\,\mathrm{mm}$ aperture of the inflector magnet. The beam is injected at a 77 mm horizontal offset to the nominal orbit, and at a $1.25°$ horizontal angle to the nominal orbit's tangent line to compensate for magnetic fringe fields which are not perfectly canceled by the inflector. The inflector is positioned along this "nominal beamline".

Because the incident beam optics are designed to optimize transmission by focusing through the narrow inflector, the injected beam phase space is mismatched with the accepted phase space of the ring (shown in Table 4.1); matching the ring acceptance would significantly reduce transmission. As discussed in Section 2.4, the pulsed kicker was weaker than expected, particularly before late in Run-3, and did not properly compensate the horizontal offset of the injected beam. These mismatches in the beam phase space, particularly the horizontal phase space, lead to oscillations in the stored beam as described in Section 4.3.4. The ring also accepts a narrow bite of the

Figure 4.5: The M5 final focus is the final beamline segment which transports the beam to the $g - 2$ ring [69].

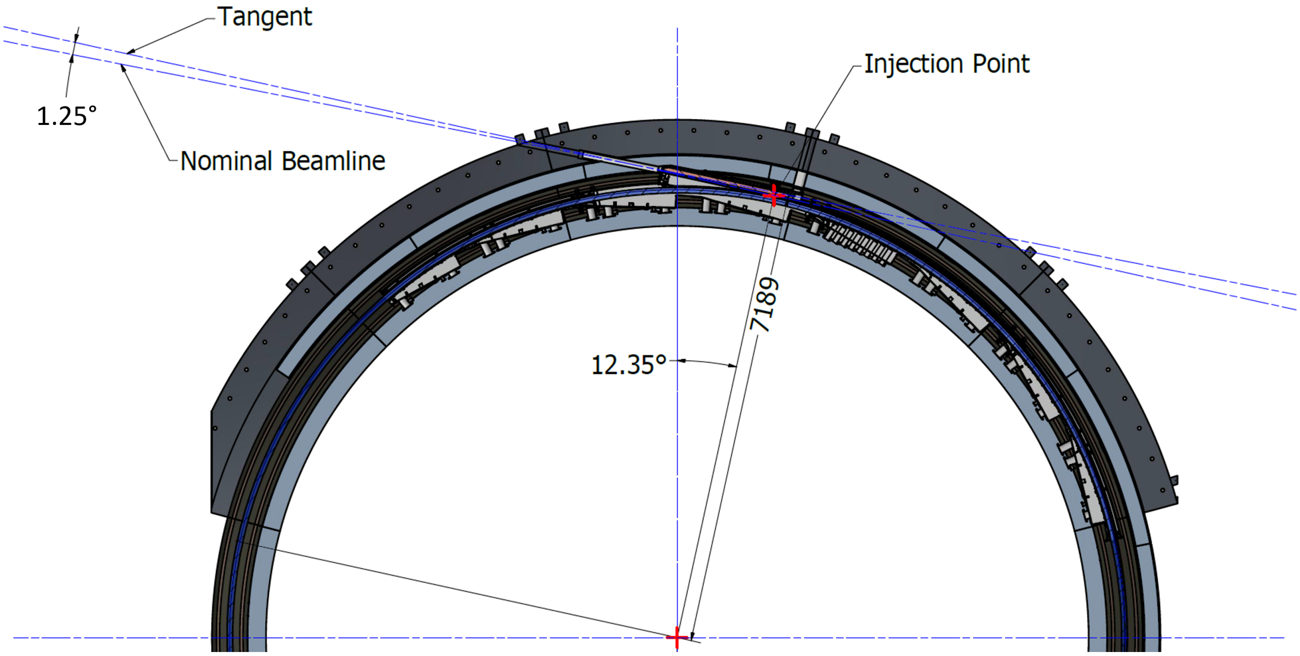

Figure 4.6: The beam is injected through the inflector into the ring at a $1.25°$ angle to the tangent line, and at a $77\,\mathrm{mm}$ horizontal offset to the nominal $7112\,\mathrm{mm}$ orbit. The angled injection path is called the "nominal beamline".

1.6% momentum width of the incident beam; a width of only $\sim 0.15\%$ is stored. These factors result in a low muon storage fraction $N_{stored}/N_{incident}$ which is highly sensitive to the phase space parameters of the incident beam.

Parameter	Inflector (design optics) [40]	Ring lattice ($n = 0.108$)
horizontal dispersion D_x	$0\,\mathrm{m}$	$R/(1-n) = 8.1\,\mathrm{m}$
horizontal β_x	$1.5\,\mathrm{m}$	$R/\sqrt{1-n} = 7.5\,\mathrm{m}$
verical β_y	$10.0\,\mathrm{m}$	$R/\sqrt{n} = 21.6\,\mathrm{m}$

Table 4.1: Values of beam optical functions in the inflector vs. ring lattice (using the expressions in Section 4.3.1). The mismatch in beam phase space is the trade-off for optimizing transmission through the inflector.

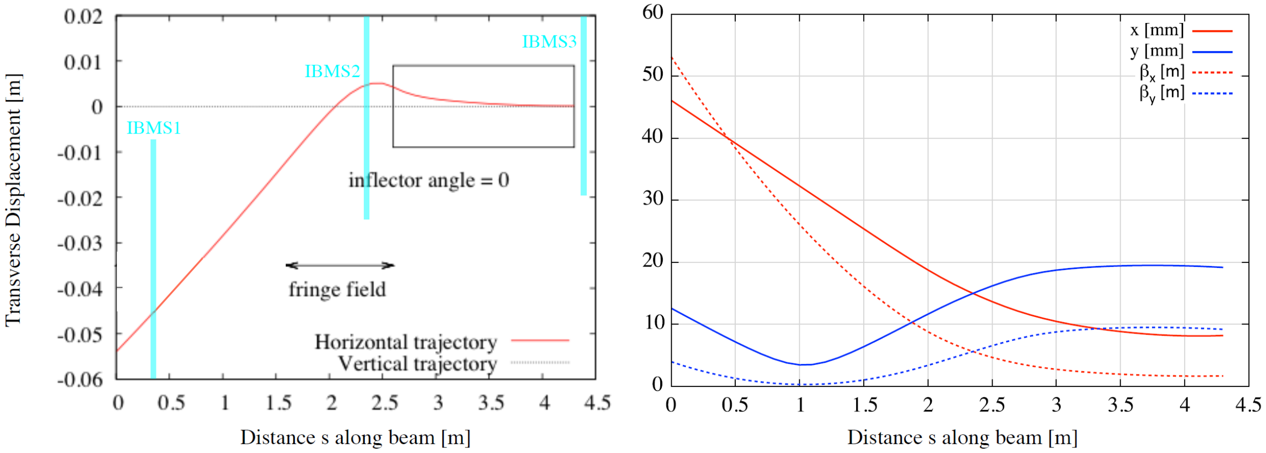

Figure 4.7: Left: Horizontal injection trajectory relative to the inflector center axis. The longitudinal s origin is $30\,\mathrm{cm}$ upstream of the magnet yoke hole. IBMS detectors shown at original planned locations, which were later adjusted. Right: β functions and transverse beam size (calculated with emittance $\epsilon_{90\%} = 40\,\mathrm{mm–mrad}$) along the injection trajectory. Figures courtesy of D. Rubin.

4.3 The Muon $g-2$ ring

In a circular ring, the particles' trajectory is described by the equations in Section 4.1 with the condition that $K_x(s)$ and $K_y(s)$ are periodic in the ring circumference. In the $g-2$ ring, the vertical magnetic dipole field provides a bending radius. The electrostatic quadrupoles vertically focus and horizontally defocus the beam, and electric quadrupole fields replace the magnetic quadrupole fields in Eqs. 4.2 and 4.3.

The lattice configuration of a quarter arc of the ring is $[\ B\,B\,Q\,Q\,BS\,BS\,Q\,Q\,Q\,Q\,B\,B\ ]$ with long bend-only segment B, short bend-only segment BS, and combined bend/quad segment Q (also shown in Figure 4.9). Parameters of the ring and the muon beam are shown in Table 4.2.

quantity	symbol	value	unit
Lorentz factor E$_\mu$/m$_\mu$	γ	29.3	
muon mass	m_μ	0.10566	GeV/c^2
nominal muon momentum	p_0	3.094	GeV/c
nominal muon energy	E	3.096	GeV
nominal muon velocity	v_0	0.999417	c
ring radius	R	7.112	m
bend field	B_0	1.45	T
quad aperture	a_q	0.05	m
length of long bend-only segment	sB	1.4580	m
length of short bend-only segment	sBS	0.2481	m
length of segment w/ quad	sQ	0.8066	m

Table 4.2: $g-2$ ring parameters

4.3.1 Smooth quad approximation

Treating the fields as constant in s and the discrete quadrupoles as continuous ("smooth quad approximation"), the fields have the form

$$\boldsymbol{B} = (0, B_0, 0) \tag{4.22}$$

$$\boldsymbol{E} = \kappa\,(x, -y, 0)\ . \tag{4.23}$$

The quadrupole strength is $k = \kappa / v_0 B_0 R$ and the dipole bend radius is $R = p_0 / B_0$, where natural units with $e = 1$ are now used. The field index $n \equiv kR^2$ describes the combined fields. R is the nominal orbit "magic radius", B_0 is the magic magnetic field, p_0 is the magic momentum, and v_0 is the nominal velocity.

Figure 4.8 shows the ring coordinate system.

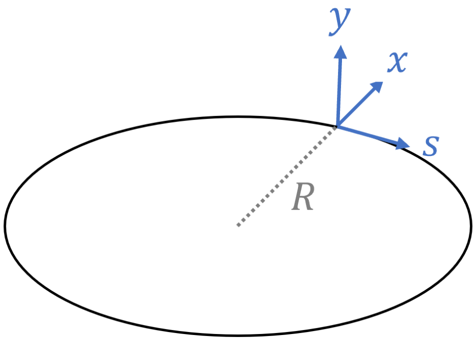

Figure 4.8: The coordinate system now moves along the ring orbit, with longitudinal coordinate s and transverse coordinates (x, y).

The focusing functions are then constant,

$$K_x = \frac{1-n}{R^2} \qquad K_y = \frac{n}{R^2}\,, \tag{4.24}$$

and the homogeneous Hill's equations become

$$x'' + \frac{1-n}{R^2}x = 0 \qquad y'' + \frac{n}{R^2}y = 0\,. \tag{4.25}$$

The horizontal focusing provided only by the magnet bend R is known as "weak focusing". Stable focusing in both planes requires $0 \le n \le 1$.

With constant K, $\beta = \frac{1}{\sqrt{K}}$ is constant (Eq. 4.11). Defining the tune ν as the phase advance (Eq. 4.9) over one turn around the ring,

$$\nu = \frac{1}{2\pi}\oint \frac{ds}{\beta} = \frac{R}{\beta}\,. \tag{4.26}$$

The horizontal and vertical trajectories describe betatron oscillation about an equilibrium position,

$$x = x_e + \sqrt{\epsilon_x \beta_x}\cos[\nu_x \frac{s}{R} + \phi_x] \qquad\qquad y = y_e + \sqrt{\epsilon_y \beta_y}\cos[\nu_y \frac{s}{R} + \phi_y]\,, \tag{4.27}$$

with horizontal and vertical tunes

$$\nu_x = \sqrt{1-n} \qquad\qquad \nu_y = \sqrt{n}\,. \tag{4.28}$$

The tunes correspond to frequencies of the betatron oscillations, which are slower than the cyclotron frequency by $\omega_x = \sqrt{1-n}\omega_c$ and $\omega_y = \sqrt{n}\omega_c$. The dispersion $D_x = \frac{R}{1-n}$ (Eq. 4.18) is also constant with constant K_x. The equilibrium radius is given by the dispersion, $x_e = \delta D_x = \delta\frac{R}{1-n}$. The vertical equilibrium position is $y_e = 0$ in the absence of a vertical dispersion.

The matrix forms of these solutions are given by the 3×3 focusing matrix with dispersion for x (Eq. A.5) and the 2×2 focusing matrix for y (Eq. A.2), with $K_x = \frac{1-n}{R^2}$ and $K_y = \frac{n}{R^2}$.

4.3.2 Discrete quadrupoles

The beam dynamics functions corresponding to the discrete quadrupole structure can be calculated with the transfer matrix formalism (Section 4.1), but the exact solutions with precisely-measured field multipoles must be calculated with a numerical model. In general, the four-fold symmetry of the quadrupole segments leads to beam functions which vary in azimuth with a four-fold symmetry, causing the ensemble beam distribution to vary with azimuth. Realistic beam functions are necessary for full beam profile reconstructions, for example to calculate beam dynamics ω_a corrections (Section 2.8) and the muon-weighted magnetic field (Chapter 7).

Figure 4.9 shows beam dynamics functions extracted from a COSY-based model of the $g-2$ ring fields, which calculates optical beam transfer maps from the differential equations of motion (D. Tarazona [70]). Here the model was configured with a magnetic field map from an example Run-2 trolley map (dipole field shown in Figure 4.10, as well as higher-order multipoles) and discrete electric quadrupole fields with Run-2 quad voltages. The azimuthal variation in the magnetic field leads to slight azimuthal asymmetries in the beam functions. Magnetic field multipoles also affect the field index and cause the average beam functions to slightly deviate from the smooth quad approximation.

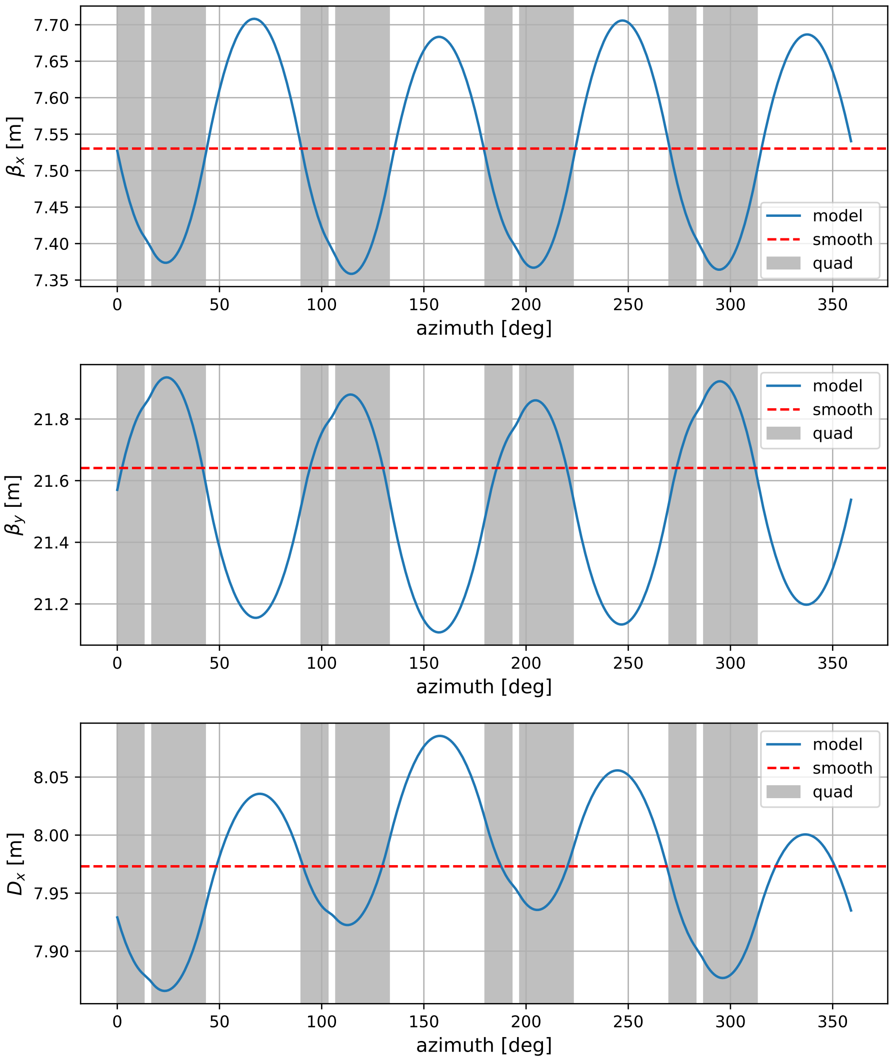

Figure 4.9: Beam functions (horizontal β_x, vertical β_y, and horizontal dispersion D_x) from COSY beam dynamics model which includes realistic ring fields. The model constructs the electric field from the discrete quadrupoles (shown in gray), and the magnetic field from a field map measured by the trolley. The fields used here correspond to an example Run-2 configuration. The red horizontal lines show the smooth quad approximation values of each function for a typical field index $n = 0.108$. The COSY azimuthal coordinates reference the upstream edge of quad Q1S (Section 7.3.5).

4.3.3 Closed orbit distortion

The equilibrium position about which betatron oscillations occur is known as the closed orbit. Dipole and quadrupole field errors cause the closed orbit to deviate away from the equilibrium position, corresponding to an azimuth-dependent offset in the beam mean position. The beam position around the ring is necessary for full beam profile reconstructions, for example to calculate beam dynamics ω_a corrections (Section 2.8) and the muon-weighted magnetic field (Chapter 7). One source of closed orbit distortions (COD) is azimuthal variation in the magnetic dipole field; variation in the vertical field causes a COD in x, and a varying radial field causes a COD in y.

$$x(\theta) = x_e(\theta) + x_{COD}(\theta) + x_\beta(\theta) \qquad\qquad y(\theta) = y_{COD}(\theta) + y_\beta(\theta) \tag{4.29}$$

where $\theta = s/R$ is the ring azimuth, and the vertical equilibrium position is zero (with zero average radial magnetic field). Allowing azimuthally-varying vertical and radial magnetic dipole fields $\boldsymbol{B} = (B_x(\theta), B_y(\theta), 0)$, the equations of motion with the smooth quad approximation become [71]

$$\frac{\partial^2 x}{\partial \theta^2} + (1-n)x = -R\frac{B_y(\theta)}{B_0} \qquad\qquad \frac{\partial^2 y}{\partial \theta^2} + ny = R\frac{B_x(\theta)}{B_0}\,. \tag{4.30}$$

The magnetic field components can be expanded in a Fourier series with respect to the azimuth

$$\begin{pmatrix} B_y(\theta) \\ B_x(\theta) \end{pmatrix} = \sum_{N=0}^{\infty} \begin{pmatrix} b_N \\ r_N \end{pmatrix} \cos[N\theta + \theta_N] \tag{4.31}$$

with amplitudes b_N, r_N (corresponding to the B_y, B_x field) and phase θ_N for each Fourier harmonic N. Replacing the magnetic field terms in the equations of motion, the solutions have the form of Eq. 4.29 with x_{COD} and y_{COD} given by

$$x_{COD}(\theta) = -R\sum_{N=0}^{\infty} \frac{\cos[N\theta + \theta_N]}{\nu_x^2 - N^2}\frac{b_N}{B_0} \qquad\qquad y_{COD}(\theta) = R\sum_{N=0}^{\infty} \frac{\cos[N\theta + \theta_N]}{\nu_y^2 - N^2}\frac{r_N}{B_0}\,. \tag{4.32}$$

where $\nu_x = \sqrt{1-n}$ and $\nu_y = \sqrt{n}$. For x_{COD} in particular, $\nu_x \lesssim 1$ so the $N = 1$ Fourier term is most significant and the $N > 1$ terms vanish quickly.

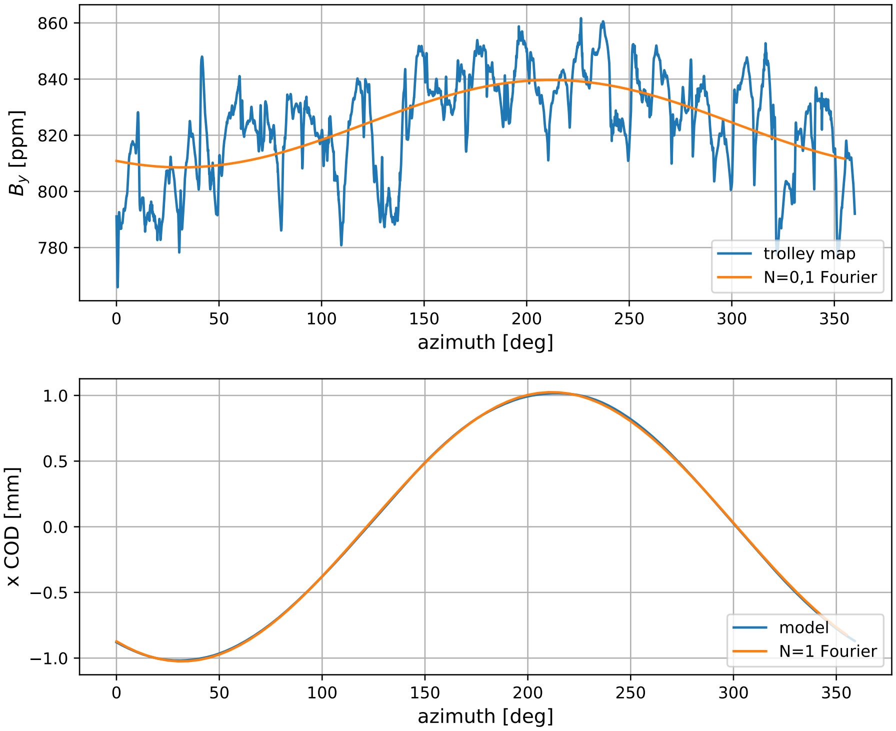

Figure 4.10: Top: Example dipole field map around the ring from Run-2 (blue) and lowest-order Fourier terms extracted from the field map (orange); $N = 0$ is the average offset and $N = 1$ is the first harmonic. Bottom: x_{COD} from COSY beam dynamics model using the above field map (blue), and x_{COD} calculated from Eq. 4.32 with only the $N = 1$ term (orange). The close agreement shows that the $N = 1$ term is dominant for x_{COD}. The COSY azimuthal coordinates reference the upstream edge of quad Q1S (Section 7.3.5).

4.3.4 Characteristic frequencies of the stored beam

Because the injected beam phase space does not uniformly fill the ring acceptance, the stored beam experiences oscillations which are characterized by several frequencies related to the cyclotron frequency ω_c and the betatron frequencies ω_x and ω_y [42]. The beam coherently oscillates at the horizontal betatron frequency ω_x due to the horizontal injection offset and the weak kick. Because $\omega_c > \omega_x > \omega_c/2$, a detector at a fixed azimuth observes an aliased frequency known as the coherent betatron oscillation (CBO), $\omega_{CBO} = \omega_c - \omega_x$. The horizontal centroid oscillates at ω_{CBO}, and the horizontal width oscillates at $2\omega_{CBO}$ and at ω_{CBO} if the stored beam is not centered at R. The vertical betatron frequency $\omega_y < \omega_c/2$ is not aliased, and vertical centroid oscillations are small because the beam is injected close to vertical center. The vertical width oscillates at $2\omega_y$, and the aliased observed frequency is known as the vertical waist $\omega_{VW} = \omega_c - 2\omega_y$.

Frequencies in Table 4.3 are calculated for a typical field index $n = 0.108$ with parameters in Table 4.2, using the smooth quad approximation.

quantity	equation	ω [rad/μs]	f [MHz]	T [μs]
ω_c	$\frac{eB_0}{m_\mu \gamma} = \frac{v}{R}$	42.15	6.71	0.149
ω_x	$\sqrt{1-n}\omega_c$	39.81	6.34	0.158
ω_y	$\sqrt{n}\omega_c$	13.85	2.20	0.454
horizontal CBO ω_{CBO}	$\omega_c - \omega_x$	2.34	0.37	2.684
vertical waist ω_{VW}	$f_c - 2f_y$	14.45	2.30	0.435
ω_a	$\frac{ea_\mu B_0}{m_\mu}$	1.44	0.23	4.366

Table 4.3: $g-2$ ring frequencies with $f = \omega/2\pi$ and $T = 1/f$ for field index $n = 0.108$

Chapter 5

Characterization of the Injected Beam

The beam dynamics of the stored muon beam depend on both the parameters of the injected beam and the fields and geometry of the storage ring. Several different software packages are used within the $g-2$ collaboration for beam dynamics modeling and simulation. In Run-1, some inconsistencies were apparent among the different beam dynamics models. In particular, the models disagreed about the time-momentum correlation introduced by the kicker, which dominated the uncertainty on the ω_a electric field correction (discussed in Chapter 6).

The experiment's primary Monte Carlo simulation for modeling realistic physics running conditions is *gm2ringsim* [68]. This software, based in *Geant4*, models the fields, materials, and geometries of the ring, and tracks circulating particles and their interactions. The simulation starts with beam injection from a point upstream of the ring (Section 5.2.2). For Run-1 simulations, the injected beam phase space was taken from a particle distribution produced by a Monte Carlo simulation of the full beamline starting at the pion production target ("end-to-end" simulation from E. Valetov [72]), combined with Run-1 beam parameter measurements (N. Froemming [68]). However, the end-to-end simulation lacks realistic verification along the beamline.

Run-1 simulation inconsistencies as well as changes in the beamline motivated this author to measure the injected beam parameters in the final beamline configuration for Muon $g-2$ production running. This measurement provides verification for the complex end-to-end simulation at injection, the most critical location for the experiment. Further, it provides realistic input for beam injection modeling. The injected beam parameters were updated in *gm2ringsim* using this measurement, which built confidence in the simulation.

5.1 Injected beam phase space measurement

This section presents a direct measurement of the transverse horizontal beam phase space at the end of the M5 beamline, the final focusing segment before injection into the ring (Section 4.2). Because the ring bend lies in the horizontal plane, the horizontal phase space is more important than the vertical. The beam phase space is derived with uncertainty estimates, with the goal of providing verified input for realistic beam injection modeling.

5.1.1 Approach

The measurement approach, known as the quadrupole scan method, is a well-known method for characterizing accelerator beams. The basic strategy [73,74] is to vary the focusing strength of a beamline quadrupole magnet and measure the horizontal beam width at a downstream screen. Then the data can be fit using an expression for the beam width as a function of quadrupole strength (Eq. 5.1) to extract the beam Twiss parameters. The quadrupole used for this measurement is Q023 in the M5 line (Figures 4.5 and 5.1) and the screen is the IBMS1 detector (Chapter 3). The analysis uses the beam transfer matrix formalism introduced in Section 4.1.

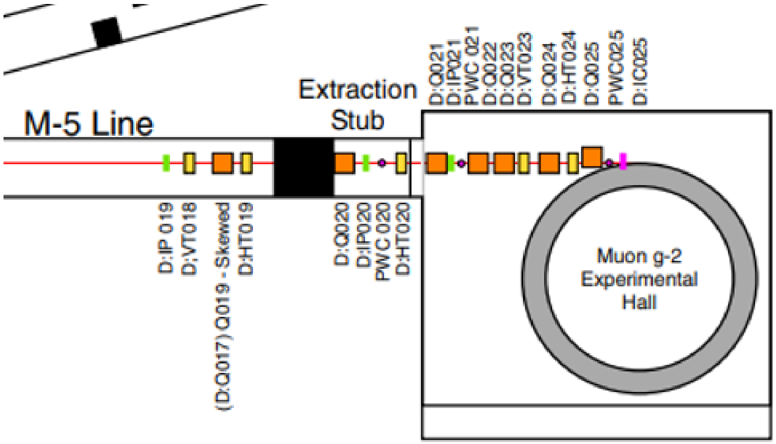

Figure 5.1: M5 final focus beamline elements [69]

This approach is illustrated for three different Q023 current setpoints in Figures 5.2 and 5.3, which shows horizontal and vertical RMS beam envelopes from a beam transport model. Higher Q023 currents produce stronger horizontal focusing and vertical defocusing fields.

As defined in Section 4.1, the ensemble beam distribution in x-x' phase space at location s can be described by a beam matrix $\boldsymbol{\sigma}(s)$ (Eq. 4.16). The initial beam $\boldsymbol{\sigma_0} = \boldsymbol{\sigma}(0)$ at the upstream end of the quadrupole can be transported to a downstream location s using the transport matrix $\boldsymbol{M} = \boldsymbol{DQ}$, where $\boldsymbol{Q}$ is the transfer matrix for a focusing quadrupole and $\boldsymbol{D}$ is the drift transfer matrix from the downstream end of the quadrupole to location s (Section 4.1). Transporting the beam from the upstream end of the quadrupole to location s, the matrix element

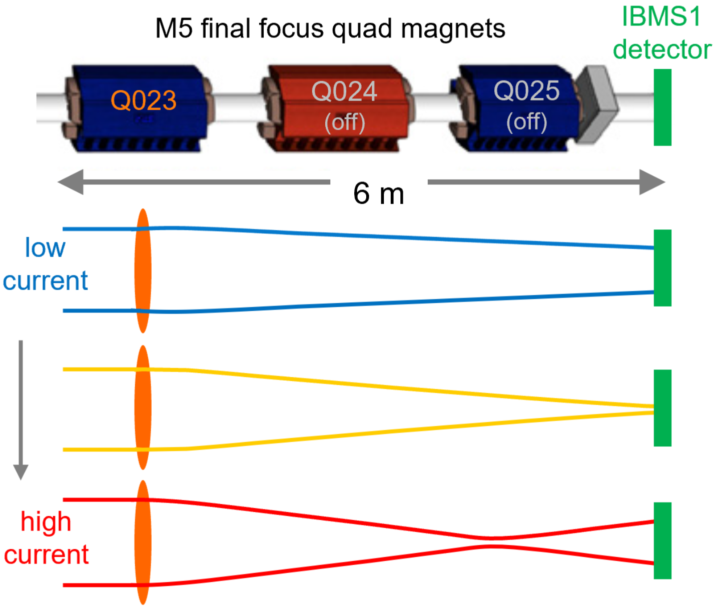

Figure 5.2: The measurement approach was to vary the focusing strength of quadrupole Q023 by varying its current, and measure the horizontal beam width at the IBMS1 detector. Here the horizontal beam envelope is illustrated for three current setpoints.

$\sigma^2_{x,s}$ gives an expression for the beam width as a function of the quadrupole strength k in terms of the initial phase space.

$$\sigma^2_{x,s} = \gamma_0\epsilon_0\, m^2_{12} + \beta_0\epsilon_0\, m^2_{11} - 2\alpha_0\epsilon_0\, m_{11}m_{12} \tag{5.1}$$

Here α_0, β_0, γ_0, and ϵ_0 are the initial Twiss parameters and m_{11}, m_{12} are the corresponding elements of the transport matrix $\boldsymbol{M}$ in terms of k, the quadrupole length L, and the drift distance d from the downstream end of the quadrupole to s.

$$m_{11} = \cos\left(\sqrt{k}L\right) - d\sqrt{k}\sin\left(\sqrt{k}L\right) \qquad\qquad m_{12} = d\cos\left(\sqrt{k}L\right) + \frac{1}{\sqrt{k}}\sin\left(\sqrt{k}L\right) \tag{5.2}$$

The beam width $\sigma_{x,s}$ was measured at the screen while the quadrupole current was scanned (as illustrated in Figure 5.3). Then Eq. 5.1 was fit to the $\sigma_{x,s}$ points with fit parameters α_0, β_0, and ϵ_0. The measurements were performed with two different screen devices, the IBMS1 detector and proportional wire chamber PWC025 located upstream of IBMS1. This analysis primarily uses the IBMS1 measurements. Performance issues were apparent in the PWC025 data, so these measurements are included for comparison only.

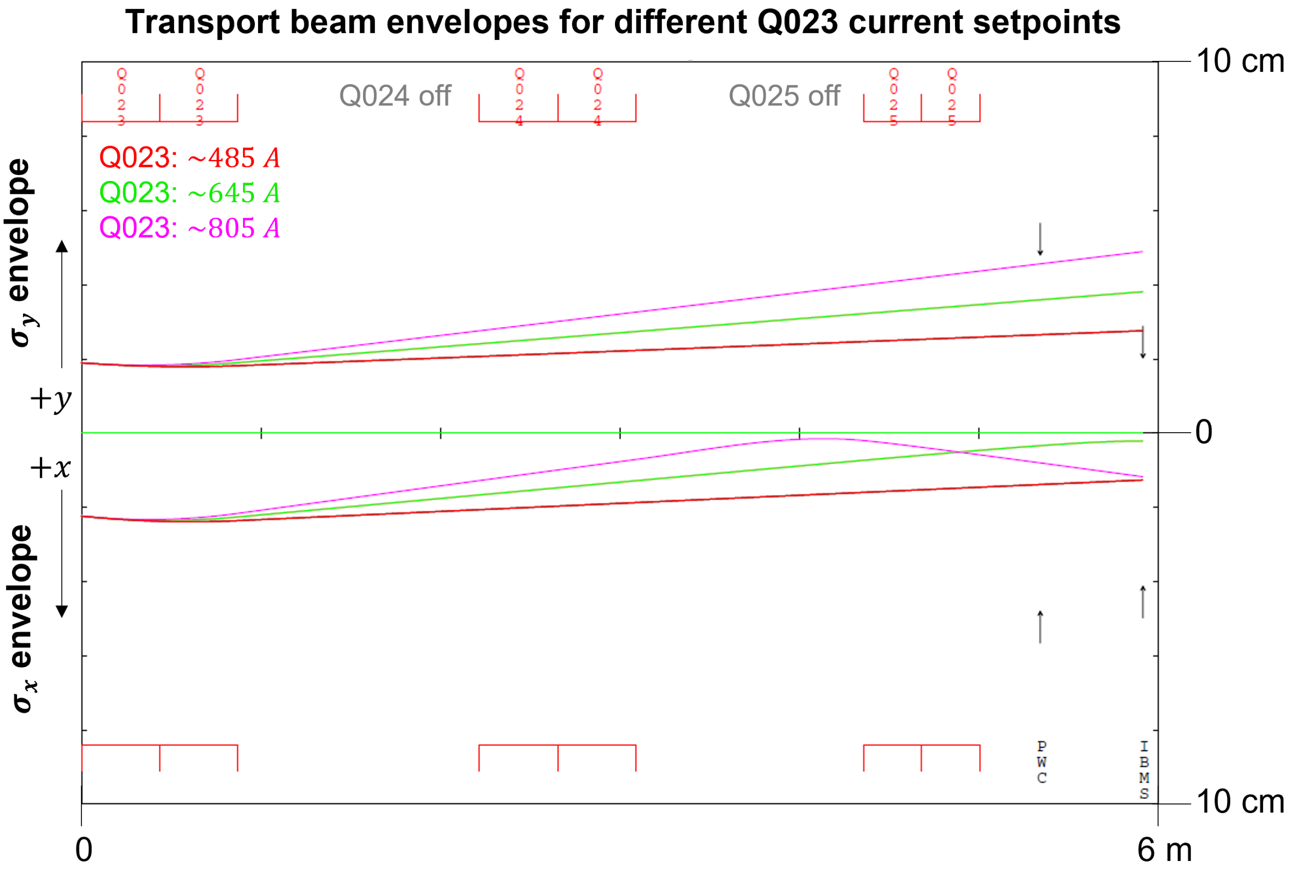

Figure 5.3: Beam envelopes for three Q023 current setpoints illustrate the quadrupole scan approach. Horizontal (σ_x, bottom) and vertical (σ_y, top) beam envelopes were generated from a beam transport model along the M5 line (Section 5.1.5). Quadrupoles Q023, Q024, & Q025 are shown as red boxes. The IBMS1 detector and the upstream proportional wire chamber PWC025 are shown as black arrows (indicating the actual detector areas). Q024 & Q025 are turned off, as they were during the actual measurement.

5.1.2 Procedure

The quadrupole current scan range was chosen to ensure coverage around the waist (minimum horizontal beam width) at the detector. The beam width (Eq. 5.1) is nearly quadratic as a function of quadrupole strength, and data points near the waist are most important for the fit. The quadrupole current adjustments were handled remotely by Accelerator Division experts B. Drendel and J. Morgan. These measurements were made in June 2021 during Run-4.

Quadrupoles Q024 & Q025, the quadrupoles downstream of Q023, were turned off for the scan. First the Q023 current was scanned over 29 points chosen to cover the waist at PWC025, with finer steps near the waist. Then to increase the IBMS1 spatial resolution, IBMS1 was translated along x in three steps of $1/3$ fiber pitch using its remote-controllable translation stage. The Q023 scan was repeated in this high-resolution configuration with 7 points to cover the waist at IBMS1. High-resolution profiles were constructed by stitching together the IBMS1X profiles from the three scans. The high-resolution x scan was repeated with Q023 at a fixed setpoint to verify that the method was not affected by hysteresis between scans.

5.1.3 Beam profile analysis

Horizontal beam widths and mean positions were extracted from the recorded beam profiles as described below.

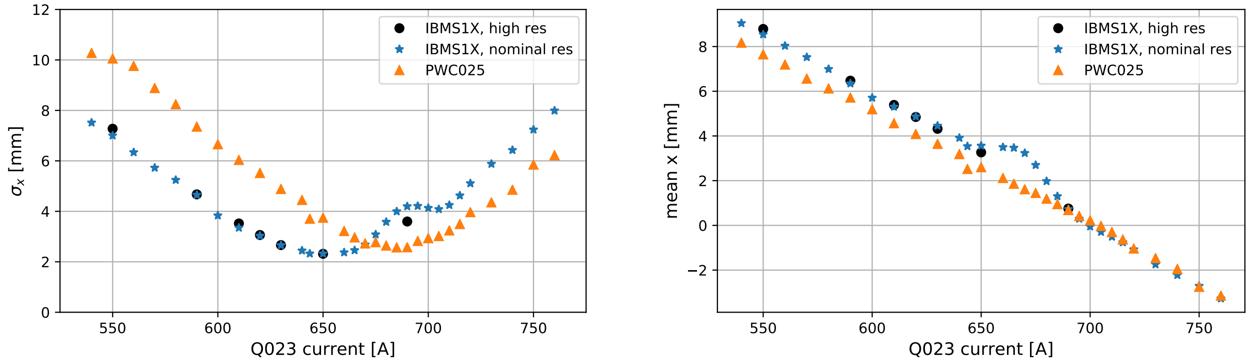

Figure 5.4: Horizontal beam widths σ_x and mean positions from IBMS1X (nominal resolution and high resolution) and PWC025 profiles.

Each PWC025 plane has 48 wires with a $2\,\mathrm{mm}$ pitch, sufficient to resolve the $\sigma_x < 3\,\mathrm{mm}$ beam waist. IBMS1 with its $5.5\,\mathrm{mm}$ fiber pitch was not expected to resolve the beam waist during the first scan, which motivated the second scan to construct high-resolution IBMS1X profiles. However, as shown in Figure 5.4, the nominal-resolution IBMS1X widths and means closely match the high-resolution widths and means over all but a small part of the scan range. In this range, the profile was distorted by the narrow beam being steered between two fibers. The nominal-resolution IBMS1X measurements in this range (Q023 currents $675\,\mathrm{A}$ to $710\,\mathrm{A}$) were therefore not included in the Twiss parameter extraction (Section 5.1.4). The beam mean position varies with current because the horizontal beam trajectory, set by dipole magnets in the M5 line, enters Q023 off-center. This results in unintended beam steering during the scan.

The beam waist measured by PWC025 was slightly larger than the waist measured by IBMS1X, but the waist at PWC025 should be smaller as it is closer to Q023. This suggests a PWC025-specific issue with measuring the beam width. PWC025 measurements are therefore not included in the main analysis and are shown for reference only. The main analysis uses the IBMS1 measurements.

High-resolution IBMS1X profiles were constructed for each Q023 setpoint by stitching together the profiles recorded in the three x steps. Each profile was normalized to the beam intensity recorded by the T0 entrance detector. This method worked very well, as demonstrated by the smooth profiles in Figure 5.5.

A Gaussian was fitted to each IBMS1X profile to extract the beam width σ_x and the mean position at each setpoint. For the high-resolution profiles, the fits included points above a 5% intensity threshold to reduce the effect of asymmetric tails. No threshold was applied in the nominal-resolution profile fits as only a few fibers were illuminated near the waist. The stitched profiles in Figure 5.5 reveal how the nominal-resolution profiles can be distorted when the beam is narrow, as seen in Figure 5.4. If only one profile (e.g. only the green profile) is recorded, the Gaussian fit could miss the profile peak and extract an incorrect width.

To verify that the method was not affected by hysteresis effects when stitching together multiple Q023 scans, a high-resolution profile was recorded with the Q023 current fixed. The fixed-current profile closely matched the profile stitched together from different Q023 scans, demonstrating consistency in the stitching method.

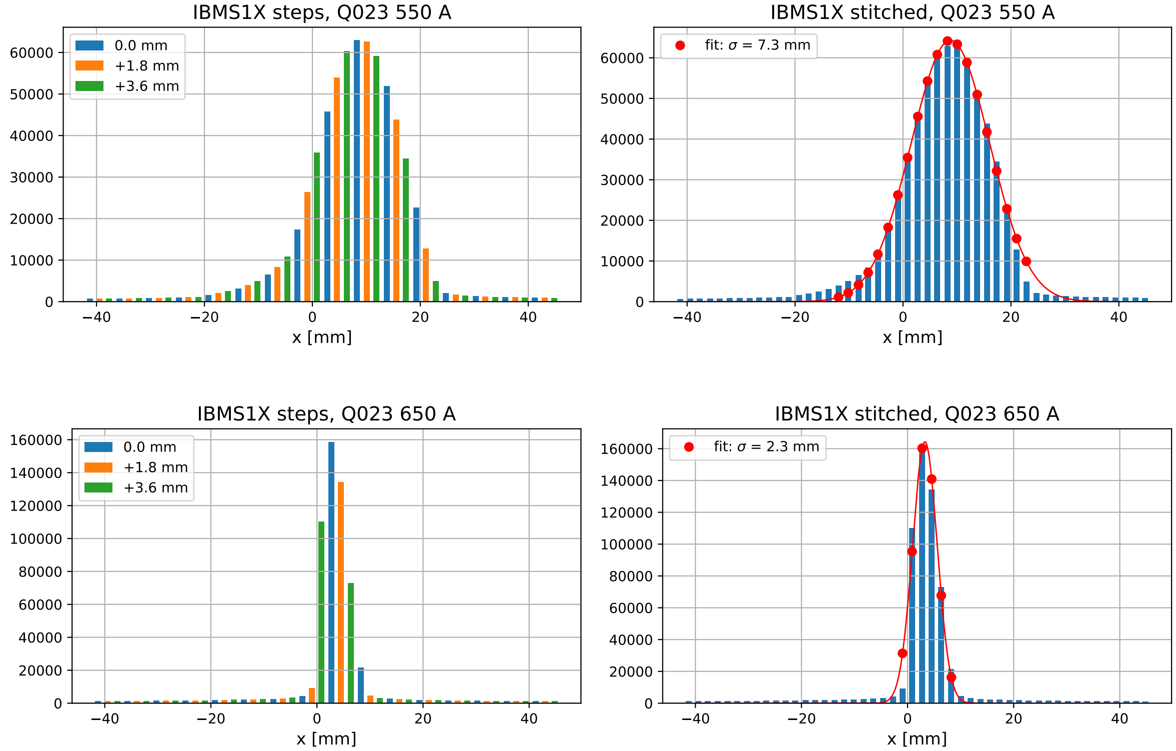

Figure 5.5: High-resolution stitched IBMS1X profiles at Q023 currents 550 A and 650 A (near the IBMS1 waist). Left: Overlayed IBMS1X profiles from each x-step of 1/3 fiber pitch. Right: x-step profiles stitched together into high-resolution profiles, with Gaussian fits. Circle markers indicate the fibers which enter the fit.

Quadrupole strength k

The quadrupole strength k is defined as in Section 4.1 as

$$k = \frac{e}{p_0}\frac{\partial B_y}{\partial x} \equiv \frac{e}{p_0} g, \tag{5.3}$$

where p_0 is the nominal magic momentum and g parameterizes the quadrupole strength per unit length. Transfer functions for $g(I)$ as a function of current I were provided by the magnet manufacturer. The Q023 strength k for each current step was then calculated according to Eq. 5.3. For the nominal Q023 current, $k(643.7\,\mathrm{A}) = 0.465\,\mathrm{m}^{-2}$.

5.1.4 Twiss parameter extraction

The Twiss parameters α_0, β_0, and ϵ_0 at the upstream end of Q023 were extracted by fitting the square of the measured beam widths σ_x^2 vs. quadrupole strength k with the expression in Eq. (5.1), with IBMS1 screen distance $d_{ibms1} = 5.043\,\mathrm{m}$. The errors were scaled such that the reduced $\chi^2 = 1$. This was a simple assumption to allow an estimate of the parameter variance, as uncertainties on the beam profiles are not explicitly evaluated.

The nominal-resolution and high-resolution IBMS1 measurements were fit separately, as shown in Figure 5.6. Extracted Twiss parameters and their corresponding fit uncertainties are shown in Table 5.1. The IBMS1X high-resolution and nominal-resolution parameters agree with each other within uncertainties; the IBMS1X high-resolution parameters provide the primary result.

Scan	α_0	$\beta_0[m]$	$\epsilon_0\ [mm \cdot mrad]$
IBMS1X high-res	-9.9 ± 0.1	44.4 ± 0.4	9.3 ± 0.1
IBMS1X nominal-res	-10.0 ± 0.6	44.8 ± 2.6	8.9 ± 0.4

Table 5.1: Extracted Twiss parameters and their fit uncertainties at the upstream end of Q023 from fitted IBMS1 beam widths.

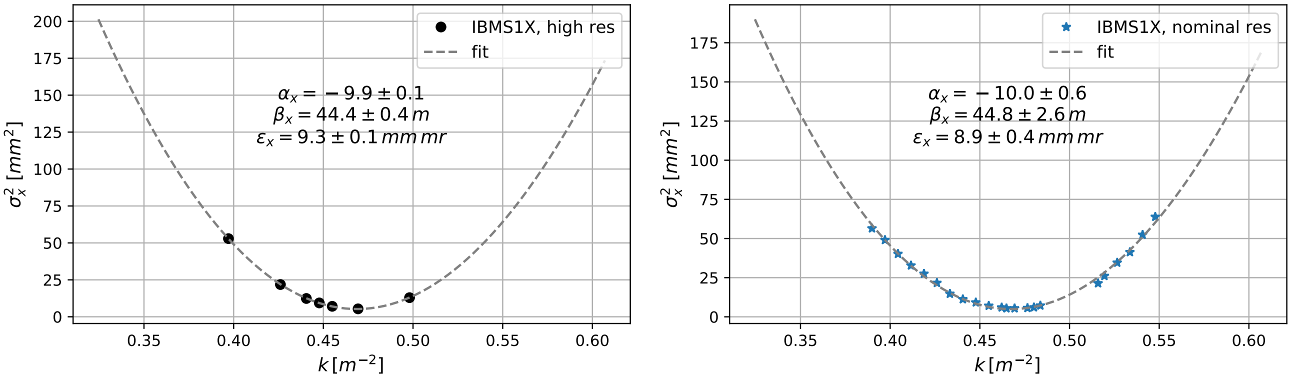

Figure 5.6: Measured points σ_x^2 vs. quadrupole strength k and corresponding functional fits with fitted Twiss parameters for IBMS1 high-resolution (top) and IBMS1 nominal-resolution (bottom) profiles. The nominal-resolution IBMS1X points with distorted profile widths were excluded from the fit.

5.1.5 Results

The phase space parameters are extracted at two positions of interest. The phase space at the upstream end of Q023, presented in Section 5.1.4, is directly measured in the quadrupole scan. This provides a direct point of comparison for end-to-end beamline simulations. The distribution must then be transported downstream from Q023 to the end of the M5 line (5.1), which is the typical starting point for modeling beam injection into the ring. The primary results for the remainder of this section use the IBMS1X high-resolution parameters from Table 5.1.

The measurement result is compared throughout this section with two beamline model configurations. The M4 and M5 beamline optics can be described by an optical lattice from a MAD model [1] with corresponding Twiss parameters [75]. The two configurations are the *operational* optics, which describe the actual magnet settings used in Run-3 and beyond, and the *TDR* optics, which describe the as-designed magnet settings from the Muon $g-2$ Technical Design Report (TDR) [36]. The Run-1 end-to-end beamline simulation [72] used the TDR optics; this end-to-end simulation provided the input distribution for Run-1 *gm2ringsim* simulations.

As discussed in Section 4.1.1, the Twiss parameters describe the 1σ x-x' phase space distribution according to Eq. 4.15. Phase space ellipses will be used in the following sections to visually compare different phase space distributions.

Upstream end of Q023

Figure 5.7 shows the measured phase space ellipse at the upstream end of Q023, compared with ellipses defined by the operational and TDR model configurations. The model provides α and β parameters but not emittance ϵ, so the measured emittance is used to define the corresponding phase space ellipse. As expected, the measurement resembles the operational settings more closely than the TDR settings.

---

[1] Methodical Accelerator Design (MAD) is an accelerator beam modeling software tool.

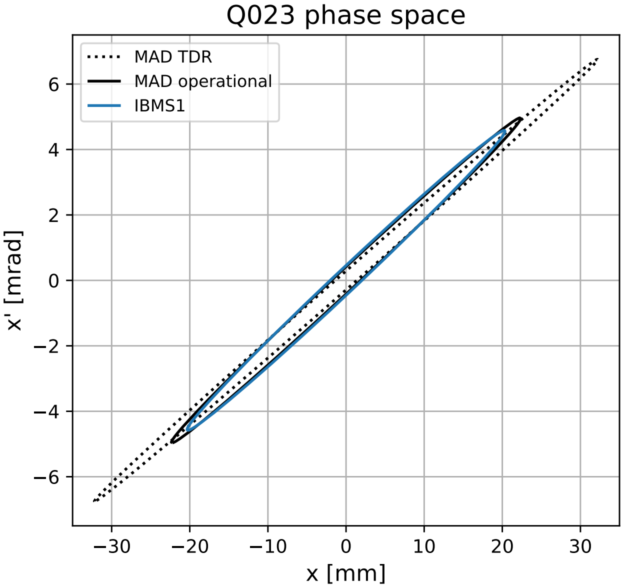

Figure 5.7: Phase space ellipse at the upstream end of Q023 defined by measured Twiss parameters (blue) compared with operational (black) and TDR (dashed) Twiss parameters (with measured emittance).

End of M5

The transfer matrix formalism described in Section 5.1.1 can be used to transport the beam downstream of Q023. As a self-consistency check of this formalism, transporting the beam to the IBMS1 location with k corresponding to the Q023 current at which the waist was observed reproduces the measured waist width.

To produce a distribution which represents the injected beam, the beam must be transported from Q023 to the end of M5 under normal operating conditions, with Q024 and Q025 at their nominal settings. In this case, the matrix $\boldsymbol{M}$ would include a $\boldsymbol{Q}$ matrix for each quadrupole and a $\boldsymbol{D}$ matrix for each drift. A simple program was created using the Graphic Transport Framework from Paul Scherrer Institute (PSI) to handle beam transport from Q023 through Q024, Q025, and the end of M5. The user defines the initial beam widths σ_x, $\sigma_{x'}$ and momentum p_0 at Q023, as well as the quadrupole fields, positions, and dimensions of Q023-25. The program handles the matrix transformations and returns the beam widths and Twiss parameters at each point. Nominal fields and dimensions for Q023-25 were taken from reference [76] with nominal operating currents, and positions of Q023-25 were taken from the MAD model. Table 5.2 shows the beamline elements and their longitudinal lengths defined in the transport program. The transport program output was shown to be consistent with the MAD model output.

Type ("card")	Label	z length [m]
BEAM	muon	0.0
QUAD	Q023	0.870
DRIFT		1.346
QUAD	Q024	0.870
DRIFT		1.270
QUAD	Q025	0.647
DRIFT		0.337
SLIT	PWC	0.000
DRIFT		0.572
SLIT	IBMS	0.000
DRIFT	End5	0.035
LENGTH		5.947

Table 5.2: Beamline elements and their lengths in z defined in the transport program.

The initial beam defined by the measured phase space can then be transported through to the end of M5. Figures 5.8 and 5.9 show the resulting beam envelope and phase space ellipse. The IBMS1 width measured under nominal conditions is marked for comparison; the transported envelope closely reproduces the nominal measured IBMS1 width. Table 5.3 shows the Twiss parameters and corresponding beam $\boldsymbol{\sigma}$ matrix elements (Eq. 4.16) at the end of M5, corresponding to the ellipse in Figure 5.9.

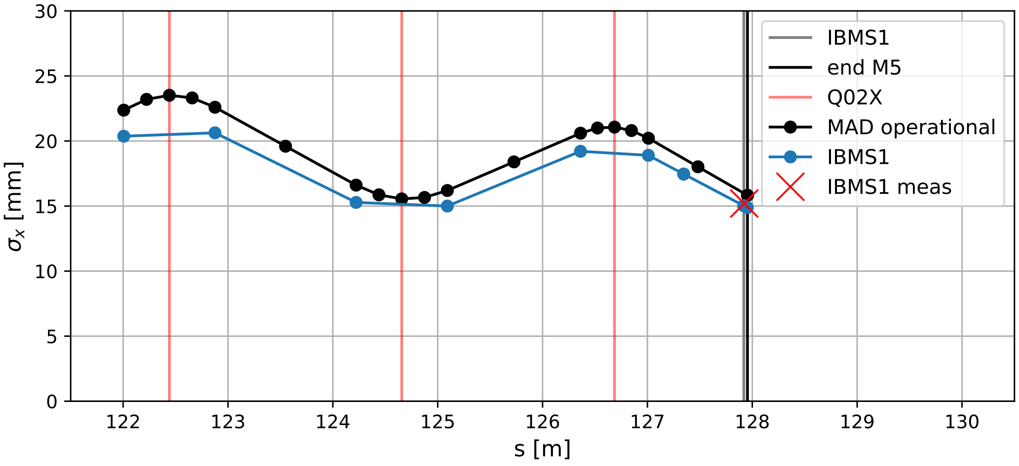

Figure 5.8: Beam envelope σ_x from transport program starting with measured (blue) initial beam conditions (corresponding to ellipse shown in Figure 5.7), compared with operational settings (black). The red vertical lines mark Q023, 24, & 25; the gray line marks IBMS1; and the black line marks the end of M5. For comparison, the measured IBMS1 width under nominal conditions is indicated with the red X.

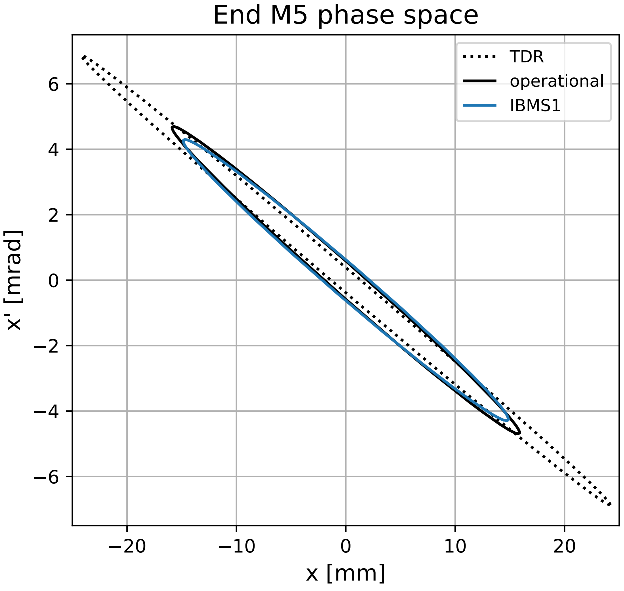

Figure 5.9: Phase space ellipses at the end of M5 from transport program outputs starting from measured parameters (blue, corresponding to Figure 5.8) and from operational settings (black) and TDR settings (dashed).

	Twiss		σ		
Initial conditions	α_s	$\beta_s[m]$	$\sigma_x[mm]$	$\sigma_{x'}[mrad]$	$\sigma_{xx'}[mm \cdot mrad]$
operational	7.9	27.1	15.90	4.70	−74.18
IBMS1	6.8	23.7	14.88	4.30	−63.28

Table 5.3: Twiss parameters and beam matrix elements at the end of M5 for initial beam given by operational optics parameters and measured parameters, corresponding to ellipses in Figure 5.9.

End of M5 results compared with previous simulations and measurements

The end-to-end beamline simulation [72] for Run-1 used the TDR M4/M5 beamline optics. The muon distribution produced by the simulation at the end of M5 is consistent with the TDR parameters, as expected. End-to-end simulations using the operational optics have not yet been completed.

During Run-1 before the upstream momentum cooling wedge was implemented (described in Section 2.2), Nathan Froemming made a quadrupole scan measurement of the beam parameters with Q020 and wire chamber PWC021 (upstream of Q023) [77] [68]. In a comparison at the end of M5, this measurement resembled the operational parameters. The *gm2ringsim* injection input for Run-1 was constructed from this measured α and β, a larger ϵ from a previous beamline simulation, and a normalized version of the end-to-end simulated distribution transformed to match the defined parameters. Diktys Stratakis et al. also previously measured the emittance using several M4/M5 quadrupoles and wire chambers [73] and [69], also before the wedge was implemented.

Table 5.4 shows the Twiss parameters from the end-to-end simulated distribution, previous measurements, *gm2ringsim* input definition, and IBMS1 measurement. The IBMS1-measured emittance is similar to Nathan's measurement and smaller than the values from simulation and Diktys' measurement.

Initial conditions	α	$\beta[m]$	$\epsilon[mm \cdot mrad]$
End-to-end simulation (TDR settings)	14.8	52.4	10.8
Previous measurement, Diktys [69]	-	-	12
Previous measurement, Nathan [68]	8.5	28	9
gm2ringsim input	8.5	28	14
IBMS1 measurement	6.8	23.7	9.3

Table 5.4: Twiss parameters at the end of M5 from end-to-end simulation, previous measurements, and *gm2ringsim* input definitions, compared with IBMS1 measurement (Table 5.3).

Asymmetric profiles and effect of upstream wedge

The recorded beam profiles are asymmetric, both in the Q023 scan (e.g. Figure 5.5) and with all quadrupoles at nominal settings. This asymmetry is a possible source of uncertainty (also discussed in Section 5.1.6), as the beam transport formalism (Section 5.1.1) describes a symmetric beam and does not account for the observed asymmetries. The primary analysis and results presented here focus on the symmetric Gaussian part of the beam profiles and ignore the asymmetric part. A Monte Carlo study of realistic beam profiles would be required to verify the asymmetric behavior and reduce the associated uncertainty.

The upstream cooling wedge affects the beam profile asymmetry, as shown by the IBMS1X profiles in Figure 5.10. For a more realistic input to *gm2ringsim*, an end-of-M5 phase space distribution can be constructed by scaling the symmetric phase space in x to match the asymmetric measured x profile. The scale function (Figure 5.11 is determined from a two-Gaussian fit to the measured IBMS1X profile (Figure 5.10). The symmetric distribution was used for Run-2/3 *gm2ringsim* simulations; in the future, the asymmetric scaling can be applied if end-to-end beamline simulations do not reproduce the measured profiles.

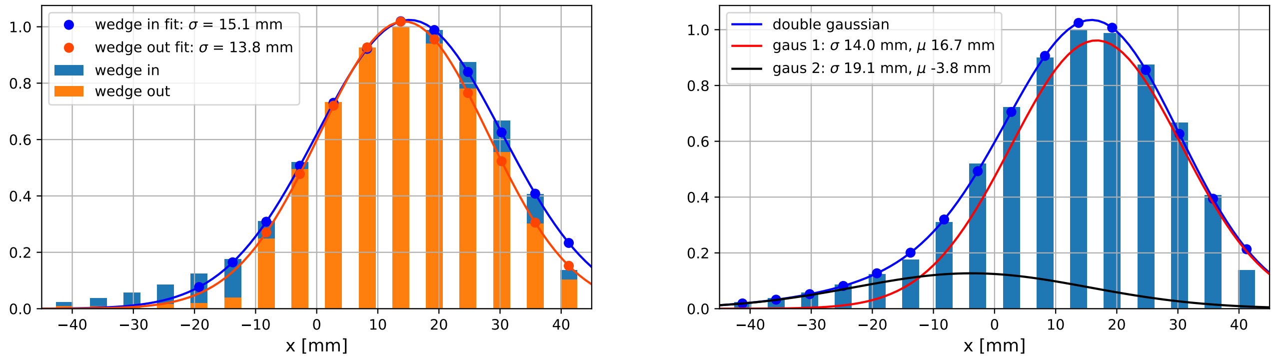

(a) Comparison of normalized IBMS1X profiles with wedge inserted (nominal configuration) and retracted, with Q023-25 at their nominal settings.

(b) Nominal IBMS1X profile (wedge inserted), fit with the sum of two Gaussians. The primary Gaussian width of $14\,\mathrm{mm}$ is similar to the wedge-retracted width of $13.8\,\mathrm{mm}$.

Figure 5.10

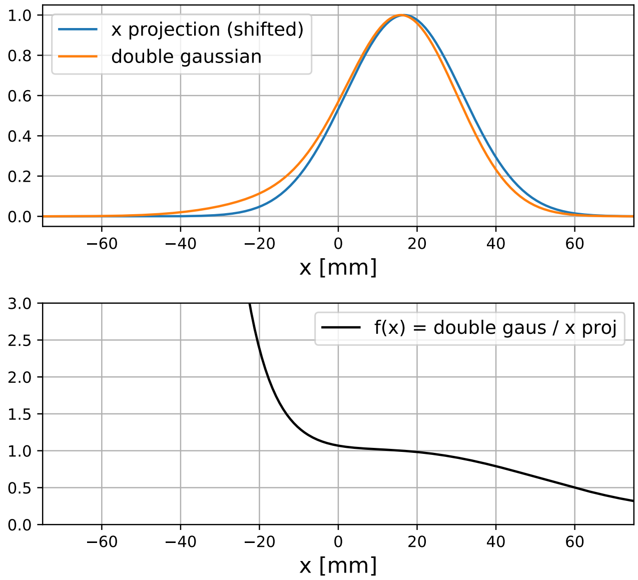

Figure 5.11: The scale function $f(x)$ (bottom) is the ratio of the fitted double gaussian to the symmetric x distribution (top).

5.1.6 Uncertainties

Several possible sources of uncertainty were analyzed and are summarized here. Table 5.5 reports the uncertainties in terms of the x-x' phase space σ matrix elements. Additional details about the uncertainty analysis are given in Appendix B.

- The fit uncertainties on the Twiss parameters (Section 5.1.3) were propagated using the fit covariance matrix.
- The effect of possible remanent magnetic fields in the downstream quadrupoles during the measurement was evaluated in the beam transport program.
- The effect of a possible nonzero dispersion originating from upstream of Q023 was determined by including dispersion in the Twiss parameters fit expression. This affects the Twiss parameters but not the x-x' distribution.
- The uncertainty on the beam width was determined by varying the contribution of the asymmetric tails in the Gaussian fit. This effect is not included in the total uncertainty, as the asymmetry is not included in this analysis and can be characterized with future beamline simulation studies (Section 5.1.5).

The central-value phase space parameters were used as input for the Run-2/3 *gm2ringsim* simulations. A *gm2ringsim* evaluation of the uncertainty is recommended, which would entail varying the input phase space distribution within uncertainties and evaluating the effect on stored beam properties. Depending on the size of the downstream effects, the measurement uncertainties may be further improved by studying the asymmetric beam profiles in the beamline simulation.

Uncertainty	$\Delta\sigma_x[mm]$	$\Delta\sigma_{x'}[mrad]$	$\Delta\sigma_{xx'}[mm\cdot mrad]$	$\Delta\epsilon\,[mm\cdot mrad]$
Twiss parameter fit	±0.03	±0.4	±1.7	±0.1
Remanent fields in Q024 & Q025	$+0.4$	$+0.1$	-3.2	$+0.4$
Nonzero dispersion	0	0	0	-1.8
Gaussian profile fit	$+1.0/-0.1$	$+0.4/-0.1$	$+1.3/-10.7$	$+1.5/-0.4$
Total (with Gaussian profile fit)	$+1.1/-0.1$	$+0.6/-0.4$	$+2.1/-11.3$	$+1.6/-1.8$
Total (without Gaussian profile fit)	$+0.40/-0.03$	$+0.4/-0.4$	$+1.7/-3.6$	$+0.4/-1.8$

Table 5.5: Uncertainties on end-of-M5 beam matrix elements and emittance. Totals are added in quadrature. The recommended total uncertainty is the **total (without Gaussian profile fit)**; the total (with Gaussian profile fit) is also shown for reference.

5.1.7 Summary

The transverse horizontal beam phase space at the end of the M5 beamline was measured using the quadrupole scan method described in Section 5.1.1. The approach was to vary the Q023 current, measure the beam width at IBMS1, and fit the data to extract the Twiss parameters at Q023 (Section 5.1.3). The extracted phase space was then transported from Q023 to the end of M5 using a beam transport program with nominal M5 quadrupole settings (Section 5.1.5). End-of-M5 results (Table 5.6) are given in terms of x-x' beam parameters as well as Twiss parameters. Sources of uncertainty are presented in Section 5.1.6.

	Twiss			σ		
Measurement	α_s	$\beta_s[m]$	$\epsilon\,[mm \cdot mrad]$	$\sigma_x[mm]$	$\sigma_{x'}[mrad]$	$\sigma_{xx'}[mm \cdot mrad]$
IBMS1	6.8	23.7	9.3	14.88	4.30	−63.28

Table 5.6: End-of-M5 horizontal Twiss parameters and beam matrix elements from IBMS1 measurement (from Table 5.3).

The measurement results are much more consistent with the operational beamline settings than the TDR beamline settings (Sections 5.1.5 and 5.1.5). The Run-1 end-to-end simulation, which provides input for *gm2ringsim* simulations, used the TDR settings and is inconsistent with the measured phase space. The operational settings need to be implemented in the end-to-end simulation to produce a more realistic output.

The symmetric distribution parameterized here was used for Run-2/3 *gm2ringsim* simulations, with an initial offset and angle optimized to match measured IBMS profiles (discussed in Section 5.2). The observed beam profiles are asymmetric, but this analysis focuses on the dominant symmetric part which is described by the beam transport formalism. A simple method to scale the distribution asymmetrically for future *gm2ringsim* simulations is laid out in Section 5.1.5.

5.2 Optimizing beam injection in gm2ringsim

The simulation team (A. Driutti and R. Fatemi) optimized the horizontal beam injection parameters in *gm2ringsim* for Run-2/3 simulations to match measured IBMS beam profiles. This required updating the IBMS detector positions, implementing the measured phase space from Section 5.1, and adjusting the injection trajectory and inflector field. After this optimization, the *gm2ringsim* storage fraction $N_{stored}/N_{incident}$ increased from 1.2% to 1.7%. The goal is to match experiment running conditions in *gm2ringsim*; beam injection parameters are tuned to optimize storage fraction in the experiment, so increasing storage fraction builds confidence in the simulation. Realistic beam injection modeling is critical for simulating realistic stored beam dynamics in *gm2ringsim*.

5.2.1 IBMS detector positions

For Run-1 simulations, IBMS detectors in *gm2ringsim* were positioned at initially-planned locations which were somewhat different from the final installed locations. For Run-2/3 simulations, the IBMS detector positions were updated to match the surveyed positions in Section 3.1.4. IBMS1, 2, and 3 had to be moved respectively $196\,\mathrm{mm}$, $49\,\mathrm{mm}$, and $274\,\mathrm{mm}$ upstream in *gm2ringsim* from their Run-1 positions. Verifying and updating the IBMS positions was important for comparing simulated and measured IBMS profiles (Section 5.2.3).

5.2.2 Injection location and beam phase space

Injected beam parameters and starting location in *gm2ringsim* are defined by a tool called "the beam gun" [68]. For Run-1 simulations, the beam gun position was defined at the nominal end-of-M5 location. [2]. After updating the IBMS detector positions for Run-2/3 simulations, IBMS1 was located upstream of the beam gun position. In order to include IBMS1 and the T0 detector in the simulation, the beam gun position was moved $139\,\mathrm{mm}$ upstream of the end of M5. From the surveyed positions of IBMS1 and the M5 quadrupole magnets, this corresponds to a distance $5376\,\mathrm{mm}$ downstream of Q023 center. The horizontal beam phase space measured with IBMS1 in Section 5.1 was then transported to this position as in Section 5.1.5. The Twiss parameters at the new beam gun position (Table 5.7) defined the horizontal phase space of the injected beam for Run-2/3 *gm2ringsim* simulations.

Twiss parameter	α_x	$\beta_x[m]$	$\epsilon_x\ [mm \cdot mrad]$
gm2ringsim new beam gun position	7.0	25.6	9.3
End of M5	6.8	23.7	9.3

Table 5.7: Measured horizontal Twiss parameters transported to end of M5 (from Table 5.6) and to the *gm2ringsim* new beam gun position.

5.2.3 Injection trajectory parameters and matching IBMS data

The *gm2ringsim* beam gun also defines initial beam injection angle and offset. With the updated Twiss parameters from Table 5.7, the horizontal offset x_0 was adjusted to match the measured IBMS1X profile (Figure 5.12) and horizontal angle x_0' was adjusted to match the measured IBMS2X profile (Figure 5.13). The beam gun defines $+x$ radially out, so the x_0 and x_0' reported here follow that convention; this is the opposite of the IBMS convention. Finally, the inflector magnetic field was adjusted to match the measured IBMS3X profile (Figure 5.14). Optimized parameters are shown in Table 5.8.

---

[2] The Run-1 beam gun position was $4300\,\mathrm{mm}$ upstream of the ring injection point (inflector exit) [68]

	offset x_0 [mm]	angle x'_0 [mrad]	inflector field B_{inf} [T]
gm2ringsim Run-2/3	-15.2	+4.0	-1.44
gm2ringsim Run-1	-7.5	+1.75	-1.46

Table 5.8: *gm2ringsim* beam gun horizontal offset x_0 and angle x'_0 and inflector field B_{inf} before and after updating to match measured IBMS profiles. The beam gun defines $+x$ radially out relative to the nominal beamline.

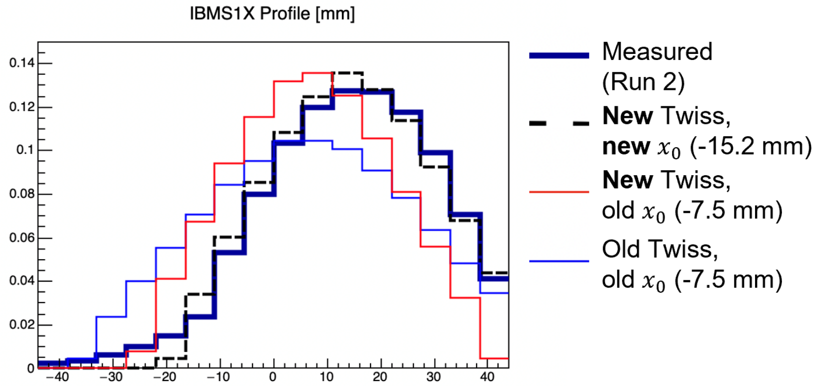

Figure 5.12: Measured IBMS1X profile (dark blue) compared with *gm2ringsim* profiles: Run-1 Twiss parameters and offset (light blue), updated Run-2/3 Twiss parameters with Run-1 offset (red), and updated Run-2/3 Twiss parameters and offset (dashed black). The updated offset $x_0 = -15.2\,\mathrm{mm}$ gave the best match to the measured profile. Figure courtesy of A. Driutti [78].

.

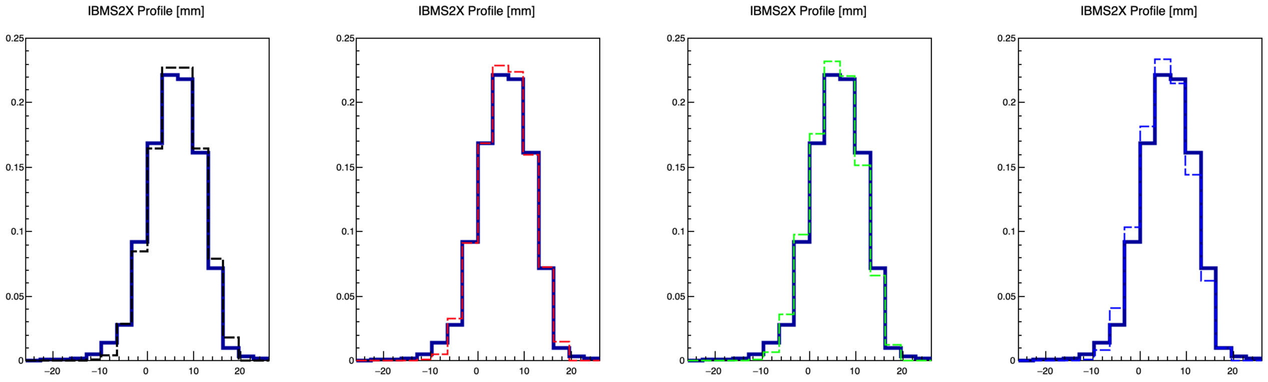

x'_0 = +3.9 mrad x'_0 = +4.0 mrad is optimal x'_0 = +4.1 mrad x'_0 = +4.2 mrad

Figure 5.13: Adjusting beam gun injection angle x'_0 to match the measured IBMS2X profile (dark blue in each plot). The angle $x'_0 = +4\,\mathrm{mrad}$ gave the best match. Figure courtesy of A. Driutti [78].

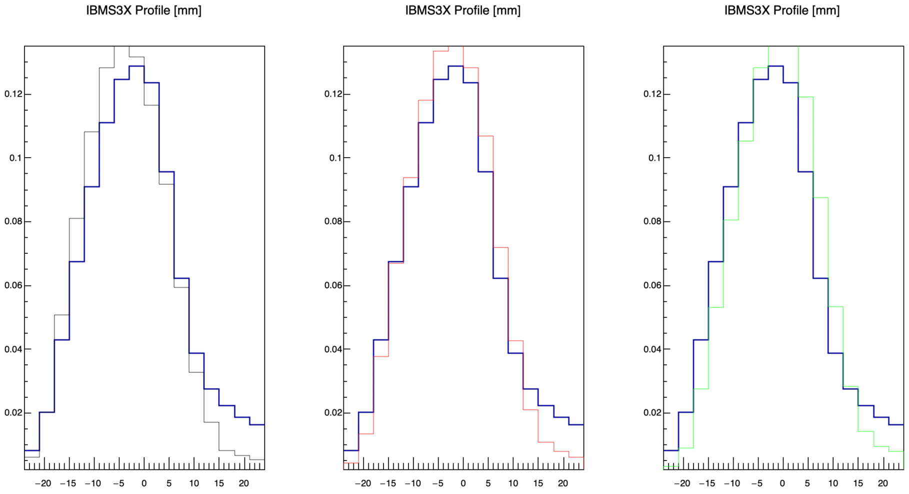

B_{inf} = -1.445 T

B_{inf} = -1.440 T is optimal

B_{inf} = -1.435 T

Figure 5.14: Adjusting *gm2ringsim* inflector field to match the measured IBMS3X profile (dark blue in each plot). Inflector field $B_{inf} = -1.44\,\mathrm{T}$ gave the best match. Figure courtesy of A. Driutti [78].

5.3 Summary

Simulation inconsistencies and changes in the beamline configuration motivated a measurement of the injected beam parameters. The horizontal phase space of the injected beam was measured with the IBMS1 detector using the quadrupole scan method. This measurement provides a realistic check of the end-to-end beamline simulation, which provides the initial distribution for injection in *gm2ringsim*. The end-to-end simulation used beamline settings corresponding to the design configuration rather than the final operational configuration, and is inconsistent with the measurement, demonstrating the need for an updated simulation with operational settings.

The measured phase space distribution provided verified input for beam injection modeling in *gm2ringsim*. Based on this measurement, the horizontal injection parameters in Run-2/3 simulations were updated to match the measured IBMS beam profiles. This verification builds confidence in the stored beam properties simulated with *gm2ringsim*.

Chapter 6

Momentum Distribution of the Stored Beam

The beam dynamics corrections to ω_a (Section 2.8.1) depend on characterizations of the stored beam. In particular, the electric field correction C_e is calculated from the momentum distribution, which is reconstructed from the Fourier fast rotation (FR) analysis. The 53 ppb uncertainty on C_e from the FR reconstruction was a significant ω_a systematic in Run-1. The uncertainty is dominated by the so-called time-momentum correlation effect, which is caused by the time-varying kick strength and leads to a distortion in the FR momentum reconstruction. This time-momentum correlation is an ongoing issue being studied in the Run-2/3 analysis, and multiple weeks of beam time in Run-6 have been dedicated to studying this effect. Understanding this correlation is critical to reduce the uncertainty on C_e to 25 ppb target uncertainty.

As the FR analysis is an indirect momentum reconstruction which provides essential input for the a_μ measurement, an independent direct beam measurement is well motivated. Based on the reliable and well-established IBMS detectors (Chapter 3), the MiniSciFi (Minimally Intrusive Scintillating Fiber) detector was conceived to directly measure and characterize the momentum distribution and the time-momentum correlation, in addition to other properties of the stored beam. The MiniSciFi detector was installed and a first measurement campaign was completed during Run-5. The configuration was modified for further measurements during Run-6. This author contributed to the detector implementation and developed the measurement concept discussed in Section 6.3.

6.1 Fast rotation momentum reconstruction

The beam rotation around the ring at the cyclotron frequency is called "fast rotation". The Fourier fast rotation (FR) analysis reconstructs the momentum distribution via a Fourier decomposition of the cyclotron frequencies observed by the calorimeters. The muons' velocity is given by $v = \beta c$, where $\beta = \sqrt{1 - 1/\gamma^2} \approx 0.9994$ at the nominal magic momentum p_0 with $\gamma = 29.3$. A muon's orbital equilibrium radius relative to the nominal radius, $x_e = r_e - R$, is related to the momentum by

$$x_e = \frac{\Delta p}{p_0} \frac{R}{1-n}\,, \tag{6.1}$$

where Δp is the momentum deviation from p_0 and n is the effective field index (Section 4.3.1). The incident muon beam has a finite momentum spread, and higher-momentum muons have a higher equilibrium radius in the storage ring. Because high-momentum and low-momentum muons have approximately the same relativistic velocity within the $45\,\mathrm{mm}$ radius aperture of the storage region, the higher-momentum muons have a slower cyclotron frequency than the lower-momentum muons, where the frequency is given by

$$\omega_c = \frac{eB_0}{m_\mu \gamma} = \frac{v}{R + x_e}\,. \tag{6.2}$$

The nominal cyclotron frequency for magic momentum muons is $f_c = \omega_c/2\pi = 6705\,\mathrm{kHz}$. As the beam circulates around the ring, the higher-frequency (lower-momentum) muons eventually overtake the lower-frequency (higher-momentum) muons, and the beam gradually debunches.

The calorimeters record the decay positron counts over time in the fill. The counts above the ω_a energy threshold correspond to an intensity which oscillates at ω_c as the beam circulates around the ring, as well as oscillating at the anomalous precession frequency ω_a and the other beam dynamics frequencies described in Section 4.3.4, within a decaying envelope corresponding to the muon lifetime. To extract the FR signal, an ω_a fit function (described in Section 2.6.3) including the muon lifetime, ω_a oscillation, and coherent betatron oscillation (CBO) is divided out from the calorimeter signal; the remainder is the FR signal, shown in Figure 6.1. For a muon beam ensemble with an initial distribution $\rho(\omega, \tau)$ of momentum-dependent cyclotron frequencies ω and injection times τ, the time structure of the FR signal $S(t)$ can be written as

$$S(t) = \int_{-\infty}^{\infty} \int_{-\infty}^{\infty} \left[\sum_{N=-\infty}^{\infty} \delta \left[t - \left(\frac{2\pi N}{\omega} + \tau \right) \right] \right] \rho(\omega, \tau)\, d\omega\, d\tau\,, \tag{6.3}$$

as described by T. Barret [44]. The δ function describes a single muon circulating with frequency ω over turns N from $-\infty$ to ∞ seen by a fixed detector, and the overall signal is given by the ensemble integral.

The real part of a complex Fourier transform, called a cosine transform, is then used to recover the frequency distribution. For an ideal beam pulse which extends infinitely in time and is symmetric about time t_0 in the first

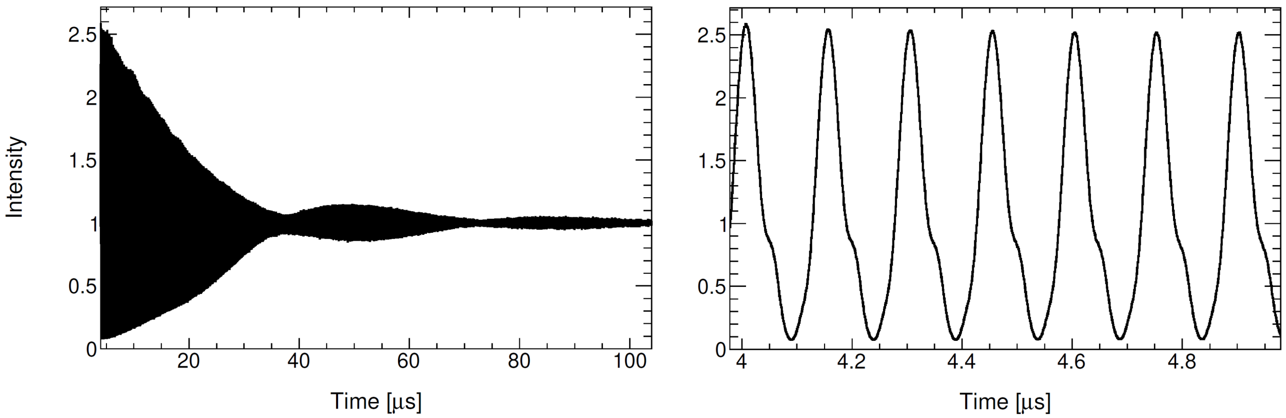

Figure 6.1: Fast rotation signal extracted from calorimeter decay positron counts by dividing out the ω_a fit function. The signal decoheres as the beam debunches (left). On a shorter timescale (right), the signal oscillates with the $149.1\,\mathrm{ns}$ cyclotron period. Figures courtesy of T. Barret [79].

turn, the cosine transform is given by

$$\hat{S}(\omega) = 2\int_{t_0}^{\infty} S(t)\cos\left(\omega(t-t_0)\right)dt\,. \tag{6.4}$$

In reality, the signal is integrated over a finite time from $t_s \approx 4\,\mu\mathrm{s}$, after the calorimeters stabilize from the initial high-intensity beam flash and later than t_0, to $t_e \approx 250\,\mu\mathrm{s}$. Following the derivation from [44], the cosine transform with finite integration time can be written as

$$\hat{S}(\omega) = \pi A\rho(\omega) - A\rho(\omega) * \frac{\sin\left(\omega(t_s-t_0)\right)}{\omega}\,, \tag{6.5}$$

if t_e is sufficiently large (longer than typical debunching time) and ω and τ are uncorrelated in $\rho(\omega,\tau)$. Here A is a constant scale factor and $\rho(\omega) = \int_{-\infty}^{\infty}\rho(\omega,\tau)d\tau$ is the true frequency distribution. The convolution term, called the "background term", is the result of the finite time window. In practice, the background term is fitted by tuning t_0 and then subtracted out, leaving only the true $\rho(\omega)$ (up to an overall scale factor). Figure 6.2 shows example FR-reconstructed distributions.

6.1.1 Time-momentum correlation

If ω and τ are correlated, the cosine transform expression is more complicated. In this case, the correlation leads to frequency-dependent weight functions which distort the true frequency distribution $\rho(\omega)$. The time-varying kicker strength causes different momenta to be stored for different times in the injected beam bunch, corresponding to a correlation between the momentum-dependent frequency ω and injection time τ. The baseline Fourier FR analysis

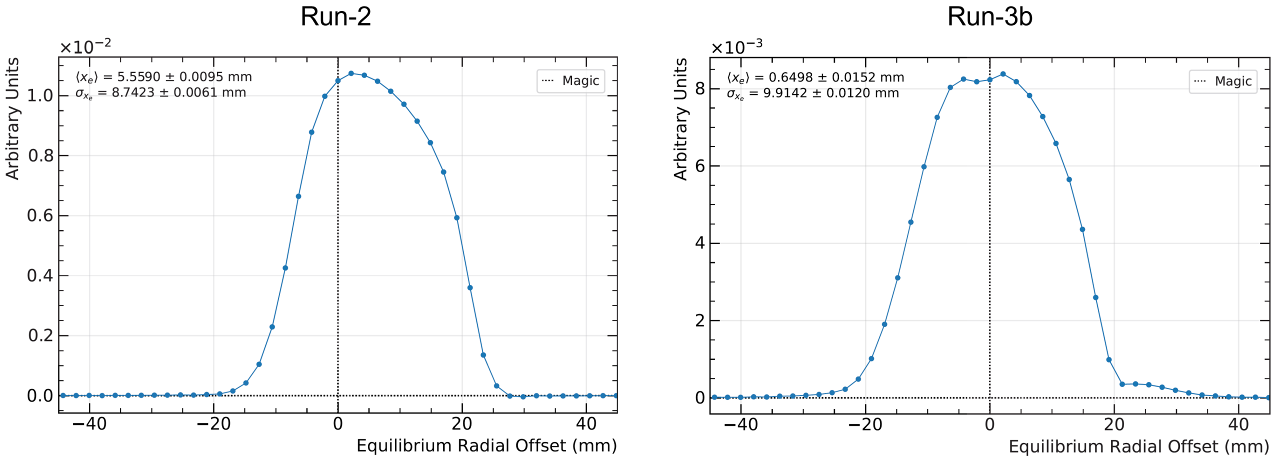

Figure 6.2: Fourier fast rotation distributions resulting from the cosine transform, in terms of equilibrium radius (Eq. 6.2), for Run-2 (left) and Run-3b (right). The Run-3b distribution corresponds to the later part of Run-3 after the kicker strength was increased and the beam was shifted closer to center ($x_e = 0$). Figures courtesy of T. Barret [44].

uses Eq. 6.5 and does not account for this distortion of the frequency reconstruction, leading to an uncertainty in the reconstructed distribution. If the time-momentum (τ-p) correlation were known via the $\rho(\omega, \tau)$ distribution, the weight functions could be analytically calculated and corrected to recover the true frequency distribution. Figure 6.3 shows an example simulated correlation.

The τ-p correlation was the dominant source of uncertainty on the electric field correction C_e and a significant ω_a systematic in Run-1. The uncertainty in Run-1 was determined from simulation by taking the difference between the truth momentum distribution and the FR reconstructed distribution, which is distorted by the correlation. Distributions from two simulations, the *Geant4*-based *gm2ringsim* program and a *BMAD*-based spin tracking program, disagreed on the difference between truth and reconstructed distributions. The τ-p correlation from these simulations was therefore not reliable enough to determine a correction for the FR reconstruction. In the Run-2/3 analysis, several methods to determine the correlation from data and simulation are being explored with the goal of correcting the distortion and reducing the corresponding uncertainty on C_e. Discrepancies are apparent among these methods, and a major effort is underway to characterize the correlation and resolve the discrepancies. Section 6.3 describes a method to characterize the correlation using the MiniSciFi detector.

6.2 MiniSciFi detector

The MiniSciFi (Minimally Intrusive Scintillating Fiber) detector was conceived to directly measure the properties of the stored beam. Its design was based on the proven IBMS detectors, particularly the IBMS3 which profiles

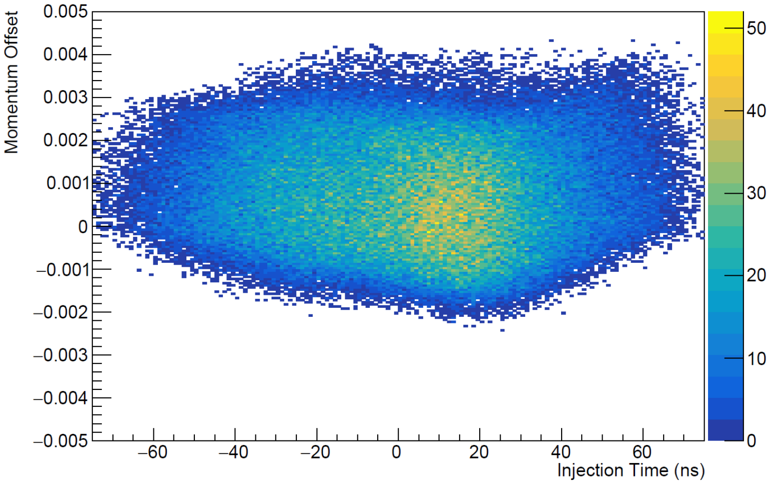

Figure 6.3: The momentum offset from p_0 as a function of injection time, simulated here from the BMAD program under Run-1 conditions, shows the τ-p correlation arising from the time-dependent kick strength. Figure courtesy of T. Barret [79].

the injected beam inside the storage ring. The detector operates in the storage ring vacuum chamber and magnetic field, which imposes design requirements similar to those for IBMS3. The MiniSciFi consists of three scintillating fibers (SciFis) spaced at $26\,\mathrm{mm}$ in one of two different orientations to characterize different beam properties (discussed in Sections 6.2.1 and 6.2.1 and shown in Figure 6.4). The design is optimized for a high-statistics beam measurement with minimal beam disturbance, which is achieved by minimizing the scattering material in the beam. The MiniSciFi has fewer and thinner SciFis than the IBMS, and the frame does not intersect the beam in the measuring position. Each $0.25\,\mathrm{mm}$ diameter SciFi [1] is coupled to a $1.3\,\mathrm{mm}^2$ silicon photomultiplier (SiPM) [2] in an arrangement similar to IBMS3. UW postdoctoral scholar C. Claessens led the MiniSciFi development program.

Previously, fiber harp detectors were used to profile the stored beam, but the fibers disturbed the beam too much for a reliable measurement over the time of the fill. One fiber harp inserted in the stored beam reduces the beam lifetime by $\sim$15% relative to the muon decay time alone [80]. The mechanical system from one fiber harp was adapted for the new MiniSciFi detector, allowing it to be remotely inserted in the stored beam for dedicated measurements with $< 0.1\,\mathrm{mm}$ precision radial positioning, and retracted for nominal running conditions. [3] Two fiber frame assemblies corresponding to each fiber orientation were constructed for interchangeable mounting on the same mechanical system. Figure 6.5 shows the MiniSciFi system before it was installed in the ring.

The SiPMs were selected for their detection efficiency, which is $\sim 3\times$ higher than the IBMS SiPMs, to enable sensitivity to single fiber hits. Each SiPM has 7,300 pixels, providing enough dynamic range to cover the intensity

---

[1] Manufacturer Kuraray

[2] Hamamatsu S14160-1315PS

[3] The system was upgraded with a lead screw and a piezoelectric motor identical to the motor used in the field mapping trolley system, which was known to be nonmagnetic to avoid perturbing the field. This motor was provided by the Argonne Lab group.

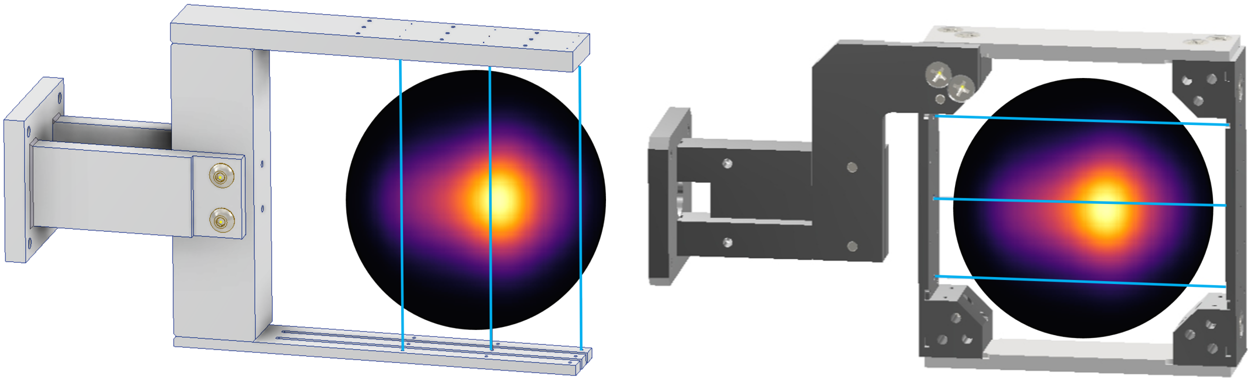

Figure 6.4: The MiniSciFi detector with scintillating fibers in vertical (left) and horizontal (right) orientations. The detector directly measures the stored beam, shown here as a transverse intensity map. CAD models courtesy of R. Roehnelt.

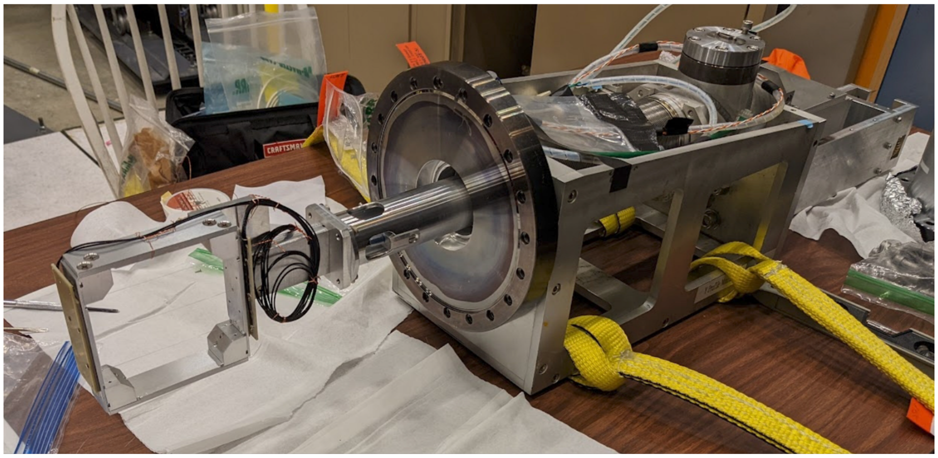

Figure 6.5: The MiniSciFi mechanical system, repurposed and upgraded from one of the fiber harps. The system is installed in the ring with the circular flange mounted on a port of the ring vacuum chamber. The detector (left side) is mounted on an arm to insert into the stored beam for dedicated measurements. Photo courtesy of C. Claessens.

variation over the fill. Four SiPMs are soldered to two boards which each fit on one side of the MiniSciFi fiber frame. The central fiber is coupled to SiPMs at both ends to enable higher-statistics summed signals. The other two fibers are coupled to a single SiPM at one end with reflective Mylar at the other end to increase light collection efficiency. Coax signal cables connect the SiPMs via vacuum feedthrough to readout electronics on the air side. A fifth SiPM on the air side is coupled by an optical fiber to a laser, which allows synchronization with the injected beam pulses and fill-to-fill jitter correction. The MiniSciFi signals are digitized over the time of each fill by a 12-bit waveform digitizer.

The initial electronics design in Run-5 replicated the IBMS3 amplifier electronics, which have a relatively slow response time and are capacitively coupled, causing an "undershoot" in the signal baseline over the $\sim$100 µs timescale of the fill. These effects were characterized to allow for correction in the offline data analysis. In Run-6, the electronics were upgraded to avoid these issues with a faster response time and DC coupling.

6.2.1 Horizontal fibers

The horizontal fiber orientation (Figure 6.4) is designed to measure the stored beam momentum distribution. Each horizontal fiber samples the fast rotation of the beam, and is insensitive to radial beam motion to the extent that the response is uniform along the fiber length. The FR signal produced by each fiber can then be analyzed using the Fourier FR method to reconstruct the momentum distribution. This reconstruction corresponds to a direct measurement of the muon beam distribution, rather than an indirect measurement via the decay positrons. Additionally, the impact of the spatial calorimeter acceptance on the FR reconstruction is not well understood. Directly sampling the beam with a horizontal fiber avoids this complication and provides a cross-check with the calorimeter-measured distribution. The horizontal MiniSciFi was installed at the 270° fiber harp location during Run-5, and was moved to the 180° location later in Run-6 (near the corresponding tracker locations indicated in Figure 2.8).

Simulations using the experiment's *gm2ringsim Geant4*-based software predicted that each stored muon would cross the central fiber ~ 2.8 times [80], resulting in a $\sim 30\times$ higher hit rate than the calorimeters. The simulations also predicted a beam lifetime reduction of $< 2\%$ and a relative beam energy loss of $< 10^{-4}/100\,\mu\mathrm{s}$ in the fill, corresponding to a radial drift of $0.5\,\mathrm{mm}/100\,\mu\mathrm{s}$; this should have negligible effect given the insensitivity to radial beam motion. The standard FR analysis with calorimeter signals requires $\sim 2 \times 10^7$ decay positrons for sufficient statistics, which takes $\sim 1\,\mathrm{h}$ to acquire under normal running conditions. With the more efficient MiniSciFi measurement, comparable statistics can be collected in $\sim 2\,\mathrm{min}$. It also enables systematic measurements under lower-efficiency experimental configurations to be realized in a reasonable time, such as the program to characterize the time-momentum correlation described in Section 6.3.

6.2.2 Vertical fibers

The vertical fiber orientation (Figure 6.4) is designed to directly measure the radial profile of the stored beam with high efficiency. Each vertical fiber samples a radial slice of the beam, and the full stored beam distribution is sampled by positioning the detector in radial steps across the beam. This method enables a beam profile measurement with a minimal number of fibers to minimize beam disturbance. The measured beam profile provides a comparison with the trackers, which reconstruct the beam profile indirectly via decay positron tracks (Section 2.5). The tracker profiles include corrections for resolution, spatial acceptance, and mechanical alignment, which can be cross-checked by comparing with the direct beam profile measurement. The measurement program in Run-6 included a series of measurements under different running conditions which affect the radial beam distribution, e.g. kicker strengths and inflector field strengths, for comparison with simulation. The vertical fibers were also used to characterize a possible upstream time-momentum correlation effect by selecting different momenta at different radial positions, described in Section 6.3.2.

The relative fiber efficiencies are calibrated from the ratio of beam intensities measured by different fibers at the same position in the beam and corrected in the analysis to eliminate acceptance effects, similar to the IBMS calibration procedure. Simulations predicted a relative beam energy loss and corresponding radial drift similar to the horizontal MiniSciFi; this drift requires correction in the analysis. The vertical MiniSciFi was installed in Run-6 at the $180°$ location and later moved to the $270°$ location.

6.3 Characterizing the correlation in time slices

One strategy to characterize the time-momentum (τ-p) correlation is to measure the stored momentum distribution in narrow time slices, effectively breaking the correlation along the injection time axis. A measurement program following this "time-slice" approach was carried out with the horizontal MiniSciFi in Run-5, and the program was expanded in Run-6 with a wider variety of running configurations.

The stored momentum distribution can be expressed in terms of the distribution of injected muons $\rho_0(p,\tau)$ and their ring storage acceptance $\epsilon(p,\tau)$, where both are functions of injection time τ and momentum p.

$$\rho(p) = \int \rho_0(p,\tau)\epsilon(p,\tau)\, d\tau \tag{6.6}$$

The momentum storage acceptance is determined by the time-dependent kick strength and encodes the τ-p correlation for any injected muon distribution. This acceptance can be probed by scanning through kicker delays, as described below. The injected muons' τ and p are uncorrelated to good approximation [4], so $\rho_0(p,\tau)$ can be separated as $\rho_0(p)\rho_0(\tau)$. The injected momentum distribution is much wider than the stored momentum width, as discussed at the beginning of Chapter 5, so $\rho_0(p)$ can be considered flat in the ring-accepted region. The injected distribution can then be reduced to $\rho_0(\tau)$, up to a scale factor.

The acceptance function ϵ for a muon is determined by the kick at the muon's arrival time τ relative to the

---

[4] Technically the delivery ring (Section 2.2) introduces a momentum-dependent path length difference due to its dispersion, but this corresponds to a time of flight difference of only ~ 1 ns per percent δ, much less than the bunch width.

kicker time. For a relative kicker delay time t_k, the stored momentum distribution can be expressed as

$$\rho(p, t_k) = \int \rho_0(\tau)\epsilon(p, \tau, t_k)\, d\tau\,. \tag{6.7}$$

A muon arriving at time τ with zero kicker delay receives the same kick as a muon arriving at $\tau + t_k$ with kicker delay t_k, so $\epsilon(p, \tau, 0) = \epsilon(p, \tau + t_k, t_k)$. The stored distribution can then be equivalently expressed as

$$\rho(p, t_k) = \int \rho_0(\tau + t_k)\epsilon(p, \tau, 0)\, d\tau\,. \tag{6.8}$$

This is a convolution integral, and it shows that a kick delayed by t_k is equivalent to a muon arriving at time $\tau + t_k$ with the original kick time. The acceptance function $\epsilon(p, \tau) \equiv \epsilon(p, \tau, 0)$ can therefore be characterized by scanning through kicker delays. Ideally the injection time distribution would be a delta function, $\rho_0(\tau + t_k) = \delta(\tau + t_k)$, and the convolution would directly yield the acceptance function,

$$\rho(p, t_k) = \epsilon(p, -t_k, 0)\, d\tau\,. \tag{6.9}$$

While a delta function is not possible in reality, the stored distribution most closely recovers the acceptance function with a narrow injection time distribution and is smeared out with wider time distributions. Under nominal conditions, the injection time width is on the same order as the kicker pulse width, as seen in Figure 2.9. Therefore for this measurement approach, the injected beam bunch must be shortened in time, as described in Section 6.3.1.

The time-slice approach for measuring the momentum acceptance can be summarized as follows. First, the injected beam bunches must be shortened in time. The kicker timing is scanned through a range of delays covering the width of the kicker pulse. The stored momentum distribution for each kicker delay t_k can be determined using the FR reconstruction and used to construct the two-dimensional distribution $\rho(p, t_k)$. This is equivalent to convolving the injected distribution with the acceptance function per Eq. 6.8, so the injected bunch $\rho_0(\tau)$ must be deconvolved from $\rho(p, t_k)$ to recover $\epsilon(p, \tau)$. Figure 6.6 shows a *gm2ringsim*-simulated acceptance function and corresponding stored momentum distribution which would be measured in this scan.

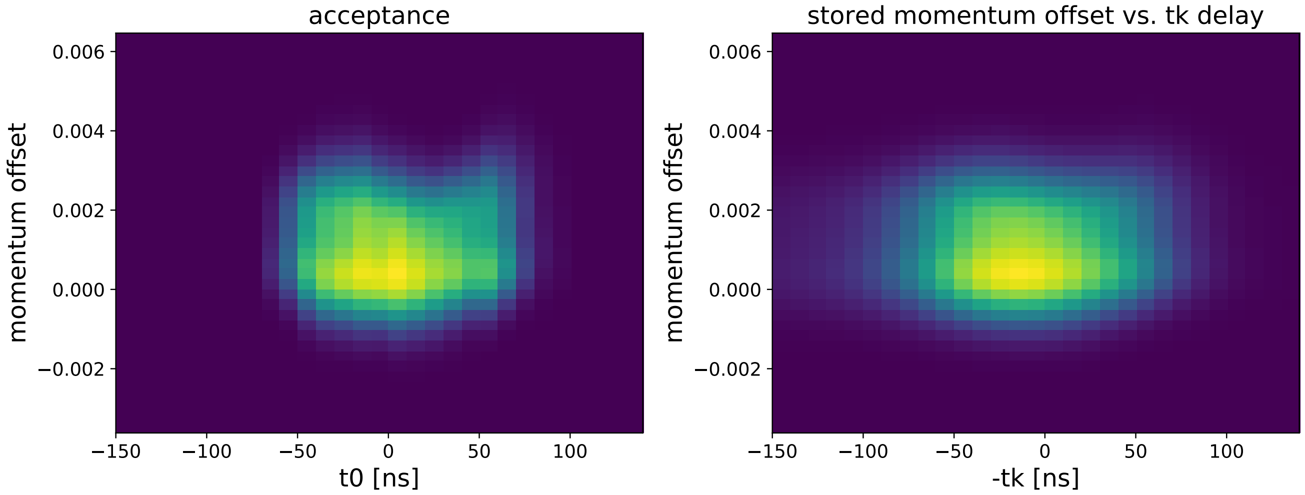

Figure 6.6: Left: Simulated momentum storage acceptance $\epsilon(\delta, \tau)$ determined from the truth storage efficency for each momentum offset δ and injection time τ. Right: Stored momentum distribution $\rho(\delta, t_k)$ constructed by convolving a shortened injected bunch from Figure 6.8 with the simulated acceptance. This is the distribution which would be measured in the kicker timing scan, and the goal is to recover the acceptance by deconvolving the injected bunch.

6.3.1 Creating short bunches

The injected beam bunches are shortened in time by "shaving" away part of the bunch using the abort kicker magnet in the delivery ring (DR), which is typically used to remove protons from the beam (Section 2.2). The delay of this DR abort kicker is reduced so that the kicker pulse partially overlaps the muon bunch, kicking out that part of the bunch (as well as the protons). This reduces the time width of the bunch at the expense of beam intensity. The DR abort kicker has a finite rise time of $\sim$180 ns, which limits the width reduction that can be achieved with this method.

Figure 6.8 shows the short bunches created with this method in Run-6, as recorded by the T0 entrance detector (Section 2.3). The shortest and sharpest distributions are achieved for bunches which have faster rise times and less structure on the early (left) side of the bunch. For these bunches the full-width-half-maximum (FWHM) was reduced from $\sim$80 ns to $\sim$40 ns, depending on the bunch, and the intensity was correspondingly reduced to $\sim 0.2\times$ the original intensity. This intensity reduction increases the time to collect the required statistics, particularly if only the sharpest bunches are selected in the analysis, but the high-efficiency direct MiniSciFi measurements make this possible on a reasonable few-hour timescale. In addition to minimizing the smearing of the acceptance function, the short bunches reduce the τ-p distortion in the FR reconstruction as they sample less of the time-varying $g-2$ kicker pulse than the nominal bunches.

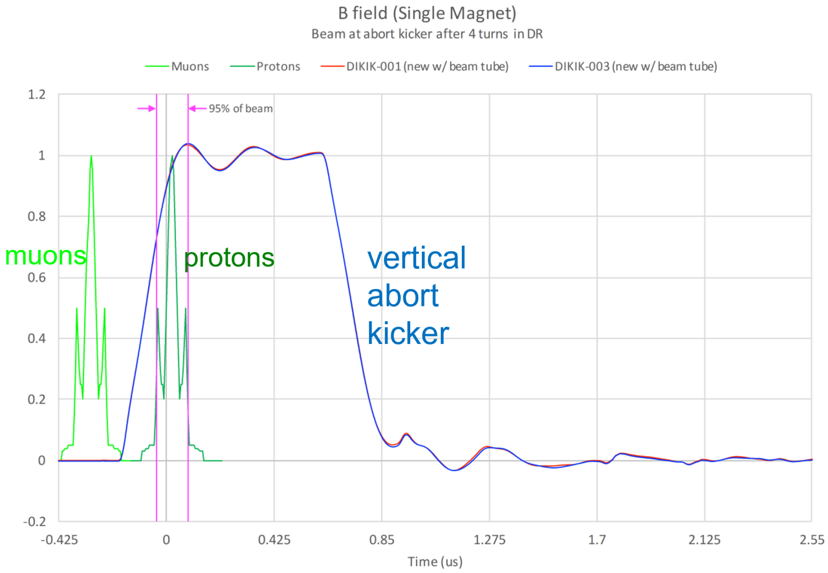

Figure 6.7: The DR abort kicker (blue pulse) is typically used to remove protons from the beam. The nominal delay configuration kicks out the proton bunch (dark green) and does not interact with the muon bunch (light green). Figure courtesy of J. Morgan.

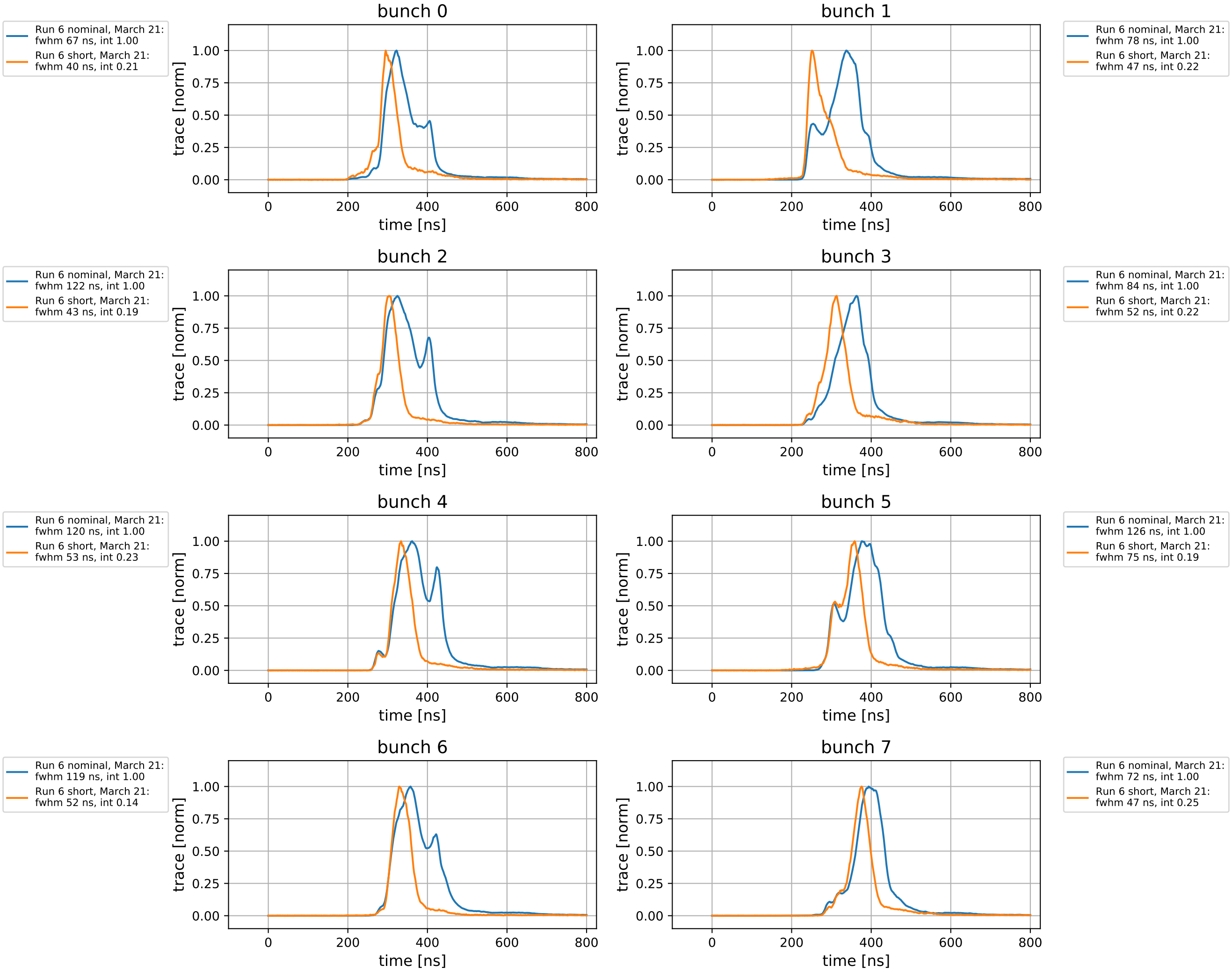

Figure 6.8: Injection time distributions in Run-6 recorded by the T0 detector for nominal bunches (blue) and short bunches (orange) created by shaving with the DR kicker.

6.3.2 Momentum dependence in short bunches

The time slice measurement approach relies on the short bunches having the same phase space and momentum properties as the nominal bunches. The DR abort kicker provides a vertical kick which affects the vertical phase space of the short bunches and does not affect the horizontal phase space. The vertical kick introduces a time dependence that can lead to a τ-p correlation-like effect in the short bunches which is not present in the nominal bunches. If this effect is present, it would require a correction to the acceptance which is measured with the time slice method.

The rising DR kicker edge (Figure 6.7) causes a time-dependent vertical kick when it overlaps the muon bunch, and the kick angle depends on momentum,

$$\Delta y'(t) \propto \frac{B(t)}{p} \approx B(t)\frac{(1-\delta)}{p_0}\,, \tag{6.10}$$

where $\delta = \Delta p/p_0$ is the momentum offset. Low-momentum muons are then kicked out of the beam aperture earlier than high-momentum muons. In particular, a magnetic septum in the DR acts as a collimator with a $41\,\mathrm{mm}$ vertical aperture [36]. Lower-momentum muons would therefore have shorter bunches, which would appear as a τ-p correlation in the short bunches at injection. Additionally, any phase space correlation between momentum and y would affect the momentum dependence of the bunch length. This was expected to be a relatively small few-ns effect over the accepted momentum width, but it had to be measured to determine the impact on the acceptance measurement.

This effect was measured in Run-6 with the vertical MiniSciFi by using the $g-2$ ring as a spectrometer. With the kicker and quadrupoles turned off, the injected beam is dispersively focused at 180° by the magnetic dipole field. Figure 6.9 illustrates the concept with trajectories calculated as follows. Using Eqs. 4.13 and 4.27, the radial trajectory as a function of azimuth θ can be expressed as

$$x(\theta) = R\delta + x_0\cos(\theta) + x_0' R\sin(\theta) \tag{6.11}$$

where the horizontal tune is $\nu_x = 1$ with the quadrupoles turned off, ω is the cyclotron frequency, R is the magic radius, and x_0 and x_0' are the initial injection offset and angle. The x_0 distribution is narrow due to the constraint from the inflector aperture. At 180° each momentum is focused to a unique radius independent of x_0', and the momenta can be selected by the vertical MiniSciFi fibers at the corresponding radial positions. The beam pulse shape in the first turn can be compared for each selected momentum to determine any momentum dependence of the injected bunch shape. The beam cannot be stored in this configuration, so only the first turn can be measured.

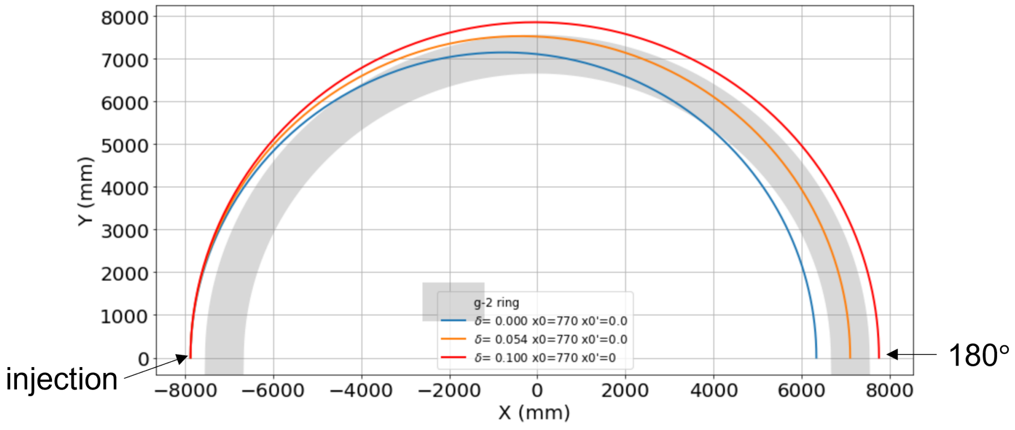

Figure 6.9: Horizontal trajectories (exaggerated $10\times$) for muons with different momenta injected at the same initial position with zero initial angle, with the ring configured at a spectrometer by turning off the kicker and quadrupoles. The blue, orange, and red trajectories correspond to momentum offsets of 0, 0.54%, and 1%, respectively. In this configuration, each momentum is focused to a unique radial position at $180°$.

Figure 6.10 shows the *gm2ringsim*-simulated momentum p vs. radius r on a plane at $180°$ under these conditions. The momenta are well-separated by radius, meaning that momentum slices can be cleanly selected by radial position. With the nominal magic magnetic field B_0, the accepted momentum is offset by $\sim +0.5\%$ from the magic momentum p_0, with a width of $\sim \pm\, 0.4\%$ momentum offset. This measurement should select momenta near p_0 which are stored in nominal conditions, so the magnetic field must be correspondingly reduced by 0.5% to center p_0 near the magic radius as shown in Figure 6.10.

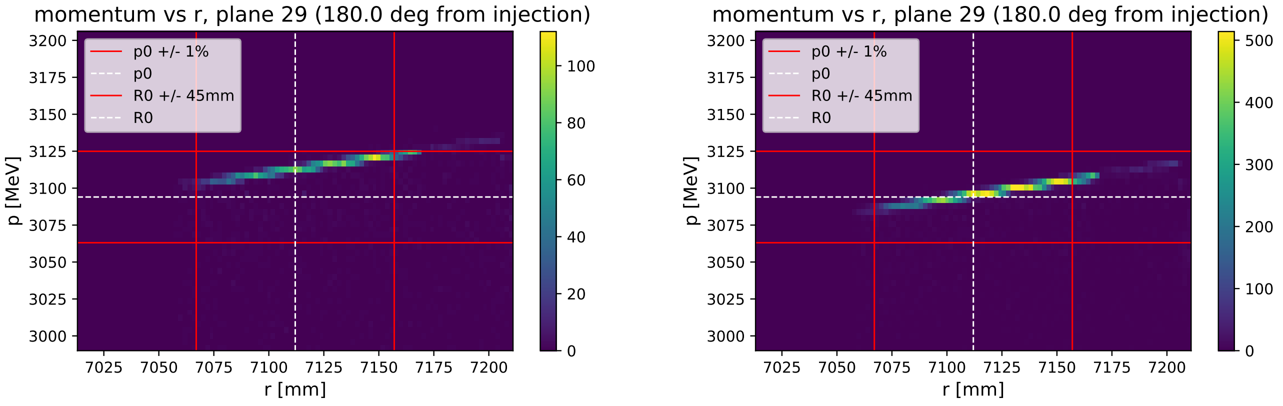

(a) Nominal magnetic field B_0

(b) Magnetic field reduced by 0.5% from B_0

Figure 6.10: Simulated momentum p vs. radial position r on a plane at $180°$, where the ring is configured as a spectrometer with kicker and quadrupoles turned off. At $180°$ the momenta can be selected by radius. To accept the magic momentum p_0, the magnetic field needs to be reduced from nominal (left) by 0.5% (right). The horizontal white line marks p_0, horizontal red lines mark $\pm 1\%$ momentum offset for reference, vertical white line marks the magic radius, and vertical red lines mark the $90\,\mathrm{mm}$ storage region aperture.

Simulations also showed scattering from material outside the storage region, such as the kicker and quad plate supports. High-momentum muons scattering on material at high radii lose energy and drift inward, smearing the p-r distribution and broadening the momenta at each radius. This scattering can be reduced with an inward x' injection angle so that the beam avoids much of the material at high radii. Turning the injection angle more inward by $\sim 5\,\mathrm{mrad}$ significantly reduced the scattering in simulations; this angle can be achieved by reducing the inflector field 2.67% from nominal. The injection angle does not change the dispersive focus, as the x_0' term in Eq. 6.11 is zero at $180°$.

The vertical MiniSciFi was scanned over $104\,\mathrm{mm}$ around the magic radius (slightly past the $90\,\mathrm{mm}$ storage region edges) in three or five steps. Five $13\,\mathrm{mm}$ steps provide nine unique fiber positions, and three $26\,\mathrm{mm}$ steps provide five fiber positions. Higher-than-nominal momenta were measured with the ring field at nominal B_0, and the magic momentum p_0 was measured by reducing the field 0.5% from nominal.

The inflector field was reduced by 2.67% for an inward x' and further reduced by 0.5% when the main field was reduced. The primary purpose was to measure the momentum-selected short bunches; the nominal bunches, which should have no momentum dependence, were measured for comparison.

The following figures show the momentum-selected bunch traces for each fiber at each radial position, with colors corresponding to radius. High (low) momenta correspond to high (low) radii, respectively. The nominal bunches shown in Figure 6.11 have the same pulse width for all momenta, confirming that no momentum dependence is present. Figure 6.12 shows the same comparison for the short bunches, centered at p_0 (with reduced magnetic field) and high momentum (with nominal field). All momenta have essentially the same pulse widths to within $< 5\,\mathrm{ns}$, meaning that no significant momentum-time dependence is introduced by the DR abort kicker. Two conclusions can be drawn from these results. First, under nominal running conditions the τ-p correlation is purely caused by the $g-2$ kicker and is not present in the nominal injected bunches. Second, the short bunch shaving method does not seem to introduce any correlation which would affect the acceptance measured with the short bunches.

There is, however, a possible additional effect from the ring acceptance which would not be captured by this measurement. The DR kicker causes a vertical betatron oscillation corresponding to a time-dependent y-y' perturbation in the transmitted beam. Muons which are accepted by the DR aperture may not fit into the vertical acceptance of the ring aperture, which could cause an additional correlation between momentum and pulse width in the stored beam. Because the spectrometer configuration only measures the beam in the first turn and does not allow the beam to be stored, the effect would not be apparent in this measurement and must be simulated. The beam phase space distribution as a function of DR kicker strength must be generated from realistic beamline simulations,

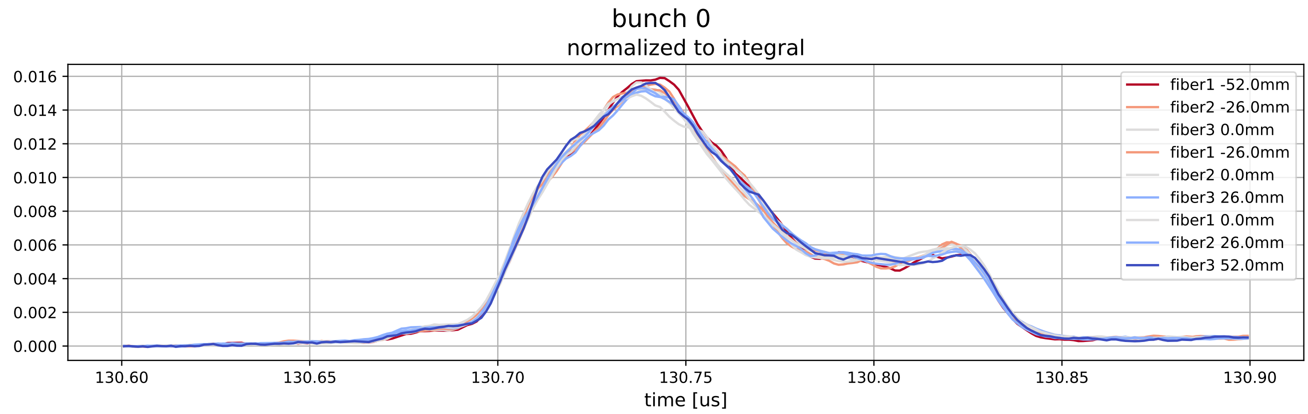

Figure 6.11: Momentum-selected nominal bunch, here showing bunch 0 in the 8-bunch sequence. Traces are measured by each fiber at each radial position and normalized by integral. The accepted momentum is centered at p_0. Red corresponds to low momentum ($\delta = -0.4\%$) and blue corresponds to high momentum ($\delta = +0.4\%$).

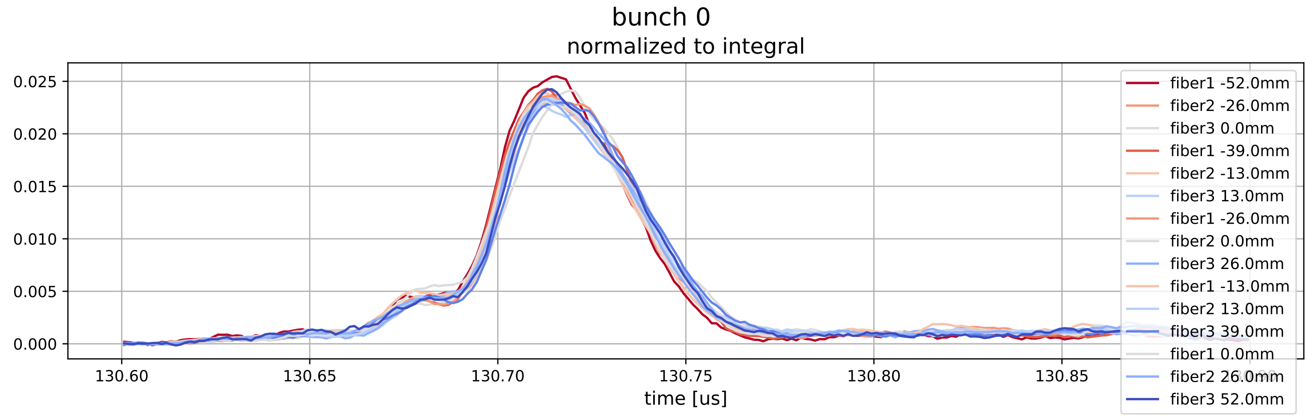

(a) Nominal momentum bite centered at p_0, with $\delta = -0.4\%$ in red and $\delta = +0.4\%$ in blue.

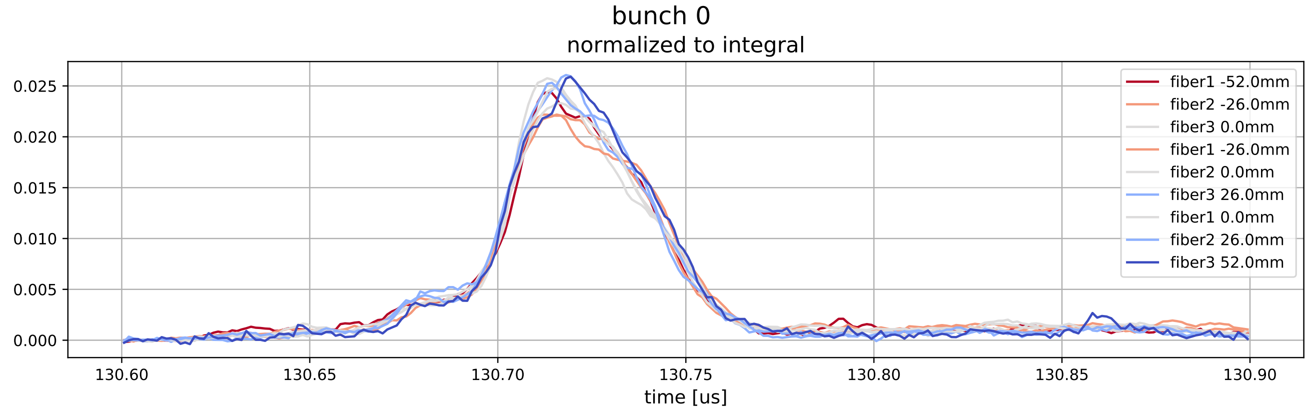

(b) High momentum bite centered at $+0.5\%$ offset, with $\delta = +0.1\%$ in red and $\delta = +0.9\%$ in blue.

Figure 6.12: Momentum-selected short bunch, here showing bunch 0. Fiber traces are normalized by integral. Red corresponds to low momentum and blue corresponds to high momentum.

which can be calibrated against vertical beam profiles at injection measured by the IBMS. The effect on the stored beam can then be simulated in *gm2ringsim* using the beamline simulation output as the initial distribution.

6.3.3 Momentum acceptance measurements

The program to measure the time-sliced momentum acceptance with the horizontal MiniSciFi in Run-5 and Run-6 included different kicker strengths and quadrupole configurations to replicate different running configurations between Run-2 and Run-6. The program also included direct measurements of the nominal fast rotation with nominal beam bunches. Analysis of both the Run-5 and Run-6 measurements is in progress, and selected preliminary results are shown below.

Nominal bunch measurement

Figure 6.13 shows the nominal FR distribution (with nominal bunches and nominal running conditions) measured in Run-5. The signal recorded by the central fiber was corrected by unfolding the measured electronics response, and the FR signals were extracted by dividing out an exponential decay corresponding to the muon lifetime. The FR distribution in terms of the cyclotron frequency was then produced using the standard Fourier FR method (Section 6.1). This nominal measurement establishes a baseline for comparison with calorimeter-measured FR distributions and with the time-slice measurements.

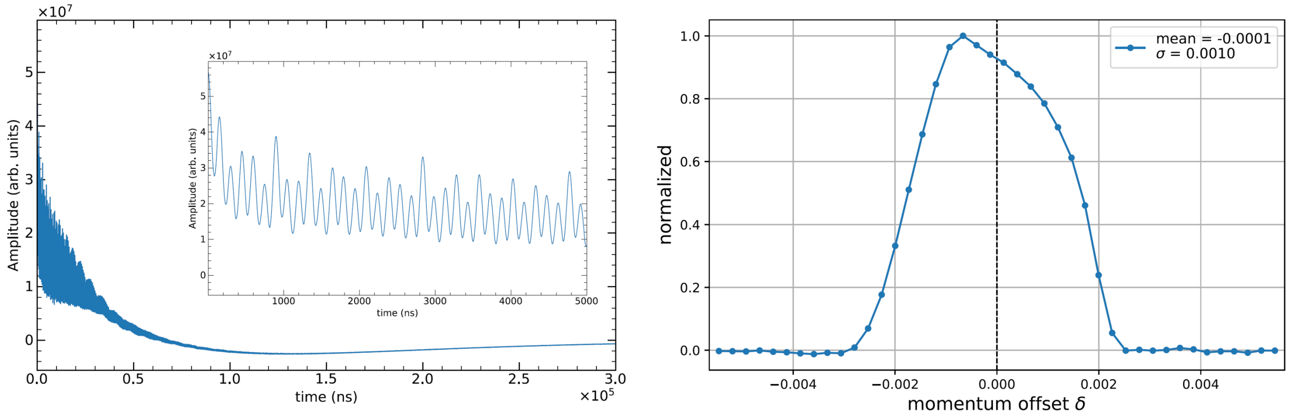

Figure 6.13: Nominal fast rotation measurement with the horizontal MiniSciFi. Left: Response-corrected MiniSciFi signal from which the FR signal is extracted. The 300 μs scale shows the amplitude decaying with muon lifetime, and the shorter 5 μs scale shows the signal oscillating at the cyclotron frequency. Right: Reconstructed FR distribution in terms of momentum offset δ. Preliminary analysis by C. Claessens.

Time-sliced short bunch measurements

The time-sliced acceptance measurements were made by scanning through a range of kicker [5] delays (nominally 11 delays), illustrated in Figure 6.14, and recording MiniSciFi data for $\sim 1\,\mathrm{h}$ per delay. The short bunches are selectively shaved on one side, which changes the mean time of the bunch and the corresponding optimum kicker delay time. The central zero delay point $t_k = 0$ is then defined as the kicker delay which maximizes storage in terms of decay positron counts ("ctags"). The delay scan range was chosen to cover the kicker pulse width by selecting extrema corresponding to $\sim 10\%$ of the maximum ctags, as shown in Figure 6.14.

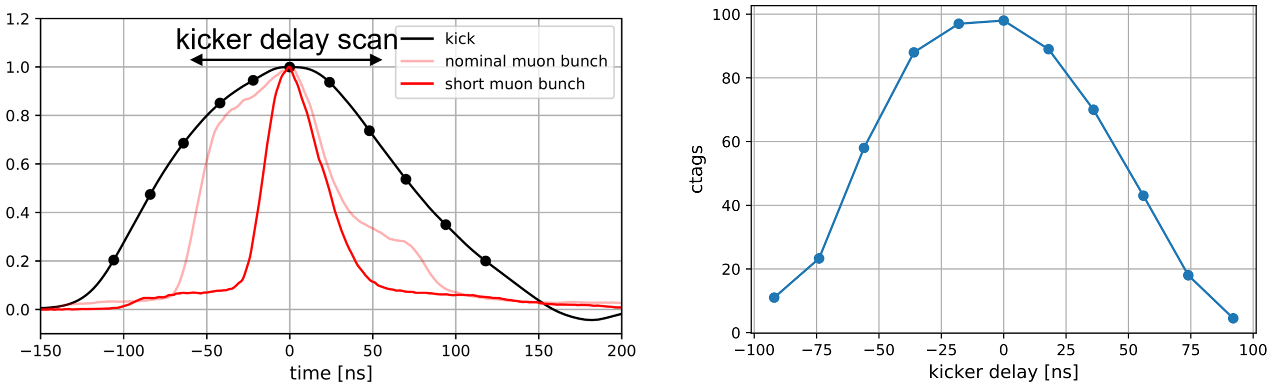

(a) The momentum acceptance due to the kicker is probed with short bunches by scanning through kicker delays (black points, for example). The kicker pulse is shown in black, nominal beam bunch in pink, and short shaved beam bunch in red. The short bunches are necessary to minimize smearing of the kicker response, as the nominal bunch width is on the same order as the kicker pulse width.

(b) Estimated decay positron counts ("ctags") per fill over a kicker delay scan with short bunches. Because the storage efficiency is a function of the kick strength, the shape follows that of the kicker pulse.

Figure 6.14

Figure 6.15 shows selected preliminary results from the Run-6 time-slice acceptance measurement under nominal Run-6 running conditions for several kicker delays. Each FR distribution corresponds to a t_k slice of the $\rho(p, t_k)$ distribution. The central kicker delay measurement at $t_k = 0$ resembles the nominal measurement in Figure 6.13, with differences which can be attributed to the short bunches reducing the distortion from the τ-p correlation. The overall shift and change in shape over t_k shows how the momentum acceptance changes as a result of the time-varying kick.

Moving forward, this analysis looks promising. For each acceptance measurement, the full stored momentum distribution $\rho(p, t_k)$ will be constructed from the FR distributions for all delay points. The acceptance function $\epsilon(p, \tau)$ will be extracted by unfolding the finite-width injection time distribution $\rho_0(\tau)$ from $\rho(p, t_k)$ as discussed

---

[5] "Kicker" refers to the $g-2$ kicker and not the DR abort kicker.

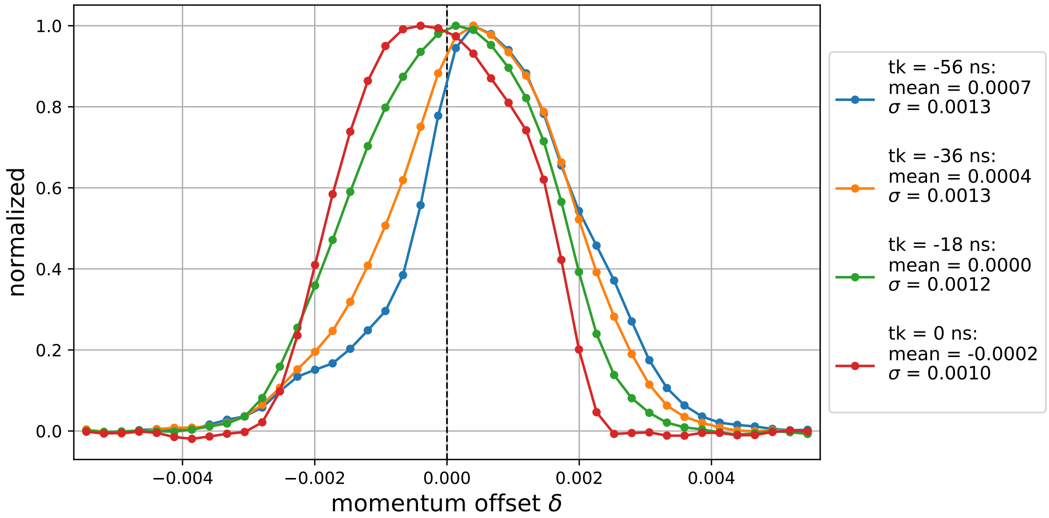

Figure 6.15: FR distributions (in terms of momentum offset δ) measured with short bunches at several kicker delay points. Each distribution corresponds to a t_k slice of the full $\rho(p, t_k)$ distribution. $t_k = 0$ is the central kicker delay and $t_k < 0$ probes the right side of the kicker pulse. Preliminary analysis by C. Claessens.

in Section 6.3. Because each bunch in the sequence of eight bunches has a distinct time distribution (as seen in Figure 6.8), the $\rho(p, t_k)$ reconstruction and unfolding must be done separately for each of the bunches. Future development will include well-known strategies to reduce sensitivity to statistical fluctuations in this unfolding step, which was an apparent challenge in initial simulation studies. Ultimately the extracted acceptance $\epsilon(p, \tau)$ for each measurement configuration can be used to determine the corresponding τ-p correlation, which can be corrected in the standard Fourier FR analysis as discussed in Section 6.1.1.

6.4 Summary

The electric field correction C_e is calculated from the fast rotation (FR) momentum reconstruction, which is an indirect reconstruction from decay positrons in the calorimeters. The uncertainty on C_e is dominated by the time-momentum (τ-p) correlation effect, which is caused by the time-varying kick strength and leads to a distortion in the reconstructed momentum distribution. This was a significant ω_a systematic in Run-1, and efforts are ongoing to reduce this uncertainty.

The MiniSciFi detector directly measures the stored beam properties with minimal disturbance and high efficiency, providing a method to cross-check the FR momentum reconstruction as well as the beam distribution reconstructed by the trackers. The MiniSciFi was installed during Run-5, and reconfigured and reinstalled for further measurements in Run-6. One approach to characterize the τ-p correlation uses short injected muon bunches to probe the momentum storage acceptance in time slices, scanning through kicker delay times and directly measuring the beam fast rotation with the horizontal MiniSciFi. An extensive program to measure the correlation with this method was carried out in Run-5 and Run-6, with significant beam time dedicated to these measurements. The analysis is in progress, but preliminary results show that the stored momentum clearly changes with kick strength. The author plans to continue assisting with this analysis after graduation.

The method to create short bunches by "shaving" with the delivery ring (DR) abort kicker may introduce an effect which would appear like an additional τ-p correlation in the short bunches. This effect was measured with the vertical MiniSciFi by selecting different momenta at different radial positions and comparing their injection time distributions. The DR abort kicker does not seem to introduce correlation in the short bunches which would affect the time-slice correlation measurements. However, a measurement-calibrated simulation is required to verify that this result holds for the stored beam.

The momentum storage acceptance measured with the time-slice method can be used to determine the τ-p correlation. The correlation can then be corrected in the Fourier FR momentum reconstruction, which would significantly reduce the uncertainty on C_e. Characterizing this correlation is critical to reduce this lingering systematic contribution.

Chapter 7

The Muon-Weighted Magnetic Field

The anomalous magnetic moment a_μ is determined as in Eq. 2.17 from the ratio of the muons' anomalous precession frequency ω_a and the NMR proton precession frequency $\tilde{\omega}_p$ in the magnetic field experienced by the muons. With this field $\tilde{B} \propto \tilde{\omega}_p$, a_μ can be expressed as [1]

$$a_\mu \propto \frac{\omega_a}{\tilde{B}} = \frac{\omega_a}{\langle B(x,y,\theta) \times M(x,y,\theta) \rangle} \,. \tag{7.1}$$

The inputs for the muon-weighted magnetic field $\tilde{B}$ are the magnetic field maps (Section 7.2) and the muon beam distributions (Section 7.3), as shown in Figure 7.1. $\tilde{B}$ is calculated by weighting the field multipole moments by the corresponding beam multipole projections (Section 7.4). Systematic uncertainties and corrections in the muon-weighting analysis are discussed in Section 7.5. This chapter presents the muon-weighted field analysis for Run-2/3, with input field maps produced by the Bloch field analysis team. [2] This author analyzed the muon-weighted magnetic field for Run-1 [81] as well as for Run-2/3 [82], but the Run-2/3 analysis is the focus of this chapter.

7.1 Magnetic field experienced by the muons

A single muon following the trajectory $\vec{X}(t)$ will acquire a spin phase ϕ (relative to the initial phase $\phi(t_0)$) until its decay at time t. Defining the time-dependent instantaneous anomalous precession frequency $\omega_a(t')$ from Eq. 7.1,

$$\phi(t) \propto a_\mu \int_{t_0}^{t} B(\vec{X}(t'))dt' \,, \tag{7.2}$$

---

[1] The proportionality factor comprises the corrections in the denominator of Eq. 2.17, and the factors relating ω_p to the magnetic field strength B in Eq. 2.10.

[2] The calculated quantity is called $\tilde{B}$ here, and may be straightforwardly converted to $\tilde{\omega}_p$ as described in Section 2.7.4.

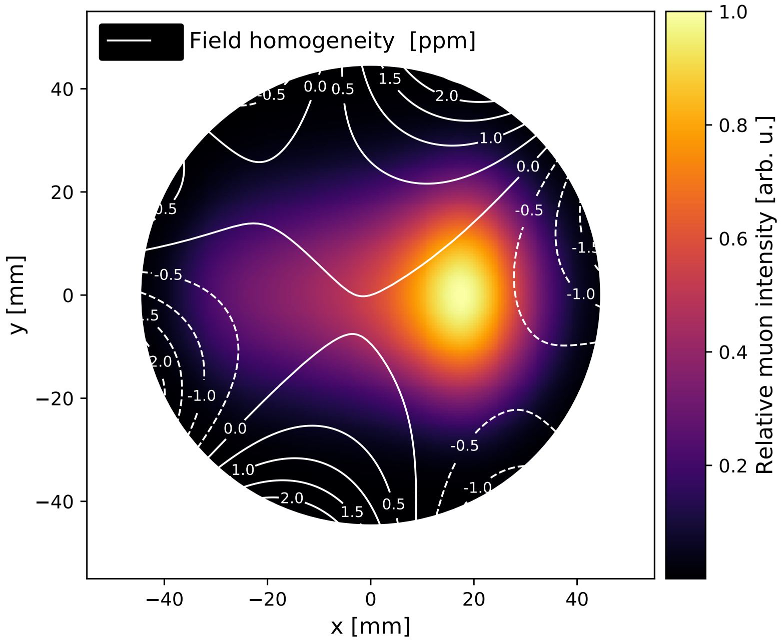

Figure 7.1: The muon-weighted magnetic field $\tilde{B}$ is the average magnetic field weighted by the muon beam distribution. The contours show a typical relative variation of the field strength and the color scale shows a typical distribution of the muon beam intensity in the transverse muon storage region.

where $B(\vec{X}(t'))$ is the magnetic field at the muon's position $\vec{X}(t')$. Equivalently, $\phi(t)$ can be expressed as an integral over the storage ring volume V.

$$\phi(t) \propto a_\mu \int_{t_0}^{t} \int_V B(\vec{x})\delta(\vec{x} - \vec{X}(t))dt'd^3x\,. \tag{7.3}$$

A single muon will sample the magnetic field in the ring over many turns in the fill. Averaging over time in the fill and over the stored muon population, the delta function describing the single muon's trajectory can be replaced by a probability density. The ensemble-averaged phase is then

$$\langle\phi(t)\rangle \propto a_\mu \int_{t_0}^{t} \int_V B(x,y,\theta)M(x,y,\theta,t)dx\,dy\,d\theta\,dt'\,. \tag{7.4}$$

Here the muon position is expressed in the ring coordinates (x, y, θ), with radial coordinate $R + x$, vertical coordinate y, and ring azimuth θ. $R = 7112\,\mathrm{mm}$ is the nominal orbit radius (called the "magic radius") and $y = 0$ defines the vertical midplane of the ring. $M(x,y,\theta,t)$ is the probability density of the muon ensemble in these coordinates.

With M and B independent of time in the fill, ω_a can then be expressed

$$\omega_a \equiv \frac{d\langle\phi(t)\rangle}{dt} \propto a_\mu \int_V B(x,y,\theta)M(x,y,\theta)dx\,dy\,d\theta = a_\mu \tilde{B}\,, \tag{7.5}$$

where $\tilde{B}$ is the muon-weighted magnetic field as in Eq. 7.1. The effect of a possible in-fill time dependence of M is considered as a systematic (Section 7.5).

7.2 Magnetic field

The Run-2/3 Bloch team field analysis produces time-interpolated azimuthal field maps called virtual trolley maps, as described in Section 2.7.3. A virtual trolley map is produced for each few-hour time interval $T_{interval}$ corresponding to the muon beam distributions (Section 7.3), using the fixed probe information corresponding only to times with ω_a data passing data quality cuts [3] and averaged over $T_{interval}$ with decay positron ("ctag") weighting.

The map is interpolated to an equally-spaced azimuthal grid using a spline. Results vary slighty depending on the spline order, so maps are produced from splines of order 1 (linear), 2 (quadratic), and 3 (cubic), shown in Figure 7.2. This variance leads to a few-ppb uncertainty on the muon-weighted field.

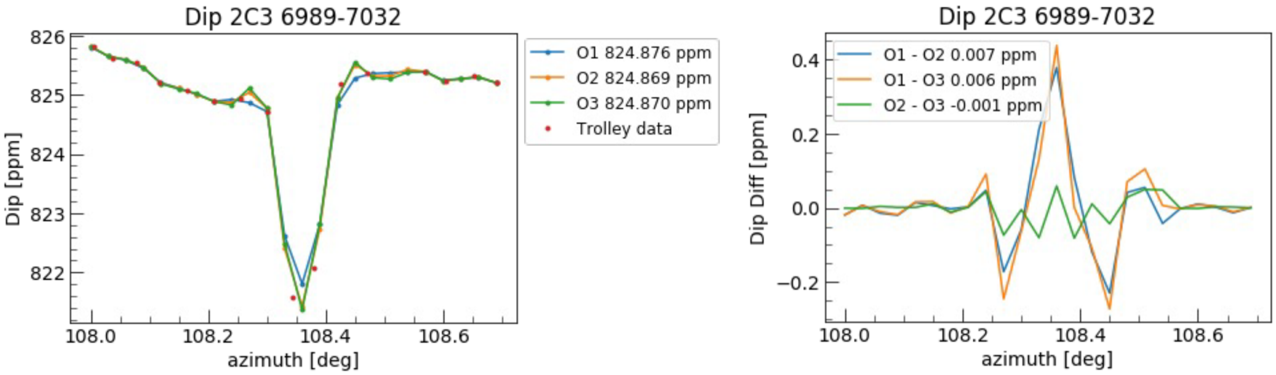

Figure 7.2: Left: Dipole moment virtual trolley map with splines of order 1 (linear), 2 (quadratic), and 3 (cubic). Right: Differences between spline orders. This example shows a region where the spline orders are significantly different, but the difference in the azimuth-average muon-weighted field is only a few ppb. Figure courtesy of S. Charity [83].

As described in Section 2.7.2, field maps are represented in the multipole basis. Table 2.2 shows multipole naming conventions, and Figure 2.23 shows spatial representations of each multipole.

---

[3] Data quality cuts for the ω_a analysis are determined at the subrun level, where subruns are DAQ time intervals of $O(10\,\mathrm{s})$.

7.3 Muon beam distribution

The muon beam distribution varies with azimuth. Muon beam distributions $M(x, y, \theta)$ as a function of transverse coordinates x, y and azimuth θ are reconstructed by extrapolating the tracker profiles around the ring. Tracker distributions are accumulated in time intervals $T_{interval} \approx 2\,\mathrm{h}$ to $3\,\mathrm{h}$ and corrected for detector resolution and acceptance. Each $T_{interval}$ is chosen for sufficient tracker statistics [4] and avoids multiple-hour gaps in the data. Only positrons with decay times between the ω_a analysis start time $t_{start} = 30.2876\,\mu\mathrm{s}$ and end time $t_{end} = 650.0644\,\mu\mathrm{s}$ [49] enter the tracker profiles.

Tracker profiles are extrapolated around the ring according to the following expressions. The extrapolation procedure described in Section 7.3.3 fixes the beam RMS widths and means to the tracker measurements at the corresponding azimuthal locations (Section 7.3.5). Examples are shown in Section 7.3.4. The relationship between the beam widths and means and the multipoles is discussed in Sections 7.4.1 and 7.4.2.

7.3.1 Beam width

The width of the beam distribution varies with azimuth due to betatron oscillations and dispersion (Section 4.3). The average RMS width is the quadrature sum of the betatron amplitude and dispersion.

$$x_{rms}(\theta) = \sqrt{\epsilon_x \beta_x(\theta) + D_x^2(\theta)\delta_{rms}^2} \tag{7.6}$$

$$y_{rms}(\theta) = \sqrt{\epsilon_y \beta_y(\theta)} \tag{7.7}$$

The beta functions $\beta_x(\theta)$, $\beta_y(\theta)$ and dispersion $D_x(\theta)$ come from the COSY beam dynamics model with representative magnetic and electric storage ring fields. These functions vary with azimuth due to the discrete electric quadrupoles. The momentum deviation $\delta = \Delta p/p_0$ is determined from the reconstructed momentum distributions from the Fourier fast rotation analysis described in Section 6.1 (with mean and RMS deviation $\langle\delta\rangle$ and δ_{rms}, shown in Table 7.1). Uncertainties on δ from the fast rotation analysis are considered in Section 7.5.5.

The emittances ϵ_x, ϵ_y are calculated from the measured tracker profile widths $x_{rms}(\theta_{tkr})$, $y_{rms}(\theta_{tkr})$.

$$\epsilon_x = \frac{1}{\beta_x(\theta_{tkr})}\left(x_{rms}^2(\theta_{tkr}) - D_x^2(\theta_{tkr})\delta_{rms}^2\right) \tag{7.8}$$

$$\epsilon_y = \frac{1}{\beta_y(\theta_{tkr})}\left(y_{rms}^2(\theta_{tkr})\right) \tag{7.9}$$

---

[4] $\geq 6 \times 10^5$ total tracks, more than sufficient to minimize statistical uncertainty

7.3.2 Beam mean

The beam mean position varies with azimuth due to closed orbit distortions and dispersion.

$$x_{mean}(\theta) = x_{COD}(\theta) + D_x(\theta)\langle\delta\rangle \tag{7.10}$$

$$y_{mean}(\theta) = 0 \tag{7.11}$$

The equilibrium radius $x_{eq}(\theta) = D_x(\theta)\langle\delta\rangle$ is offset from the magic radius due to the mean momentum deviation $\langle\delta\rangle$, and varies with azimuth due to the variation of the dispersion. Closed orbit distortions (COD) shift the closed orbit away from the equilibrium position. Azimuthal variation in the magnetic dipole field causes a radial COD (Section 4.3.3), which can be written as the dominant $N = 1$ term of a Fourier series.

$$x_{COD}(\theta) \approx -\frac{R}{\nu_x^2 - 1}\frac{b_1(m_1)}{B_0}\cos(\theta + \theta_1(m_1)) \tag{7.12}$$

Here $R = 7112\,\mathrm{mm}$ is the magic radius and B_0 is the nominal field. $\nu_x = \sqrt{1-n}$ is the horizontal tune for an effective field index n (shown in Table 7.1). $b_1(m_1)$ and $\theta_1(m_1)$ are the Fourier amplitude and phase of the magnetic dipole m_1 vs. azimuth. The Fourier components are extracted with a fast Fourier transform (FFT) from field maps in each $T_{interval}$, and x_{COD} is calculated for each individual $T_{interval}$. The FFT treats samples as equally-spaced, and uses field maps which are spline-interpolated (Section 7.2) to 12k equally-spaced azimuthal points.

	Run-2	**Run-3a**	**Run-3b**
mean momentum deviation $\langle\delta\rangle$	0.00069	0.00060	0.00008
RMS momentum deviation δ_{rms}	0.00109	0.00112	0.00124
effective field index n	0.10801	0.10749	0.10762

Table 7.1: Average momentum deviation (mean and RMS) and effective field index n in each run, provided from the fast rotation analysis. (n values are taken from coherent betatron oscillation fits in the analysis.)

An azimuthally-varying radial magnetic dipole field would cause a vertical COD. Because the radial field dependence on azimuth is not measured during the experiment, y_{COD} is set to zero and considered separately as a systematic (Section 7.5.4).

Misalignments of the electric quadrupole plates also cause radial and vertical CODs by steering the beam. These are considered separately as a systematic (Section 7.5.4).

7.3.3 Beam profile reconstruction

Muon beam distributions $M(x, y, \theta)$ are reconstructed by shifting and scaling the tracker profiles to account for the azimuthal dependence of the transverse beam profile. Beam RMS widths and means are fixed to the tracker measurements at the corresponding azimuthal locations (defined in Section 7.3.5). Each tracker station is extrapolated separately, then the reconstructed distributions from both stations are summed to get the nominal beam distribution.

Profiles are shifted by the $x_{mean}(\theta)$ and $y_{mean}(\theta)$ defined in Eq. 7.10, and scaled by width factors κ_x, κ_y calculated from the x_{rms} and y_{rms} defined in Eq. 7.6. For each tracker station,

$$\kappa_x^{tkr}(\theta) = \frac{x_{RMS}(\theta)}{x_{RMS}(\theta_{tkr})} \tag{7.13}$$

$$\kappa_y^{tkr}(\theta) = \frac{y_{RMS}(\theta)}{y_{RMS}(\theta_{tkr})} \tag{7.14}$$

The beam profile as a function of azimuth is reconstructed in seventy-two $5°$ bins centered at θ_j. Beam profiles consist of a 2D histogram for each θ_j bin. The 2D tracker profile histograms $M_{tkr}(x, y)$ are transformed to $M_{tkr}\left(x(\theta), y(\theta), \theta\right)$ by shifting and scaling in x , y using a linear interpolation method. The measured tracker profile means $\bar{x}_{mean}$ and $\bar{y}_{mean}$ are subtracted from x and y before scaling with the width factors in Eqs. 7.13 and 7.14. Then the x profile is shifted relative to $\bar{x}_{mean}$ by $x_{mean}(\theta)$, and the y profile is shifted back to $\bar{y}_{mean}$.

$$x(\theta_j) = \kappa_x^{tkr}(\theta_j)\left(x - \bar{x}_{mean}(\theta_{tkr})\right) + \bar{x}_{mean}(\theta_{tkr}) + \underbrace{x_{mean}(\theta_j) - x_{mean}(\theta_{tkr})}_{\substack{x_{COD}(\theta_j) + D_x(\theta_j)\langle\delta\rangle \\ -x_{COD}(\theta_{tkr}) - D_x(\theta_{tkr})\langle\delta\rangle}} \tag{7.15}$$

$$y(\theta_j) = \kappa_y^{tkr}(\theta_j)\ \left(y - \bar{y}_{mean}(\theta_{tkr})\right) + \bar{y}_{mean}(\theta_{tkr}) \tag{7.16}$$

The nominal beam profile is the sum of the profiles from both stations.

$$M(x, y, \theta_j) \equiv M_{12}(x, y, \theta_j) + M_{18}(x, y, \theta_j) \tag{7.17}$$

7.3.4 Example beam profiles

Figure 7.3 shows example tracker profiles and projections and Figure 7.4 shows example reconstructed beam profiles from each run. The closed orbit distortion (COD), and corresponding variation in $x_{mean}(\theta)$, was reduced in Run-3 compared to Run-2 due to reduced azimuthal variation of the dipole field from magnet shimming. The COD variation over time was also reduced in Run-3 due to improved temperature stability from hall cooling. In Run-3b, the overall x_{mean} and the oscillation due to dispersion are reduced due to the increased kick strength, which reduced the momentum deviation $\langle\delta\rangle$.

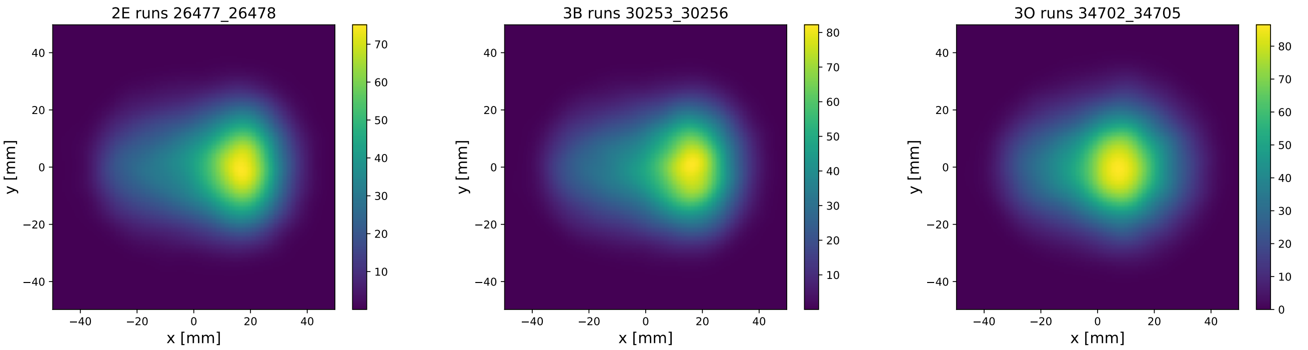

(a) Run-2 (from dataset DS-2E) **(b)** Run-3a (from dataset DS-3B) **(c)** Run-3b (from dataset DS-3O)

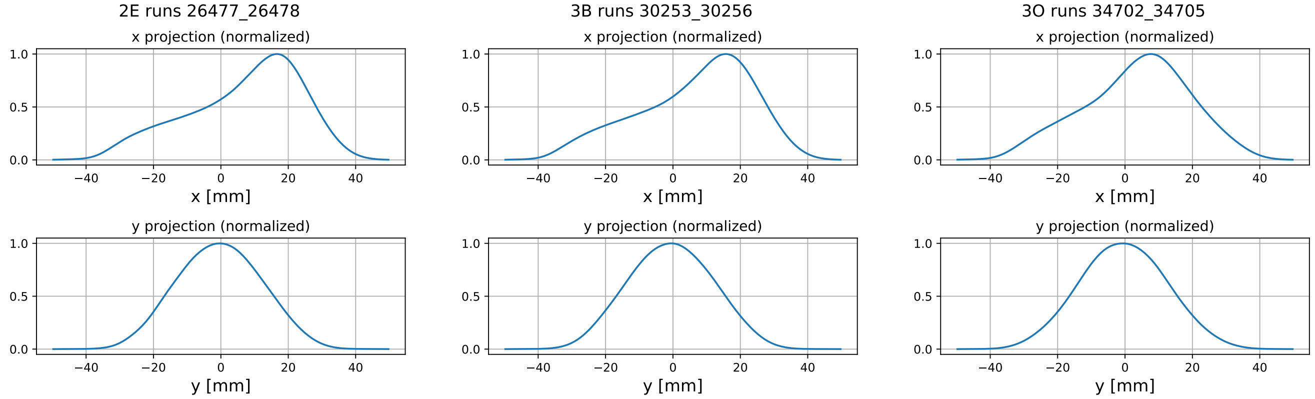

(d) Run-2 (from dataset DS-2E) **(e)** Run-3a (from dataset DS-3B) **(f)** Run-3b (from dataset DS-3O)

Figure 7.3: Tracker profiles from station 12 and x, y projections for example time intervals in Run-2, Run-3a, and Run-3b.

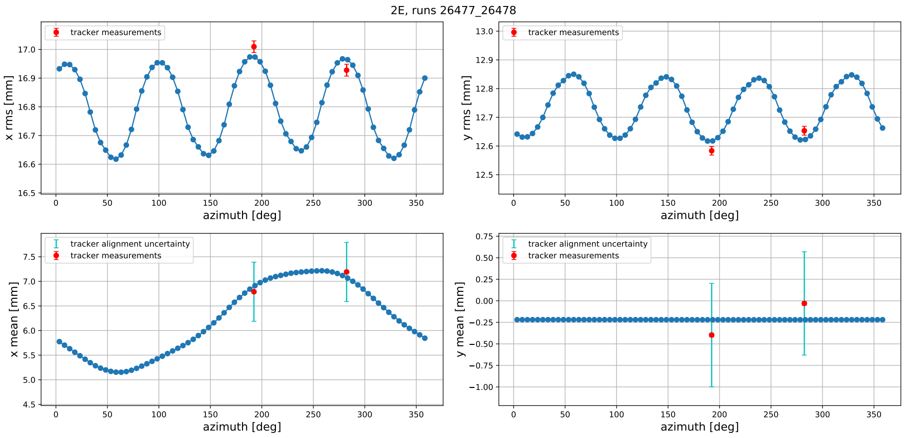

(a) Run-2 (from dataset DS-2E)

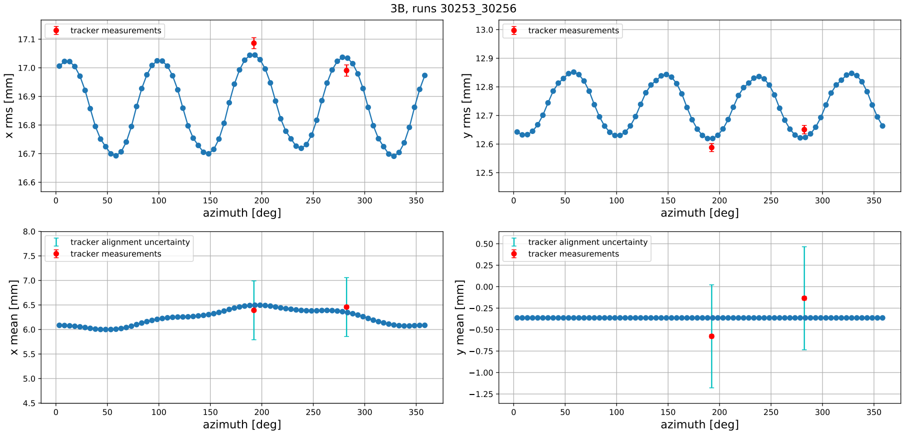

(b) Run-3a (from dataset DS-3B)

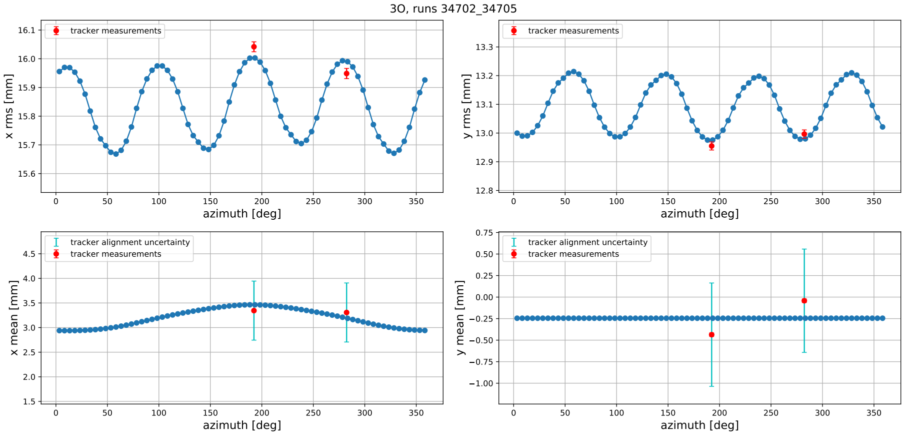

(c) Run-3b (from dataset DS-3O)

Figure 7.4: Reconstructed beam profiles for example time intervals in Run-2, Run-3a, and Run-3b. The red points show tracker measurements (with statistical error bars) used to reconstruct the azimuthal profiles. The cyan error bars on the means show the $0.6\,\mathrm{mm}$ tracker alignment uncertainty. The profiles in blue are the sum of those reconstructed from each tracker, which would each match the corresponding red measurement. The agreement of the means between stations is well within the tracker alignment uncertainty. The $x_{mean}(\theta)$ variation due to the closed orbit distortion caused by dipole field variation is reduced in Run-3 compared to Run-2. The overall x_{mean} is reduced in Run-3b with the increased kick strength. y_{mean} is treated as constant; the vertical closed orbit distortion is set to zero and treated as an uncertainty.

7.3.5 Azimuthal coordinate system

The field azimuthal coordinate system references the ring 12 o'clock position at the center of yoke A (see Figures 2.8 and 4.6). The COSY model and beam dynamics functions reference the upstream edge of the electric quadrupole Q1S, which is 33.35° downstream of the field reference. Beam distributions are reconstructed in the COSY θ coordinates; beam multipole projections are converted to field θ coordinates for the muon weighting analysis. Unless otherwise noted, all θ positions are in field coordinates.

The tracker stations (12, 18) have mean sensitivity at $(\theta_{12} \approx 192.3^\circ,\, \theta_{18} \approx 282.4^\circ)$ in field coordinates. The trackers have narrow RMS azimuthal sensitivity $(\sigma_{12} \approx 4.9^\circ,\, \sigma_{18} \approx 4.8^\circ)$, so the distributions are treated as localized at $(\theta_{12},\, \theta_{18})$.

7.4 Muon weighting

The muon-weighted field $\tilde{B}$ is defined as the field map weighted by the muon distribution. Because the Run-2/3 Bloch team field analysis produces azimuthal field maps, the baseline muon weighting procedure is defined as a function of azimuth. [5]

$$\tilde{B} = \langle MB \rangle_\theta = \frac{\int_A dx\, dy \int_{2\pi} d\theta\, M(x,y,\theta) B(x,y,\theta)}{\int_A dx\, dy \int_{2\pi} d\theta\, M(x,y,\theta)} \approx \langle \tilde{B}_{2D}(\theta_j) \rangle_\theta \tag{7.18}$$

where A is the $45\,\mathrm{mm}$ radius transverse muon storage region, x, y are the transverse coordinates, θ is the azimuth, $M(x,y,\theta)$ is the reconstructed muon distribution, and $B(x,y,\theta)$ is the azimuthal field map. $\tilde{B}$ is calculated in each time interval $T_{interval}$ using M and B in the same $T_{interval}$. ($T_{interval}$ is implicit in the following references to M and B.)

$\tilde{B}$ is approximated as the average of the 2D weighted field $\tilde{B}_{2D}$ over the azimuthal bins θ_j defined by the reconstructed beam distribution. In the following expressions, $M(x,y)$ and $B(x,y)$ are implicitly defined in a given θ_j bin (but θ_j is left out for simplicity.)

$$\tilde{B}_{2D} = \frac{\int_A M(x,y) B(x,y)\, dx\, dy}{\int_A M(x,y)\, dx\, dy} \tag{7.19}$$

Replacing $B(x,y)$ with the multipole expansion in Section 2.7.2 and rearranging,

$$\tilde{B}_{2D} = \frac{\sum_{i=1}^{N_{max}} m_i \int_A M(x,y) f_i(x,y)\, dx\, dy}{\int_A M(x,y)\, dx\, dy} \equiv \sum_{i=1}^{N_{max}} m_i k_i\,, \tag{7.20}$$

where the polar coordinates r, Θ have been converted to x, y in $f_i(x,y)$. N_{max} is the maximum multipole order included in the sum, nominally $N_{max} = 12$.[6] Then $\tilde{B}$ is determined by averaging $\tilde{B}_{2D}$ over the azimuthal bins.

$$\tilde{B} = \langle \sum_{i=1}^{N_{max}} m_i(\theta_j) k_i(\theta_j) \rangle_\theta \tag{7.21}$$

The coefficients k_i are multipole projections of the muon distribution. The k_i give the fractional contribution of

---

[5] This was an update from Run-1 analysis, which produced azimuth-averaged field maps. In Run-1, the azimuthal interference effects had to be evaluated separately.

[6] This was an update from Run-1 analysis which used $N_{max} = 9$; trolley multipole fitting residuals were found to be minimized by including higher-order moments up to $N_{max} = 12$. The S_{14} moment (m_{13}) is set to zero. [51].

each field moment to the total weighted field $\tilde{B}$.

$$k_i \equiv \frac{\int_A M(x,y) f_i(x,y) dx\, dy}{\int_A M(x,y) dx\, dy} \tag{7.22}$$

In each 5° bin centered at θ_j, multipole projections $k_i(\theta_j)$ are extracted from the beam profile as in Eq.(7.22). The dipole moment weight k_1 is equal to 1 by definition. In practice the k_i integration range is $-45\,\mathrm{mm}$ to $45\,\mathrm{mm}$ in x and y.

Each virtual trolley moment m_i is averaged in bins θ_j by sampling the spline function (Section 7.2) with 100k samples per bin (effectively integrating the function), then averaging over the bin. This process is repeated for splines of order 1, 2, and 3, representing different possible field distributions between trolley samples. The central $\tilde{B}$ value is calculated from the average result over the spline orders, and the variance in spline orders is assigned as an uncertainty from azimuthal averaging (Section 7.5.1).

Figure 7.5 shows the procedure to calculate $\tilde{B}$ described by Eq. 7.21. Features of the beam projections are discussed in Sections 7.4.1 and 7.4.2.

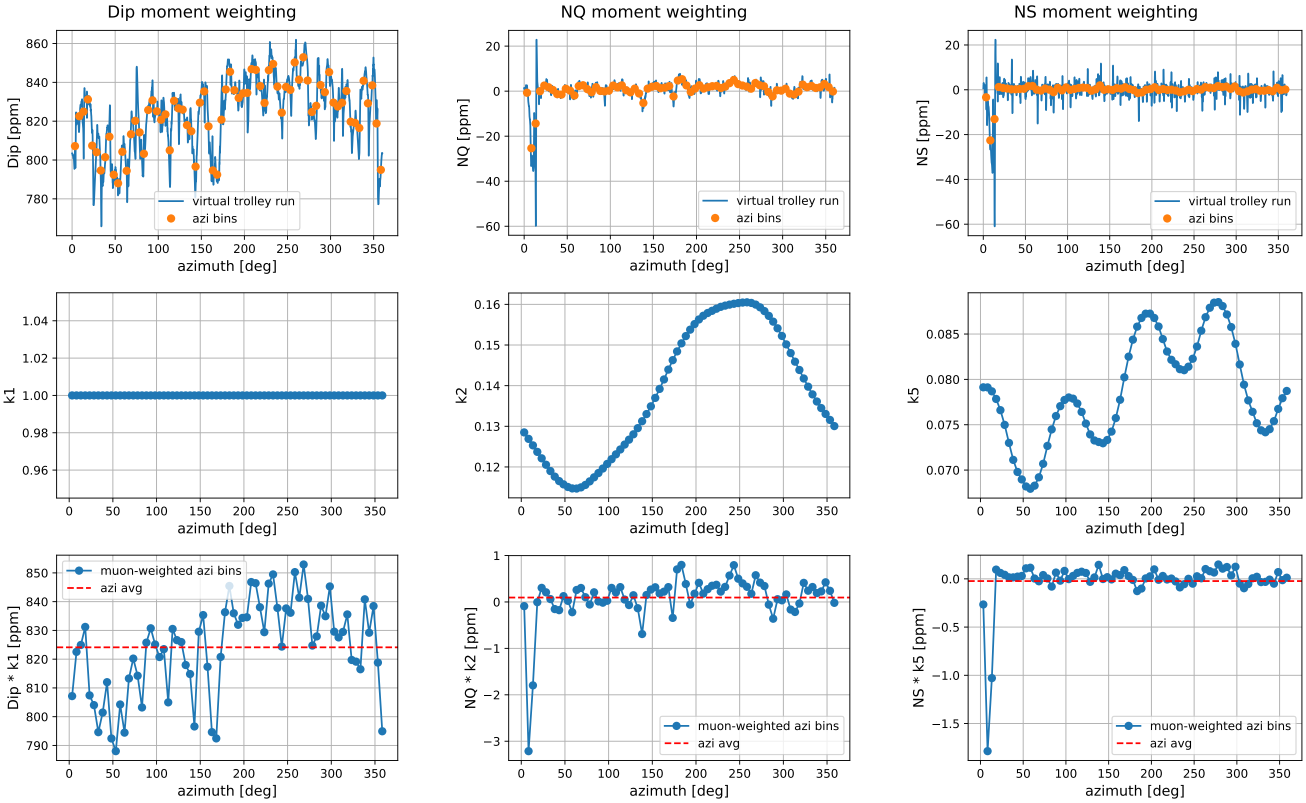

Figure 7.5: Muon weighting procedure for an example time interval in Run-2. The dominant contributions to the total weighted field (Dip, NQ, and NS moments) are shown. Top: The virtual trolley map (blue) is averaged in bins θ_j to get $m_i(\theta)$ (orange). Center: Beam projections $k_i(\theta)$ in the same θ_j bins. Bottom: The muon-weighted moment is the product of $m_i(\theta)$ and $k_i(\theta)$, which is then averaged in θ (red line).

7.4.1 Results

Figures 7.6 and 7.7 show the $\tilde{B}$ results for Run-2 and Run-3, with a breakdown of the individual multipole moment contributions and beam multipole projections. Table 7.2 shows run-average beam multipole projections. All run-averaged values are ctag-weighted averages, calculated with decay positrons ("ctags") in each time interval as weights. The NQ projection (k_2) couples mainly to the beam x_{mean}, and the NS projection (k_5) couples to both the beam x_{rms} and x_{mean}. These beam projections are dominant due to the radial asymmetry of the beam, and the NQ and NS moments are therefore the dominant multipole contributions to the muon-weighted field. In Run-3b when the beam is more radially centered, the NQ and NS beam projections are reduced.

	Run-2	**Run-3a**	**Run-3b**
Dip (k_1)	1.000	1.000	1.000
NQ (k_2)	0.139	0.136	0.073
SQ (k_3)	-0.001	-0.006	-0.005
SS (k_4)	0.001	-0.001	0.000
NS (k_5)	0.081	0.076	0.046
SO (k_6)	0.000	-0.001	0.000
NO (k_7)	-0.001	-0.001	-0.006
ND (k_8)	-0.002	-0.001	0.003
SD (k_9)	0.001	0.001	0.000
N12 (k_{10})	-0.004	-0.003	0.001
S12 (k_{11})	0.000	0.000	0.000
N14 (k_{12})	-0.001	-0.001	0.001
S14 (k_{13})	0.000	0.000	0.000

Table 7.2: Average beam multipole projections in each run (averaged over the run with ctag weighting). Projections are normalized to beam profile intensity and are unitless.

Table 7.3 shows run-average multipole contributions to the total muon-weighted field $\tilde{B}$. The weighted NQ moment is dominant in each run. In Run-2 the NQ and NS moments have opposite signs but the weighted NQ contribution is larger and dominates the total multipole contribution. In Run-3 the magnet temperature was better controlled due to improved cooling in the experimental hall, reducing variation of the field moments over time. In Run-3a the NQ and NS moments have opposite signs and reduced magnitudes from Run-2. In Run-3b, the NQ and NS moments have the same signs as in Run-2, and the muon-weighted contributions are further reduced both due to the reduced field moments and the better-centered beam.

	Run-2	**Run-3a**	**Run-3b**
Total contribution from all multipoles (ppb)	47.4	-6.9	2.6
NQ ($k_2 m_2$) (ppb)	66.1	-10.2	4.0
SQ ($k_3 m_3$) (ppb)	-0.2	0	0.2
SS ($k_4 m_4$) (ppb)	0.5	0	0.1
NS ($k_5 m_5$) (ppb)	-24.5	0.7	-0.4
SO ($k_6 m_6$) (ppb)	0.1	-0.1	-0.1
NO ($k_7 m_7$) (ppb)	1.5	0.1	0.2
ND ($k_8 m_8$) (ppb)	-0.4	-0.4	-0.3
SD ($k_9 m_9$) (ppb)	0	0	0
N12 ($k_{10} m_{10}$) (ppb)	3.0	2.3	-0.4
S12 ($k_{11} m_{11}$) (ppb)	0	0	0.1
N14 ($k_{12} m_{12}$) (ppb)	1.4	0.6	-0.7
S14 ($k_{13} m_{13}$) (ppb)	0	0	0

Table 7.3: Muon-weighted multipole contributions to $\tilde{B}$ in each run (averaged over the run with ctag weighting), with $k_i m_i$ as shorthand for $\langle k_i(\theta_j) m_i(\theta_j) \rangle_\theta$. The sum of all multipole contributions is shown at the top. Contributions of < 0.05 ppb are shown as zero.

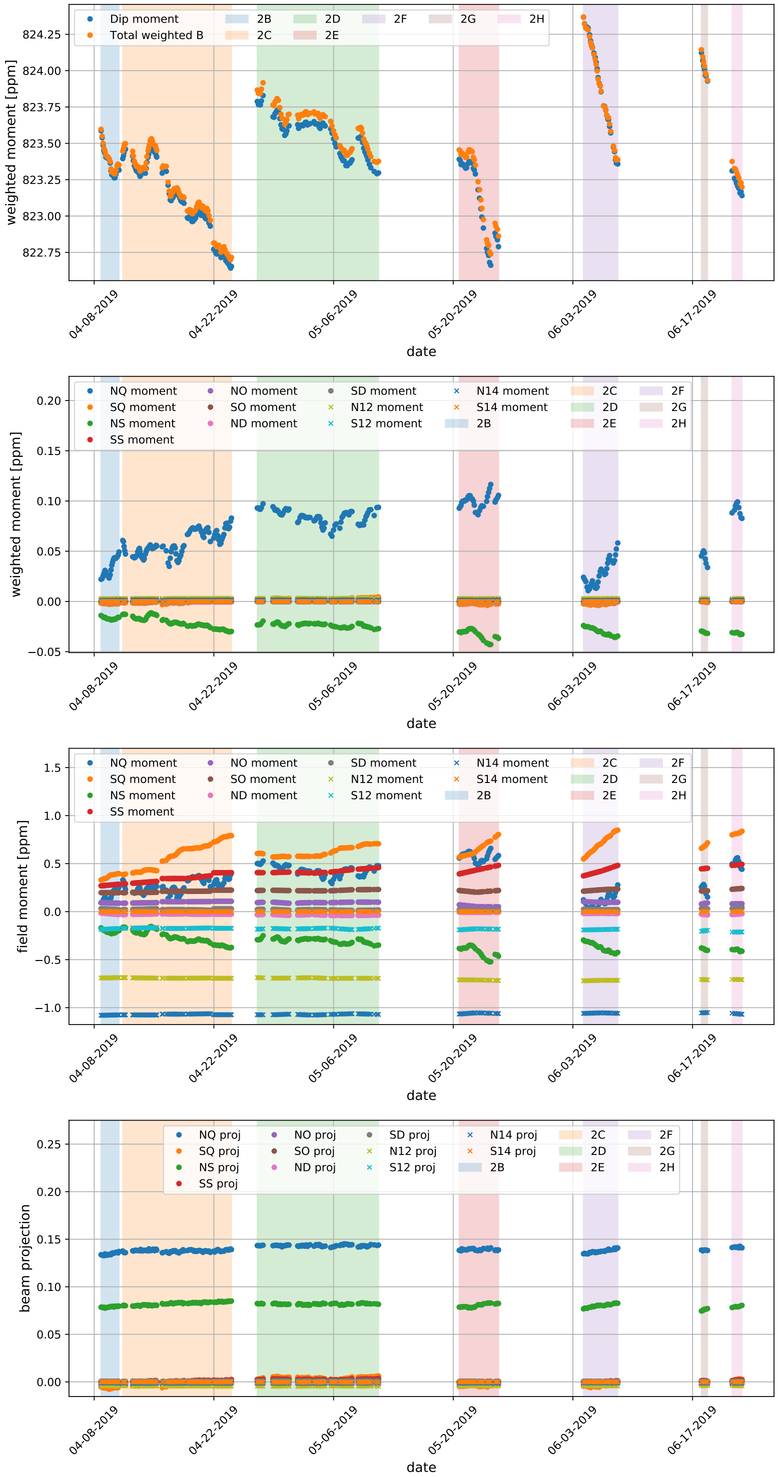

Figure 7.6: Baseline muon-weighted field results for Run-2. Colored bands indicate datasets. Top plot: Azimuth-average dipole moment (blue) and total weighted field including contributions from muon-weighted multipole moments (orange). Second plot: Individual muon-weighted multipole moment contributions, $\langle k_i(\theta_j) m_i(\theta_j) \rangle_\theta$. Third plot: Unweighted azimuth-average field multipole moments m_i. Bottom plot: Azimuth-average beam multipole projections k_i. The time variation of the muon-weighted moments is mainly due to variation of the field; the beam projections are relatively stable.

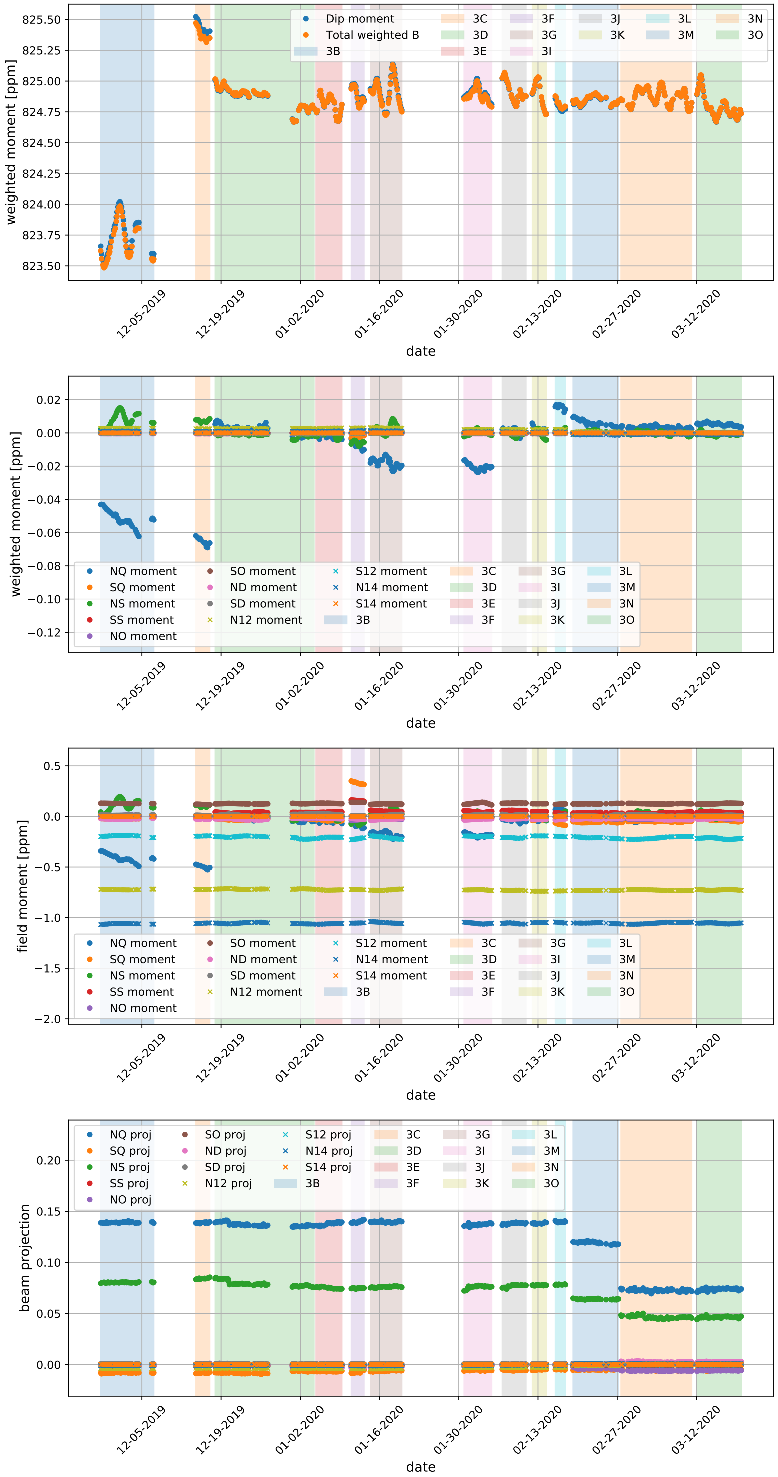

Figure 7.7: Baseline muon-weighted field results for Run-3. Colored bands indicate datasets. Top plot: Azimuth-average dipole moment (blue) and total weighted field including contributions from muon-weighted multipole moments (orange). Second plot: Individual muon-weighted multipole moment contributions, $\langle k_i(\theta_j)m_i(\theta_j)\rangle_\theta$. Third plot: Unweighted azimuth-average field multipole moments m_i. Bottom plot: Azimuth-average beam multipole projections k_i. The time variation of the muon-weighted moments is mainly due to variation of the field, although the variation is less than in Run-2. The beam projections are relatively stable, except for the reduction in Run-3b due to the stronger kick.

7.4.2 Azimuthal effects

Figure 7.8 shows dominant beam projections corresponding to the beam profiles in Figure 7.4. The NQ projection (k_2) couples mainly to the beam x_{mean}, and the θ dependence is dominated by the closed orbit distortion. Azimuthal variation in k_2 is reduced in Run-3 compared to Run-2 due to the reduced COD, and the oscillation due to dispersion is reduced in Run-3b. The NS projection (k_5) couples to both the beam x_{rms} and x_{mean}, and the θ dependence shows features of both.

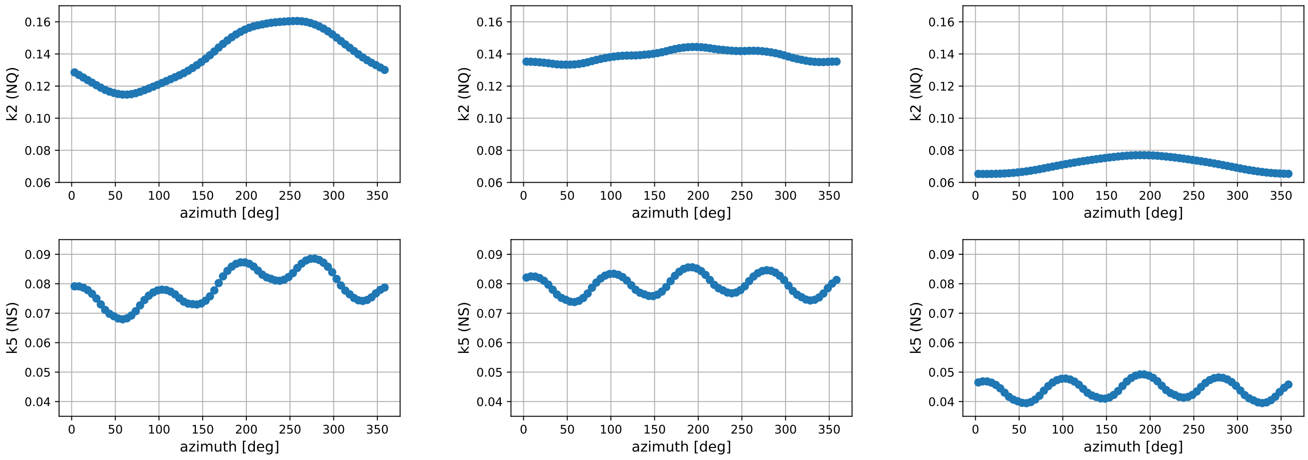

(a) Run-2 (from dataset DS-2E) **(b)** Run-3a (from dataset DS-3B) **(c)** Run-3b (from dataset DS-3O)

Figure 7.8: NQ and NS beam projections (k_2 and k_5) vs. azimuth for example time intervals in Run-2, Run-3a, and Run-3b.

The azimuthal interference between the beam projections $k_i(\theta)$ and field moments $m_i(\theta)$ affects the total muon-weighted field $\tilde{B}$ given by Eq. 7.21. This effect is seen in Figure 7.9 by comparing the standard $\tilde{B} = \langle MB \rangle_\theta$ ("3D") with $\tilde{B}$ calculated from azimuth-averaged beam projections and field moments, $\langle M \rangle_\theta \langle B \rangle_\theta$ ("2D average"). The effect is driven by the closed orbit distortion (COD) amplitude and phase, shown in Figure 7.10. In Run-2 the difference is 6 to 30 ppb; in Run-3 when the COD amplitude is reduced, the difference is only 2 to 8 ppb.

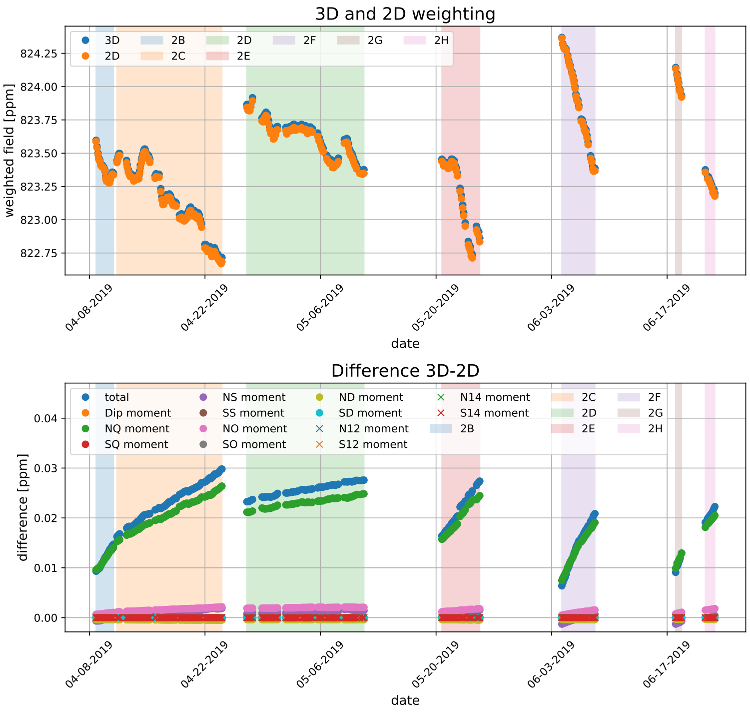

(a) Run-2

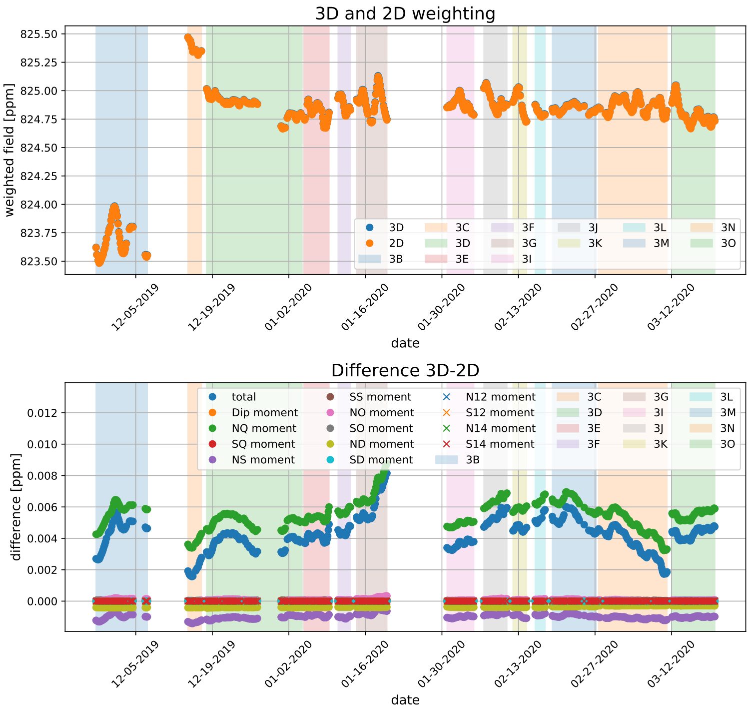

(b) Run-3

Figure 7.9: Standard "3D" muon-weighted field compared with "2D average" calculated with azimuth-averaged beam projections and field moments, for Run-2 and Run-3. Colored bands indicate datasets. Top plots show $\tilde{B}$ values and bottom plots show differences between "3D" and "2D average", with a breakdown of the difference in each moment.

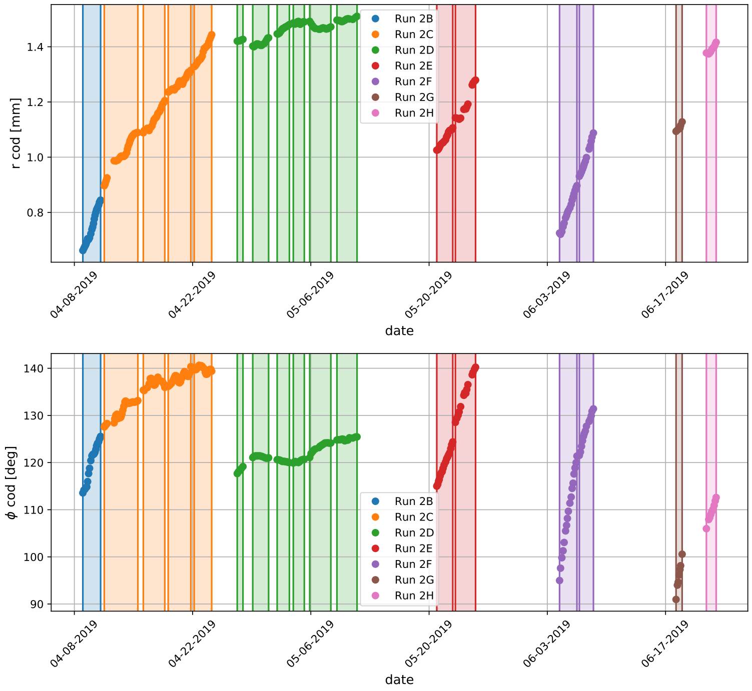

(a) Run-2

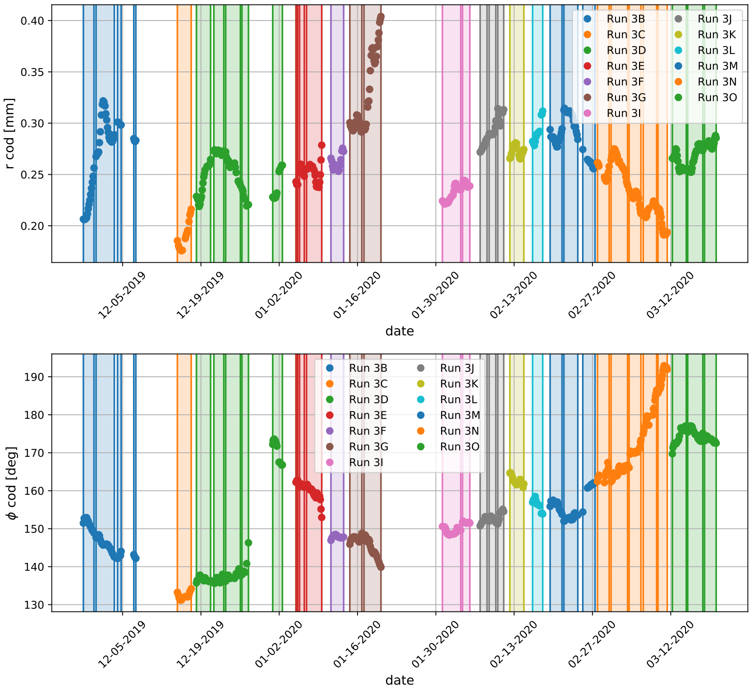

(b) Run-3

Figure 7.10: Closed orbit distortion amplitude (top) and phase (bottom) for Run-2 and Run-3. Colored bands indicate datasets. The COD amplitude is smaller and varies less in Run-3 compared with Run-2.

7.5 Corrections and Uncertainties

Uncertainties in the field and the beam contribute to the overall uncertainty on $\tilde{B}$. Using $\tilde{B} = \sum_i k_i m_i$ as shorthand for Eq. 7.21, the uncertainty is propagated using the covariance K_{ij} between variables,

$$\delta\tilde{B}^2 = \sum_{a,b}\sum_{i,j} \frac{\partial B}{\partial a_i} K_{ij}(a_i, b_j) \frac{\partial B}{\partial b_j}\,, \tag{7.23}$$

where the variables a and b represent k or m. The field moments m_i are correlated with each other [51], but the beam projections k_i are uncorrelated and their covariance is diagonal. The k_i and m_i are uncorrelated in general, so the cross term does not contribute. The uncertainty on $\tilde{B}$ is then

$$\delta\tilde{B}^2 = \delta\tilde{B}^2_{field} + (m_i\,\delta k_i)^2\,. \tag{7.24}$$

The field uncertainties $\delta\tilde{B}_{field}$ include correlations between moments, and are discussed below in Section 7.5.1. Beam uncertainties cause uncertainties δk_i in the beam projections; these and the corresponding $\delta\tilde{B}$ contributions are discussed in the subsequent sections. The uncertainties from the beam which enter in the muon weighting are the focus of this uncertainty analysis.

7.5.1 Field uncertainties

Uncertainties on the field multipole moments are propagated using the beam projections as weights. The combined uncertainty includes correlations between moments.

$$\delta\tilde{B}^2_{field} = \sum_{i,j} k_i K_{ij}(m_i, m_j) k_j \equiv \sum_i \left[k_i^2 \delta m_i^2 + \sum_{j>i} 2r(i,j)(k_i k_j)\delta m_i \delta m_j \right] \tag{7.25}$$

where i, j run over all moments, K_{ij} is the covariance matrix between moments, δm_i is the uncertainty for moment m_i, and $r(i,j)$ is the correlation coefficient between moments.

Except for the azimuthal averaging uncertainty below, field-specific uncertainties are not the subject of the muon-weighted field analysis. Field uncertainties are separated into uncorrelated and correlated uncertainties, discussed here briefly. Preliminary total uncertainties of each type for Run-2/3 are shown in Table 7.4 for reference.

	Run-2	**Run-3a**	**Run-3b**
$\delta\tilde{B}$ (ppb) from uncorrelated field tracking uncertainties	15.4	10.7	16.0
$\delta\tilde{B}$ (ppb) from correlated field uncertainties	45.4	46.2	44.7

Table 7.4: Preliminary uncorrelated and correlated total uncertainty on $\tilde{B}$, combined (with ctag weighting) for trolley pairs in each run.

Uncorrelated

Uncorrelated uncertainties are independent between trolley pairs and are therefore reduced by averaging multiple trolley pairs. These uncertainties come from tracking the field drift over time between trolley runs. The dominant source of tracking uncertainty is the non-linear drift remaining after tying the fixed probe measurements to the trolley runs, as described in Section 2.7.3.

This remaining drift between trolley runs is treated as a Brownian bridge, and the uncertainty is estimated by a model of possible random walks with rate-of-change parameter M. Tracking uncertainties are zero at the trolley runs and maximum at the midpoint between trolley runs. For intervals with just one starting or ending trolley run, the drift is treated as a random walk fixed at the single trolley run, and uncertainty is maximum at the other end of the interval. Uncorrelated uncertainties are combined within each trolley pair using a covariance matrix to account for the correlation between measurements in the time interval. For each multipole moment i, the covariance matrix between times $t_m \leq t_n$ in an interval $0, T$ is given by [41]

$$K^i_{m,n} = M_i \frac{t_m(T - t_n)}{T}\,, \text{ Brownian bridge (two bounding trolley runs)} \tag{7.26}$$

$$K^i_{m,n} = M_i t_m\,, \text{ random walk (one bounding trolley run)}\,. \tag{7.27}$$

M_i is the RMS of time-normalized azimuth-average sync offsets (difference between fixed probes and ending trolley run after tying), with units of ppb/$\sqrt{\text{hour}}$.

The overall uncertainty for each multipole moment i for the trolley pair interval, accounting for the correlation between measurements, is propagated with decay positron count ("ctag") weights c_m at time t_m

$$\delta m_i = \sqrt{c_m K^i_{mn} c_n}\,. \tag{7.28}$$

The δm_i are then combined to $\delta\tilde{B}_{uncorr}$ by weighting with the beam projections as in Eq. 7.25. For a dataset with

N trolley pairs and c_{tp} ctag weights in each pair, the uncorrelated field uncertainty is given by

$$\delta\tilde{B}_{uncorr} = \sqrt{\frac{\sum_{tp=0}^{N}\left(c_{tp}\delta\tilde{B}_{tp}^{uncorr}\right)^2}{\left(\sum_{tp=0}^{N} c_{tp}\right)^2}}. \tag{7.29}$$

Correlated

Correlated uncertainties are common to all trolley pairs and are not reduced by averaging multiple trolley pairs. The largest source of correlated uncertainty in the field measurement is systematics from extracting multipole moment maps from the NMR frequencies measured by the trolley probes. These systematics include extraction of the NMR frequency from the free induction decay signals, eddy currents induced by trolley motion in the magnetic field, and different experiment configurations between the trolley field measurement and ω_a measurement periods.

Azimuthal averaging

$\tilde{B}$ is calculated with virtual trolley maps which are sampled from splines of order 1, 2, and 3 and averaged in azimuthal bins (described in Section 7.4). The central $\tilde{B}$ value is taken from the average of the spline orders. The truth distribution between trolley samples is unknown, so the variance in $\tilde{B}$ calculated from the different spline orders is assigned as an uncertainty in the azimuthal averaging. This uncertainty is correlated between trolley pairs.

$$\tilde{B}_{avg} = \frac{1}{3}\sum_{n=1}^{3}\tilde{B}_n \tag{7.30}$$

$$\delta\tilde{B}^2 = \frac{1}{3}\sum_{n=1}^{3}(\tilde{B}_n - \tilde{B}_{avg})^2 \tag{7.31}$$

$\tilde{B}_{avg}$ gives the central value of $\tilde{B}$. $\tilde{B}_n$ is calculated as in Eq. 7.21, with order n splines used to average the moments m_i in azimuthal bins θ_j. The variance of $\tilde{B}$ implicitly includes the correlations between moments in Eq. 7.25.

Figure 7.11 shows the uncertainty on $\tilde{B}$ from the azimuthal averaging. Table 7.5 shows the run-averaged uncertainties, which are $\leqq$ 2 ppb.

	Run-2	**Run-3a**	**Run-3b**
$\delta\tilde{B}$ (ppb) from azimuthal averaging	0.8	1.4	1.7

Table 7.5: Uncertainty on $\tilde{B}$ from azimuthal averaging with different spline orders, averaged (with ctag weighting) for datasets in each run.

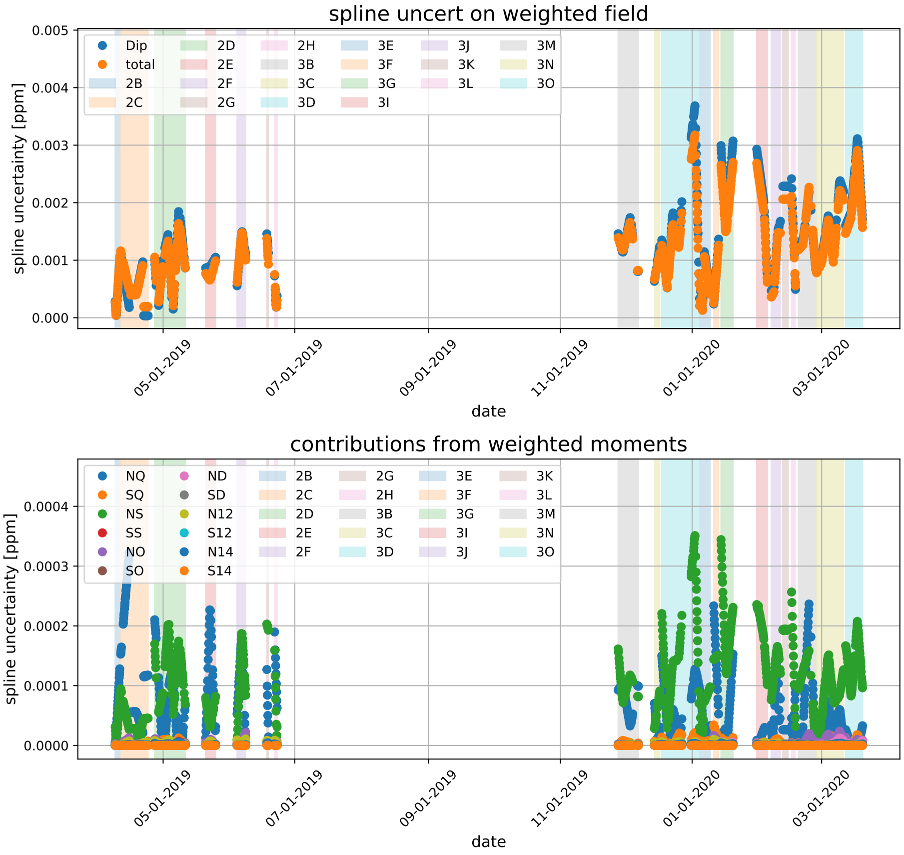

Figure 7.11: Uncertainty on $\tilde{B}$ from azimuthal averaging, calculated as the variance from spline orders. Top: Total uncertainty (orange) and contribution from dipole moment (blue), which is the majority of the total uncertainty. Bottom: Uncertainty from weighted multipole moments, which contribute according to beam projection weights.

7.5.2 Tracker uncertainty

Tracker-specific systematics cause uncertainties in the beam distribution, which lead to uncertainties in $\tilde{B}$. The relevant uncertainties for muon weighting are tracker resolution, acceptance, and alignment. These systematics were evaluated by varying each parameter and producing corresponding beam distributions in the usual time intervals $T_{interval}$, then evaluating the effect on $\tilde{B}$. In general, the parameters were varied symmetrically by the 1σ uncertainty on each parameter (for example, tracker position was varied by $\pm 0.6\,\mathrm{mm}$ in each direction); the corresponding effects on $\tilde{B}$ were approximately symmetric. The uncertainty on $\tilde{B}$ was taken as the absolute change in $\tilde{B}$ due to each varied parameter, averaged over each dataset.

In Run-1, the tracker acceptance and resolution uncertainties were $\leqq$ 2 ppb and $<$ 1 ppb, respectively. For Run-2/3, these uncertainties were evaluated for a few selected datasets to verify they are still insignificant. Since the tracker corrections affect the beam mean and width, datasets with large field multipole moments were selected to represent worst-case effects [7]. The tracker alignment uncertainty was significant in Run-1, so it was evaluated for all Run-2/3 datasets.

Tracker acceptance

The tracker profiles are corrected for detector acceptance by re-weighting tracker vertex positions by a spatial acceptance function. The acceptance correction changes the profile width as well as the radial mean due to asymmetry of the acceptance function. The acceptance systematic was evaluated by rescaling the radial and vertical acceptance functions simultaneously by $\pm 20\%$ relative to the peak acceptance, effectively bending the acceptance at the edges. Figure 7.12 shows the acceptance correction functions and the rescaling variation.

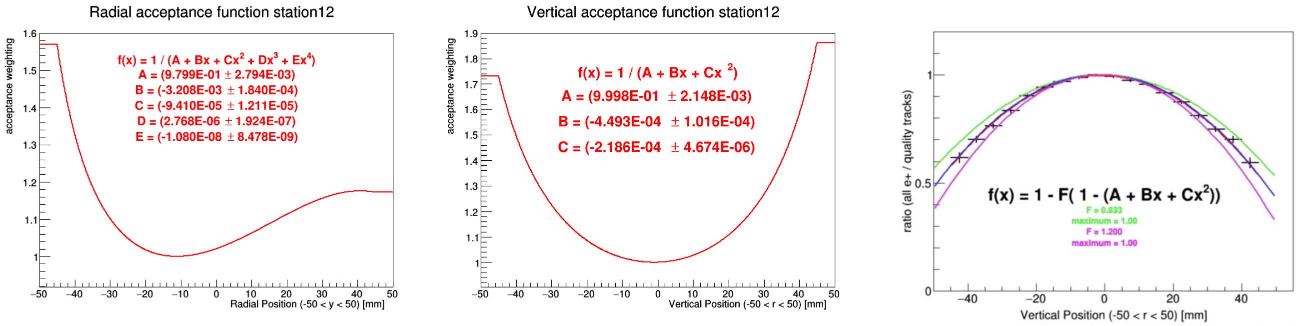

(a) Tracker acceptance correction functions **(b)** Varying the vertical acceptance

Figure 7.12: Radial and vertical tracker acceptance functions (left) used for the nominal acceptance correction [84]. The radial (not shown) and vertical (shown here, right) acceptance are rescaled by $\pm 20\%$, which bends the acceptance at the edges relative to the maximum [85]. Figures courtesy of J. Mott and J. Price.

---

[7] Dataset DS-2E has large NQ, NS, SQ, and SS moments; DS-3B has large NQ and NS moments; and DS-3O represents the better-centered beam, although the multipole moments are not the largest.

Figure 7.13 shows the effect on $\tilde{B}$ for the selected datasets, all $\leqq 2$ ppb. The effect of varying the acceptance dominantly couples to the NQ moment due to the change in radial mean, and is driven by the NQ field moment magnitude. The effect on the selected dataset in each run is taken as the uncertainty for the run, shown in Table 7.6.

	Run-2	**Run-3a**	**Run-3b**
$\delta\tilde{B}$ (ppb) due to tracker acceptance	2.1	1.1	0.1

Table 7.6: Uncertainty on $\tilde{B}$ due to tracker acceptance, averaged (with ctag weighting) for the selected dataset in each run.

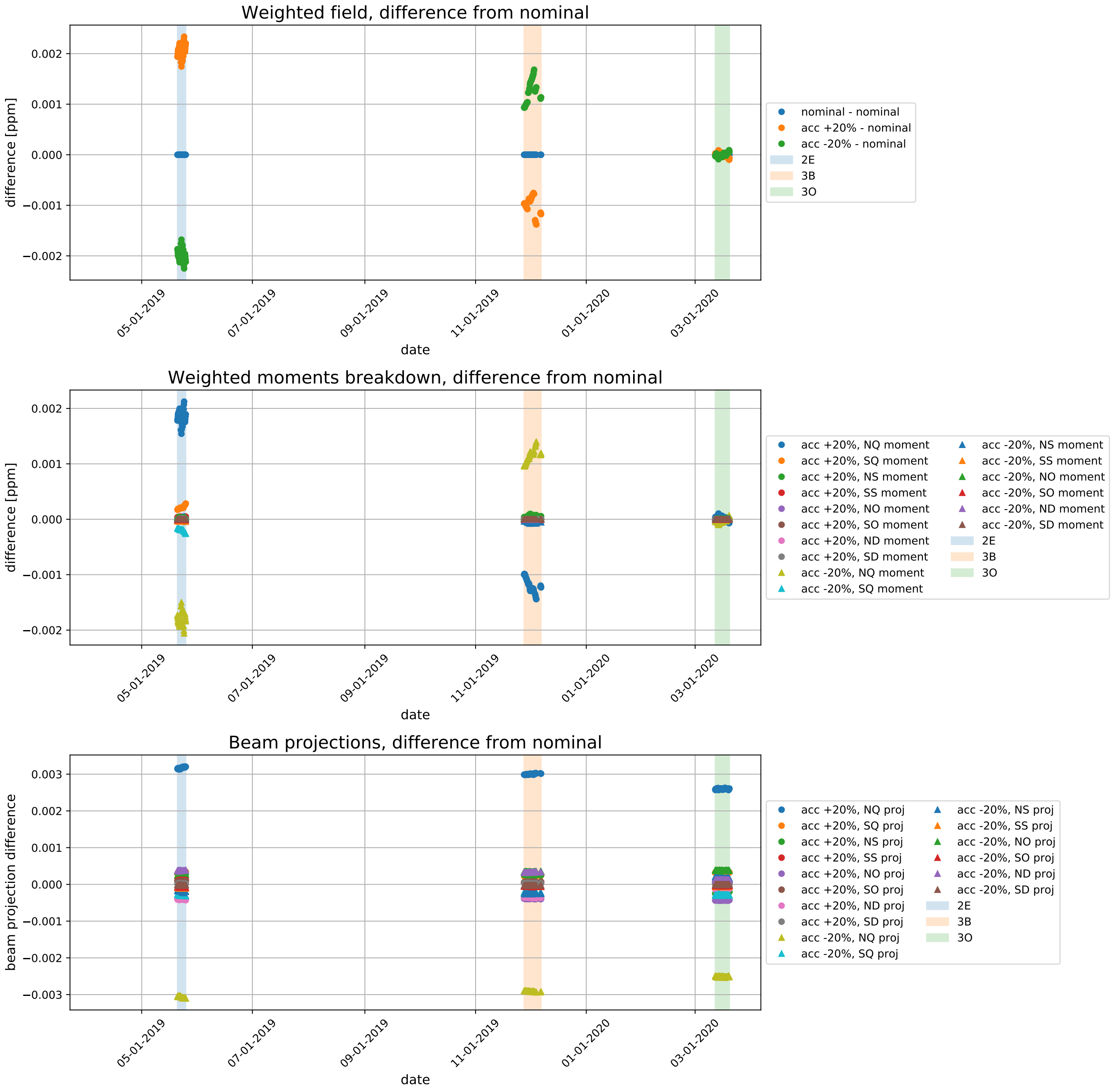

Figure 7.13: Effect on $\tilde{B}$ of varying the tracker acceptance (top), and a breakdown of the contribution of each weighted field moment (center) and beam projection (bottom).

Tracker resolution

The measured tracker profiles are wider than the actual beam distribution due to the resolution of the trackers, so the resolution correction narrows the tracker profiles. The nominal resolution is approximately $(3.3 \pm 0.5)\,\mathrm{mm}$ (radial) and $(2.7 \pm 0.5)\,\mathrm{mm}$ (vertical) [84]. The resolution systematic was evaluated by varying the radial and vertical resolution simultaneously by $\pm 0.5\,\mathrm{mm}$.

Figure 7.14 shows the effect on $\tilde{B}$ for the selected datasets; the effect is ~ 0.1 ppb. Varying the resolution dominantly changes the ND (k_8) beam projection, but this change and the ND field moment are both small. The effect on the selected dataset in each run is taken as the uncertainty for the run, shown in Table 7.7.

	Run-2	**Run-3a**	**Run-3b**
$\delta\tilde{B}$ (ppb) due to tracker resolution	0.1	0.1	0.1

Table 7.7: Uncertainty on $\tilde{B}$ due to tracker resolution.

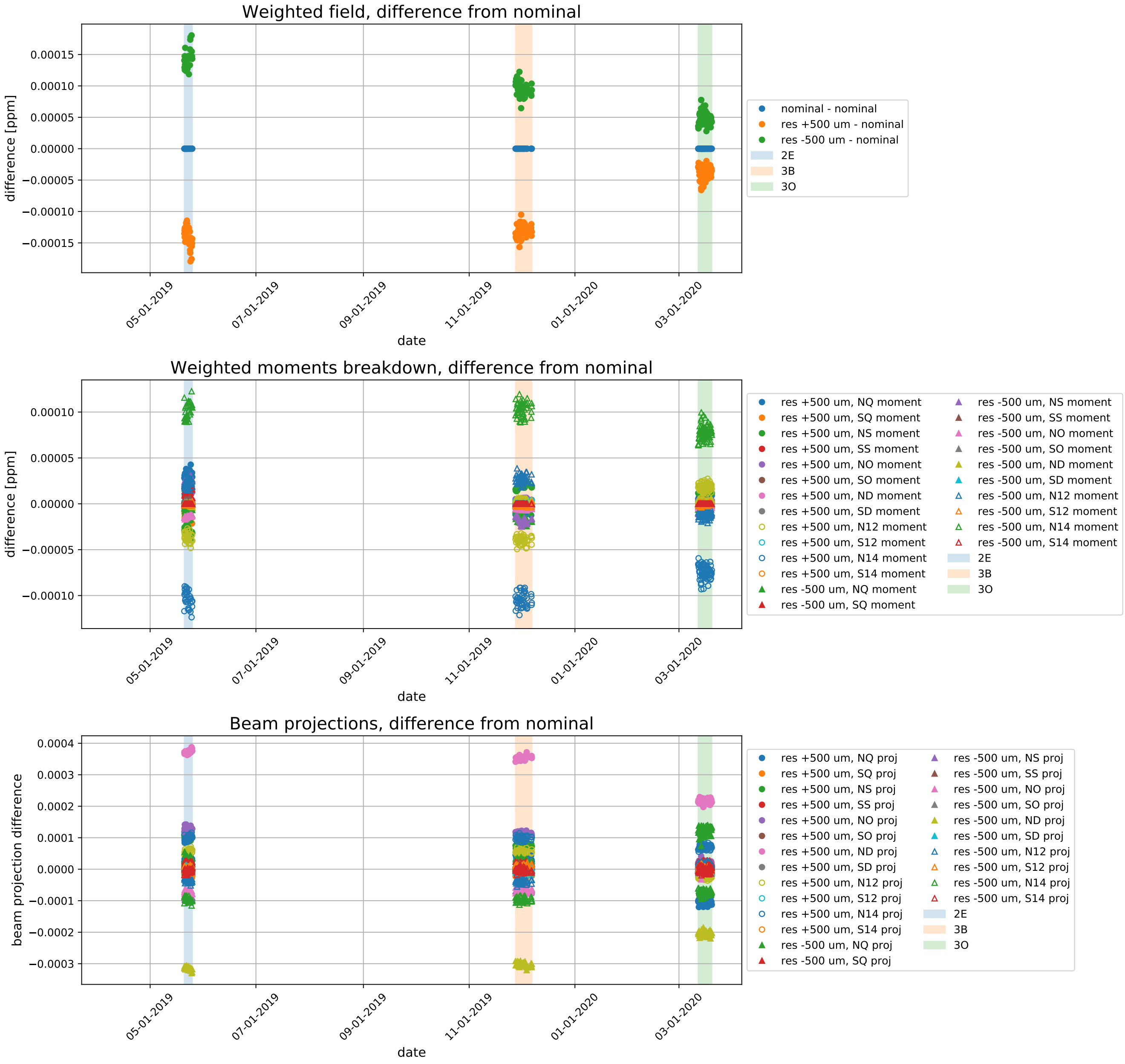

Figure 7.14: Effect on $\tilde{B}$ of varying the tracker resolution (top), and a breakdown of the contribution of each weighted field moment (center) and beam projection (bottom).

Tracker alignment

The uncertainty in the tracker profile position due to tracker alignment is $\pm 0.6\,\mathrm{mm}$ in x and y. In the Run-1 analysis [81], it was determined that the largest change in the total summed beam profile and the largest effect on $\tilde{B}$ occurs when both tracker stations are misaligned in the same direction. In Run-2/3, the alignment systematic was conservatively evaluated by shifting the tracker profiles in x or y by $\pm 0.6\,\mathrm{mm}$ (in the same direction) before correcting for resolution and acceptance and reconstructing the azimuthal beam profiles.

Figure 7.15 shows the effect of misalignment on $\tilde{B}$. The magnitude and sign of the effect are driven by the magnitude and sign of the corresponding quadrupole moment (NQ or SQ moments for x or y misalignments, respectively), with sub-dominant contributions from the corresponding sextupole (NS or SS) and octupole (NO or SO) moments. In Run-2, the effect of the y misalignment is larger than that of the x misalignment, and both are on the order of the Run-1 effects due to the NQ and SQ field moments. In Run-3, the effects of both are generally reduced because the NQ and SQ moments are reduced. Table 7.8 shows run-averaged uncertainties due to each misalignment.

	Run-2	**Run-3a**	**Run-3b**
$\delta\tilde{B}$ (ppb) due to tracker y alignment	10.7	0.6	0.4
$\delta\tilde{B}$ (ppb) due to tracker x alignment	4.5	1.3	0.3

Table 7.8: Uncertainty on $\tilde{B}$ due to tracker alignment, averaged (with ctag weighting) for datasets in each run.

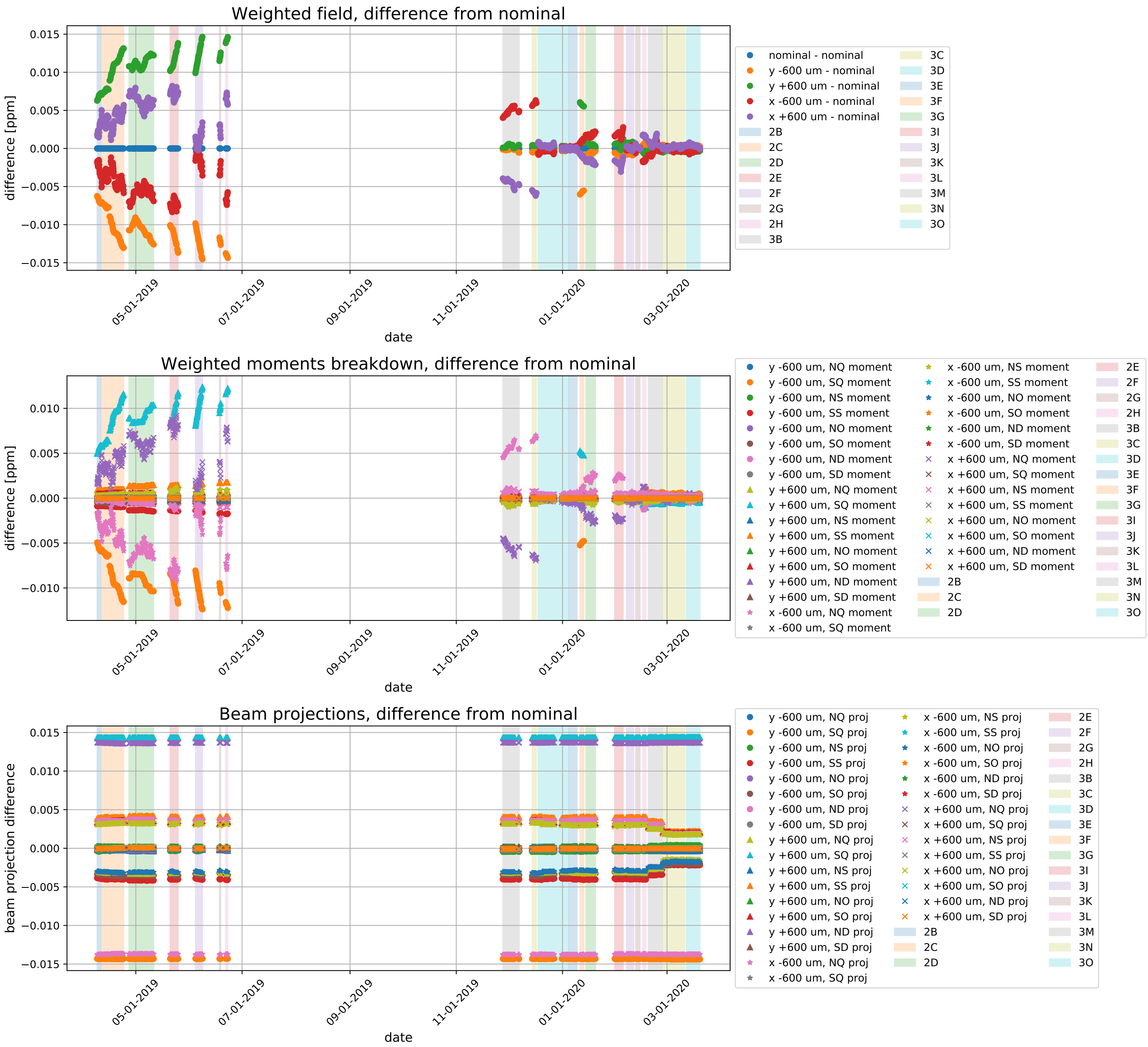

Figure 7.15: Effect on $\tilde{B}$ of varying the tracker alignment by $\pm 0.6\,\mathrm{mm}$ (top), and a breakdown of the contribution of each weighted field moment (center) and beam projection (bottom).

Tracker statistical uncertainty

The uncertainty on $\tilde{B}$ due to tracker profile statistics is insignificant. Typical statistical uncertainties on tracker profiles in each $T_{interval}$ are $\sim$($30\,\mu\mathrm{m}, 20\,\mu\mathrm{m}$) for (x_{mean}, y_{mean}) and $\sim$($20\,\mu\mathrm{m}, 15\,\mu\mathrm{m}$) for (x_{rms}, y_{rms}). For the means, this corresponds to $\leqq 5\%$ of the $0.6\,\mathrm{mm}$ tracker alignment uncertainty. For the RMS, this corresponds to $\sim 0.1\%$ of the typical x_{rms} and y_{rms}. Both contributions would be well below 1 ppb. Similarly, a Run-1 study [86] by A. Tewsley-Booth showed a < 1 ppb effect from tracker statistical uncertainty.

7.5.3 Calorimeter acceptance

The muon-weighted field $\tilde{B}$ should represent the field experienced by the muons whose decay positrons enter the ω_a analysis. Up to this point, this distribution was approximated by the full beam distribution in the ring. The beam profiles should therefore be corrected for calorimeter acceptance to represent the distribution detected by the calorimeters. The Run-1 calorimeter acceptance correction was used to estimate the effect on $\tilde{B}$ in Run-2/3. In Run-1 [81], the calorimeter acceptance correction was applied for one dataset, and the resulting ~3 ppb change in $\tilde{B}$ was taken as an uncertainty.

The acceptance correction is more than a simple spatial weighting function. Because each muon circulates around the ring hundreds of times and can decay at any position, its probability distribution must be included in the correction. This probability depends on the muon's betatron amplitudes A_x, A_y and equilibrium radius x_{eq}. The correction procedure developed by J. Mott [85] was to deconvolve the (x, y) tracker profiles to obtain a distribution of (A_x, A_y, x_{eq}), calculate the total acceptance probability for each (A_x, A_y, x_{eq}) using acceptance maps from simulation, and construct the corrected (x, y) distribution using the acceptance probabilities as weights. The correction de-weights muons not detected by the calorimeters, as seen from the ratio of corrected and uncorrected profiles in Figure 7.16.

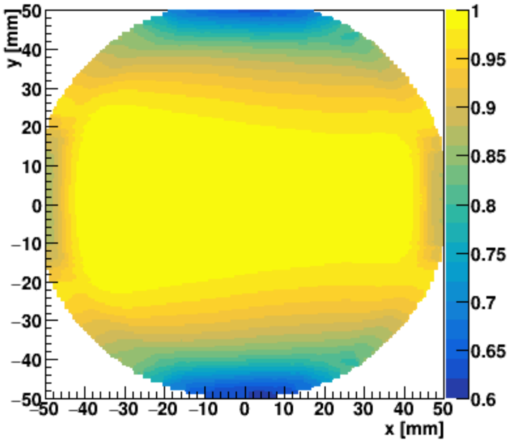

Figure 7.16: Ratio of azimuth-averaged calorimeter-acceptance-corrected and uncorrected muon distributions from Run-1.

The change in beam projections Δk_i from the Run-1 beam profiles was used as a rough estimate for Run-2/3. The acceptance correction dominantly affects the NQ and NS projections, shown in Table 7.9. The uncertainty was estimated as the change in $\tilde{B}$ (Table 7.10) calculated from $\Delta k_i(\theta_j)$ and ctag-weighted run-averaged field moments $m_i(\theta_j)$. The effect is ≤ 1 ppb, reduced from Run-1 due to reduced NQ and NS field moments. The full calorimeter acceptance correction was therefore not repeated in Run-2/3.

	Δk_i
NQ (k_2)	-0.0019
NS (k_5)	0.0015

Table 7.9: Dominant average beam projection changes due to calorimeter acceptance correction in Run-1.

	Run-2	**Run-3**
$\delta\tilde{B}$ (ppb) due to calo acceptance	-1.0	0.2

Table 7.10: Change in $\tilde{B}$ due to Run-1 calorimeter acceptance correction, taken as an estimate of the uncertainty on $\tilde{B}$ in Run-2/3. Signs correspond to the sign of the change, but uncertainties are taken as the absolute value.

7.5.4 Closed orbit distortions

The nominal reconstructed beam distributions include the radial closed orbit distortion x_{COD} due to the magnetic dipole field and zero vertical closed orbit distortion y_{COD}. Systematic effects include y_{COD} due to a radial magnetic field, and x_{COD} and y_{COD} due to misalignment of the electric quadrupole plates.

COD systematics were evaluated by linearly scaling a unit beam displacement and determining the corresponding change in the beam projections Δk_i as a function of azimuth, illustrated in Figure 7.17. Typical COD amplitudes are sufficiently small that the beam projection change is approximately linear and can be expressed as $\Delta k_i \approx \frac{dk_i}{dx}\Delta x$. The effect on the weighted field due to a closed orbit distortion $\Delta x(\theta)$ is then

$$\Delta\tilde{B} = \langle\sum_i \frac{dk_i(\theta_j)}{dx}\Delta x(\theta_j) \cdot m_i(\theta_j)\rangle_\theta \,, \tag{7.32}$$

and similar for $\Delta y(\theta)$. In the following sections, the $\Delta x(\theta)$ and $\Delta y(\theta)$ are replaced with x_{COD} and y_{COD}. The COD effects were evaluated at the dataset level with dataset-average field moments and beam distributions.

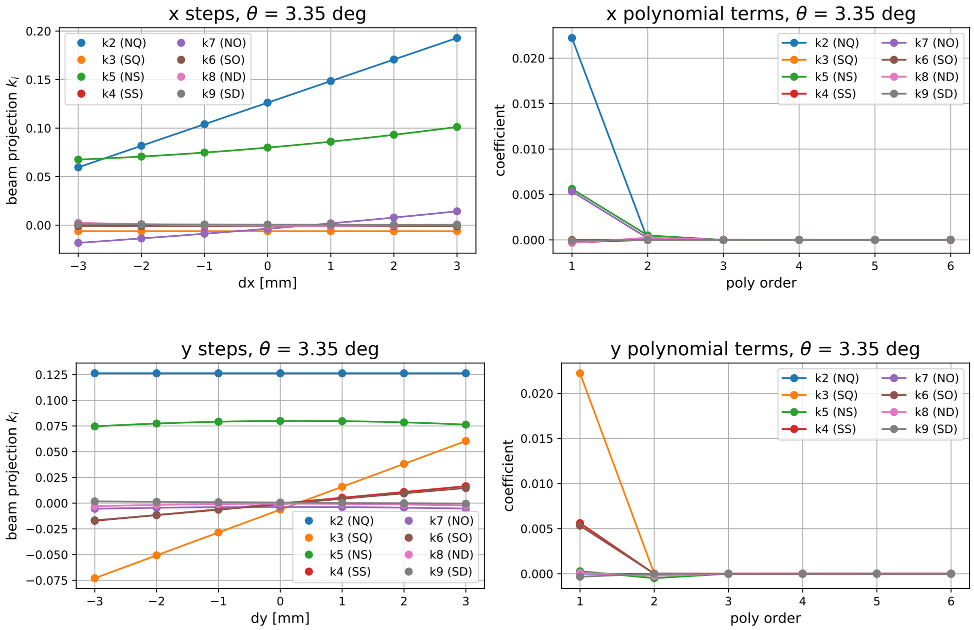

Figure 7.17: Beam projections and polynomial terms for x (top) and y (bottom) steps in an example θ bin, for dataset DS-2B.

Radial magnetic field

An azimuthally-varying radial magnetic dipole field would cause a vertical closed orbit distortion y_{COD}. Such a COD can be expanded in a Fourier series as in Section 4.3.3. The radial field is not measured or tracked during production running, but it was measured by R. Osofsky before Run-1 and corresponding y_{COD} Fourier components were extracted [50]. The systematic due to a y_{COD} caused by a radial field was conservatively estimated with a Fourier $N = 1$ amplitude of $0.5\,\mathrm{mm}$, approximately double the $N = 1$ amplitude from the pre-Run-1 measurement. The effect of y_{COD} on $\tilde{B}$ was evaluated as described above (Section 7.5.4). The worst case of phases ranging from 0 to 2π was taken as the uncertainty, as shown in Figure 7.18. The magnitude of the effect is driven by the azimuthal interference between y_{COD} and the skew field moments. Uncertainties for each dataset are shown in Figure 7.20. Run-averaged uncertainties are shown in Table 7.11.

For comparison, the effect of the pre-Run-1-measured y_{COD} was also evaluated. This y_{COD} is provided by the COSY model using the pre-Run-1 radial field map (Figure 7.19). The effect on $\tilde{B}$ is ≤ 1 ppb (shown in Figure 7.20), and well within the uncertainty determined above.

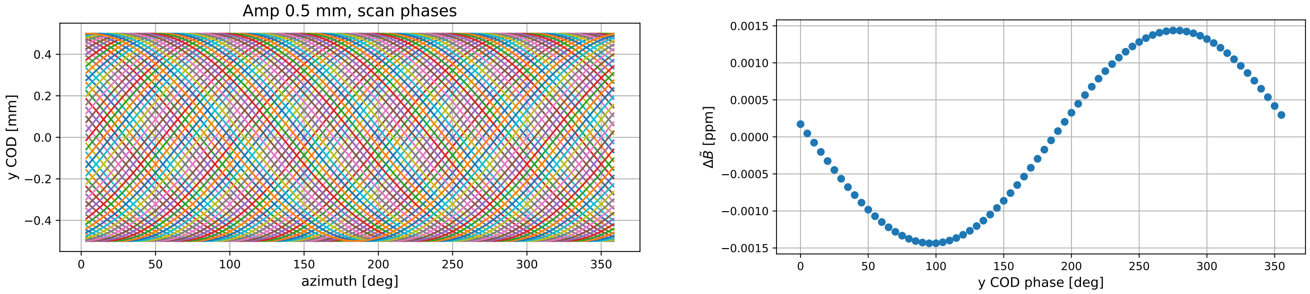

(a) y_{COD} with $N = 1$ amplitude of $0.5\,\mathrm{mm}$ and phases ranging from 0 to 2π

(b) Change in $\tilde{B}$ due to each y_{COD} in Figure 7.18a. The worst-case effect is ± 1.4 ppb, which is taken as the uncertainty for this dataset.

Figure 7.18: Example y_{COD} uncertainty estimation in Run-2 (dataset DS-2F)

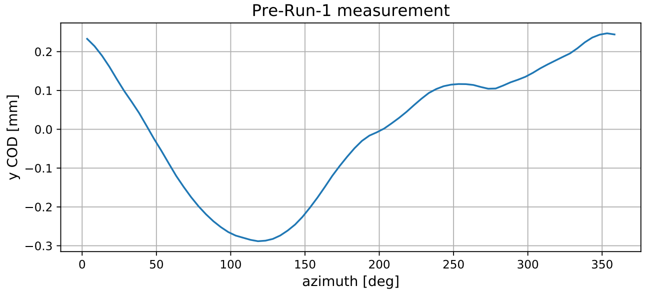

Figure 7.19: y_{COD} from the pre-Run-1 radial field measurement, provided by the COSY model

	Run-2	**Run-3a**	**Run-3b**
$\delta\tilde{B}$ (ppb) due to y_{COD} from radial B	1.8	3.7	2.9

Table 7.11: Uncertainty on $\tilde{B}$ due to a vertical COD caused by a radial field, averaged (with ctag weighting) for datasets in each run.

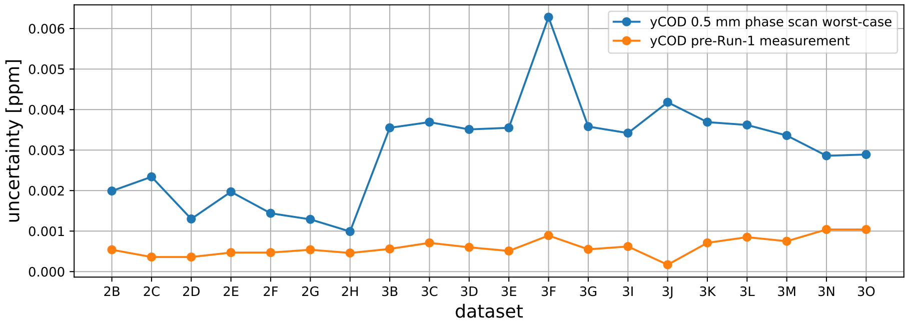

Figure 7.20: Uncertainty on $\tilde{B}$ per dataset due to a vertical COD caused by a radial field (blue), with the effect of the pre-Run-1-measured y_{COD} for comparison (orange).

Electric quadrupole misalignment

Misalignments of the electric quadrupole plates cause an x_{COD} or y_{COD} by steering the beam. Quadrupole plates were surveyed in Run-1 [87], and M. Syphers calculated the expected CODs [88] due to measured displacements of the quad centroids (Table 7.12) using a model based on the transport matrix formalism introduced in Section 4.1. Survey uncertainties cause uncertainties on the CODs. The effect on $\tilde{B}$ was estimated from a distribution of CODs caused by quad centroid displacements with random uncertainties.

quad	dx [mm]	dy [mm]
Q1S	-0.490 (0.700)	2.235 (0.354)
Q1L	-0.245 (0.492)	-0.980 (0.350)
Q2S	-0.995 (0.430)	-0.675 (0.354)
Q2L	-0.035 (0.458)	0.380 (0.350)
Q3S	-0.200 (0.480)	0.750 (0.350)
Q3L	0.115 (0.437)	-1.965 (0.354)
Q4S	-0.345 (0.700)	-1.315 (0.354)
Q4L	0.085 (0.522)	-0.220 (0.350)

Table 7.12: Measured electric quadrupole centroid displacements and corresponding uncertainties.

The total COD due to quad displacements is a linear combination of CODs from individual quad displacements, and the COD scales linearly with the displacement. x and y CODs for individual quad centroid displacements were calculated from M. Syphers' model [88] with 18.3 kV quad voltage [8], then scaled by displacements generated in a Monte Carlo. Displacements in the Monte Carlo were randomly sampled from a distribution defined by the survey central values and uncertainties. To check effects of possible correlations between quads, CODs were also generated for all 6561 combinations of 0, $\pm 1\sigma$ centroid displacements ("corner cases").

---

[8] Actual quad voltages were 18.3 kV in Run-2 and 18.2 kV in Run-3, but the corresponding difference in the calculated CODs was only a few μm. The 18.3 kV CODs were therefore used in this study for both runs.

The CODs due to the central measured displacements were fixed to the measured tracker mean positions, as they would be in the beam reconstruction procedure. (Unlike the radial field case, the quad displacements have a central measurement which is treated here as a correction.) All Monte Carlo CODs were fixed to the same offset and vary relative to the central CODs.

Effects of the CODs on $\tilde{B}$ were evaluated as described in Section 7.5.4. Figure 7.21 shows the CODs from the Monte Carlo and the corner cases; Figure 7.22 shows the distribution of corresponding changes in $\tilde{B}$ for an example dataset. The effect of the central COD corresponds to the mean of the $\tilde{B}$ distribution, which gives the correction to $\tilde{B}$. The RMS of the Monte Carlo distribution gives the uncertainty on $\tilde{B}$. The corner cases show that correlations between quads would not have a larger effect than the random alignment errors in the Monte Carlo. Corrections and uncertainties for each dataset are shown in Figure 7.23. Run-averaged corrections and uncertainties are shown in Table 7.13.

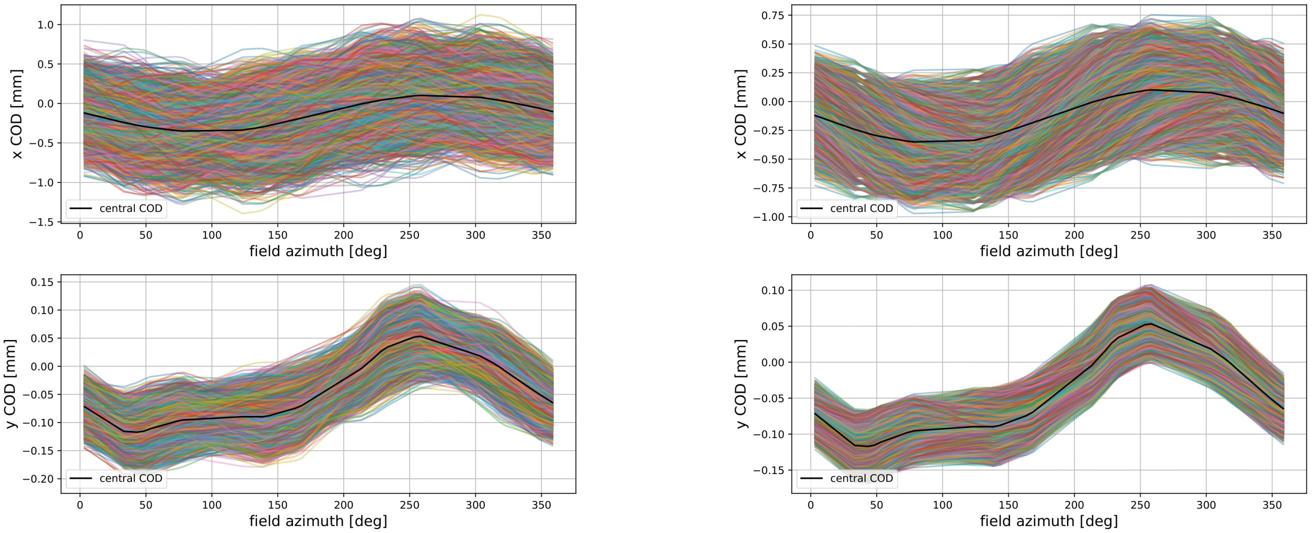

(a) Monte Carlo distribution of x (top) and y (bottom) CODs caused by random alignment errors relative to measured quad displacements. The black "central CODs" are caused by the central measured quad displacements.

(b) Distribution of x (top) and y (bottom) CODs for all "corner case" combinations of 0, $\pm 1\sigma$ alignment errors relative to measured quad displacements. The black "central CODs" are caused by the central measured quad displacements.

Figure 7.21: CODs due to quad misalignments

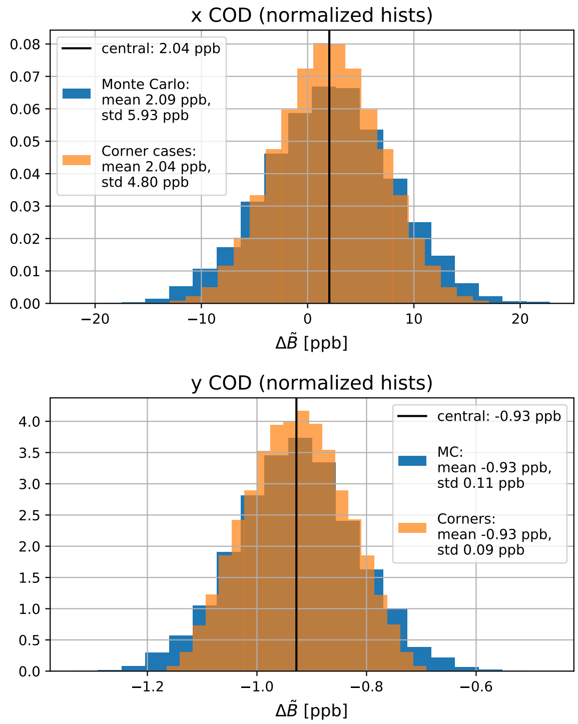

Figure 7.22: Distribution of change in $\tilde{B}$ due to x (top) and y (bottom) CODs from Monte Carlo (blue) and corner cases (orange) for DS-2F. The mean and RMS of the Monte Carlo distribution give the correction and uncertainty to $\tilde{B}$.

	Run-2	**Run-3a**	**Run-3b**
	correction $\Delta\tilde{B}$ (uncertainty $\delta\tilde{B}$)		
x_{COD} quad misalignment (ppb)	$+1.3(5.9)$	$+2.7(6.7)$	$+2.5(6.3)$
y_{COD} quad misalignment (ppb)	$-0.9(0.1)$	$-0.5(0.2)$	$-0.3(0.2)$

Table 7.13: Correction and uncertainty to $\tilde{B}$ due to CODs caused by electric quadrupole misalignments, averaged (with ctag weighting) for datasets in each run.

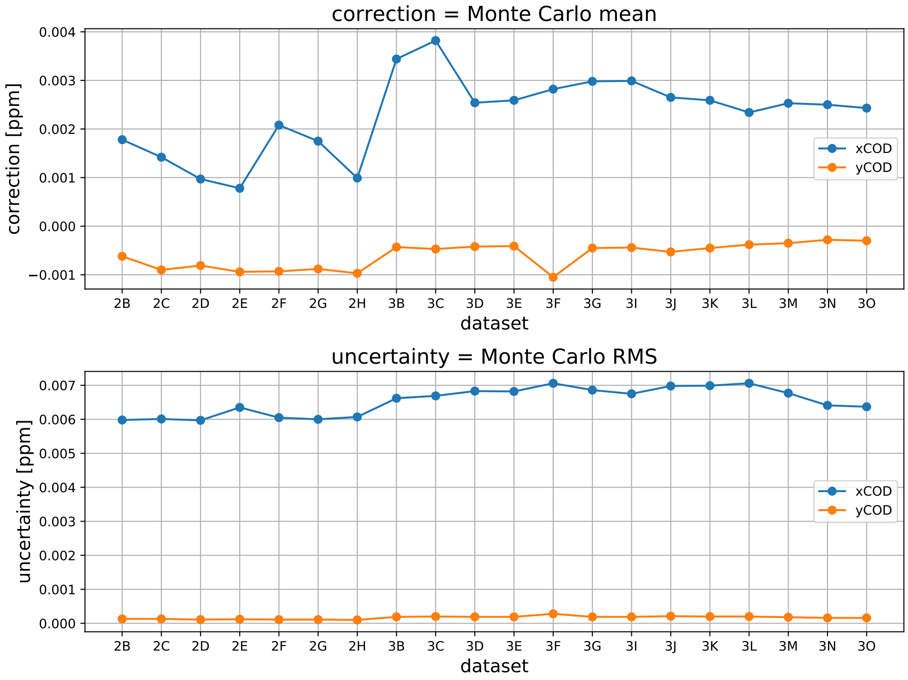

Figure 7.23: Correction and uncertainty to $\tilde{B}$ per dataset due to CODs caused by electric quadrupole misalignments.

7.5.5 Momentum deviation

The momentum deviation δ used in the beam reconstruction procedure (Section 7.3) is determined from the Fourier fast rotation analysis (Section 6.1). The mean deviation $\langle\delta\rangle$ is an input to $x_{mean}(\theta)$ (Eq. 7.10), and the RMS deviation δ_{rms} is an input to $x_{rms}(\theta)$ (Eq. 7.6). The uncertainty on δ is dominated by the momentum-time correlation systematic. The shift in δ caused by the correlation was estimated by comparing the Fourier fast rotation results with results from a new analysis method in Run-2/3 which handles the correlation systematic differently [89]. Typical differences in $\langle\delta\rangle$ and δ_{rms} are $\mathcal{O}(0.0001)$.

Similar to the tracker systematics (Section 7.5.2), $\langle\delta\rangle$ and δ_{rms} were varied and corresponding beam distributions were produced, then the effect on $\tilde{B}$ was evaluated. The effect was studied for selected datasets [9] with relatively large N=4 Fourier amplitudes in the NQ and NS moments, since the δ factors multiply $D_x(\theta)$ which contributes an N=4 component to $x_{mean}(\theta)$ and $x_{rms}(\theta)$.

Figure 7.24 and Figure 7.25 show the approximately linear effect on $\tilde{B}$ of individually varying $\langle\delta\rangle$ and δ_{rms} by ± 0.0001 for the selected datasets (with both parameters required to be ≥ 0). $\langle\delta\rangle + 0.0003$ was included as an additional check. The δ_{rms} effect is < 0.1 ppb, so the uncertainty is effectively zero. The $\langle\delta\rangle$ effect is sub-ppb, but

---

[9] datasets DS-2E and DS-3F, as well as DS-3O to represent the better-centered beam in Run-3b

is taken as an uncertainty (Table 7.14) (with values < 0.1 ppb rounded to zero).

	Run-2	**Run-3a**	**Run-3b**
$\delta\tilde{B}$ (ppb) due to mean momentum offset $\langle\delta\rangle$	0.2	0	0

Table 7.14: Uncertainty on $\tilde{B}$ due to a ± 0.0001 uncertainty in $\langle\delta\rangle$, averaged (with ctag weighting) for the selected dataset in each run.

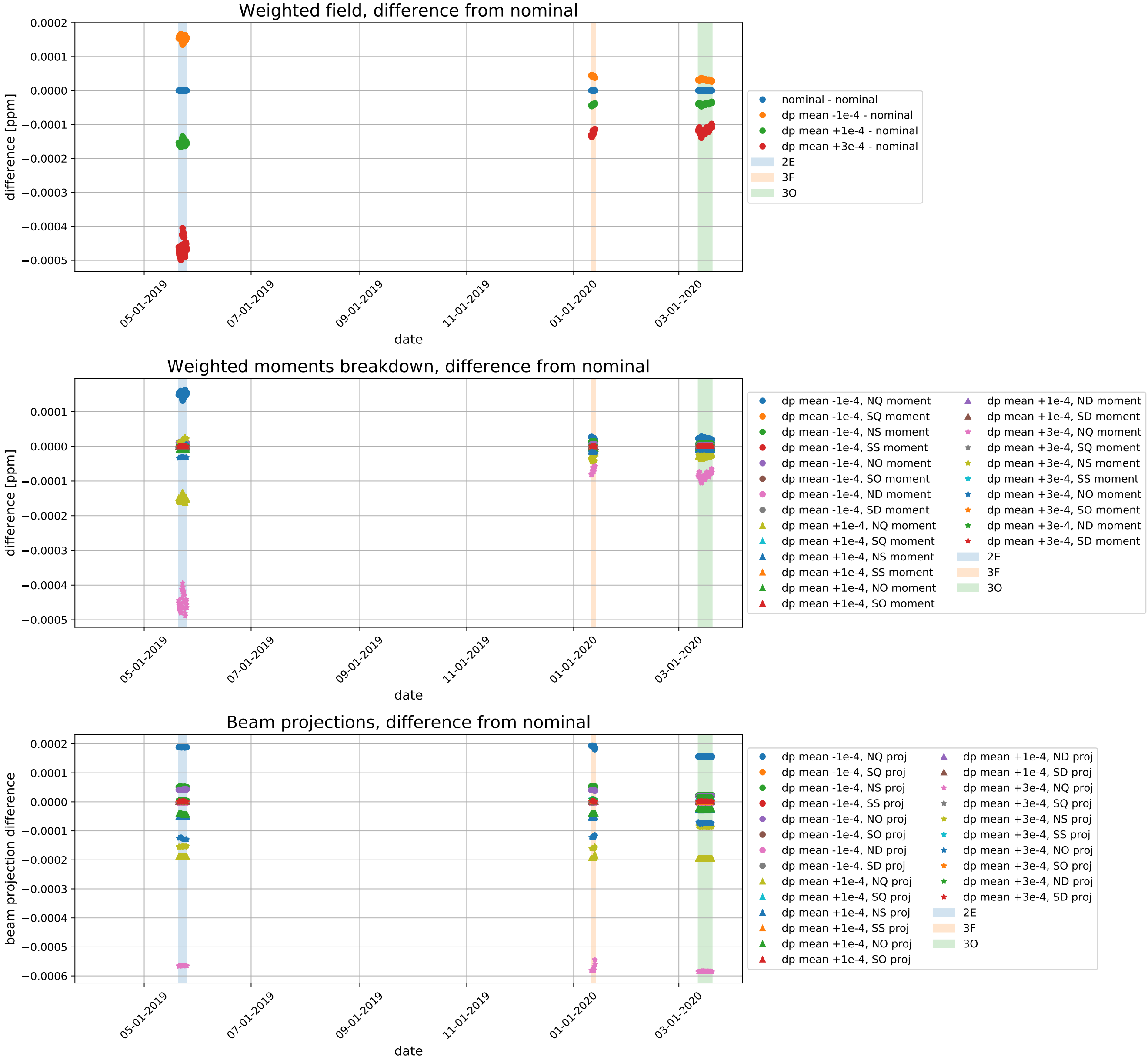

Figure 7.24: Effect on $\tilde{B}$ of varying the mean momentum offset $\langle\delta\rangle$ (top), and a breakdown of the contribution of each weighted field moment (center) and beam projection (bottom).

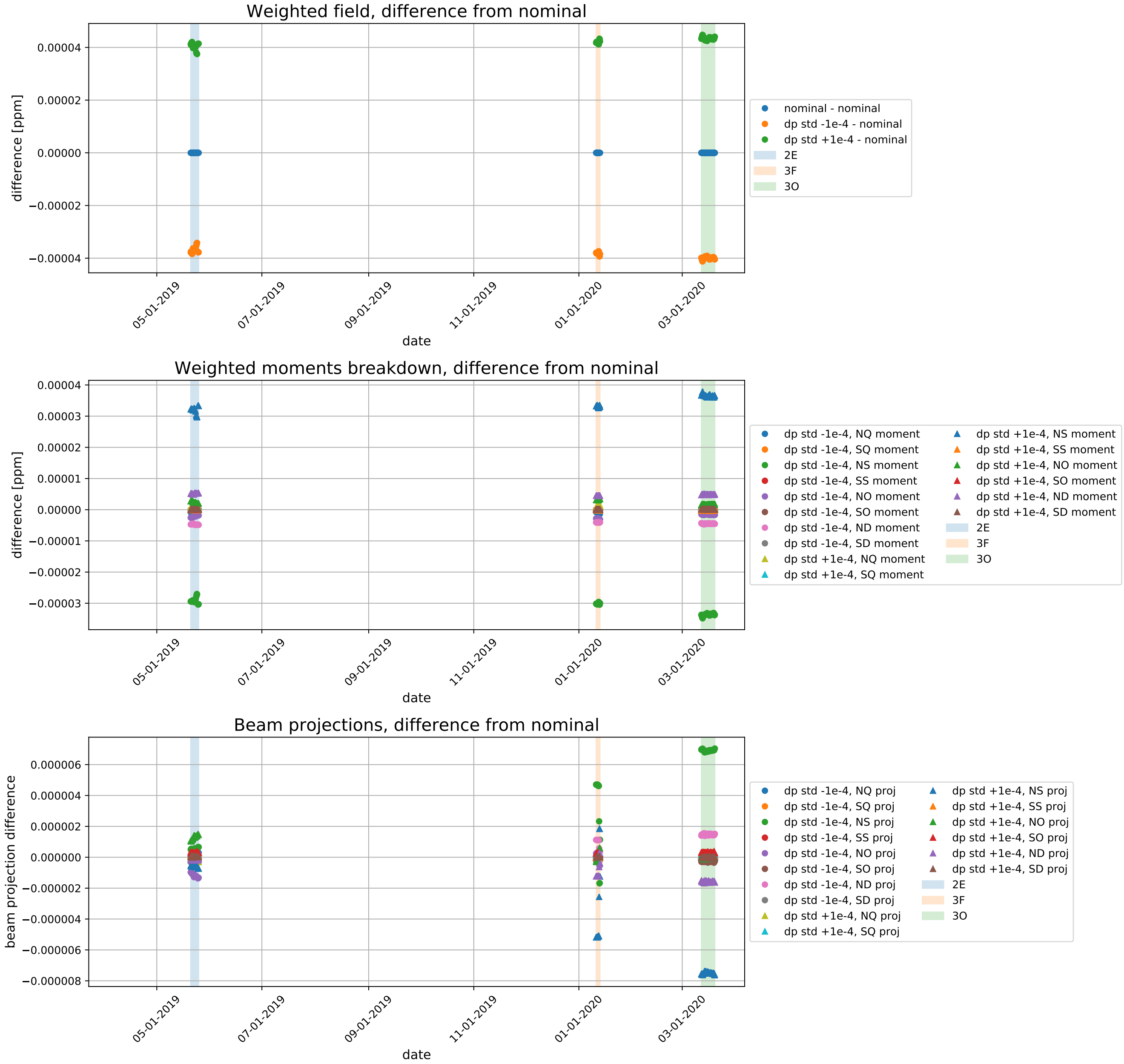

Figure 7.25: Effect on $\tilde{B}$ of varying the RMS momentum offset δ_{rms} (top), and a breakdown of the contribution of each weighted field moment (center) and beam projection (bottom).

7.5.6 In-fill time dependence

In Run-1 the damaged electric quadrupole resistors caused the muon distribution to change over time in the fill, leading to an in-fill time dependence of $\tilde{B}$ which had to be corrected (discussed in Section 2.8). The resistors were replaced before Run-2/3, but some time dependence of the beam remains due to muon losses [55, 56].

A time-dependent field $\tilde{B}(t)$ causes a time-dependent $\omega_a(t)$ which shifts the extracted ω_a; this requires a correction to $\tilde{B}$. For a field with linear time dependence $\frac{d\tilde{B}}{dt}$, the correction relative to $\tilde{B}(t_{start})$ at the analysis start time is $\frac{d\tilde{B}}{dt} \times 2\tau_\mu$ where τ_μ is the lab-frame muon lifetime [90]. However, the standard $\tilde{B}$ corresponds to the time $t_{start} + \tau_\mu$, the weighted mean time for an exponentially-decaying muon population. The required correction is therefore $\Delta\tilde{B} = \frac{d\tilde{B}}{dt} \times \tau_\mu$.

The time-dependent muon distribution effect was estimated with tracker profiles over time in the fill. E. Bottalico provided the time-binned tracker profiles integrated over each run from the phase-acceptance correction analysis [55,56]. The time was randomized before binning to average out beam dynamics frequencies and preserve early-to-late time dependence. Figure 7.26 shows the tracker profile means and widths over time.

The weighted field was calculated for each tracker profile in each time bin, using field moments averaged (with ctag weighting) over the run. Figure 7.27 shows the relative change in $\tilde{B}$ over time in the fill. $\frac{d\tilde{B}}{dt}$ was estimated with a linear fit between 30 µs and 150 µs, although the fit would overestimate the change at late times.

The largest time dependence is seen in tracker station 12 in Run-2, with $\frac{d\tilde{B}}{dt} = 0.007$ ppb/µs. The corresponding correction would be $\Delta\tilde{B} = \frac{d\tilde{B}}{dt} \times \tau_\mu = 0.4$ ppb. Because this effect was roughly estimated at only the run-averaged level and found to be sub-ppb and thus insignificant, the in-fill time dependence correction is taken as zero for Run-2/3.

Transient fields

Magnetic field transient effects from the electric quadrupoles and kicker eddy currents could cause a time-dependent closed orbit distortion. In the Run-1 muon-weighted field analysis [81] these were estimated to affect the x_{COD} amplitude by $< 20\,\mu\mathrm{m}$, corresponding to a few-percent or sub-ppb effect.

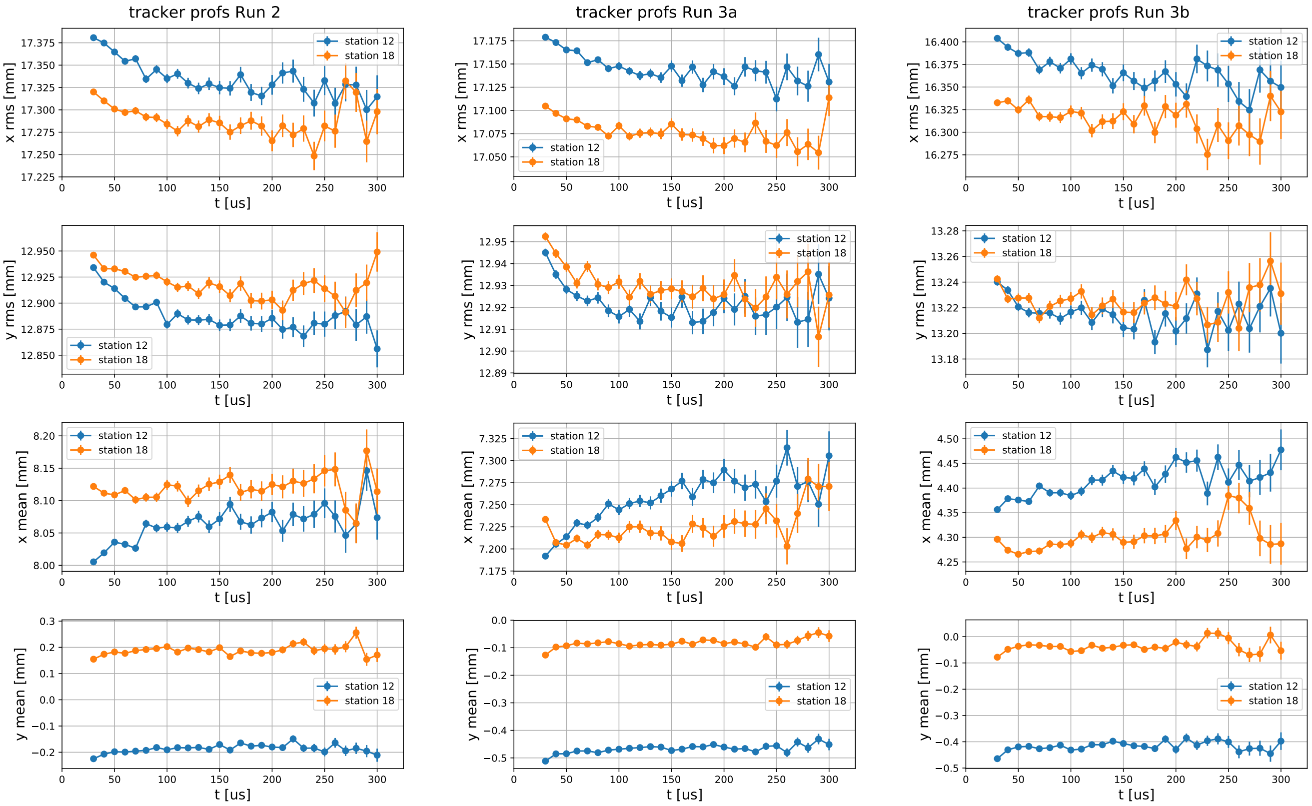

Figure 7.26: Tracker profile in-fill-time dependence (E. Bottalico [56]) from the analysis start time of 30 µs in Run-2, Run-3a, and Run-3b.

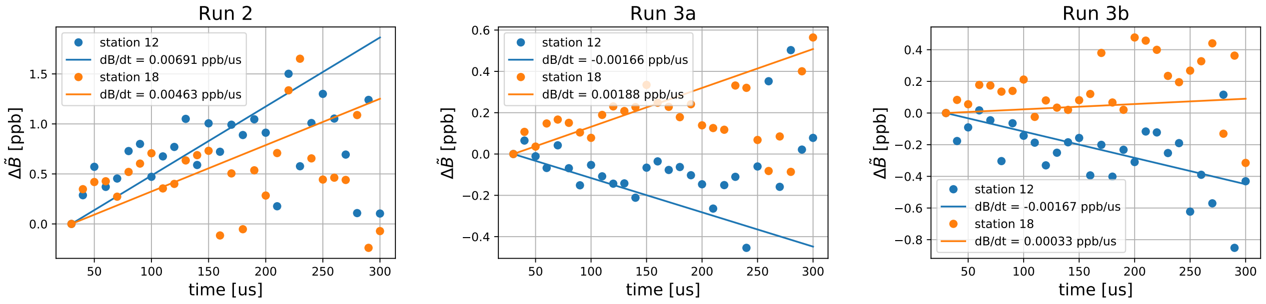

Figure 7.27: $\tilde{B}$ relative change over time in fill in Run-2, Run-3a, and Run-3b

7.6 Summary

The magnetic field experienced by the muons is one of the two experimental observables required to extract a_μ. This muon-weighted magnetic field $\tilde{B}$ is calculated by weighting the magnetic field by the muon beam distribution.

Muon beam distributions are reconstructed in intervals $T_{interval} \approx 2\,\mathrm{h}$ to $3\,\mathrm{h}$ by extrapolating the tracker profiles around the ring using beam dynamics functions (Section 7.3). The beam width varies with azimuth due to betatron oscillations and dispersion, and the beam mean varies due to closed orbit distortions and dispersion.

The Bloch team field analysis for Run-2/3 produced time-interpolated azimuthal field maps called "virtual trolley maps" in each $T_{interval}$ (Section 7.2). The baseline muon weighting procedure for Run-2/3 (Section 7.4) is defined as a function of azimuth. $\tilde{B}$ is calculated by weighting the field multipole moments by the corresponding beam multipole projections in each $T_{interval}$.

Corrections and uncertainties on $\tilde{B}$, described in Section 7.5, are summarized in Table 7.15. The dominant uncertainties are from the tracker y alignment in Run-2, which was reduced in Run-3 due to the smaller SQ field moment, and the x closed orbit distortion due to electric quadrupole misalignments.

	correction $\Delta\tilde{B}$ (ppb)			uncertainty $\delta\tilde{B}$ (ppb)		
	Run-2	**Run-3a**	**Run-3b**	**Run-2**	**Run-3a**	**Run-3b**
Field specific						
Azimuthal averaging				0.8	1.4	1.7
Detector effects						
Tracker acceptance		-		2.1	1.1	0.1
Tracker resolution		-		0.1	0.1	0.1
Tracker y alignment		-		10.7	0.6	0.4
Tracker x alignment		-		4.5	1.3	0.3
Calo acceptance		-		1.0	0.2	0.2
Closed orbit distortion and azimuthal effects						
y_{COD} from radial B		-		1.8	3.7	2.9
x_{COD} from quad misalignment	$+1.3$	$+2.7$	$+2.5$	5.9	6.7	6.3
y_{COD} from quad misalignment	-0.9	-0.5	-0.3	0.1	0.2	0.2
Mean momentum offset $\langle\delta\rangle$		-		0.2	0	0
Other effects						
In-fill time dependence		0			0	
Total	$+0.4$	$+2.3$	$+2.2$	13.6	8.3	7.1

Table 7.15: Corrections and uncertainties on $\tilde{B}$ in each run. Uncertainties are added in quadrature.

Chapter 8

Conclusions

This thesis presents a variety of challenging beam dynamics effects in the Muon $g-2$ experiment which are critical for meeting the experiment's 140 ppb precision goal, and contributions by the author of this thesis toward reaching this goal.

The Inflector Beam Monitoring System (IBMS) detectors, described in Chapter 3, were developed to support muon beam injection into the storage ring. Muon storage efficiency is highly sensitive to beam injection, making it essential for meeting the experimental goal of 21× BNL statistics. The IBMS assists with beam tuning, injection modeling, and continuous beam monitoring. A measurement of the horizontal beam injection parameters, discussed in Chapter 5, was motivated by simulation inconsistencies and changes in the beamline configuration. This measurement provides a point of verification for complex beamline simulations, and delivers realistic input for beam injection modeling which is an important prerequisite for simulation of the stored beam.

The electric field correction to ω_a is calculated from the fast rotation momentum reconstruction, and its uncertainty is dominated by the time-momentum (τ-p) correlation effect introduced by the time-varying kicker, as discussed in Chapter 6. This correlation is a significant systematic which is the subject of ongoing efforts. Based on the successful IBMS detector design, the MiniSciFi (Minimally Intrusive Scintillating Fiber) detector was developed to directly profile the stored beam and characterize the τ-p correlation. Multiple weeks of beam time have been dedicated to measuring the correlation using shortened muon bunches. One challenge in the analysis will be unfolding the injected muon bunch shape from the measured momentum distribution. The final result will provide input to correct the τ-p correlation in the fast rotation reconstruction, which is critical to reduce the uncertainty in this remaining significant systematic.

Characterizing the beam dynamics of the stored beam is also important for calculating the muon-weighted magnetic field, one of the two experimental observables required to determine a_μ. The muon-weighted magnetic field analysis for Run-2/3 is presented in Chapter 7. A host of possible uncertainties was evaluated, with the most notable contributions caused by alignment uncertainties of both the tracker detectors and the electric focusing quadrupoles. This analysis demonstrated that the relevant systematics are well-controlled, and the corresponding uncertainties are sub-dominant in the overall magnetic field uncertainty.

8.1 Outlook

With the Run-2/3 result set to reduce the statistics-dominated uncertainty by a factor of two, significant improvements in nearly all the dominant systematics, and the $21\times$ BNL statistics goal achieved in Run-6, the Muon $g-2$ experiment is poised to deliver an experimental measurement of a_μ to 140 ppb precision. The anticipated experimental precision strongly motivates ongoing efforts in the theory community to achieve comparable precision in the standard model prediction of a_μ, and to resolve discrepancies in the hadronic contributions.

8.1.1 Run-2/3

The Run-2/3 result is planned for upcoming release, with an expected net uncertainty of $\lessapprox 230$ ppb. The imminent ω_a unblinding will reveal the a_μ result.

Recently the ω_a results from seven different analysis groups were relatively unblinded, leaving a common overall blinding factor. Cross-checks and consistency tests between groups are underway. For example, the groups are ensuring consistent treatment in the ω_a fit of the radial coherent betatron oscillation (CBO) decoherence over the fill, caused by the momentum-dependent spread in betatron frequencies. This will likely remain one of the larger ω_a systematics in Run-2/3, of $\mathcal{O}(30\text{ppb})$. The systematic and statistical uncertainties on ω_a are expected to be $\sim$40 ppb and $\sim$200 ppb, respectively.

Of the beam dynamics corrections to ω_a discussed in Section 2.8.1, the dominant Run-1 uncertainty on the phase-acceptance correction is reduced from 75 ppb to $\sim$20 ppb after replacing the damaged quadrupole resistors. The 53 ppb uncertainty on the electric field correction due to the τ-p correlation was also significant in Run-1, and remains one of the highest priorities for the analysis of Run-2/3 and beyond. Two new methods are being used to analyze the correlation; one involves a multi-parameter fit to the calorimeter fast rotation signals [89], and another involves a beam matrix transformation of the tracker radial beam profile [91]. Active progress is being made toward consistency between the methods, but more work is needed to fully characterize the effect. Areas which need to be better understood include the methods' sensitivity to differences in the correlation, effects of the different injected muon bunch shapes, and the evolution of the correlation over the runs. The Run-2/3 uncertainty on the electric field correction is still being determined; it will likely be reduced from Run-1, but may not yet reach the 25 ppb target.

The total uncertainty on $\tilde{\omega}'_p$ is expected to be $\sim$50 ppb, well below the design goal of 70 ppb. This is largely thanks to an improved measurement of the quadrupole-induced transient magnetic field (Section 2.8.2), which reduced the corresponding uncertainty from 92 ppb in Run-1 to $\sim$20 ppb.

8.1.2 Run-4/5/6

After the Run-2/3 result is released, the remaining data collected in Runs 4, 5, & 6 ("Run-4/5/6") will be analyzed and released together. A non-exhaustive selection of prospects for Run-4/5/6 analysis is given below.

The muon-weighted magnetic field will likely have similar characteristics to Run-3b, in which the muon weighting had an effect of only < 3 ppb. This was due to improved transverse uniformity of the magnetic field which significantly reduced the field multipole moments, and the improved kick strength which moved the beam closer to radial center. Additionally, improved thermal stability in the experimental hall reduced variation of the field moments over time in Run-3. With similar field uniformity and stability in Run-4/5/6, the analysis could potentially be simplified by performing the muon weighting at the dataset timescale of $\mathcal{O}$(2 weeks) rather than the few-hour timescale. This should first be studied in a dataset with worst-case field moments and variation. Many of the muon weighting systematics were reduced to < 1 ppb in Run-3b due to the reduced field moments, and can likely be spot-checked in Run-4/5/6 rather than evaluating them in detail.

As muon weighting systematics are sub-dominant, efforts are better spent to reduce more dominant field systematics. Along these lines, the $\sim$20 ppb uncertainty due to experiment configuration differences between trolley field measurement periods and ω_a measurement periods will likely be reduced in Run-4/5/6 by a dedicated measurement, and the $\sim$15 ppb uncertainty from the kicker-induced transient magnetic field will benefit from an independent magnetometer measurement which is currently being analyzed.

The MiniSciFi measurements of the radial stored beam distribution (Section 6.2.2) observe the CBO and its decoherence, and will provide information complementary to the trackers for reducing this systematic in the ω_a fit. Analysis of the MiniSciFi τ-p correlation measurements will provide an independent characterization of the effect, hopefully helping to resolve some of the outstanding issues in the Run-2/3 methods and further reduce the uncertainty.

One important area with opportunities for improvement is simulation of the full beamline (discussed in Chapter 5), which produces a beam phase space distribution before injection into the storage ring. Previous simulations captured the design beamline configuration, but the operating configuration is significantly different. For example, the momentum-cooling wedge (Section 2.2) is not included in the simulation, but it is known to impact the horizontal beam phase space as well as correlations between spin phase and momentum which enter in ω_a beam dynamics corrections [92]. Verifying with real beam measurements, at the ring injection location and along the beamline where possible, is essential to establish realistic conditions. And updated beamline simulation would improve understanding of the input for simulating the stored beam dynamics, which could assist with a variety of outstanding beam dynamics effects.

8.1.3 Standard model prediction

The current standard model (SM) theory prediction a_μ^{SM} is that recommended by the Muon $g-2$ Theory Initiative in 2020 (Section 1.2). The 369 ppb uncertainty is dominated by the hadronic contributions, especially the hadronic vacuum polarization (HVP). Theory groups aim to reduce these uncertainties by 2025 for an a_μ^{SM} prediction with similar precision to the 140 ppb experiment goal [26]. The HVP contribution in particular has the potential to significantly affect the SM value, with the theory community working to understand recent discrepancies in the calculation (Section 1.2.3).

The 2020 recommended a_μ^{HVP} value was calculated from a dispersion integral of experimental $e^+e^- \to$ hadrons cross sections, which is dominated by the low-energy $\pi^+\pi^-$ channel. Lattice QCD calculations of a_μ^{HVP} are approaching a precision similar to the data-driven method; of particular note, the BMW20 result in 2021 corresponds to an SM value which would reduce the tension with experiment to 1.5σ. Lattice groups are working to rigorously cross-check this result. While a discrepancy between dispersion and lattice calculations would constitute a major puzzle if it persists, another mystery has developed in the dispersion approach. The $\pi^+\pi^-$ cross section measurement by CMD-3 released in 2023 disagrees with all previous measurements, and would correspond to an SM prediction closer to the experiment value, potentially within 1.5σ. No immediate explanation for the difference is apparent, and future measurements of this cross section will be essential to understand the discrepancy. The Theory Initiative plans to address these HVP issues and recommend an updated a_μ^{SM} value by late 2023.

With the current ambiguity in the SM prediction, the 4.2σ tension between experiment and theory stands to be either reduced or reinforced following the updated prediction and the Run-2/3 release. The final 140 ppb precision a_μ measurement will be crucial to interpret whether a_μ is revealing new physics beyond the standard model (BSM), which would guide future BSM physics searches.

Bibliography

[1] Richard L. Garwin, Leon M. Lederman, and Marcel Weinrich. Observations of the failure of conservation of parity and charge conjugation in meson decays: the magnetic moment of the free muon. *Phys. Rev.*, 105:1415–1417, Feb 1957.

[2] T. Albahri et al. Measurement of the positive muon anomalous magnetic moment to 0.46 ppm. *Phys. Rev. Lett.*, 126:141801, Apr 2021.

[3] G. W. Bennett et al. Final report of the e821 muon anomalous magnetic moment measurement at bnl. *Phys. Rev. D*, 73:072003, Apr 2006.

[4] T. Aoyama et al. The anomalous magnetic moment of the muon in the standard model. *Physics Reports*, 887:1–166, 2020. The anomalous magnetic moment of the muon in the Standard Model.

[5] John David Jackson. *Classical Electrodynamics*. Wiley, 1999. 3rd ed.

[6] J. J. Sakurai and Jim Napolitano. *Modern Quantum Mechanics*. Addison-Wesley. 2nd ed.

[7] Matthew D. Schwartz. *Quantum Field Theory and the Standard Model*. Cambridge University Press, 2013.

[8] J. E. Nafe, E. B. Nelson, and I. I. Rabi. The hyperfine structure of atomic hydrogen and deuterium. *Phys. Rev.*, 71:914–915, Jun 1947.

[9] Darragh E. Nagle, Renne S. Julian, and Jerrold R. Zacharias. The hyperfine structure of atomic hydrogen and deuterium. *Phys. Rev.*, 72:971–971, Nov 1947.

[10] Julian Schwinger. On quantum-electrodynamics and the magnetic moment of the electron. *Phys. Rev.*, 73:416–417, Feb 1948.

[11] P. Kusch and H. M. Foley. The magnetic moment of the electron. *Phys. Rev.*, 74:250–263, Aug 1948.

[12] Richard H. Parker et al. Measurement of the fine-structure constant as a test of the standard model. *Science*, 360(6385):191–195, 2018.

[13] Léo Morel, Zhibin Yao, Pierre Cladé, and Saida Guellati-Khelifa. Determination of the fine-structure constant with an accuracy of 81 parts per trillion. *Nature*, 588:61–65, 12 2020.

[14] X. Fan, T. G. Myers, B. A. D. Sukra, and G. Gabrielse. Measurement of the electron magnetic moment. *Phys. Rev. Lett.*, 130:071801, Feb 2023.

[15] Mark Thomson. *Modern particle physics*. Cambridge University Press, New York, 2013.

[16] R. L. Workman et al. Review of particle physics. *PTEP*, 2022, 2022.

[17] M. Davier and W. J. Marciano. The theoretical prediction for the muon anomalous magnetic moment. *Ann. Rev. Nucl. Part. Sci.*, 54:115–140, 2004.

[18] Alexander Keshavarzi, Daisuke Nomura, and Thomas Teubner. Muon $g-2$ and $\alpha(M_Z^2)$: A new data-based analysis. *Phys. Rev. D*, 97:114025, Jun 2018.

[19] Aida X. El-Khadra. Muon $g-2$ in the sm: status and prospects. `https://indico.fnal.gov/event/58272/contributions/262207/`, 2023. P5 Town Hall.

[20] M. Davier, A. Hoecker, B. Malaescu, and Z. Zhang. A new evaluation of the hadronic vacuum polarisation contributions to the muon anomalous magnetic moment and to $\alpha(m_z^2)$. *The European Physical Journal C*, 80(3), mar 2020.

[21] CMD-3 Collaboration, F. V. Ignatov, et al. Measurement of the $e^+e^- \to \pi^+\pi^-$ cross section from threshold to 1.2 gev with the cmd-3 detector, 2023.

[22] Fedor Ignatov. Measurement of the $e^+e^- \to \pi^+\pi^-$ cross section with the cmd-3 detector. `https://indico.fnal.gov/event/59052/`, 2023. Scientific seminar and discussion on new CMD-3 result.

[23] Sz. Borsanyi et al. Leading hadronic contribution to the muon magnetic moment from lattice QCD. *Nature*, 593(7857):51–55, apr 2021.

[24] G. Colangelo, A.X. El-Khadra, M. Hoferichter, A. Keshavarzi, C. Lehner, P. Stoffer, and T. Teubner. Data-driven evaluations of euclidean windows to scrutinize hadronic vacuum polarization. *Physics Letters B*, 833:137313, oct 2022.

[25] Luchang Jin. Lattice qcd and the muon $g-2$. `https://www.int.washington.edu/program/schedule/1208/2`, 2023. New physics searches at the precision frontier, University of Washington Institute for Nuclear Theory.

[26] G. Colangelo et al. Prospects for precise predictions of a_μ in the standard model, 2022.

[27] T. Blum, P. A. Boyle, V. Gülpers, T. Izubuchi, L. Jin, C. Jung, A. Jüttner, C. Lehner, A. Portelli, and J. T. Tsang. Calculation of the hadronic vacuum polarization contribution to the muon anomalous magnetic moment. *Phys. Rev. Lett.*, 121:022003, Jul 2018.

[28] Alex Keshavarzi, Kim Siang Khaw, and Tamaki Yoshioka. Muon $g-2$: A review. *Nuclear Physics B*, 975:115675, 2022.

[29] Peter Athron, Csaba Balázs, Douglas H. J. Jacob, Wojciech Kotlarski, Dominik Stöckinger, and Hyejung Stöckinger-Kim. New physics explanations of a^μ in light of the FNAL muon $g-2$ measurement. *Journal of High Energy Physics*, 2021(9), sep 2021.

[30] Andrzej Czarnecki and William J. Marciano. Muon anomalous magnetic moment: A harbinger for "new physics". *Physical Review D*, 64(1), jun 2001.

[31] Dominik Stockinger. Theory: Which bsm models can still accommodate a large deviation. https://gm2-docdb.fnal.gov/cgi-bin/sso/ShowDocument?docid=24318, 2020. GM2-doc-24318.

[32] V. Bargmann, Louis Michel, and V. L. Telegdi. Precession of the polarization of particles moving in a homogeneous electromagnetic field. *Phys. Rev. Lett.*, 2:435–436, May 1959.

[33] W. Liu et al. High precision measurements of the ground state hyperfine structure interval of muonium and of the muon magnetic moment. *Phys. Rev. Lett.*, 82:711–714, Jan 1999.

[34] William D Phillips, William E Cooke, and Daniel Kleppner. Magnetic moment of the proton in h2o in bohr magnetons. *Metrologia*, 13(4):179, oct 1977.

[35] Peter J. Mohr, David B. Newell, and Barry N. Taylor. Codata recommended values of the fundamental physical constants: 2014. *Rev. Mod. Phys.*, 88:035009, Sep 2016.

[36] J. Grange et al. Muon (g-2) technical design report. 2015.

[37] Diktys Stratakis et al. Accelerator performance analysis of the fermilab muon campus. *Phys. Rev. Accel. Beams*, 20:111003, Nov 2017.

[38] Diktys Stratakis. Application of passive wedge absorbers for improving the performance of precision-science experiments. *Phys. Rev. Accel. Beams*, 22:053501, May 2019.

[39] Hannah Binney. *Precession frequency analysis for Run-2 and Run-3 of the Muon $g-2$ experiment*. PhD thesis, University of Washington, 2022.

[40] David Rubin. Injection and storage in the muon ring. `https://gm2-docdb.fnal.gov/cgi-bin/sso/ShowDocument?docid=2820`, 2015. GM2-doc-2820.

[41] T. Albahri et al. Magnetic-field measurement and analysis for the muon $g-2$ experiment at fermilab. *Phys. Rev. A*, 103:042208, Apr 2021.

[42] T. Albahri et al. Beam dynamics corrections to the run-1 measurement of the muon anomalous magnetic moment at fermilab. *Phys. Rev. Accel. Beams*, 24:044002, Apr 2021.

[43] A.P. Schreckenberger et al. *Nuclear Instruments and Methods in Physics Research Section A: Accelerators, Spectrometers, Detectors and Associated Equipment*, 1011:165597, sep 2021.

[44] Tyler Barrett. Fast rotation analysis of run-2 and run-3. `https://gm2-docdb.fnal.gov/cgi-bin/sso/ShowDocument?docid=28236`, 2023. GM2-doc-28236.

[45] B.T. King et al. The straw tracking detector for the fermilab muon g-2 experiment. *Journal of Instrumentation*, 17(02):P02035, feb 2022.

[46] Aaron T. Fienberg. *Measuring the Precession Frequency in the E989 Muon $g-2$ Experiment*. PhD thesis, University of Washington, 2019.

[47] K.S. Khaw et al. Performance of the muon $g-2$ calorimeter and readout systems measured with test beam data. *Nuclear Instruments and Methods in Physics Research Section A: Accelerators, Spectrometers, Detectors and Associated Equipment*, 945:162558, 2019.

[48] T. Albahri et al. Measurement of the anomalous precession frequency of the muon in the fermilab muon $g-2$ experiment. *Phys. Rev. D*, 103:072002, Apr 2021.

[49] Kevin Labe. Cornell preliminary analysis report, run 2/3. `https://gm2-docdb.fnal.gov/cgi-bin/sso/ShowDocument?docid=26301`, 2021. GM2-doc-26301.

[50] Rachel Osofsky. *Magnetic Field Determination for Run 1 of the Fermilab Muon $g-2$ Experiment*. PhD thesis, University of Washington, 2019.

[51] Simon Corrodi et al. E989 note 294: Run 2/3 field documentation: Review. `https://gm2-docdb.fnal.gov/cgi-bin/sso/ShowDocument?docid=28082`, 2023. GM2-doc-28082.

[52] Kevin Labe. Clock system documentation. `https://gm2-docdb.fnal.gov/cgi-bin/sso/ShowDocument?docid=10995`, 2019. GM2-doc-10995.

[53] On Kim. E989 note 267: The origin of the pitch correction. https://gm2-docdb.fnal.gov/cgi-bin/sso/ShowDocument?docid=25124, 2021. GM2-doc-25124.

[54] Josh LaBounty. E989 note 303: Muon losses and estimation of c_{ml} in run-2/3. `https://gm2-docdb.fnal.gov/cgi-bin/sso/ShowDocument?docid=28451`, 2023. GM2-doc-28451.

[55] Elia Bottalico et al. E989 note 292: Phase acceptance note - run-2/3. `https://gm2-docdb.fnal.gov/cgi-bin/sso/ShowDocument?docid=28030`. GM2-doc-28030.

[56] Elia Bottalico. *Beam Dynamics corrections in the measurement of the anomalous precession frequency at the Muon $g-2$ experiment at Fermilab*. PhD thesis, Universita di Pisa, 2023.

[57] James Mott. Run 2/3 analysis: Overview and plans. https://gm2-docdb.fnal.gov/cgi-bin/sso/ShowDocument?docid=25318, 2021. GM2-doc-25318.

[58] David Tarazona. Beam dynamics: Differential decay & latest results. https://gm2-docdb.fnal.gov/cgi-bin/sso/ShowDocument?docid=28702, 2023. GM2-doc-28702.

[59] Slawomir S. Piatek. Physics and operation of an mppc. Technical report, Hamamatsu Corporation and New Jersey Institute of Technology, 2014.

[60] J. Kaspar et al. Design and performance of SiPM-based readout of pbf2 crystals for high-rate, precision timing applications. *Journal of Instrumentation*, 12(01):P01009–P01009, jan 2017.

[61] W. R. Leo. *Techniques for Nuclear and Particle Physics Experiments*. Springer-Verlag, 1987.

[62] S. Eidelman et al. Review of particle physics. *Physics Letters B*, 592:1+, 2004.

[63] K. Wille. *The Physics of Particle Accelerators*. Oxford, 2005.

[64] D. A. Edwards and M. J. Syphers. *An Introduction to the Physics of High Energy Accelerators*. Wiley, 1993.

[65] Mike Syphers. Beam dynamics primer – i. `https://gm2-docdb.fnal.gov/cgi-bin/sso/ShowDocument?docid=14142`, 2018. GM2-doc-14142.

[66] Mike Syphers. Beam dynamics primer – ii. `https://gm2-docdb.fnal.gov/cgi-bin/sso/ShowDocument?docid=14145`, 2018. GM2-doc-14145.

[67] Wolfgang Hillert. Transverse linear beam dynamics i. `https://indico.cern.ch/event/685255/contributions/2957931/`, 2018. Introduction to Accelerator Physics 2018.

[68] Nathan Froemming. *Optimization of Muon Injection and Storage in the Fermilab* $g-2$ *Experiment: From Simulation to Reality*. PhD thesis, University of Washington, 2018.

[69] Diktys Stratakis, Brian Drendel, James P. Morgan, Michael J. Syphers, and Nathan S. Froemming. Commissioning and first results of the fermilab muon campus. *Phys. Rev. Accel. Beams*, 22:011001, Jan 2019.

[70] David Alberto Tarazona. *Beam Dynamics Characterization and Uncertainties in the Muon* $g-2$ *Experiment at Fermilab*. PhD thesis, Michigan State University, 2021.

[71] Joe Grange. Closed orbit distortions. `https://gm2-docdb.fnal.gov/cgi-bin/sso/ShowDocument?docid=2548`, 2019. GM2-doc-2548.

[72] Eremey Valetov. Muon g-2 end-to-end beamline simulations, and systematic analyses of muon losses and origin effects. `https://gm2-docdb.fnal.gov/cgi-bin/sso/ShowDocument?docid=19979`, 2020. GM2-doc-19979.

[73] Joe Bradley, Brian Drendel, and Diktys Stratakis. First measurement of traverse beam optics for the fermilab muon campus using a magnet scanning technique. *Nuclear Instruments and Methods in Physics Research Section A: Accelerators, Spectrometers, Detectors and Associated Equipment*, 903:32–37, 2018.

[74] Alejandro Ramirez et al. Measurement and analysis of beam phase-space distributions for the fermilab muon campus accelerator complex. `https://gm2-docdb.fnal.gov/cgi-bin/sso/ShowDocument?docid=13819`, 2018. GM2-doc-13819.

[75] Beam-ring interface documentation and studies. `https://cdcvs.fnal.gov/redmine/projects/g-2/wiki/BeamTeamIBMSInjection`.

[76] Jim Morgan. M4 and m5 line magnet names, currents and lattice. `https://gm2-docdb.fnal.gov/cgi-bin/sso/ShowDocument?docid=1568`, 2018. GM2-doc-1568.

[77] Nathan Froemming. M5 final-focus beam studies. `https://gm2-docdb.fnal.gov/cgi-bin/sso/ShowDocument?docid=10938`, 2018. GM2-doc-10938.

[78] Brynn MacCoy Anna Driutti, Renee Fatemi. Injection tuning studies for gm2ringsim. `https://gm2-docdb.fnal.gov/cgi-bin/sso/ShowDocument?docid=26665`, 2022. GM2-doc-26665.

[79] Tyler Barrett. E989 note 245: Run 1 fast rotation analysis with the fourier method. `https://gm2-docdb.fnal.gov/cgi-bin/sso/ShowDocument?docid=23636`, 2020. GM2-doc-23636.

[80] Brynn MacCoy Christine Claessens, Peter Kammel. The minimally intrusive scintillating fiber detector (miniscifi). `https://gm2-docdb.fnal.gov/cgi-bin/sso/ShowDocument?docid=26632`. GM2-doc-26632.

[81] Brynn MacCoy, Peter Kammel, et al. E989 note 281: Muon b-field weighting report for bloch team. `https://gm2-docdb.fnal.gov/cgi-bin/sso/ShowDocument?docid=24447`. GM2-doc-24447.

[82] Brynn MacCoy et al. E989 note 314: Run 2/3 muon weighted field documentation. `https://gm2-docdb.fnal.gov/cgi-bin/sso/ShowDocument?docid=28482`. GM2-doc-28482.

[83] Saskia Charity. Field maps. E989 DocDB 28687, `https://gm2-docdb.fnal.gov/cgi-bin/sso/ShowDocument?docid=28687`, 2023. GM2-doc-28687.

[84] James Mott. Beam measurements: Run 1. `https://gm2-docdb.fnal.gov/cgi-bin/sso/ShowDocument?docid=22002`, 2020. GM2-doc-22002.

[85] Tyler Barrett and James Mott. Measurement of the pitch correction for run 1. `https://gm2-docdb.fnal.gov/cgi-bin/sso/ShowDocument?docid=23912`, 2020. GM2-doc-23912.

[86] Alec Tewsley-Booth. Muon-weighting uncertainty update. `https://gm2-docdb.fnal.gov/cgi-bin/sso/ShowDocument?docid=23891`, 2020. GM2-doc-23891.

[87] Jason D. Crnkovic et al. Muon g-2 storage ring beam dynamics. `https://gm2-docdb.fnal.gov/cgi-bin/sso/ShowDocument?docid=9191`, 2020. GM2-doc-9191.

[88] M. J. Syphers. Closed orbit distortions from quad alignment. `https://gm2-docdb.fnal.gov/cgi-bin/sso/ShowDocument?docid=13351`, 2018. GM2-doc-13351.

[89] Rob Carey. Extended cern-style fast rotation analysis: A brief introduction. `https://gm2-docdb.fnal.gov/cgi-bin/sso/ShowDocument?docid=28457`, 2023. GM2-doc-28457.

[90] Simon Corrodi. Transient fields: Run-1. E989 DocDB 22101, `https://gm2-docdb.fnal.gov/cgi-bin/sso/ShowDocument?docid=22101`, 2020. GM2-doc-22101.

[91] David Tarazona. Time-momentum & e-field status. `https://gm2-docdb.fnal.gov/cgi-bin/sso/ShowDocument?docid=28830`, 2023. GM2-doc-28830.

[92] Josh LaBounty. Run-6 momentum-phase measurements. `https://gm2-docdb.fnal.gov/cgi-bin/sso/ShowDocument?docid=28723`, 2023. GM2-doc-28723.

Appendix A

Beam Transfer Matrices

Chapter 4 introduces some fundamental beam dynamics concepts. Beam trajectory solutions can be obtained by a piecewise transfer matrix calculation, as discussed in Section 4.1. Here the standard transfer matrix forms are given explicitly.

For a constant dipole field with $K_x = \frac{1}{R^2}$ and $\Psi = \frac{s}{R}$:

$$\boldsymbol{M(s)} = \begin{pmatrix} \cos\left(\frac{s}{R}\right) & R\sin\left(\frac{s}{R}\right) \\ -\frac{1}{R}\sin\left(\frac{s}{R}\right) & \cos\left(\frac{s}{R}\right) \end{pmatrix} \tag{A.1}$$

For a constant quadrupole field with $K_x = -k$ and $\Psi = \sqrt{k}s$:

$$\boldsymbol{M(s)} = \begin{cases} \begin{pmatrix} \cos\left(\sqrt{k}s\right) & \frac{1}{\sqrt{k}}\sin\left(\sqrt{k}s\right) \\ -\sqrt{k}\sin\left(\sqrt{k}s\right) & \cos\left(\sqrt{k}s\right) \end{pmatrix} & K_x > 0, \text{Focusing Quad} \\ \\ \begin{pmatrix} \cosh\left(\sqrt{k}s\right) & \frac{1}{\sqrt{k}}\sinh\left(\sqrt{k}s\right) \\ \sqrt{k}\sinh\left(\sqrt{k}s\right) & \cosh\left(\sqrt{k}s\right) \end{pmatrix} & K_x < 0, \text{Defocusing Quad} \end{cases} \tag{A.2}$$

For a field-free drift section:

$$\boldsymbol{M(s)} = \begin{pmatrix} 1 & s \\ 0 & 1 \end{pmatrix} \tag{A.3}$$

Section 4.1.2 introduces the 3×3 transfer matrix for trajectories with dispersion $D(s)$. For a constant dipole field with $\Psi = \frac{s}{R}$:

$$\boldsymbol{M(s)} = \begin{pmatrix} \cos(\Psi) & R\sin(\Psi) & R(1-\cos(\Psi)) \\ -\sin(\Psi)/R & \cos(\Psi) & \sin(\Psi) \\ 0 & 0 & 1 \end{pmatrix} \tag{A.4}$$

For a combined-function magnet such as the $g-2$ ring (Section 4.3) with constant dipole and quadrupole fields, a focusing quadrupole/bend section with $K_x = \left(\frac{1}{R^2} - k\right) > 0$ and $\Psi = \sqrt{K_x}s$ can be expressed as:

$$\boldsymbol{M(s)} = \begin{pmatrix} m_{11} & m_{12} & m_{13} \\ m_{21} & m_{22} & m_{23} \\ 0 & 0 & 1 \end{pmatrix} = \begin{pmatrix} \cos(\Psi) & \frac{1}{\sqrt{K_x}}\sin(\Psi) & \frac{1}{RK_x}\left(1-\cos(\Psi)\right) \\ -\sqrt{K_x}\sin(\Psi) & \cos(\Psi) & \frac{1}{R\sqrt{K_x}}\sin(\Psi) \\ 0 & 0 & 1 \end{pmatrix} \tag{A.5}$$

Here m_{ij} are the corresponding 2×2 matrix elements. The matrix can equivalently be written in terms of the dispersion D_x and the 2×2 matrix elements:

$$\boldsymbol{M(s)} = \begin{pmatrix} m_{11} & m_{12} & D_x(s) \\ m_{21} & m_{22} & D'_x(s) \\ 0 & 0 & 1 \end{pmatrix} \tag{A.6}$$

Appendix B

Injected Beam Phase Space Uncertainty Analysis

Section 5.1 presented a measurement of the horizontal phase space of the injected beam. The uncertainty analysis summarized in Section 5.1.6 is detailed here.

In addition to the uncertainty on the Twiss parameters from the fit to data (Section 5.1.3), several other sources of uncertainty were considered. These include the Gaussian fit to the beam profiles measured at PWC025 and IBMS1, possible issues with the PWC025 detector performance, remanent magnetic fields in the downstream quadrupoles (Q024 & Q025) during the measurement, a possible nonzero dispersion originating upstream of Q023, and an offset in the beam upstream of Q023 causing the optics to be off-axis. Another possible source of uncertainty is the asymmetric observed beam profiles not described by the beam transport formalism, discussed in Section 5.1.5. Uncertainties are reported in terms of the x-x' phase space σ matrix elements.

B.1 Q023 Twiss parameters

The covariance matrix $\boldsymbol{V}$ for the extracted Q023 Twiss parameters was produced as described in Section 5.1.4. The corresponding covariance matrix $\boldsymbol{U}$ for the beam widths and correlation coefficients at the end of M5 was calculated with the standard error propagation procedure, as follows.

$$\boldsymbol{U} = \boldsymbol{A}\,\boldsymbol{V}\,\boldsymbol{A^T}, \text{ with } A_{ij} = \frac{\partial \sigma_i}{\partial t_j} \tag{B.1}$$

where $\sigma = \begin{pmatrix} \sigma_x^2 & \sigma_{xx'} & \sigma_{x'}^2 \end{pmatrix}$ is defined at the end of M5 and $t = \begin{pmatrix} \alpha_0 & \beta_0 & \epsilon_0 \end{pmatrix}$ is defined at Q023.

As usual, the diagonal covariance matrix elements U_{ii} are equal to the variances $\delta\sigma_i^2$. Table B.1 shows the resulting uncertainties on the end-of-M5 beam widths and correlation coefficients for the IBMS1X high-resolution scan (Q023 Twiss parameters in Table 5.1).

$\delta\sigma_x$ $[mm]$	$\delta\sigma_{x'}$ $[mrad]$	$\delta\sigma_{xx'}$ $[mm \cdot mrad]$
± 0.03	± 0.4	± 1.7

Table B.1: Propagated uncertainties on the end-of-M5 beam widths and correlation coefficients from extracted Q023 Twiss parameter uncertainties.

For reference, the numerical covariance matrices $\boldsymbol{V}$ (for α_0, β_0 $[m]$, ϵ_0 $[m \cdot rad]$) and $\boldsymbol{U}$ (for σ_x^2 $[m^2]$, $\sigma_{xx'}$ $[m \cdot rad]$, $\sigma_{x'}^2$ $[rad^2]$) are as follows.

$$\boldsymbol{V} = \begin{pmatrix} 7.75 \times 10^{-3} & -3.48 \times 10^{-2} & 4.51 \times 10^{-9} \\ -3.48 \times 10^{-2} & 1.57 \times 10^{-1} & -1.91 \times 10^{-8} \\ 4.51 \times 10^{-9} & -1.91 \times 10^{-8} & 4.51 \times 10^{-15} \end{pmatrix}, \quad \boldsymbol{U} = \begin{pmatrix} 1.01 \times 10^{-12} & 1.75 \times 10^{-12} & 3.04 \times 10^{-12} \\ 1.75 \times 10^{-12} & 3.05 \times 10^{-12} & 5.29 \times 10^{-12} \\ 3.04 \times 10^{-12} & 5.29 \times 10^{-12} & 9.18 \times 10^{-12} \end{pmatrix} \tag{B.2}$$

B.2 Gaussian beam profile fit

A Gaussian fit was used to extract the width σ_x of each beam profile (described in Section 5.1.3). Specific choices in this approach can produce slightly different σ_x values, especially in the case of an asymmetric beam profile. To determine the effect of the width extraction on the fitted Twiss parameters, the width method was varied and new Twiss parameters were extracted for each variation. Then the initial beam defined by each new set of Twiss parameters was transported to the end of M5 (using the combined transfer matrix given by the transport program), and the uncertainty was determined from the resulting variation.

Because the IBMS1X high-resolution measurement provides the primary results, this uncertainty was only evaluated for the IBMS1X high-resolution profiles. Nominally, a Gaussian fit with a 5% minimum intensity threshold was used to extract the width. The method was varied in two ways:

1. Varied the threshold for the Gaussian fit from 0 (all fibers included) to 25%, which varies how much the tails contribute to the fit.
2. Calculated the standard deviation directly (no Gaussian fit) with a threshold of 3% or 5%.

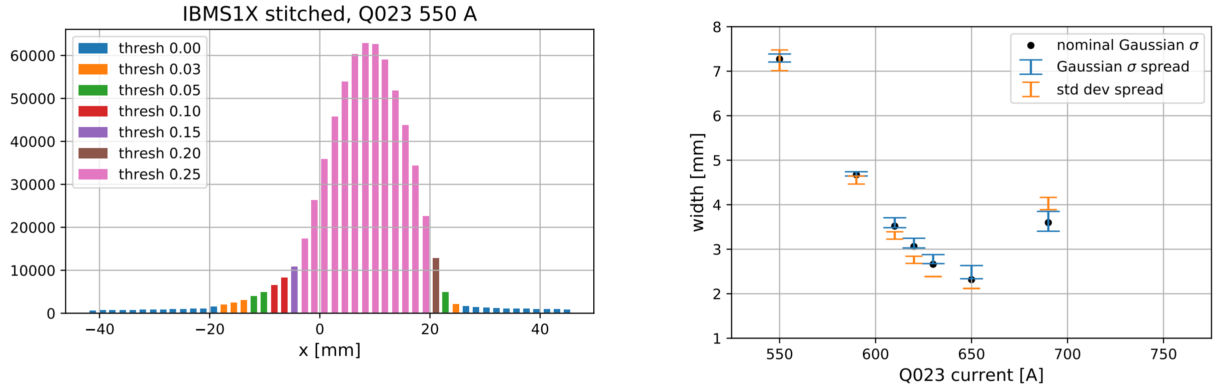

Figure B.1: Left: IBMS1X high-resolution profile with intensity threshold varied from 0 to 25%, shown here for Q023 current 550 A. Right: Spread of extracted widths with the two varied width methods (orange and blue bars), compared with nominal width (black points).

With the maximum and minimum widths from each method variation (upper and lower error bars in Figure B.1), Twiss parameters at Q023 were extracted and transported to the end of M5. Table B.2 shows the resulting maximum variation in the Twiss parameters and the end-of-M5 beam widths and correlation coefficients.

Q023			**End of M5**		
$\Delta\alpha_0$	$\Delta\beta_0$ $[m]$	$\Delta\epsilon_0$ $[mm \cdot mrad]$	$\Delta\sigma_x$ $[mm]$	$\Delta\sigma_{x'}$ $[mrad]$	$\Delta\sigma_{xx'}$ $[mm \cdot mrad]$
-1.4	-4.1	-0.4	-0.1	-0.1	-10.7
$+1.0$	$+7.0$	$+1.5$	$+1.0$	$+0.4$	$+1.3$

Table B.2: Maximum variation (difference from nominal) of Q023 Twiss parameters and end-of-M5 beam widths and correlation coefficients, due to varying the profile fit and width extraction method.

The profile fit uncertainty is largely due to the asymmetric beam profiles (discussed further in Section 5.1.5). This uncertainty describes effects which are not included in the present analysis, and which can be reduced by modeling more realistic asymmetric beam profiles as a function of Q023 current; further Monte Carlo studies should reduce the uncertainty. This uncertainty is therefore a conservative estimate which is included for reference, but is not a true source of uncertainty for this analysis as it corresponds to the asymmetric profiles not fully described by the beam transport formalism.

B.3 Remanent field in downstream quadrupoles

Possible remanent magnetic fields in Q024 & Q025 after they were turned off would affect beam widths measured during the Q023 current scans. The effect was checked in the transport program (Section 5.1.5) by defining nonzero magnetic fields in Q024 & Q025, and comparing σ_x at IBMS1 with the case of zero field in Q024 & Q025.

Quadrupole strengths k in the remanent field case were calculated as in Section 5.1.3, using the "Down-Ramp" measurements for Q024 & Q025 with $I = 0$. Table B.3 shows $k(I = 0)$ for Q024 & Q025. Quadrupole fields were defined as positive (horizontally focusing) in the transport program, representing the most extreme effect where Q024 & Q025 remanent fields have the same sign as Q023.

Quadrupole	$k(I = 0)[\mathrm{m}^{-2}]$
Q024	0.0035
Q025	0.0096

Table B.3: Quadrupole strengths with zero current $k(I = 0)$ for Q024 & Q025.

Figure B.2 shows the difference in σ_x at IBMS1 due to remanent fields in Q024 & Q025 for three Q023 current settings, with a linear fit to estimate the effect at intermediate currents. To evaluate the corresponding effect on the fitted Twiss parameters, the measured σ_x points were shifted by subtracting the fit line as a function of current to correct for a possible remanent field effect. As in Section B.2, new Twiss parameters were extracted from the shifted points, the corresponding initial beam was transported to the end of M5, and the uncertainty was determined from the resulting variation at the end of M5. Table B.4 shows the variation of the Twiss parameters and the end-of-M5 beam widths and correlation coefficients.

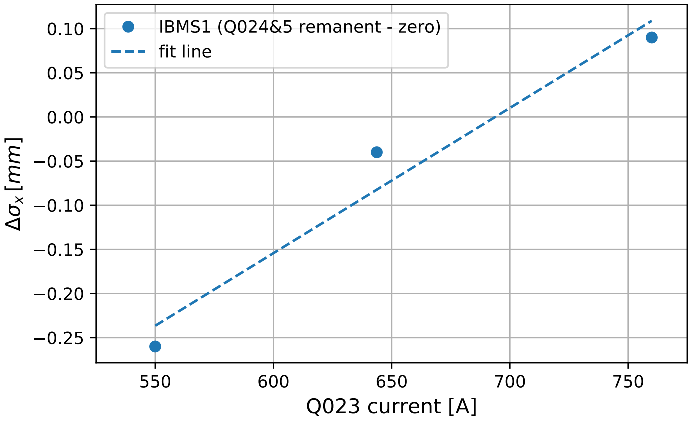

Figure B.2: Difference in σ_x at IBMS1 due to remanent fields in Q024 & Q025, and a linear fit used to estimate the effect for intermediate Q023 current settings. The difference $\Delta\sigma_x = \sigma_x(\text{remanent fields}) - \sigma_x(\text{zero fields})$.

Q023			End of M5		
$\Delta\alpha_0$	$\Delta\beta_0$ $[m]$	$\Delta\epsilon_0$ $[mm \cdot mrad]$	$\Delta\sigma_x$ $[mm]$	$\Delta\sigma_{x'}$ $[mrad]$	$\Delta\sigma_{xx'}$ $[mm \cdot mrad]$
-0.01	-0.1	$+0.4$	$+0.4$	$+0.1$	-3.2

Table B.4: Variation (difference from nominal) of Q023 Twiss parameters and end-of-M5 beam widths and correlation coefficients due to possible remanent fields in Q024 & Q025.

B.4 Dispersion

Dispersion is the momentum-dependent component of the beam trajectory (Section 4.1.2). The TDR lattice has zero dispersion at the end of M5, but the operational lattice has a nonzero dispersion at the end of M5. Up to this point, the expression for the beam width (Eq. 5.1) used to extract the Twiss parameters at Q023 assumed zero dispersion. In the case of a nonzero dispersion, a more convenient form of the matrix transport equation from Section 5.1.1 can be written.

$$\begin{pmatrix} x_s \\ x'_s \\ \delta \end{pmatrix} = \boldsymbol{M} \begin{pmatrix} x_0 \\ x'_0 \\ \delta \end{pmatrix}, \qquad \boldsymbol{M} = \begin{pmatrix} m_{11} & m_{12} & D_{x,s} \\ m_{21} & m_{22} & D'_{x,s} \\ 0 & 0 & 1 \end{pmatrix} \tag{B.3}$$

Here $\delta = \frac{\Delta p}{p_0}$ is the momentum offset, and $\boldsymbol{M}$ is the 3×3 matrix (Section 4.1.2) which includes the dispersion D_x at location s and the elements m_{ij} of the original 2×2 transport matrix from Section 5.1.1.

D_x is a trajectory defined for $\delta = 1$, and the dispersion $D_{x,0}$ at the upstream end of Q023 can be transported to location s.

$$\begin{pmatrix} D_{x,s} \\ D'_{x,s} \\ 1 \end{pmatrix} = \begin{pmatrix} m_{11} & m_{12} & 0 \\ m_{21} & m_{22} & 0 \\ 0 & 0 & 1 \end{pmatrix} \begin{pmatrix} D_{x,0} \\ D'_{x,0} \\ 1 \end{pmatrix} \tag{B.4}$$

The new expression for the beam width including a nonzero dispersion is then

$$\sigma_{x,s}^2 = \epsilon_s\beta_s + \sigma_\delta^2 D_{x,s}^2 = \gamma_0\epsilon_0\, m_{12}^2 + \beta_0\epsilon_0\, m_{11}^2 - 2\alpha_0\epsilon_0\, m_{11}m_{12} + \sigma_\delta^2 \left(m_{11}D_{x,0} + m_{12}D'_{x,0}\right)^2 , \tag{B.5}$$

assuming an axisymmetric beam profile (mean $x = 0$). (In reality the measured beam profiles were not axisymmetric due to the off-axis optics discussed in Section B.5.) To determine the effect of a nonzero dispersion on the extracted Twiss parameters and corresponding end-of-M5 phase space, the fitting procedure in Section 5.1.4 was repeated using Eq. B.5 as the fit function. The RMS momentum offset was taken as $\sigma_\delta = 1.6\%$ [42], and $D_{x,0}$ and $D'_{x,0}$ at Q023 were taken from the operational MAD lattice. Table B.5 shows the resulting Twiss parameters extracted from the IBMS1X high-resolution and PWC025 scans.

	Scan	α_0	$\beta_0[m]$	$\epsilon_0\,[mm \cdot mrad]$
with D_x	IBMS1	-8.0 ± 0.1	35.5 ± 0.4	7.5 ± 0.1
	PWC025	-7.1 ± 0.4	32.3 ± 1.9	13.0 ± 0.5
zero D_x	IBMS1	-9.9 ± 0.1	44.4 ± 0.4	9.3 ± 0.1
	PWC025	-8.3 ± 0.4	37.6 ± 2.0	15.1 ± 0.6

Table B.5: Extracted Twiss parameters (shown with their fit uncertainties) at the upstream end of Q023 from IBMS1X high-resolution and PWC025 scans, including the effect of a nonzero dispersion. For comparison, zero-dispersion results from Table 5.3 are also shown.

As in Section 5.1.5, the initial beam at Q023 defined by the Twiss parameters in Table B.5 was transported to the end of M5 using the transport program, including initial dispersion $D_{x,0}$ and $D'_{x,0}$ from the operational MAD file and $\sigma_\delta = 1.6\%$ (as was used in the fit function). Figure B.3 shows that the resulting beam widths and correlation coefficients are equivalent in the zero-dispersion and nonzero-dispersion cases. The D_x and D'_x widen the beam and reduce the extracted β and ϵ at Q023, but the beam distribution is not affected. The same overall phase space can be described without or with dispersion (left and right sides of Eq. B.6, respectively), and is transported with the same matrix. The variation in beam widths and correlation coefficients between the two cases is zero (Table B.6).

$$\begin{pmatrix} x \\ x' \end{pmatrix}_{zero\,disp} = \begin{pmatrix} x + \delta D_x \\ x' + \delta D'_x \end{pmatrix}_{with\,disp} \tag{B.6}$$

$\Delta\sigma_x$ $[mm]$	$\Delta\sigma_{x'}$ $[mrad]$	$\Delta\sigma_{xx'}$ $[mm \cdot mrad]$
0	0	0

Table B.6: Variation (difference from nominal) in end-of-M5 beam widths and correlation coefficients due to a nonzero dispersion. The beam distribution is unaffected by a nonzero dispersion, so the variation is zero.

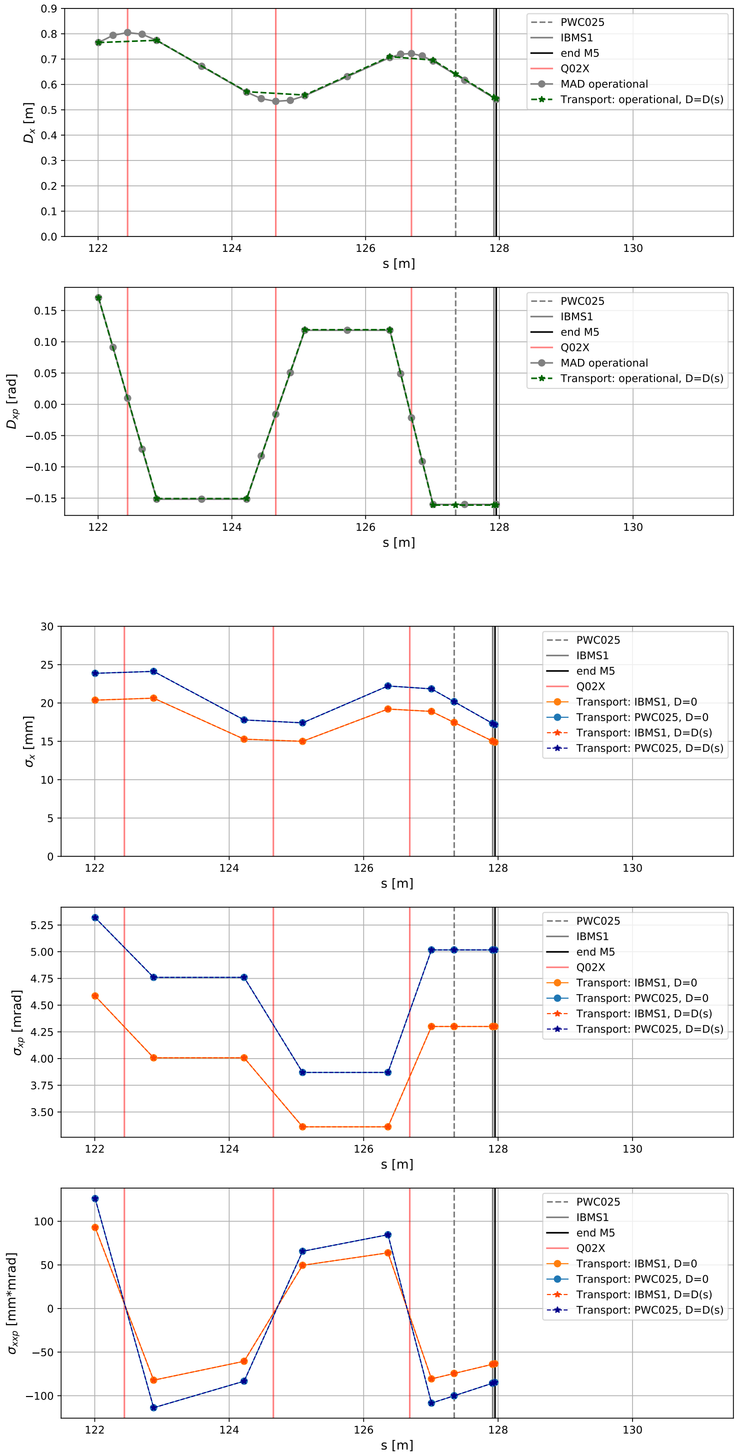

Figure B.3: Top: Dispersion D_x and D'_x from transport program with operational settings (green) and from operational MAD lattice (gray). Bottom: Beam widths σ_x and $\sigma_{x'}$ and correlation coefficient $\sigma_{xx'}$ from transport program including dispersion. Blue and orange correspond to IBMS1 and PWC025 initial beam conditions, respectively. Circles and stars correspond to zero dispersion and nonzero dispersion, respectively. The red vertical lines mark Q023, 24, & 25; the gray lines mark PWC025 and IBMS1; and the black line marks the end of M5.

B.5 Off-axis optics

Horizontal dipole magnets HT020 and HT024 steer the beam horizontally (Figure 5.1). HT020 is upstream of Q023 and causes the beam to enter Q023 off-axis in x and x'. The beam transport formalism (Section 5.1.1) describes a beam which is symmetric about the optical axis, and does not capture any possible effects of off-axis optics. Likewise, the transport program transports the beam along the optical axis using first-order transfer matrix multiplication. Because the dipoles were at their nominal setpoints during the Q023 scan measurements, the off-axis optics are a possible source of uncertainty. A Monte Carlo study using a phase space distribution representing the actual angle and offset of the beam entering Q023 would be required to determine if the effect is significant.